

ELEVATED TEMPERATURE DEFORMATION AND FORMING  
BEHAVIOUR OF AA7075 ALUMINUM SHEET MATERIAL

ELEVATED TEMPERATURE DEFORMATION AND FORMING  
BEHAVIOUR OF AA7075 ALUMINUM SHEET MATERIAL

By IBRAHIM AHMED ABDELATY, B.A., M.Sc.

A Thesis Submitted to the School of Graduate Studies in Partial Fulfilment of the  
Requirements for the Degree Doctor of Philosophy

McMaster University © Copyright by Ibrahim Ahmed Abdelaty, November 2019



McMaster University DOCTOR OF PHILOSOPHY (2019) Hamilton, Ontario

TITLE: Elevated Temperature Deformation and Forming Behaviour of AA7075 Aluminum Sheet Material AUTHOR: Ibrahim Ahmed Abdelaty, B.A. (Military Technical Collage, Cairo, Egypt), M.Sc. (Military Technical Collage, Cairo, Egypt) SUPERVISOR: Professor M. Jain NUMBER OF PAGES: xxvii, 270

## ABSTRACT

Aluminum alloys are considered an attractive candidate in industry for automotive panels and structural parts for their high strength to weight ratio and consequently their higher potential for reduced fuel consumption and reduced carbon emission to environment. Wrought aluminum alloys from AA5xxx and AA6xxx series have been predominantly used in the manufacturing of automotive panels in the past. However, automotive industry is looking at aluminum alloys from AA7xxx series for further light weighting of automotive structural components. Specifically, AA7075 alloy has been of much interest especially in the context of hot stamping process since its room temperature formability is quite limited.

This thesis aims at understanding the room and elevated temperature formability of automotive AA7075 sheet metal in different tempers (F, O and T6). Also, the relationship between formability, fracture, other mechanical properties, and microstructural and surface characteristics of this alloy are investigated in the low temperature range, 180°C-260°C, in isothermal forming of this alloy. SEM-based microstructure studies for void-induced damage and fractographic analysis as well as X-Ray diffraction (XRD) studies for analyzing undeformed and deformed grain orientation distribution (bulk texture) are carried out for different AA7075 sheet metal tempers. In addition, a study of development of surface roughness and material flow localization as a function of strain path and temperature is carried out. Lastly, two different strain rate and temperature dependent constitutive material models for AA7075 sheet are utilized in conjunction with the well-

known Marciniak-Kuczynski (or M-K) theory to predict the forming limits in the above experimental temperature range.

## ACKNOLEGDEMENTS

First, all thanks are to the Merciful God who helped me to finish this modest work.

I would like to express my deepest sense of gratitude to Professor Mukesh Jain, who has readily guided and helped me to accomplish this work. Special thanks also go to my doctoral supervisory committee members, Drs. Hatem Zurob and Peidong Wu, for their assistance and advice to help me in complete this thesis.

I am also grateful to Novelis Aluminum for supporting my research and providing technical suggestions in progress review meetings.

Thanks are due to all staff members of Centre for Automotive Materials and Corrosion (CAMC) at McMaster University for their help and technical support, and especially Dr. Mike Bruhis, who spent much time and effort in training me and supporting my experimental work. Also, I am grateful to Dr. Anantheshwara Kommunje, a senior member of Professor Jain's research group, who helped me to use many of the lab tools and machines properly during my experimental work. I am also grateful to Dr. Zhutian Xu who guided me with the work related to the analytical prediction of forming limits. I would like to thank my colleague Mohamed Shaker for his friendship and many useful technical discussions.

Special appreciation goes to the technical staff members of the Department of Mechanical Engineering at McMaster University, Ron Lodewyks, Michael Lee, Mark MacKenzie, and John Colenbrander for their enthusiastic support of my research work.

Special thanks to my country, Egypt, for supporting and funding my visit to McMaster University.

Last, but not least, neither appreciation nor gratitude could ever pay back to my family for their patience and understanding during the hard times of this work, and especially my wife Amany, and my children Omar, Jana and Layan.

## Table of Contents

1-Introduction and Objectives.....	1
1.1 Introduction .....	1
1.2 Thesis Objectives .....	5
1.3 Thesis Outline .....	7
2-Literature Review .....	8
2.1 General characteristics of precipitation hardening aluminum alloys .....	8
2.2 Processing of precipitation-hardenable aluminum sheet.....	11
2.3 AA7xxx sheet heat-treatments and resulting microstructures.....	13
2.4 Mechanical properties of AA7xxx aluminum sheet.....	18
2.5 Introduction to forming and fracture limits.....	20
2.6 Experimental formability characteristics of AA7075 sheet .....	25
2.7 Microstructure and texture evolution and damage development in AA7xxx sheet during forming.....	30
2.7.1 Surface roughening of deformed sheet material.....	32
2.7.2 Strain hardening and necking characteristics of deformed AA7075 sheet.....	36
2.7.3 Void-induced damage at room and elevated temperatures in aluminum alloys	39
2.7.4 Crystallographic texture in aluminum alloys.....	44
2.8 Summary .....	59
3-Experimental Methodology .....	60
3.1 Material selection and microstructural characterization .....	61
3.1.1 Chemical composition .....	61
3.1.2 Material heat treatment.....	63
3.1.3 Specimen preparation for microscopic studies .....	64
3.1.3.1 Optical microscopy .....	64
3.1.3.2 Scanning electron microscopy .....	67
3.1.4 Microstructure characterization .....	67
3.1.4.1 Microstructural image processing.....	69
3.1.4.2 SEM fractographic image processing .....	71
3.1.5 Crystallographic texture characterization .....	72

3.1.5.1 Specimen preparation.....	72
3.1.5.2 XRD Equipment.....	73
3.1.5.3 XRD data analysis.....	74
3.1.6 Experimental surface roughness data .....	75
3.1.6.1 Surface roughness measurement equipment.....	75
3.1.6.2 Surface roughness testing and data analysis procedure .....	77
3.2 Grid imprinting, strain measurement, mechanical properties and sheet formability characterization .....	78
3.2.1 Specimen machining, periodic grid imprinting and off-line strain measurement .....	81
3.2.2 Uniaxial tensile testing .....	84
3.2.2.1 Tensile test grips and specimen design .....	84
3.2.2.2 Room temperature tests.....	85
3.2.2.3 Elevated temperature tests .....	87
3.2.3 Formability testing.....	88
3.2.3.1 Formability testing using MTS test system .....	88
3.2.3.1.1 Test tooling.....	88
3.2.3.1.2 Test specimen geometries for attaining different strain paths.....	89
3.2.3.1.3 Test procedure .....	90
3.2.3.1.4 FLD determination procedure .....	91
3.2.3.2 Formability testing using MACRODYNE press .....	92
3.2.3.2.1 Test specimen geometries for attaining different strain paths.....	95
3.2.3.2.2 Limit strain determination methodology.....	96
3.3 Summary .....	98
4-Experimental Results and Discussion.....	99
4.1 Material characterization.....	99
4.1.1 Chemical composition, material processing and initial microstructure.....	99
4.2 Uniaxial tensile stress-strain curves .....	105
4.2.1 Room temperature uniaxial tensile test results .....	105
4.2.2 Elevated temperature uniaxial tensile test results.....	108

4.3 AA7075 formability test results .....	119
4.3.1 Punch load versus displacement characteristics from dome tests .....	120
4.3.2 Strain distributions in dome test specimens.....	122
4.3.3 Experimental FLDs.....	131
4.3.4 Continuous strain distributions over the dome surface in room temperature tests .....	136
4.3.5 Comparison of room temperature FLDs of O and T6 temper AA7075 sheets	142
4.3.6 Effect of punch radius on FLDs of O temper AA7075 sheet .....	144
4.4 Microstructure studies .....	145
4.4.1 Initial sheet surface roughness and its evolution .....	145
4.4.1.1 Surface roughness evolution in uniaxial tension test samples .....	146
4.4.1.2 Surface roughness evolution in forming limit (dome) test samples.....	149
4.4.2 Necking and fracture characteristics of uniaxial tensile test samples.....	157
4.4.3 Necking and microstructural characteristics of dome test samples .....	165
4.4.4 Fractographic analysis of damage in deformed uniaxial tensile test samples .	176
4.4.5 Fractographic analysis of void damage in dome test samples .....	184
4.4.6 XRD texture analysis.....	189
4.4.6.1 Un-deformed textures .....	189
4.4.6.2 Deformed textures from dome test samples.....	193
5-Analytical Prediction of FLD for AA7075-O Sheet.....	211
5.1 M-K methodology .....	211
5.2 Hutchinson-Neale (H-N) model .....	227
5.3 FLD prediction by using Field-Backofen constitutive law .....	232
5.4 FLD prediction by using Voce-Kocks constitutive law .....	238
5.5 FLD prediction limitations .....	245
5.6 Summary .....	246
6-Conclusions and Future Work .....	248
6.1 Conclusions .....	248
6.2 Suggestions for Future Work .....	253



## List of Figures

Figure 1.1 Aluminum structural and body components in Audi A8 (Altan, 2005).....	2
Figure 2.1 Schematic drawing of TMP steps for 7xxx series, as modified from reference (Fribourg, 2009).....	12
Figure 2.2 3D optical micrograph of AA7075-T651 grain structure (Pedersen et al., 2011).....	16
Figure 2.3 High resolution TEM images of ternary Al-Zn-Mg alloy showing; (a) GP zones after natural aging, (b) fully coherent, near spherical, GP zones in naturally aged alloy, and (c) $\eta$ plates (see region E in the image) in the peak-aged condition (Mukhopadhyay, 2009).....	17
Figure 2.4 BSE image of AA7075-T651 from FIB tomography revealing grains, $Mg_2Si$ constituents, precipitates, and pores (Singh et al., 2016).....	17
Figure 2.5 Strain rate sensitivity index ( $m$ ) versus temperature for AA7075-T6 from (Hui et al., 2012). ....	20
Figure 2.6 A schematic FLD strain space including limit strain curve (FLC) (Hsu et al., 2008).....	21
Figure 2.7 A schematic diagram representing FLD with the “V” shaped FLC and various ideal strain paths utilized for determination of FLD based on the methodology proposed Nakazima (Nakazima et al., 1968).....	23
Figure 2.8 A schematic diagram representing FLC, typical strain paths and fracture forming limit line (FFL) (Isik et al., 2014).....	25
Figure 2.9 FLD of 1.6 mm thick AA7075-O sheet at room temperature (Silva et al., 2015).....	26
Figure 2.10 AA7075-T6 limiting dome heights at different forming temperatures (Hui et al., 2012).....	28
Figure 2.11 Digitized AA7075-T6 FLD at different temperatures (Huang et al., 2010)...	28
Figure 2.12 Digitized experimental and predicted FLDs for AA7075-O at room temperature (Yang et al., 2015). ....	29
Figure 2.13 Test samples of uniaxial tensile test (left), wide plate bending (middle) and hydraulic bulge test (right) (Yang et al., 2015). ....	30
Figure 2.14 Types of surface defects; (a) elastic distortion, (b) point defects, (c) atomic surface steps caused by single dislocations, (d) larger crystallographic slip steps, (e) surface twins or athermal stress-induced transformation phenomena, (f) non-crystallographic glide traces, (g) surface cracks, (h) orange peel phenomena, (i)	

individual surface deformations, (j) ridging and roping phenomena (Raabe et al., 2003).	33
Figure 2.15 Uniaxial tensile test based schematic of load – deformation curve; (1) Linear elastic portion, (2) proportional limit, (3) yielding (strain hardening start point), (4) ultimate strength, (5) plastic instability (necking), (6) fracture point and (7) unload – reload result in strain hardening (Gupta et al., 2015).	37
Figure 2.16 Uniaxial tensile true stress – strain curves of AA7075-T6 (Huo et al., 2016).	38
Figure 2.17 Uniaxial tensile true stress-strain curves for AA7075-T6 at 220°C (Hui et al., 2012).	39
Figure 2.18 Ductile fracture mechanism (Kanvinde & Deierlein, 2007).	40
Figure 2.19 SEM images for dimple rupture of AA6016-T4 after tensile test at room temperature; (a) low magnification, and (b) high magnification (Thuillier et al., 2012).	42
Figure 2.20 AA6016-T4 X-ray tomography sample shape; (a) whole sample, (b) middle zone A with $R = 6$ mm, (c) middle zone A with $R = 2.5$ mm and (d) middle zone A with $R = 1$ mm (Thuillier et al., 2012).	42
Figure 2.21 SEM fractographic images for AA2024-T3 tensile samples; (a) test temperature of 350°C, (b) test temperature of 450°C and (c) test temperature of 493°C (Wang et al., 2011).	43
Figure 2.22 A schematic illustration of grain orientation in a plate or sheet of polycrystalline material; (a) random grain orientation, and (b) preferred orientation (Prasad & Wanhill, 2017).	45
Figure 2.23 Two coordinate systems, one for specific grains ( $K_A$ and $K_B$ ) in the polycrystalline sheet and the other for the entire sheet specimen ( $X$ , $Y$ and $Z$ ) (H.-J. Bunge, 2013).	46
Figure 2.24 Euler space; (a) $K_A$ and $K_B$ are parallel, (b) rotation of $K_B$ around $Z'$ axis by $\phi_1$ , (c) rotation of $K_B$ around $X'$ axis by $\phi$ and (d) rotation of $K_B$ around $Z'$ axis by $\phi_2$ (H.-J. Bunge, 2013).	46
Figure 2.25 ODF show 5 ideal orientations (Cube, Goss, Brass, Copper and T (also called S)) for FCC metals and alloys at $\phi_2 = 0^\circ$ and $45^\circ$ (Bowen, 1990).	47
Figure 2.26 A schematic representation of different texture orientations in (111) pole figure for FCC material (Moghaddam et al., 2016).	48
Figure 2.27 Extruded sheet metals microstructure; (a) AA7108 and (b) AA7030 (Lademo et al., 2008).	50
Figure 2.28 Mid-thickness pole figures of extruded sheet metals; (a) AA7108 and (b) AA7030 (Lademo et al., 2008).	50

Figure 2.29 Through-thickness microstructure; (a) AA7108 extruded, cold rolled and annealed, (b) AA7108 extruded, cold rolled and annealed at low temperature (400°C for 5 min.), (c) AA7030 extruded, cold rolled and annealed and (d) AA7030 extruded, cold rolled and annealed at low temperature (350°C for 5 min.) (Lademo et al., 2008). .....	52
Figure 2.30 (111) pole figure of cold rolled and heat treated sheet metal; (a) Material A, (b) Material B, (c) Material C and (d) Material D (Lademo et al., 2008). .....	53
Figure 2.31 Through thickness optical microscope images for room temperature fractured tensile samples; (a) AA7108 extruded, cold rolled and annealed, (b) AA7108 extruded, cold rolled and annealed at low temperature (400°C for 5 min.), (c) AA7030 extruded, cold rolled and annealed and (d) AA7030 extruded, cold rolled and annealed at low temperature (350°C for 5 min.) (Lademo et al., 2008). .....	55
Figure 2.32 (111) pole figures of AA7075 and AA7020; (a) AA7075-T7351 starting material, (b) AA7075 after 70% reduction, (c) AA7020-T651 starting material and (d) AA7020 after 70% reduction (Narayanan et al., 2012). .....	56
Figure 2.33 Mid-thickness ODFs after 70% thickness reduction; (a) AA7075 and (b) AA7020 (Narayanan et al., 2012). .....	57
Figure 2.34 Shear bands observed in cold rolled alloys; (a) AA7075 after 50% reduction, (b) AA7075 after 70% reduction, (c) AA7020 after 50% reduction and (d) AA7020 after 70% reduction (Narayanan et al., 2012). .....	58
Figure 3.1 Inductively coupled plasma ICP-OES device type VISTA-PRO used for composition analysis of AA7075 sheet. ....	62
Figure 3.2 A schematic drawing of ICP set-up (Laboratory, 2014). ....	62
Figure 3.3 Heat treatment furnace type KF-KILN. ....	64
Figure 3.4 STRUERS precision saw device. ....	65
Figure 3.5 STRUERS automatic grinder/polisher device. ....	65
Figure 3.6 AA7075 LDH sample preparation for microscopic examination. ....	66
Figure 3.7 Photographs of a mounted AA7075 dome sample; (a) before carbon coating and (b) after carbon coating. ....	67
Figure 3.8 A photograph of KEYENCE model VHX-2000 digital optical microscope. ....	69
Figure 3.9 A photograph of JOEL 6610LV scanning electron microscope. ....	69
Figure 3.10 Image delineation step; (a) Initial image and (b) post- delineation image. ....	70
Figure 3.11 Image binarization by thresholding; (a) before thresholding and (b) after thresholding. ....	71
Figure 3.12 Processing of a SEM fractographic image from fracture surface of a uniaxial tension AA7075 test specimen at room temperature using KEYENCE digital optical	

microscope image processing software; (a) original SEM image and (b) image after processing. ....	72
Figure 3.13 A photograph of X-ray equipment type Bruker D8 DISCOVER with DAVINCI diffractometer for bulk texture measurements on AA7075 samples. ....	74
Figure 3.14 ALICONA non-contact optical roughness measurement system. ....	76
Figure 3.15 Non-contact surface roughness measurements; (a) AA7075-O un-deformed sheet metal and (b) AA7075-O uniaxial tensile sample tested at 220°C with test speed of 1 mm/min. ....	77
Figure 3.16 Illustrations showing speckle patterns of different quality and contrast; (a) low contrast, (b) high contrast with disturbed large spots and (c) good high contrast pattern (ARAMIS, 2007). ....	78
Figure 3.17 ARAMIS online strain measurement system. ....	79
Figure 3.18 A schematic of DIC methodology for strain measurements (Lagattu et al., 2004). ....	81
Figure 3.19 Electrochemical etching process; (a) schematic of device setup (Ozturk et al., 2009) and (b) photographs of deformed (dome) and un-deformed test samples of one specific strain path applied with a periodic grid pattern. ....	83
Figure 3.20 ARGUS offline strain measurement system. ....	83
Figure 3.21 Uniaxial tensile test sample; (a) photograph of the test sample and (d) sample drawing with dimensions (Comley, 2007) (all sample dimensions are in mm). ....	85
Figure 3.22 Grips utilized for tensile testing; (a) grips and tensile test sample assembly, and (b) disassembled grips and test sample. ....	85
Figure 3.23 Servo-hydraulic MTS uniaxial tensile test machine equipped with INSTRON environmental chamber for elevated temperatures tests. Strain measurement system, ARAMIS-2D with a single CCD camera, mounted on a tripod was used to record images of the deforming test specimens. ....	86
Figure 3.24 Photograph of the elevated temperature FLD tooling; (a) detail drawing and (b) actual tooling. ....	89
Figure 3.25 Test specimen geometries for obtaining experimental FLDs using small punch tooling (all dimensions in mm) (Guowei Zhou, 2015). ....	90
Figure 3.26 ARGUS strain map of uniaxial strain path specimen tested at 180°C; (a) actual deformed sample and (b) ARGUS strain map. ....	92
Figure 3.27 MACRODYNE 150 Ton hydraulic press equipped with 101.6 mm punch diameter dome test tooling. ....	94
Figure 3.28 ARAMIS online strain measurement system CCD cameras attached to MACRODYNE 150 Ton hydraulic press and located directly above the deforming dome specimen. ....	94

Figure 3.29 Test specimen drawings for attaining different strain paths deformed with 101.6 mm diameter hemispherical punch during dome tests (all dimensions are in mm).....	95
Figure 3.30 Schematic illustration of time-dependent approach for obtaining the FLD of sheet material from continuous strain map data for each strain path from the literature (Martínez-Donaire et al., 2014). ....	97
Figure 4.1 A schematic of AA7075 processing steps (Fribourg, 2009). ....	100
Figure 4.2 A collage of optical micrographs of un-deformed AA7075-O sheet representing 3D microstructure from LT, ST and ND planes (Mag. 200 X). ....	102
Figure 4.3 A collage of optical micrographs of un-deformed AA7075-T6 sheet representing 3D microstructure from LT, ST and ND planes (Mag. 200 X). ....	102
Figure 4.4 A collage of EBSD pattern from three orthogonal planes for AA7075-O sheet. ....	104
Figure 4.5 3D volumetric representations of EBSD for AA7075-T6 sheet.....	104
Figure 4.6 Flow stress-strain curves for AA7075-F in rolling direction. Tests conducted at speeds of 1 and 10 mm/min at room temperature.....	107
Figure 4.7 Flow stress-strain curves for AA7075-O in rolling direction. Tests conducted at speeds of 1 and 10 mm/min at room temperature.....	107
Figure 4.8 Flow stress-strain curves for AA7075-T6 in rolling direction. Tests conducted at speeds of 1 and 10 mm/min at room temperature.....	108
Figure 4.9 Flow stress-strain curves for AA7075-O in rolling direction. Tests conducted at speeds of 1 and 10 mm/min at three elevated temperatures. ....	110
Figure 4.10 Flow stress-strain curves for AA7075-F in rolling direction. Tests conducted at a speed of 1 mm/min at three elevated temperatures.....	111
Figure 4.11 Flow stress-strain curves for AA7075-F in rolling direction. Tests conducted at a speed of 10 mm/min at three elevated temperatures.....	111
Figure 4.12 Flow stress-strain curves for AA7075-O in rolling direction. Tests conducted at a speed of 1 mm/min at three elevated temperatures.....	112
Figure 4.13 Flow stress-strain curves for AA7075-O in rolling direction. Tests conducted at a speed of 10 mm/min at three elevated temperatures.....	112
Figure 4.14 Flow stress-strain curves for AA7075-T6 in rolling direction. Tests conducted at a speed of 1 mm/min at three elevated temperatures.....	112
Figure 4.15 Flow stress-strain curves for AA7075-T6 in rolling direction. Tests conducted at a speed of 10 mm/min at three elevated temperatures.....	113
Figure 4.16 A plot of yield stress versus test temperature for the sheet material in three temper states tested at a test speed of 1 mm/min.....	115

Figure 4.17 A plot of yield stress versus test temperature for the sheet material in three temper states tested at a test speed of 10 mm/min.....	115
Figure 4.18 Experimental and power law fitted flow stress-strain curves of AA7075-O. Tests conducted at speeds of 1 and 10 mm/min at room temperature and three elevated temperatures. ....	117
Figure 4.19 Onset of diffused necking for AA7075-O tensile test samples tested at speed of 1 mm/min. ....	118
Figure 4.20 Onset of diffused necking for AA7075-O tensile test samples tested at speed of 10 mm/min. ....	119
Figure 4.21 Punch load versus displacement curves from hemispherical dome stretching tests for AA7075-O sheet. The graphs correspond to test at, (a) room temperature, (b) 180°C, (c) 220°C, and (d) 260°C.....	121
Figure 4.22 ARGUS strain maps of various specimen geometries tested for AA7075-O at 220°C. White areas in the strain maps are regions where strain calculations could not be completed due to poor image quality.....	123
Figure 4.23 Major strain distributions for 12.5 mm width dome specimens (UT) in O temper formed at room temperature and 220°C. ....	125
Figure 4.24 Major strain distributions for 70 mm width dome specimens (PST) in O temper formed at room temperature and 220°C. ....	126
Figure 4.25 Major strain distributions for 100 mm width dome specimens (BBT) in O temper formed at room temperature and 220°C. ....	126
Figure 4.26 A comparison of major strain distributions for 12.5 mm width dome specimens (UT) in O and T6 tempers formed at 220°C.....	127
Figure 4.27 A comparison of major strain distributions for 70 mm width dome specimens (PST) in O and T6 tempers formed at 220°C. ....	128
Figure 4.28 A comparison of major strain distributions for 100 mm width dome specimens (BBT) in O and T6 tempers formed at 220°C.....	128
Figure 4.29 ARGUS strain maps from various specimen geometries of AA7075-T6 dome specimens tested at 220°C. ....	130
Figure 4.30 FLD of AA7075-O sheet at room temperature ( $FLD_0 = 0.28$ ).....	132
Figure 4.31 FLD of AA7075-O sheet at 180°C ( $FLD_0 = 0.37$ ).....	133
Figure 4.32 FLD of AA7075-O sheet at 220°C ( $FLD_0 = 0.4$ ).....	133
Figure 4.33 FLD of AA7075-O sheet at 260°C ( $FLD_0 = 0.38$ ).....	134
Figure 4.34 A comparison of FLCs of AA7075-O sheet at different forming temperatures. ....	134
Figure 4.35 FLD of AA7075-T6 sheet at 220°C ( $FLD_0=0.2$ ).....	136
Figure 4.36 A comparison of FLDs of AA7075-O and T6 sheets at 220°C.....	136

Figure 4.37 A typical major strain map of a full dome specimen from a continuously recorded ARAMIS data set during the test.....	137
Figure 4.38 Major and minor strain distributions for AA7075-O dome specimens of different specimen width tested by using 101.6 mm diameter punch tooling at room temperature, (a) width 12.7 mm (UT), (b) width 127 mm (PST), and (c) width 177.8 mm (BBT).....	139
Figure 4.39 Major and minor strain distributions for AA7075-T6 dome specimens of different specimen width tested by using 101.6 mm diameter punch tooling at room temperature, (a) width 12.7 mm (UT), (b) width 127 mm (PST), and (c) width 177.8 mm (BBT).....	140
Figure 4.40 UT, PST and BBT path for dome specimens in the O-temper specimens tested by using 101.6 mm diameter punch tooling at room temperature.....	141
Figure 4.41 UT, PST and BBT path for dome specimens in the T6-temper specimens tested by using 101.6 mm diameter punch tooling at room temperature.....	142
Figure 4.42 FLCs of AA7075-O and AA7075-T6 temper sheets at room temperature using 101.6 mm diameter hemispherical punch. ....	144
Figure 4.43 FLCs of AA7075-O sheet at room temperature from two different NAKAZIMA test tool set-ups. ....	145
Figure 4.44 2D surface roughness maps (NP plane) of un-deformed sample in the; (a) as-fabricated (F), (b) fully- annealed (O) and (c) peak-aged (T6) temper conditions. The scanned sample surface area is 1.6 mm x 1.6 mm.....	148
Figure 4.45 2D surface roughness maps (NP plane) of deformed samples under the following tempers and test conditions; (a) O-temper tested with test speed of 1 mm/min at room temperature, (b) O-temper tested with test speed of 1 mm/min at 220°C, (c) T6-temper tested with test speed of 1 mm/min at room temperature, and (d) T6-temper tested with test speed of 1 mm/min at 220°C.....	149
Figure 4.46 3D surface roughness maps of deformed O-temper samples obtained using 50.8 mm punch at room temperature corresponding to; (a) UT at the pole and (b) UT in the neck region, (c) PST at the pole, (d) PST in the neck region, (e) BBT at the pole, and (f) BBT in the neck region. ....	152
Figure 4.47 3D surface roughness maps of deformed O-temper samples obtained using 50.8 mm punch at 220°C corresponding to; (a) UT at the pole and (b) UT in the neck region, (c) PST at the pole, (d) PST in the neck region, (e) BBT at the pole, and (f) BBT in the neck region.....	153
Figure 4.48 3D surface roughness maps of deformed T6-temper samples obtained using 101.6 mm punch at room temperature corresponding to; (a) UT at the pole and (b) UT in the neck region, (c) PST at the pole, (d) PST in the neck region, (e) BBT at the pole, and (f) BBT in the neck region. ....	154

Figure 4.49 3D surface roughness maps of deformed T6-temper samples obtained using 50.8 mm punch at 220°C corresponding to; (a) UT at the pole and (b) UT in the neck region, (c) PST at the pole, (d) PST in the neck region, (e) BBT at the pole, and (f) BBT in the neck region.....	155
Figure 4.50 A photograph of fractured UT sample of AA7075-O formed by using 101.6 mm diameter hemispherical punch tooling at room temperature. ....	156
Figure 4.51 Through-thickness section from LT plane of etched AA7075-O uniaxial tension test sample tested at a speed of 1 mm/min at room temperature. ....	157
Figure 4.52 Uniaxial tensile test fracture thickness strain versus test temperature for O-temper sheet. ....	161
Figure 4.53 Optical micrograph of through-thickness section of an etched AA7075-O uniaxial tensile sample tested at 10 mm/min and 220°C showing highly elongated grains.....	162
Figure 4.54 Uniaxial tensile test fracture thickness strain versus test temperature for T6 temper sheet. ....	165
Figure 4.55 A close-up view of through-thickness fractured region of etched T6 temper etched tensile test specimen tested at 10 mm/min and 220°C showing intergranular fracture.....	165
Figure 4.56 AA7075-T6 fractured dome samples deformed by 101.6 mm diameter punch tooling set at room temperature; (a) UT, (b) PST, and (c) BBT.....	167
Figure 4.57 Low magnification SEM images of the necked region (LT plane) of dome test samples from various test conditions; (a-c) O-temper UT, PST and BBT specimens tested at RT with thickness strain of -0.425, -0.45 and -0.55 respectively, (d-f) O-temper UT, PST and BBT specimens tested at 220°C with thickness strain of -0.415, -0.555 and -0.725 respectively, and (g-i) T6-temper UT, PST and BBT specimens tested at 220°C with thickness strain of -0.35, -0.25 and -0.525 respectively. ....	168
Figure 4.58 Low magnification OM images of the necked region of dome test samples (LT plane) from various test conditions; (a-c) O-temper UT, PST and BBT specimens tested at RT with thickness strain of -0.425, -0.45 and -0.55 respectively, (d-f) O-temper UT, PST and BBT specimens tested at 220°C with thickness strain of -0.415, -0.555 and -0.725 respectively, and (g-i) T6-temper UT, PST and BBT specimens tested at 220°C with thickness strain of -0.35, -0.25 and -0.525 respectively. ....	169
Figure 4.59 Field measurements of void area from necked dome samples tested under different test conditions; (a-c) O-temper UT, PST and BBT specimens tested at RT, (d-f) UT, PST and BBT specimens tested at 220°C, and (g-i) T6-temper UT, PST and BBT specimens tested at 220°C. ....	171



Figure 4.60 Field measurements of precipitate area from necked dome samples tested under different test conditions; (a-c) O-temper UT, PST and BBT specimens tested at RT, (d-f) UT, PST and BBT specimens tested at 220°C, and (g-i) T6-temper UT, PST and BBT specimens tested at 220°C.....	172
Figure 4.61 SEM image of through thickness neck region of polished PST dome sample of AA7075-O; (a) deformed at RT, and (b) deformed at 220°C. ....	173
Figure 4.62 SEM image of through thickness neck region of polished dome sample of AA7075-T6 deformed at 220°C; (a) UT, and (b) PST. ....	174
Figure 4.63 SEM fractographic images of fracture surfaces of AA7075-O uniaxial tension samples tested at room temperature corresponding to test speeds; (a, c and e) 1 mm/min, and (b, d and f) 10 mm/min.....	178
Figure 4.64 SEM fractographic images of fracture surfaces for AA7075-O uniaxial tension sample tested at 220°C corresponding to test speeds; (a, c and e) 1 mm/min, and (b, d and f) 10 mm/min. ....	179
Figure 4.65 SEM fractographic images after image processing of fractured AA7075-O uniaxial tension sample tested at 10 mm/min; (a) room temperature test, and (b) 220°C test. ....	180
Figure 4.66 SEM fractographic images of fracture surfaces of failed T6 uniaxial tension samples tested at room temperature corresponding to test speeds; (a, c) 1 mm/min, and (b, d) 10 mm/min where zone (1) presents cleavage-like while zone (2) shows micro-void coalescence. ....	182
Figure 4.67 SEM fractographic images of fracture surfaces of AA7075-T6 uniaxial tension samples tested at 220°C corresponding to test speeds; (a, c) 1 mm/min, and (b, d) 10 mm/min. ....	183
Figure 4.68 SEM fractographic images after image processing of fractured AA7075-T6 uniaxial tension sample tested at 10 mm/min; (a) room temperature test, and (b) 220°C test. ....	183
Figure 4.69 SEM fractographic images from the mid-thickness region of failed O-temper dome samples tested at room temperature for the following strain paths; (a, b) UT sample, (c, d) PST sample, and (e, f) BBT sample.....	185
Figure 4.70 SEM fractographic images from the mid-thickness region of failed O-temper dome samples tested at 220°C for the following strain paths; (a, b) UT sample, (c, d) PST sample, and (e, f) BBT sample. ....	186
Figure 4.71 SEM fractographic images from the mid-thickness region for AA7075-T6 dome samples formed at 220°C; (a) and (b) UT sample, (c) and (d) PST sample and (e) and (f) BBT sample. ....	187
Figure 4.72 {111} PFs for un-deformed AA7075 sheets; (a) as fabricated (or F temper), (b) fully-annealed (or O temper) and (c) peak-aged (or T6 temper). ....	190

Figure 4.73 ODFs for AA7075-F un-deformed sheet material.....	191
Figure 4.74 ODFs for AA7075-O un-deformed sheet. ....	192
Figure 4.75 ODFs for AA7075-T6 un-deformed sheet. ....	192
Figure 4.76 {111} PFs at the pole of dome in O-temper material deformed at room temperature; (a) UT sample, (b) PST sample and (c) BBT sample.....	194
Figure 4.77 {111} PFs in the neck region of dome in O-temper material deformed at room temperature in; (a) UT sample, (b) PST sample, and (c) BBT sample. ....	194
Figure 4.78 ODFs at the pole of AA7075-O UT strain path dome sample deformed at room temperature.....	195
Figure 4.79 ODFs in the neck of AA7075-O UT strain path dome sample deformed at room temperature.....	196
Figure 4.80 ODFs at the pole of AA7075-O PST strain path dome sample deformed at room temperature.....	196
Figure 4.81 ODFs in the neck of AA7075-O PST strain path dome sample deformed at room temperature.....	197
Figure 4.82 ODFs at the pole of AA7075-O BBT strain path dome sample deformed at room temperature.....	197
Figure 4.83 ODFs in the neck of AA7075-O BBT strain path dome sample deformed at room temperature.....	198
Figure 4.84 {111} PFs from the pole region for O-temper dome samples deformed at 220°C corresponding to strain paths; (a) UT sample, (b) PST sample, and (c) BBT sample.....	199
Figure 4.85 {111} PFs from the neck region for O-temper dome samples deformed at 220°C corresponding to strain paths; (a) UT sample, (b) PST sample, and (c) BBT sample.....	200
Figure 4.86 ODFs at the pole of AA7075-O UT strain path dome sample deformed at 220°C.....	201
Figure 4.87 ODFs in the neck of AA7075-O UT strain path dome sample deformed at 220°C.....	201
Figure 4.88 ODFs at the pole of AA7075-O PST strain path dome sample deformed at 220°C.....	202
Figure 4.89 ODFs in the neck of AA7075-O PST strain path dome sample deformed at 220°C.....	202
Figure 4.90 ODFs at the pole of AA7075-O BBT strain path dome sample deformed at 220°C.....	203
Figure 4.91 ODFs in the neck of AA7075-O BBT strain path dome sample deformed at 220°C.....	203

Figure 4.92 {111} PFs from the pole region of the T6-temper dome sample deformed at 220°C corresponding to strain paths, (a) UT sample, (b) PST sample, and (c) BBT sample.....	205
Figure 4.93 {111} PFs from the neck region of the T6-temper dome sample deformed at 220°C corresponding to strain paths, (a) UT sample, (b) PST sample, and (c) BBT sample.....	205
Figure 4.94 ODFs at the pole of AA7075-T6 UT strain path dome sample deformed at 220°C.....	206
Figure 4.95 ODFs in the neck of AA7075-T6 UT strain path dome sample deformed at 220°C.....	207
Figure 4.96 ODFs at the pole of AA7075-T6 PST strain path dome sample deformed at 220°C.....	207
Figure 4.97 ODFs in the neck of AA7075-T6 PST strain path dome sample deformed at 220°C.....	208
Figure 4.98 ODFs at the pole of AA7075-T6 BBT strain path dome sample deformed at 220°C.....	208
Figure 4.99 ODFs in the neck of AA7075-T6 BBT strain path dome sample deformed at 220°C.....	209
Figure 4.100 Effect of punch-sheet contact lubrication conditions on neck region location for AA7075-T6 full sample deformed at 220°C; (a) punch-sheet dry contact and (b) 1.5 mm thick silicon rubber sheet located between punch and sheet metal during deformation.....	209
Figure 5.1 A schematic drawing of sheet geometry with an imperfection band B in the thickness direction and perpendicular to the major stress axis from the original M-K model. ....	214
Figure 5.2 Experimental digitized flow stress-strain curve for AA6016-T4 sheet and fitted curves of Swift and Voce hardening laws (Butuc et al., 2003). ....	220
Figure 5.3 Digitized experimental and predicted FLDs with Swift hardening law (Butuc et al., 2003). ....	221
Figure 5.4 Digitized experimental and predicted FLDs with Voce hardening law (Butuc et al., 2003). ....	222
Figure 5.5 Digitized experimental and predicted FLDs for AA7075-O at room temperature with different inhomogeneity factors (Yang et al., 2015). ....	223
Figure 5.6 Effect of strain hardening coefficient $n$ on stretch forming for tension – tension side of theoretical FLD for three different isotropic materials ( $r = 1$ , $\varepsilon_0 = 0.0014$ , $f_0 = 0.98$ ) (Sowerby & Duncan, 1971). ....	224

Figure 5.7 Effect of plastic strain ratio $r$ on stretch forming for tension – tension side of theoretical FLD for three different materials ( $n = 0.2$ , $\varepsilon_0 = 0.0014$ , $f_0 = 0.98$ ) (Sowerby & Duncan, 1971).....	225
Figure 5.8 Digitized experimental and predicted FLD for AA6016-T4 by using Yld96 yield function (Aretz, 2007; Butuc et al., 2003).....	226
Figure 5.9 Digitized experimental and predicted FLD for AA6016-T4 by using Yld2003 yield function using different biaxial $r$ value (Aretz, 2007; Butuc et al., 2003).....	227
Figure 5.10 A schematic drawing of H-N model.....	228
Figure 5.11 2D scheme drawing for stress transformation. ....	230
Figure 5.12 Comparison of fitted and experimental curves based on the F-B model; (a) 1 mm/min; (b) 10 mm/min. ....	234
Figure 5.13 The variation of $n$ and $m$ with absolute temperature.....	235
Figure 5.14 The predicted FLCs for different temperatures based on the F-B model. ....	236
Figure 5.15 The predicted FLCs for different temperatures based on the H-N and F-B models.....	237
Figure 5.16 Comparison of fitted and experimental curves based on the V-K model; (a) 1 mm/min and (b) 10 mm/min.....	240
Figure 5.17 $\sigma_s$ and $\sigma_0$ versus absolute temperature curves; (a) $\sigma_s$ and (b) $\sigma_0$ . ....	242
Figure 5.18 Digitized flow stress includes saturation stress ( $\sigma_s$ ), initial strain hardening rate ( $\theta_0$ ) and characteristic strain ( $\varepsilon_c$ ). Dashed line represent the exact elastic part of the curve (Kocks, 1976).....	243
Figure 5.19 The predicted FLCs at different temperatures based on V-K model: (a) MK-VK method and (b) HN-VK method. ....	244

## List of Tables

Table 2.1 Chemical composition limits for select age-hardening aluminum alloys (wt. %) (Alloys, 2015).....	9
Table 2.2 Typical 2xxx and 7xxx commercial aerospace aluminum alloys used in airframe structures (Prasad et al., 2013). ....	10
Table 2.3 Mechanical properties for selected commercial precipitation hardening alloys (Porter & Easterling, 1981).....	11
Table 2.4 Solid solubility of alloying elements in precipitation hardening aluminum alloys (Polmear, 2006).....	11
Table 2.5 Temper designation for aluminum alloys (Campbell, 2008).....	14
Table 2.6 Uniaxial tensile properties for AA7075 sheet in various tempers, tested at room temperature. ....	18
Table 2.7 Selected forming parameters for AA7075-O (Mohammad Tajally & Emadoddin, 2011).....	19
Table 2.8 Types of surface defects created during elastic – plastic deformation (Raabe et al., 2003). ....	34
Table 2.9 FCC ideal texture orientations and its positions in Euler space (Olaf Engler & Hirsch, 2009; O Engler & Lücke, 1992; JR Hirsch, 1990; Suwas & Gurao, 2008)...	48
Table 2.10 TMP conditions of AA7108 and AA7030 sheets prior to mechanical and formability tests (Lademo et al., 2008).....	49
Table 3.1 ICP detection limit of alloying elements in AA7075 sheet. ....	63
Table 3.2 Automatic grinding and polishing processes procedure. ....	66
Table 3.3 ALICONA roughness measurement system technical specifications. ....	76
Table 4.1 Chemical composition of AA7075 (in weight %). ....	99
Table 4.2 Average grain length, width and aspect ratios for un-deformed O and T6 tempers.....	103
Table 4.3 EBSD-based measurements of average grain length, width and aspect ratio from ND plane for AA7075-O and T6 sheet samples. ....	105
Table 4.4 Material property data from the room and elevated temperature uniaxial tensile tests. ....	114
Table 4.5 Strain hardening exponent and strength coefficient for AA7075-O at room and elevated temperatures. ....	116
Table 4.6 Onset of diffused necking initiation conditions for O temper at elevated temperatures.....	118

Table 4.7 Average LDH data and standard deviation of AA7075-O for dome specimens tested at room temperature, 180°C, 220°C, and 260°C. All data are in mm. ....	122
Table 4.8 Distance from pole to the neck in O and T6 temper hemispherical dome specimens formed by using 50.8 mm diameter punch tooling at room temperature and 220°C. ....	127
Table 4.9 Average surface roughness Ra and average area surface roughness Sa for undeformed and uniaxially deformed (5 mm from fracture) AA7075-O and AA7075-T6 sheet materials. ....	147
Table 4.10 Surface roughness measurements for AA7075 dome samples. ....	156
Table 4.11 Fracture thickness and thickness strain at fracture for 2 mm thick AA7075-O tensile test specimens. ....	158
Table 4.12 Through-thickness OM images of fractured AA7075-O tensile test specimens tested under different test conditions. ....	160
Table 4.13 AA7075-T6 uniaxial test specimen thickness at fracture and thickness strain at fracture from under different test conditions. ....	163
Table 4.14 OM images of through-thickness fractured AA7075-T6 tensile test specimens tested under different test conditions. ....	164
Table 4.15 Void and precipitate areas from field measurements for AA7075-O and T6 dome specimens in uniaxial, plane and biaxial strain paths at room temperature and 220°C. ....	176
Table 4.16 Average dimples area percentage of AA7075-O and T6 fractured dome samples deformed to fracture by using 50.8 mm diameter punch at room temperature and 220°C. ....	188
Table 4.17 Un-deformed sheet metal texture data from PFs and ODFs for {111} family of planes. ....	193
Table 4.18 Texture data in the form of PFs and ODFs for {111} family of planes deformed at room temperature for O-temper dome samples. ....	198
Table 4.19 Texture data in the form of PFs and ODFs for {111} family of planes deformed at 220°C for O-temper dome samples. ....	204
Table 4.20 Texture data in the form of PFs and ODFs for {111} family of planes deformed at 220°C for T6-temper dome samples. ....	210
 Table 5.1 F-B polynomial fit parameters. ....	 233
Table 5.2 V-K fit parameter values. ....	239

## List of Abbreviations

AA	Aluminum Alloy
AATDS	Aluminum Alloy Temper Designation System
ASTM	American Society for Testing and Materials
BBT	Balanced Biaxial Strain Path
BEC	Back Scattered Electron
CCD	Couple Charged Device
CNC	Computer Numerical Control
DC	Direct Chill
DIC	Digital Image Correlation
DSA	Dynamic Strain Aging
DRV	Dynamic Recovery
DRX	Dynamic Recrystallization
EBSD	Electron Backscattered Diffraction
F-B	Field-Backofen
FCC	Face Centered Cubic
FEM	Finite Element Model
FIB	Focused Ion Beam
FLC	Forming Limit Curve
FLD	Forming Limit Diagram
FLD <sub>0</sub>	Lower point of Forming Limit Curve at Plane Strain Path
FLCF	Forming Limit Curve at Fracture
GADDS	General Area Detector Diffraction System
GP	Guinier – Preston Zone
GTN	Gurson – Tvergaard – Needleman
HDR	High Dynamic Range
H-N	Hutchinson-Neale
HPS	Hemispherical Punch Stretching
HRTEM	High Resolution Transmission Electron Microscope
ICP	Inductively Coupled Plasma
ISO	International Standardization Organization
ITMT	Intermediate Thermal Mechanical Treatment
LDH	Limiting Dome Height
Max.	Maximum
Min.	Minimum
M-K	Marciniak-Kuczynski
MPa	Mega Pascal
ND	Normal Direction
ODF	Orientation Distribution Function
OES	Optical Emission Spectrometer
OM	Optical Microscope

PF	Pole Figure
PST	Plane Strain Tension Path
RD	Rolling Direction
RT	Room Temperature
SE	Secondary Electron
SEI	Secondary Electron Imaging
SEM	Scanning Electron Microscope
ST	Short Transvers
t-d	Time-dependent
TD	Transvers Direction
TEM	Transmission Electron Microscope
TMP	Thermo-mechanical Processing
UT	Uniaxial Tension Strain Path
V-K	Voce-Kocks



## List of Symbols

Al	Aluminum
a	Atomic Spacing
at%	Atomic Percentage
Cr	Chromium
Cu	Copper
°C	Degree Celsius
$f_0$	Imperfection Factor
Fe	Iron
K	Strength Coefficient
Mg	Magnesium
Mn	Manganese
m	Strain Rate Sensitivity Index
n	Strain Hardening Exponent
O	Full Annealed Heat Treatment
r	Plastic Strain Ratio
$R_a$	Roughness Value
Sa	Area Roughness
Sc	Scandium
Si	Silicon
SiC	Silicon Carbide
T	Absolute Temperature
Ti	Titanium
$t_0^A$	Nominal Sheet Thickness
$t_0^B$	Sheet Imperfection Thickness
wt%	Weight Percentage
Zn	Zinc
Zr	Zirconium
$\epsilon_1$	Major Strain
$\epsilon_2$	Minor Strain
$\alpha_{ssss}$	Super Saturated Solid Solution
$\eta$	Metastable Coherent Precipitates
$\eta$	Stable Non-coherent Precipitates
$\varphi_1, \phi, \varphi_2$	Euler Angles
$\beta$ – fibre	Rolling textures consist of the so-called $\beta$ – fibre running from the copper orientation (“Cu”) $\{112\}<111>$ through the S orientation $\{123\}<634>$ to the brass orientation (“Bs”) $\{011\}<211>$
$\sigma_m$	Mean Stress or Hydrostatic Stress = $1/3(\sigma_1 + \sigma_2 + \sigma_3)$
$\sigma_1$	Major In-plane Principal Stress

$\sigma_2$	Minor In-plane Principal Stress
$\sigma_3$	Through-thickness Normal Stress
$\dot{\epsilon}$	Strain Rate
$\alpha$	Stress Ratio = $(\frac{\sigma_2}{\sigma_1})$
$\bar{\sigma}$	Effective Stress
$\phi$	Stress Ratio = $(\frac{\bar{\sigma}}{\sigma_1})$
$d\epsilon_1$	Major Strain Increment
$d\epsilon_2$	Minor Strain Increment
$d\epsilon_3$	Through Thickness Strain Increment
$d\bar{\epsilon}$	Effective strain Increment
$\rho$	Strain Ratio = $(\frac{d\epsilon_2}{d\epsilon_1})$
$\beta$	Strain Ratio = $(\frac{d\bar{\epsilon}}{d\epsilon_1})$
$\varphi$	Groove Orientation Angle
$\sigma_s$	Saturation Stress
$\sigma_0$	Initial Yield Stress
$\epsilon_r$	Relaxation Strain
$\sigma_{s0}$	Reference Saturation Stress
$\sigma_{k0}$	Reference Yield Stress
$k$ & $k_B$	Boltzmann Constant

## 1-Introduction and Objectives

### 1.1 Introduction

Automotive industry has been using aluminum alloys for several decades to reduce the weight of the vehicles to improve their fuel efficiency and consequently reduce the automotive carbon footprint. Most of this effort has been towards the use of AA5xxx and AA6xxx series aluminum rolled sheet materials in the lower strength grades with reasonably good room temperature formability for automotive outer body panels. Consequently, many automotive companies routinely incorporate aluminum body panels made from AA5xxx and AA6xxx sheet materials. Table 1.1 shows mechanical properties of some of the common wrought automotive aluminum alloys of AA5xxx and AA6xxx series.

Table 1.1 Mechanical properties of some commercial AA5xxx and AA6xxx aluminum alloys

Alloy	Yield strength (MPa)		Tensile strength (MPa)		Reference
	Min.	Max.	Min.	Max.	
5052-O	65	-	170	215	ASTM-B209M-14
5083-O	125	200	275	350	
5182-O	128		282		(Li et al., 2013)
5456-O	130	205	290	365	ASTM-B209M-14
5754-O	200	270	80	-	
6061-O	-	85	-	150	
6061-T4	110	-	205	-	
6061-T6	240	-	290	-	
6022-T4	170		305		(Tian et al., 2017)
6111-T4	140		350		(Baczynski et al., 2000; Jain et al., 1996)

The next push, however, is towards stamped parts made from even higher strength aluminum sheet materials for their use in automotive structural components such as door inner, B-pillar etc. (Jürgen Hirsch, 2011; Hui et al., 2012). Figure 1.1 shows structural and body components for Audi A8 manufactured from different aluminum alloys, including high strength aluminum AA7xxx series, according to the desired application.

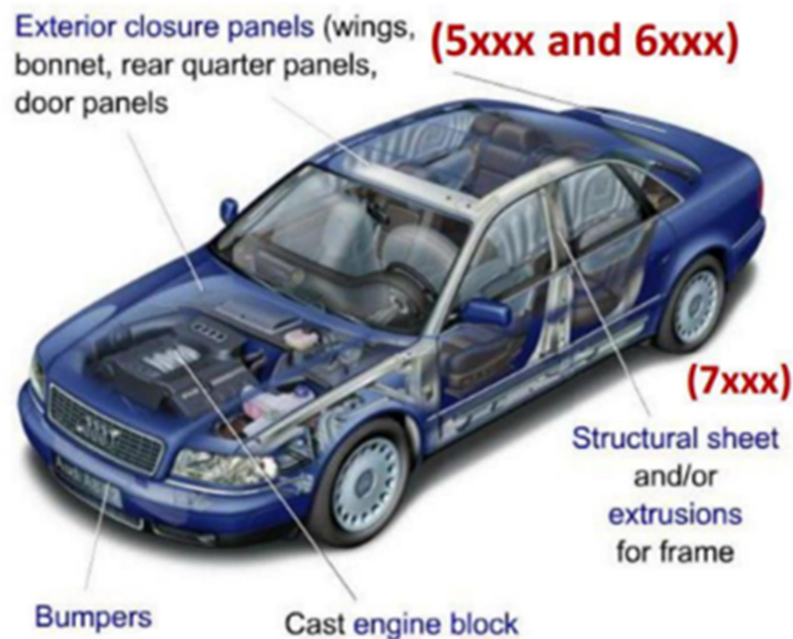


Figure 1.1 Aluminum structural and body components in Audi A8 (Altan, 2005).

AA7075 is a common AA7xxx series aluminum alloy in industry that has a high strength to weight ratio suitable for structural stamped components. It is commonly used in sheet and plate form in aerospace structural and skin panel applications as well as in other applications that require high strength. It is a precipitation hardening alloy containing 5.1-6.1% Zn, 2.1-2.9% Mg, 1.2-2% Cu, 0.5% Fe, 0.4% Si, 0.3% Mn, 0.18-0.28% Cr, 0.2% Ti (in weight%) and the balance is aluminum (Alloys, 2015). AA7075 is a wrought alloy,

which means that it is heavily deformed by thermo-mechanical processing in to plate or sheet form. It is hardened by aging heat treatment, which results in the final microstructure and properties. It can be formed into simple shapes at room temperature in softer tempers such as in the annealed (or O temper) and solution heat-treated (or W temper) conditions.

AA7075-T6 (or peak aged) has a higher strength compared to the other classes of precipitation hardening aluminum alloys AA2xxx and AA6xxx. It has a minimum yield and ultimate tensile strength, according to ASTM-B209M-14, of about 435 MPa and 510 MPa respectively. Consequently, AA7075 with its higher light weighting potential is being considered over high strength steels for some structural automotive parts.

One of the main challenges in the use of AA7075 alloy in the automobiles, however, is its limited formability at room temperature for producing low-cost structural parts by sheet stamping. Consequently, elevated temperature forming in the form of warm forming and hot stamping is being considered to enhance its formability. While much effort is underway in the academia and automotive industry to adopt hot stamping die quenching process to AA7075 (it is already well established for high strength steel sheet), there are still many challenges to overcome. In fact, no commercial-scale hot stamping process is yet available for making real automotive parts from AA7075 sheet. The first step in the development of hot stamping process for AA7075 aluminum sheet still involves studies at more fundamental level to relate elevated temperature formability to material microstructure, crystallographic texture, and surface considerations. More generally, to improve and fully exploit the formability of AA7075 sheet into automotive parts at higher

temperatures, a better understanding of the relationship between basic mechanical property, microstructure, damage development, fracture at large strains and formability is needed. While some effort has been made to characterize the formability of AA7075 sheet at higher temperatures in recent years the details of formability assessment procedure, such as the procedure for obtaining elevated temperature forming limit diagrams (or FLDs), are often missing (Huang et al., 2010; Hui et al., 2012). Also, a quantitative inter-relationships between basic mechanical properties, microstructure and elevated temperature formability of AA7075 sheet in the scientific literature is lacking. Further, qualitative observation of surface roughness development, texture and other microstructural aspects of plastic flow localization and damage development under complex multi-axial forming modes in AA7075 sheet are needed. Lastly, no studies have been reported in the literature on the effect of different sheet tempers on elevated temperature formability of AA7075 sheet.

The main objective of the present work is to develop qualitative and quantitative inter-relationships between room and elevated temperature formability measures such as uniaxial tensile ductility and forming limits, and associated microstructural, texture, surface roughness and damage development parameters in AA7075 sheet under O and T6 temper states. This objective will help fill the above noted knowledge gaps in the literature by carrying out a systematic experimental study at different scales involving large and miniature test specimens. The overarching industrial objective is to enable the use of higher strength AA7075 sheet materials in different tempers to produce lightweight automotive stamped parts.

The experimental methodology employed to fill the knowledge gaps will include multi-axial out-of-plane forming tests at elevated temperatures on larger-scale laboratory-based test specimens, as well as complementary small-scale test specimens to characterize the evolution of microstructure, texture, surface roughness and material damage arising from large plastic deformation associated with sheet forming.

## **1.2 Thesis Objectives**

The main objectives of this research work as noted above can be summarized into four sub-objectives as follows:

[1]. Investigate how the different sheet tempers of rolled AA7075 sheet (as fabricated, annealed, and artificially aged) and resulting microstructure and crystallographic texture affect the uniaxial tensile properties, general formability, and forming limits of AA7075 sheet as well as changes to microstructure, texture and ductile damage development at room temperature. This objective will be achieved by conducting uniaxial tension tests at room temperature and chosen initial strain rates, and by analyzing the deformation characteristics of the sheet materials at different scales.

[2]. Investigate how the elevated temperature and strain rate (or forming test speed) affect the plastic flow and formability characteristics and specifically the forming limits of AA7075-O and AA7075-T6 sheet in uniaxial tension and multi-axial, out-of-plane, forming modes by conducting forming tests at a range of temperatures. The temperature range chosen for the study is below the recrystallization temperature of AA7075 of about 300°C to assess the effectiveness of lower temperature and thus lower cost alternative of

enhancing formability of AA7075 sheet. A set of mechanical and forming tests in the forming temperatures range of 180°C-260°C, with an increment of 40°C, will be chosen.

[3]. Investigate how the initial and subsequently deformed microstructure and texture of AA7075-O and T6 sheets such as grain size, grain orientation, and precipitate characteristics cause the development of surface roughness, strain over the deformed surface, plastic instability (or localized necking) at large strains, internal damage and fracture under uniaxial tension and multi-axial large plastic deformation and forming. Necking and fracture characteristics of uniaxial tension and dome test samples will be investigated. Furthermore, fractographic analyses of damage will be carried out in uniaxial and dome samples after fracture. Finally, bulk texture analyses for un-deformed sheet in F, O and T6 temper condition and dome test samples for uniaxial tension, plane strain tension and balanced biaxial strain tension in O and T6 temper condition are investigated.

[4]. Analyze and apply the experimental results from the previous objectives towards the development of a suitable mathematical model to predict the forming limits of fully annealed AA7075 sheet at a range of elevated temperatures. The study will have a focus on selection and use of suitable constitutive material models from the literature to capture strain, strain rate and temperature dependent hardening (and softening) towards prediction of forming limits of AA7075 sheet. A well-known forming limit prediction model called Marciniak-Kuczynski (or M-K) model will be adopted in conjunction with different constitutive laws to predict forming limit curves (or FLCs) of AA7075-O sheet at different experimental forming temperatures.



### **1.3 Thesis Outline**

Besides the current first chapter on Introduction and Objectives, the thesis consists of five other chapters (Chapters 2-6) as follows. Chapter 2 presents a brief review of relevant literature as per the thesis objectives noted above including general characteristics of precipitation hardening aluminum alloys, AA7xxx sheet processing, heat treatments, mechanical properties, microstructure and texture evolution during deformation, and experimental formability characteristics. The emphasis will be on AA7075 rolled sheet where possible. Chapter 3 presents the experimental methodologies associated with various larger-scale mechanical and forming tests and smaller-scale microstructural studies. Chapter 4 presents all experimental results and discussion of the results pertaining to the first 3 objectives. Chapter 5 presents an analytical model for prediction of FLD for AA7075-O and associated results and discussion pertaining to Objective 4. Chapter 6 presents the main conclusions of the research as well as some suggestions for future work. The thesis ends with a list of references associated with all of the Chapters noted above.

## **2-Literature Review**

This chapter presents a review of literature related to material properties, microstructure and formability of precipitation-hardenable aluminum sheet materials with a focus on AA7xxx series sheet. First, a review of precipitation hardening behavior of aluminum alloys in general is presented, including steps in the processing of 7xxx series aluminum sheet material and its resulting microstructure in various tempers. Second, a review of factors that affect the room and elevated temperature uniaxial tensile material properties and sheet formability of 7xxx sheet in various tempers, and specifically the tensile properties and formability of AA7075 sheet. Lastly, microstructure, surface roughness and texture evolution, and damage development, in precipitation-hardenable aluminum sheet materials at large plastic strains typical of sheet forming are reviewed.

### **2.1 General characteristics of precipitation hardening aluminum alloys**

Precipitation-hardenable wrought aluminum alloys consist of three main alloy series; 2xxx (Al–Cu, Al–Cu–Mg), 6xxx (Al–Mg–Si) and 7xxx (Al–Zn–Mg, Al–Zn–Mg–Cu) (Davis, 1993; Kaufman, 2000; Polmear, 2006; Starke & Staley, 1996; A. K. Vasudevan & Doherty, 2012). Table 2.1 illustrates the chemical composition of selected precipitation-hardenable alloys according to ASTM B209M – 14. The strengthening mechanism for these alloys, which leads to higher strength, is dispersion strengthening due to specific precipitation hardening processes. High melting point alloying elements such as Cr, Mn and/or Zr (i.e., transition elements) are added to wrought alloy compositions to form specific types of precipitates called dispersoids which controls grain size by preventing grain growth. In addition, Mg and Cu are added to provide hardening precipitates that

strengthen the matrix as well as offer substantial resistance to dislocation motion. Combination of grain size and dislocation strengthening leads to higher strength in these materials. Increased strength in combination with lightweight of aluminum has enabled extensive use of 2xxx and 7xxx aluminum alloys in aerospace applications as shown in Table 2.2 (Prasad et al., 2013). AA6xxx series aluminum sheet materials have been in use in the automotive stamping industry due to their good formability in the naturally aged temper (or T4) state, their capacity to increase overall strength, stiffness and dent resistance of the formed part after the paint bake process. The paint baked parts from AA6xxx series sheet also exhibit good weldability, corrosion resistance and relatively lower cost compared to 2xxx and 7xxx series alloys (Troeger & Starke, 2000).

Table 2.1 Chemical composition limits for select age-hardening aluminum alloys (wt. %) (Alloys, 2015)

Alloy	Si	Fe	Cu	Mn	Mg	Cr	Zn	Ti	Other elements		Al
									Each	Total	
2024	0.5	0.5	3.8– 4.9	0.3– 0.9	1.2– 1.8	0.1	0.25	0.15	0.05	0.15	remainder
2124	0.2	0.3	3.8– 4.9	0.3– 0.9	1.2– 1.8	0.1	0.25	0.15	0.05	0.15	remainder
2219	0.2	0.3	5.8– 6.8	0.2– 0.4	0.02	...	0.1	0.02– 0.1	0.05	0.15	remainder
6013	0.6– 1	0.5	0.6– 1.1	0.2– 0.8	0.8– 1.2	0.1	0.25	0.1	0.05	0.15	remainder
6061	0.4– 0.8	0.7	0.15– 0.4	0.15	0.8– 1.2	0.04– 0.35	0.25	0.15	0.05	0.15	remainder
7072	0.7 Si + Fe		0.1	0.1	0.1	...	0.8– 1.3	...	0.05	0.15	remainder
7075	0.4	0.5	1.2–2	0.3	2.1– 2.9	0.18– 0.28	5.1– 6.1	0.2	0.05	0.15	remainder

Table 2.2 Typical 2xxx and 7xxx commercial aerospace aluminum alloys used in airframe structures (Prasad et al., 2013).

Product	Strength levels	Alloy/temper	Applications
Sheet	Damage tolerant	2024-T3, 2524-T3/351	Fuselage/pressure cabin skins
Plate	Damage tolerant	2024-T351, 2324-T39, 2624-T351, 2624-T39	Lower wing covers
	Medium strength	2024-T62	Tactical aircraft fuselage panels
	Medium strength	2124-T851	Tactical aircraft bulkheads
	Medium strength	7050-T7451, 7X75-T7XXX	Internal fuselage structures
	High strength	7150-T7751, 7055-T7751, 7055-T7951, 7255-T7951	Upper wing covers
	Medium strength	7050-T7451	Spars, ribs, other internal structures
Forgings	High strength	7175-T7351, 7050-T7452	Wing/fuselage attachments
Extrusions	Damage tolerant	2024-T3511, 2026-T3511, 2024-T4312, 6110-T6511	Lower wing stringers Fuselage/pressure cabin stringers
	Medium/high strength	7075-T73511, 7075-T79511, 7150-T6511, 7175-T79511, 7055-T77511, 7055-T79511	Fuselage stringers and frames, upper wing stringers, floor beams, seat rails

Table 2.3 presents mechanical properties for three commonly used commercial precipitation hardening aluminum alloys used for structural applications (Porter & Easterling, 1981). It is obvious that AA7075 has the highest strength but slightly lower elongation value than the AA2024 and AA6061 aluminum alloys. This is because the two major alloying elements in AA7075, namely Zn and Mg, have higher percentage solid

solubility in aluminum, as shown in Table 2.4, and thus provide a significant precipitation hardening contribution to its strength (Polmear, 2006).

Table 2.3 Mechanical properties for selected commercial precipitation hardening alloys (Porter & Easterling, 1981).

Alloy	Precipitate	Yield Strength (MPa)	Tensile Strength (MPa)	Elongation (%)
2024	Al <sub>2</sub> CuMg	390	500	13
6061	Mg <sub>2</sub> Si	280	315	12
7075	MgZn <sub>2</sub>	500	570	11

Table 2.4 Solid solubility of alloying elements in precipitation hardening aluminum alloys (Polmear, 2006).

Element	Temperature for maximum solid solubility (°C)	Maximum solid solubility	
		(wt%)	(at%)
Copper (Cu)	548	5.65	2.40
Chromium (Cr)	661	0.77	0.40
Iron (Fe)	655	0.05	0.025
Magnesium (Mg)	450	17.4	18.5
Manganese (Mn)	658	1.82	0.90
Silicon (Si)	577	1.65	1.59
Titanium (Ti)	665	~ 1.3	~ 0.74
Zinc (Zn)	443	82.8	66.4

## 2.2 Processing of precipitation-hardenable aluminum sheet

Thermo-mechanical processing (TMP) of 7xxx series alloys consists of direct chill (or DC) casting of ingots followed by complete ingot homogenization and slow cooling. Subsequent steps include scalping of the surface of the ingot and several passes of warm ingot or billet rolling and recrystallization anneal that result in breakdown of the as-cast dendritic structure and production of solute species and precipitates that accompany the conversion of billet to a plate. Further hot rolling produces a complex, partially

polygonised dislocation structure and continuous recrystallization from high temperature deformation as the thickness of the plate is reduced to 3 – 6 mm range (Waldman et al., 1974). Another more recent process is often termed as “Intermediate Thermal Mechanical Treatment (or ITMT)” (Di Russo et al., 1974; Wert et al., 1981). This process involves partial recrystallization of the DC ingot followed by warm rolling, recrystallization anneal and hot rolling to reduce the grain size by discontinuous recrystallization. Hot rolling is followed by multi-stand cold rolling with intermediate recrystallization or warm rolling to achieve the final sheet thickness. It is to be noted that the exact process followed by the aluminum sheet producers is often a trade secret and is not reported in the literature. Figure 2.1 shows a general schematic of TMP of 7xxx aluminum alloys (Fribourg, 2009). The final stage of processing is age-hardening treatment by artificial ageing in which the alloy is strengthened by precipitation hardening mechanism and hence acquires its final mechanical properties.

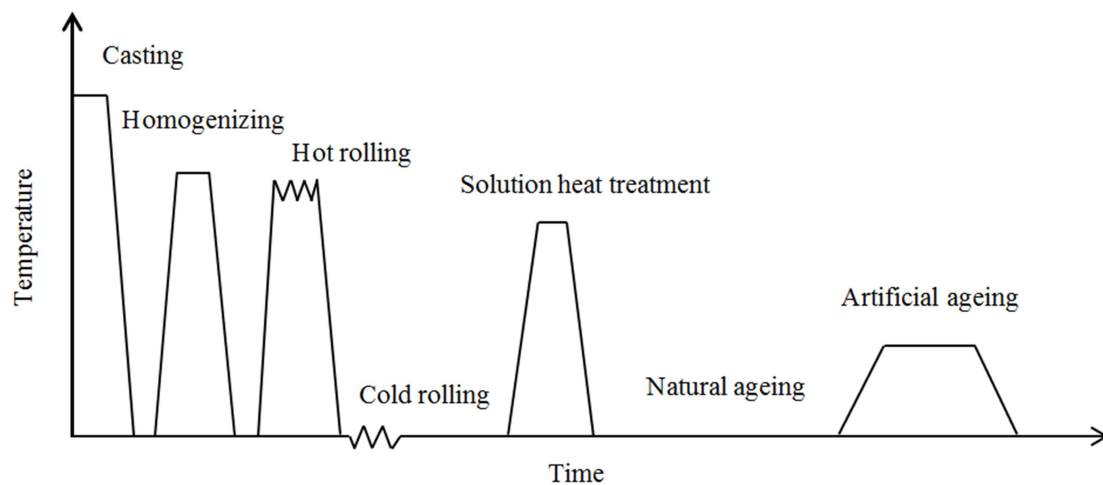


Figure 2.1 Schematic drawing of TMP steps for 7xxx series, as modified from reference (Fribourg, 2009).

### **2.3 AA7xxx sheet heat-treatments and resulting microstructures**

The heat-treatment of precipitation-hardening aluminum alloys consists of the following steps; (i) solutionizing at a temperature above the solubility curve (480°C-500°C), (ii) quenching, usually in water but sometimes in air, and (iii) ageing (or precipitation) at room temperature (natural aging to T4 temper) or at elevated temperature up to 200°C (artificial aging to T6 temper) (Altenpohl, 1982). The aging heat-treatment affects the microstructure and final physical and mechanical properties of the alloy. During the ageing stage, the yield stress increases up to a maximum, reaching a so called “hardness peak”, after which it decreases. This peak yield stress state is referred to as T6 temper. The tempers before the hardness peak are referred to as “under-aged” tempers (T3 temper, for example). Similarly, the tempers after the hardness peak are called “over-aged” tempers (such as T7). According to the Aluminum Alloy Temper Designation System (AATDS), a letter and additional number(s) following the alloy designation in which the letter indicates the main type of treatment and the number(s) means a specific combination of basic operations. Table 2.5 presents various temper designations for aluminum alloys.

Table 2.5 Temper designation for aluminum alloys (Campbell, 2008).

Suffix letter “F”, “O”, “H”, “T” or “W” indicates basic treatment condition	First suffix digit indicates secondary treatment influence properties	Second suffix digit for condition H only indicates residual hardening
F-As fabricated		
O-Annealed-wrought products only		
H-Cold worked, strain hardening		
	1-Cold worked only	2-1/4 hard
	2-Cold worked and partially annealed	4-1/2 hard
	3-Cold worked and stabilized	6-3/4 hard
		8-Hard
W-Solution heat treated		9-Extra hard
T-Heat treated, stable		
T1-Cooled from an elevated temperature shaping operation + natural aged		
T2-Cooled from an elevated temperature shaping operation + cold worked + natural aged		
T3- Solution treated + cold worked + natural aged		
T4- Solution treated + natural aged		
T5- Cooled from an elevated temperature shaping operation + artificial aged		
T6-Solution treated + artificial aged		
T7-Solution treated + overaged		

Precipitates form during various ageing treatments after the material is fully solutionized, i.e., heated up to the solutionizing temperature and rapidly quenched. There are three types of precipitates that exist in 7xxx series. The first type, which depend on percentage of alloying elements and Zn/Mg ratio, are called hardening precipitates and designated as  $\eta$  ( $\text{MgZn}_2$ ), T ( $\text{Al}_2\text{Mg}_3\text{Zn}_3$ ), S ( $\text{Al}_2\text{CuMg}$ ) and  $\Theta$  ( $\text{Al}_2\text{Cu}$ ) (Camacho et al., 2003). These



precipitates are mainly responsible for high strength and generally occur in the size range 1-10 nm. Second category of precipitates, referred to as dispersoids, contain small amount of transition elements such as Zr, Sc, Cr and Mn that are added to the alloy to form compounds such as  $\text{Al}_6\text{Mn}$ ,  $\text{Al}_3\text{Zr}$  and  $\text{Al}_{20}\text{Cu}_2\text{Mn}_3$  which controls grain size and prevent recrystallization during material processing. The size of dispersoids is in the range 20-200 nm. Finally, constituent particles or intermetallic compounds such as  $\text{Al}_3\text{Fe}$ ,  $\text{Al}_7\text{Cu}_2\text{Fe}$  and  $\text{Mg}_2\text{Si}$  which are still larger, of the order of tens of microns, and form during the casting process due to impurities such as Fe and Si (Jordon et al., 2009; Mondal & Mukhopadhyay, 2005; Starink, 2001; Z. Zhao & Frankel, 2007). Another heat treatment called annealing (leading to O-temper) for 7xxx wrought alloys includes heating the as-fabricated alloy from room temperature to  $413^\circ\text{C}$  for 3 hours followed by furnace cooling. During this specific treatment three microstructural processes take place; (i) stress relief (or recovery) in the early stages, (ii) recrystallization, and (iii) grain growth. The purpose of O-temper heat treatment is to give the alloy more ductility and elongation to enhance its room temperature formability but at the expense of mechanical strength.

Figure 2.2 shows a 3D optical micrograph of grain structure of rolled AA7075 sheet in the T651 temper condition (Pedersen et al., 2011). The grains in the rolling direction are highly elongated (the so-called ‘pancake’ shape) and aligned to the rolling direction (RD).

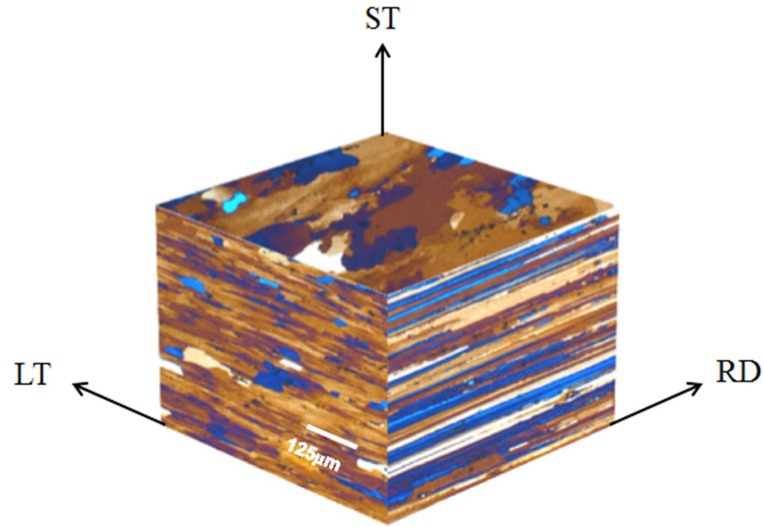


Figure 2.2 3D optical micrograph of AA7075-T651 grain structure (Pedersen et al., 2011).

The resulting precipitates from the aging process can be most clearly observed by transmission electron microscopy (TEM). Figure 2.3 presents conventional bright field TEM and high resolution TEM (HRTEM) micrographs of Al-Zn-Mg alloy as GP zones in naturally aged alloy (T4 temper, left image). HRTEM micrographs show fully coherent near spherical GP zones in the same treatment conditions (middle image), and HRTEM of  $\eta$  plate precipitates in peak aged treatment (T6 temper, right image). The size of GP zones, which is the early stage in precipitation, during or immediately after quenching process, is approximately 3 nm while size of semi-coherent  $\eta$  plates precipitates is about 2 nm thick and 10 nm in length.

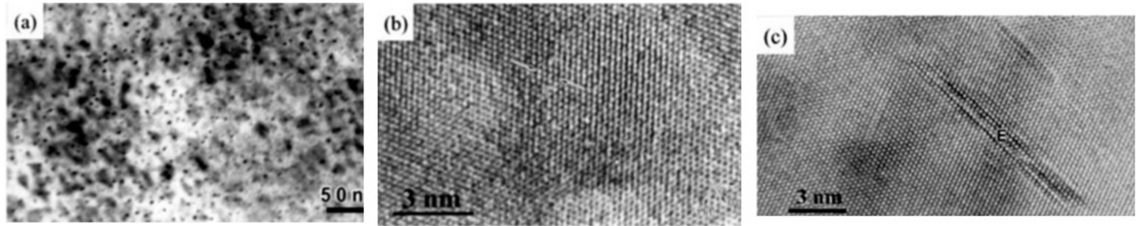


Figure 2.3 High resolution TEM images of ternary Al-Zn-Mg alloy showing; (a) GP zones after natural aging, (b) fully coherent, near spherical, GP zones in naturally aged alloy, and (c)  $\eta$  plates (see region E in the image) in the peak-aged condition (Mukhopadhyay, 2009).

Another experimental technique used to quantify size and distribution of different types of precipitates is referred to as Focused Ion Beam (FIB) tomography. In this technique, a controlled ion beam is utilized to carry out surface milling (slicing) with simultaneous SEM imaging of the milled surface after each pass. After imaging, all images are stacked and aligned using a software for 3D image construction, visualization and quantitative analysis. Figure 2.4 shows a 2D back scattered electron (BSE) image of AA7075-T651 alloy from FIB tomography experiment. The image includes visually identifiable grain boundaries, intermetallic compounds with stoichiometric composition of  $Mg_2Si$  and some pores. Also, due to the atomic number difference between matrix (aluminum) and precipitates, the precipitated appears as relatively small white dots.

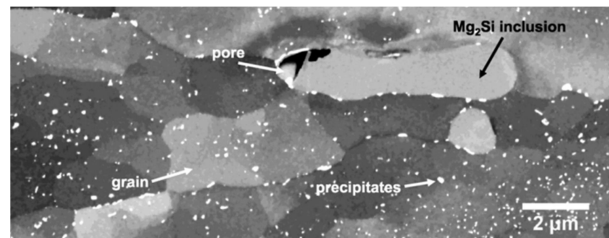


Figure 2.4 BSE image of AA7075-T651 from FIB tomography revealing grains,  $Mg_2Si$  constituents, precipitates, and pores (Singh et al., 2016).

## 2.4 Mechanical properties of AA7xxx aluminum sheet

Various studies have been reported in the literature on uniaxial tensile mechanical properties of AA7xxx aluminum, and specifically on AA7075 sheet in various tempers tested at room temperature. Table 2.6 summarizes some of the mechanical properties for select AA7075 heat treatments. Tensile properties from these studies suggest that the best formability as measured by tensile elongation values are exhibited in the O temper condition compared to the aged (T6) and overaged (T7) tempers.

Table 2.6 Uniaxial tensile properties for AA7075 sheet in various tempers, tested at room temperature.

Temper	Yield Strength (MPa)	Tensile Strength (MPa)	Elongation (%)	r-value	References
W (15 min.)	137	–	–	0.829	(Leacock et al., 2013)
O	88 – 125	190 – 234	15.5 – 22	0.877	(Leacock et al., 2013; Liu et al., 2013; M Tajally et al., 2009; Mohammad Tajally et al., 2010)
T6	442 – 480	537 – 543	11 – 13.5	–	(Janbakhsh et al., 2014)
T7	454	505	11	–	(A. Vasudevan & Suresh, 1982)

There are limited mechanical properties data, such as strain hardening index  $n$  and strain rate sensitivity  $m$  values, available for AA7075 sheet at higher temperatures of interest in warm and hot forming. In general, there is a decrease in strain hardening and increase in strain rate hardening (i.e., a lower  $n$  and a higher  $m$  value) and consequently early saturation in flow stress with increasing temperature. Table 2.7 presents  $r$  and  $n$  values for

AA7075 in the annealed condition at different temperatures. A study carried out by Tajally et al. (Mohammad Tajally & Emadoddin, 2011) on AA7075-O sheet annealed at various temperatures (270, 350, 400, and 450°C) found that the maximum plastic strain ratio (r-value) and n-value are obtained when the material is annealed at 400°C. In addition, the higher r-value occurred at 45° orientation for all annealed materials.

Table 2.7 Selected forming parameters for AA7075-O (Mohammad Tajally & Emadoddin, 2011).

Annealing temperature (°C)	Orientation	r	n
270	0	0.49	0.093
	45	0.79	0.13
	90	0.52	0.109
350	0	0.62	0.114
	45	0.92	0.164
	90	0.7	0.12
400	0	0.77	0.2155
	45	1.02	0.257
	90	0.79	0.23
450	0	0.66	0.2382
	45	0.94	0.1381
	90	0.72	0.24

Figure 2.5 shows the m-value peaks at about 180°C (Hui et al., 2012). The material anisotropy also changes with an increase in temperature due to the complicated effect of dynamic recovery, a softening mechanism that reduces dislocation density by cross-slip of screw dislocations as well as climb of edge dislocations, and dynamic recrystallization, which is a softening mechanism that eliminates a large number of dislocations by migration of high angle grain boundaries, during elevated temperature deformation which

in turns leads to a change in grain orientation distribution (or texture) and hence a change in material anisotropy.

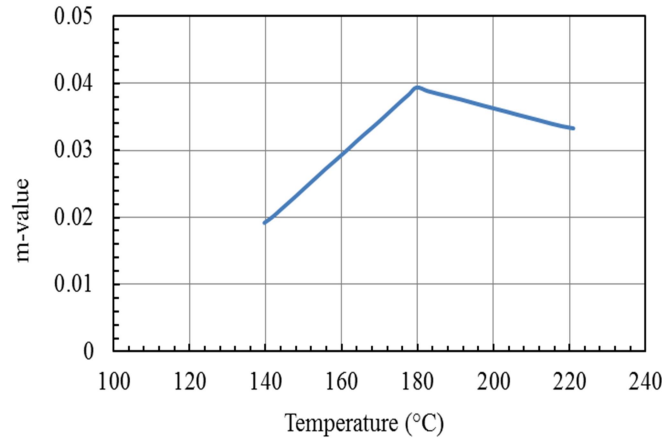


Figure 2.5 Strain rate sensitivity index ( $m$ ) versus temperature for AA7075-T6 from (Hui et al., 2012).

## 2.5 Introduction to forming and fracture limits

Sheet metal formability refers to the ability of flat sheets or blanks to deform into desired complex out-of-plane shapes under certain plastic deformation conditions using forming presses and tooling and without failure or excessive localized necking (thinning). A useful and widely accepted representation of sheet formability is a forming limit diagram (or FLD), a 2D principal strain space representation of the surface strain on a deformed sheet or part. This space consists of a major tensile strain (or first principle strain) plotted along the ordinate and a minor strain (which can be compressive, zero or tensile) plotted along the abscissa, as shown below in Figure 2.6. In the FLD space lies a “V” shaped forming limit curve (or FLC) which represents the locus of all possible necked strain states, the so- called limit strains. A point on this locus is reached via different strain

paths emanating radially from zero major and minor strain point and ranging from uniaxial tension strain path on the tension-compression side of FLD to the equi-biaxial tension strain path on the tension-tension side of FLD. The strain paths also include the plane strain tension path where the minor strain has a zero value. Typical forming processes such as stretching, cup drawing, embossing, stretch flanging consists of one of the above strain paths or a combination of them to attain the desired shape.

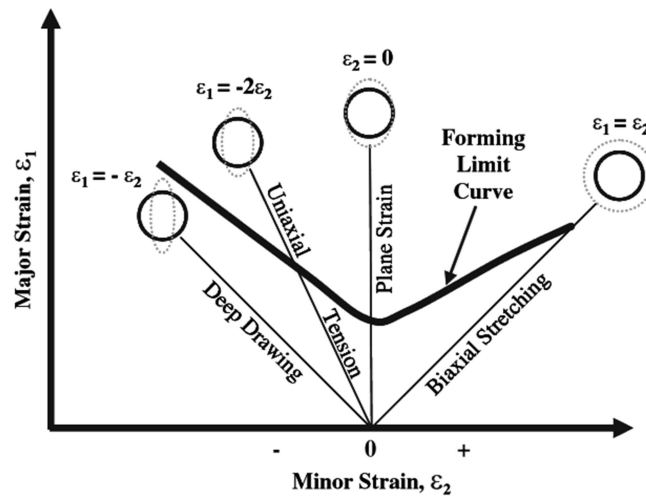


Figure 2.6 A schematic FLD strain space including limit strain curve (FLC) (Hsu et al., 2008).

FLD representation was originally proposed by Keeler (Keeler, 1968) for tension – tension region and extended to include tension – compression region by Goodwin (Goodwin, 1968). The strain states below the FLC represent the safe condition for forming whereas any strain state above the FLC is considered unsafe due to localized necking or even fracture. Materials with good formability results in FLCs which lie further up along the major strain axis compared to the materials with poor formability. A

FLC situated at the higher major strain levels enables forming of parts with complex features that require higher strain limits to form.

Nakazima formability test (Nakazima et al., 1968), first developed in the sixties, is perhaps the most commonly used test methodology to obtain an experimental FLD by forming specimens of various widths with a hemispherical punch in a die with a circular opening that incorporates a lock-bead all around the central opening. The various specimen widths allow the attainment of different radial strain paths that reach the FLC at different points. In other words, a change in specimen width in the Nakazima test leads to a change in major and minor strain state for onset of localized necking. A uniaxial tension strain path (UT), for example, can be achieved by forming a narrow width sample with a hemispherical punch in which it stretches in the major strain direction ( $\epsilon_1 > 0$ ) but contracts in the minor strain direction ( $\epsilon_2 < 0$ ) till it reaches the onset of localized necking (i.e., FLC). Similarly, for obtaining the strain limit for the plane strain tension path (PST), a wider specimen that satisfies the plane strain condition in which the minor strain is equal to zero ( $\epsilon_2 = 0$ ) is utilized. Further, the balanced biaxial strain path (BBT) can be achieved by a full dome sample in which both principal directions are equally stretched ( $\epsilon_1 = \epsilon_2$ ). In general, about 6-7 strain paths from a combination of specimen geometry and various lubrication conditions between the punch and sheet are utilized to obtain a reliable FLC. A modern variant of the Nakazima test has been standardized in the form of ASTM-E2218-15 and ISO 12004-2:2008 standards (see Figure 2.7).



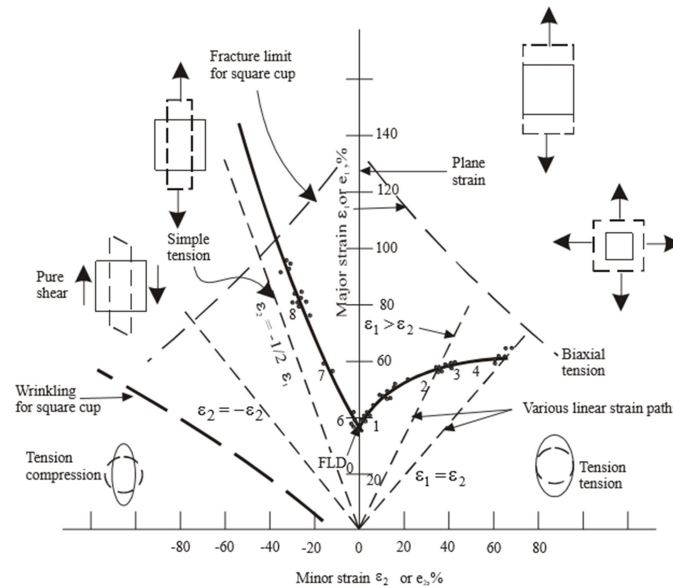


Figure 2.7 A schematic diagram representing FLD with the “V” shaped FLC and various ideal strain paths utilized for determination of FLD based on the methodology proposed Nakazima (Nakazima et al., 1968).

While FLD (or FLC) is a very useful measure of formability of a sheet material, the experimental methodology, as illustrated by the Nakazima test methodology, requires a large number of hemispherical dome tests with various specimen geometries and lubrication conditions. The tests are typically stopped at the onset of necking and local major and minor strain values in the vicinity of the neck are determined from the various specimens to construct the FLC. For strain measurement, a position dependent method is utilized in which the test specimens are imprinted with surface grids prior to the test, and the surface of the deforming dome specimens with grids are either continuously imaged during the test or after the test. A recent approach for limit strain measurement is called the time-dependent (or t-d) method in which a set of points on a line perpendicular to the necking zone are used to calculate the limit strains. The onset of localized necking and

then fracture occur when the point just outside the necking has zero strain rate and the point inside necking region shows the highest strain value. So, when the outside point strain rate attains maximum value, the limit strains are determined at the same time. The advantage of this method is that it can be used to determine FLDs practically. This method will be explained in depth in Chapter 3. Elevated temperature FLD determination involves added complexity of conducting dome tests at elevated temperature in a temperature controlled environment of a furnace. Even the specimen placement and clamping in the tooling inside the furnace (prior to the test) can cause some perturbation in the thermal history of the sample. Also, grid quality often deteriorates at higher temperature and makes the strain measurement process more challenging.

It is to be noted that a forming limit curve at fracture (FLCF) can also be constructed in a manner similar to the FLC where the various hemispherical dome specimens are now taken to fracture and the major and minor strains at fracture line on the dome specimen are obtained to construct the FLCF as shown in Figure 2.8. The FLCF incorporates strains to necking as well as strain development within the neck which typically grows under plane strain condition of the neck until the onset of fracture. Consequently, FLCF lies above the FLC of the sheet material in the major strain direction except for situations where the onset of fracture precedes the onset of necking due to extensive microstructural damage within the sheet during large plastic deformation. High strength precipitation hardening alloys such as those from AA6xxx and AA7xxx series often show the latter type of behavior at room temperature.

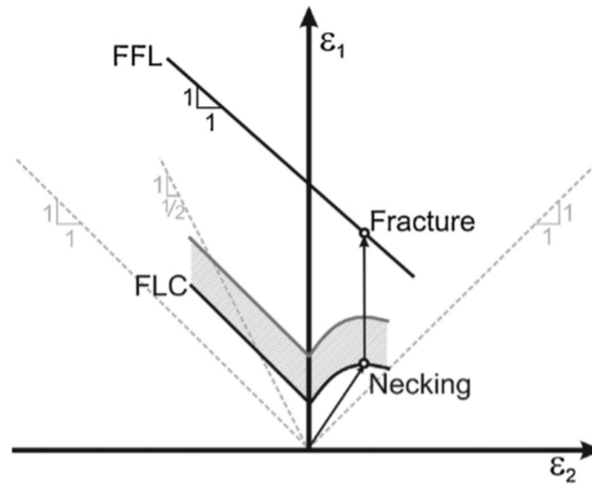


Figure 2.8 A schematic diagram representing FLC, typical strain paths and fracture forming limit line (FFL) (Isik et al., 2014).

## 2.6 Experimental formability characteristics of AA7075 sheet

As stated earlier, AA7075 sheet materials have limited formability at room temperature. FLD of 1.6 mm thick AA7075-O sheet at room temperature, obtained by Silva et al. (Silva et al., 2015) using standard Nakazima test with punch diameter of 100 mm is shown in Figure 2.9. A digital image correlation (DIC) technique using ARAMIS online optical strain measurement system was used to track the outer surface strain evolution and construct the FLC. As shown, some differences can arise in the position of FLCs obtained from different approaches. Also, a slight shift to the right of the plane strain path in the lowest major limit strain value, corresponding to about 0.2 in Figure 2.9, has been reported in the literature. One common explanation for the shift offered in the literature has to do with biaxial tensile pre-straining that occurs during the sheet clamping process from the lock beads in the Nakazima test.

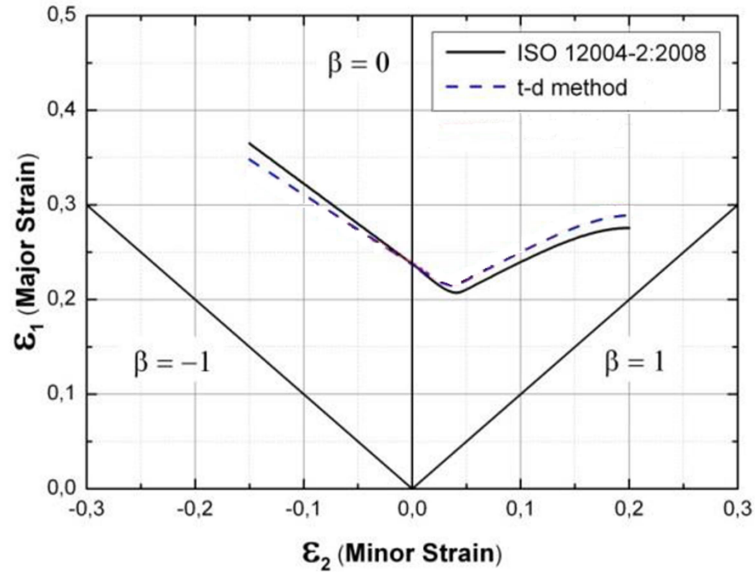


Figure 2.9 FLD of 1.6 mm thick AA7075-O sheet at room temperature (Silva et al., 2015).

Hui et al. (Hui et al., 2012) investigated the formability of AA7075-T6 experimentally by conducting limiting dome height (or LDH) tests at room and elevated temperatures. The author used a hemispherical punch of 100 mm diameter and a clamping force of 100 KN to prevent metal flow. The test speed was 5 mm/s while a load drop of 0.8 KN was set to capture the neck before fracture. The author concluded that the LDH values increased with forming temperature but saturated at a temperature of 220°C, as shown in Figure 2.10. There is inadequate description of the test procedures, i.e., the authors did not specify time taken for transfer pre-heated blank into the warm forming die. It is to be noted that the forming study did not involve any complementary study of the effect of microstructure features on formability. Huang et al. (Huang et al., 2010) obtained experimental FLCs of 2 mm thick AA7075-T6 aluminum sheet at 4 different

temperatures in the range 100°C- 250°C as shown in Figure 2.11. The FLCs have been digitized from the original paper of Huang et al. It is to be noted that experimental details related to FLD procedure were not presented by Huang et al. For example, the authors did not provide the thermal history of the test specimens such as holding time at the desired temperature prior to the test. The results in Figure 2.11 reveal an upward shift of FLDs to larger limit strains at higher temperatures. This increase, however, appears to be non-uniform, i.e., there is a sudden rise in the FLD curve from 150°C to 200°C. However, no explanation for this rather dramatic improvement in FLD in a certain temperature range has been offered by the author. This sudden rise in FLD may be due to partial dissolution of GP zones and  $\eta'$  precipitates which can lead to improvement in ductility. A typical dissolution temperature for GP zones and  $\eta'$  precipitates is 50 - 150°C and 200 - 250°C respectively (Kumar & Ross, 2016; Kumar et al., 2014; Löffler et al., 1983). Also, the authors were focused primarily on formability assessment and did not attempt to correlate microstructure to formability.

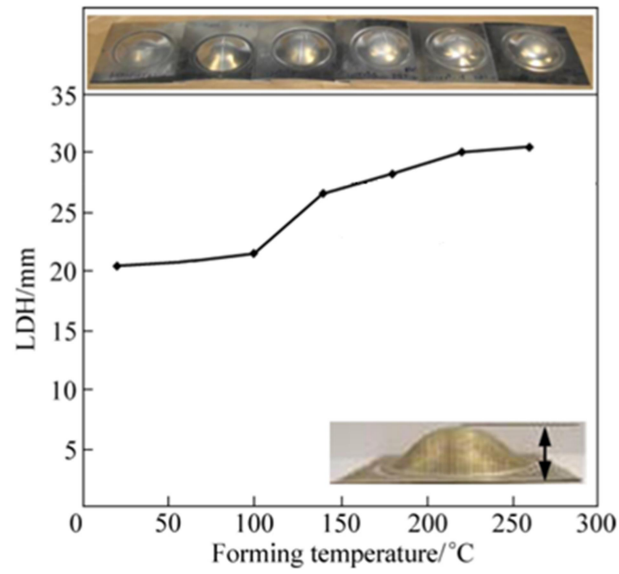


Figure 2.10 AA7075-T6 limiting dome heights at different forming temperatures (Hui et al., 2012).

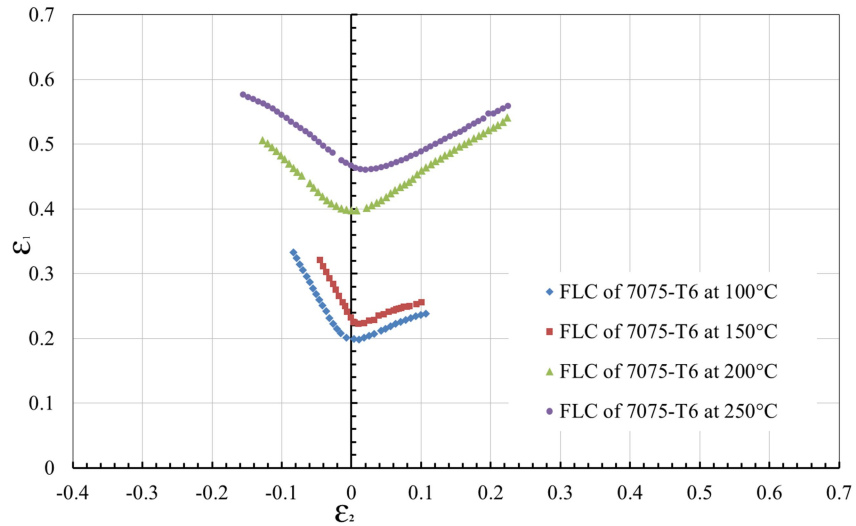


Figure 2.11 Digitized AA7075-T6 FLD at different temperatures (Huang et al., 2010).

Yang et al. (Yang et al., 2015) carried out FLD prediction of AA7075-O by using a modified M-K model based on a ductile fracture criterion and conventional M-K model. The author then compared their results with experimental FLD at room temperature (see Figure 2.12). Three clusters of experimental FLC data points were obtained from uniaxial tensile, wide plate bending and hydraulic bulge tests (see Figure 2.13 for deformed sample geometries for the three tests). The experimental FLC shows a plane strain limit strain ( $FLD_0$ ) of about 0.18 ( $\epsilon_1 = 0.18$ ). Unfortunately, no details related to material chemical composition, processing, and thermal history (i.e., heat treatment procedure) were reported in this study.

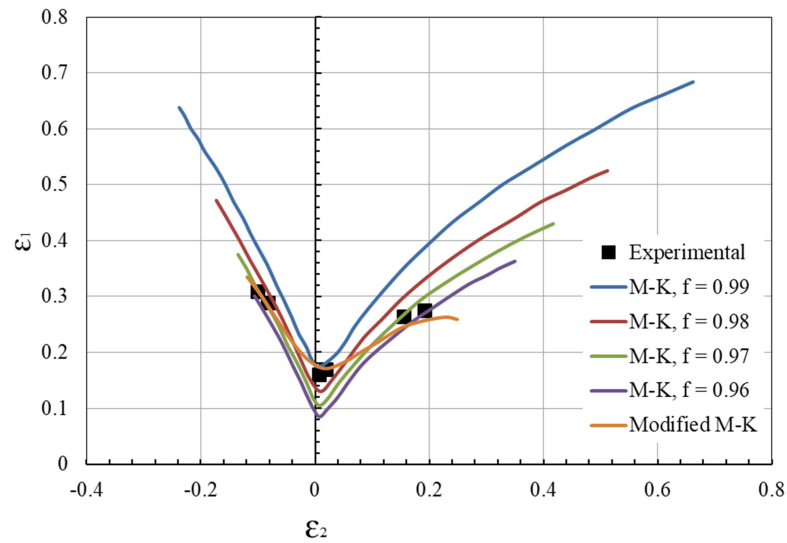


Figure 2.12 Digitized experimental and predicted FLDs for AA7075-O at room temperature (Yang et al., 2015).

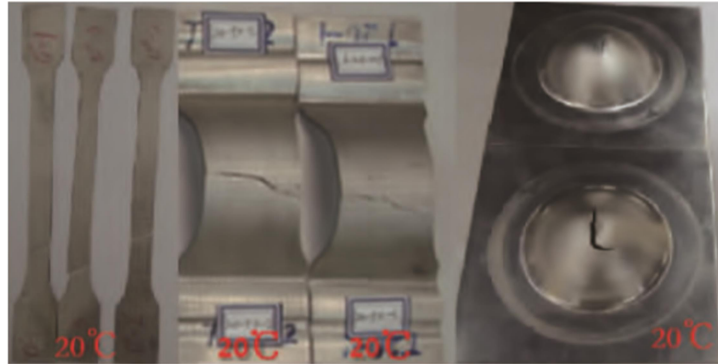


Figure 2.13 Test samples of uniaxial tensile test (left), wide plate bending (middle) and hydraulic bulge test (right) (Yang et al., 2015).

In summary, while some FLC data is available in the literature for AA7075 sheet, most of the papers available in the literature did not describe their sheet material adequately. For example, thermal history of the specimens subjected to elevated temperature dome test, holding time of samples at the desired temperature prior to the test, and microstructure characterization, such as grain size of test samples before and after deformation, are not reported. Also, the papers did not describe the experimental FLD determination procedure with sufficient details and clarity. To the best of our knowledge, there are no published experimental FLDs for AA7075-O sheet at elevated temperature in the literature based on any standard testing protocol such as the ISO 12004-2:2008 (Nakazima test).

## **2.7 Microstructure and texture evolution and damage development in AA7xxx sheet during forming**

Plastic deformation of polycrystalline aluminum alloys occurs largely by crystallographic slip at room and elevated temperatures (Gray III, 2012; Hansen & Jensen, 1999; Korbel & Bochniak, 1995). At room temperature, the microstructure evolution in FCC materials, including aluminum alloys, occurs primarily in the form of increase in dislocation



density, formation of jog and dislocation tangles and sub-grains. Also, there is some change in the grain size depending upon the level of plastic strain. At elevated temperatures, the dislocation motion is thermally activated and therefore they are able to move past obstacles more easily and in abundance by climb and other thermal mechanisms. Also, dislocations travelling on same slip systems can annihilate each other at room and elevated temperatures. The overall kinetics of dislocation multiplication and annihilation is governed by not only the strain rate and temperature but also the resistance arising from precipitates and other constituent particles. Thus, the work hardening and subsequent softening behavior of plastically deforming sheet materials is complex. For softer temper materials (O temper, for example), the work hardening can prevail to larger strains and the onset of necking is delayed. However, precipitation-hardenable materials in the cold-rolled state or with harder tempers often exhibit early onset of localization due to their limited work hardening behavior at room temperature. However, at elevated temperature, the material can undergo dynamic recovery, recrystallization and grain growth depending on the forming temperature and time period of deformation (Lin et al., 2008). Such grain level morphological and crystallographic texture changes can result in changes to the surface roughening behavior as well as formability of the sheet material (Zhao et al., 2004). Additionally, for both O-temper and T6 temper AA7075 sheet materials, ductile damage fracture mechanisms involving void formation around precipitates or constituent particles (El-Magd & Brodmann, 2001; Hahn & Rosenfield, 1975; Teirlinck et al., 1988) as well as fracture of constituent particles can occur even prior to localized (or even diffuse) necking leading to early onset of fracture. Such ductile

damage mechanisms can be prevalent in high strength aluminum alloys at room temperature as well as elevated temperatures. There are typically three stages in development of ductile fracture; void nucleation, growth, and coalescence, the latter resulting in macroscopic (specimen-scale) fracture (Garrison & Moody, 1987; Kanvinde & Deierlein, 2007; Noell et al., 2017; Puttick, 1959; Rakin et al., 2000).

In this sub-section, a brief review of literature on several microstructural topics that affect the forming behavior such as plastic instability and forming limits of aluminum sheet materials is presented. These include; (i) grain induced surface roughening during large plastic deformation, (ii) localized necking and fracture characteristics of failed specimens from shear band formation and void induced damage during large plastic deformation, and (iii) crystallographic texture changes that accompany large plastic strains.

### **2.7.1 Surface roughening of deformed sheet material**

Surface roughness results from plastic deformation of sheet metals. Excessive surface roughening, ridging or roping can create initiation sites for strain localization (Becker, 1998; Wouters et al., 2006; Zhao et al., 2004). Two main categories of microstructural surface defects resulting from plastic deformation are referred to as intrinsic and extrinsic defects (Raabe et al., 2003). The intrinsic defects are created due to microstructure dynamics, in the bulk material during and after plastic deformation while extrinsic defects arises from external effects by mechanical contact, i.e., friction and contact conditions between deforming sheet material and the forming tools and non-homogeneity of forming forces or by corrosion. Figure 2.14 show different types of surface defects.

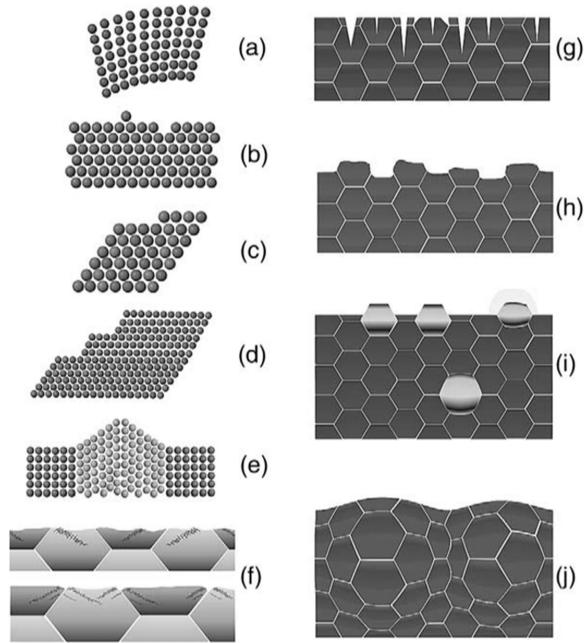


Figure 2.14 Types of surface defects; (a) elastic distortion, (b) point defects, (c) atomic surface steps caused by single dislocations, (d) larger crystallographic slip steps, (e) surface twins or athermal stress-induced transformation phenomena, (f) non-crystallographic glide traces, (g) surface cracks, (h) orange peel phenomena, (i) individual surface deformations, (j) ridging and roping phenomena (Raabe et al., 2003).

Table 2.8 summarizes different types of surface defects and associated deformation mechanisms. Ridging and roping phenomena, considered as intrinsic surface defects, appears on sheet metal surface as corrugated bands due to deformation of large sets of grains. This particular surface defect results from sheet metal deformation subjected to large strains. Surface roughness had been investigated experimentally and numerically in sheet metal formability due to its importance. It was found that surface roughness is affected by certain parameters such as strain and grain size (Becker, 1998). Becker made investigation about the effect of microstructure and mechanical properties on sheet metal

surface roughness numerically taking into account crystallographic slip mechanism and grain rotation during plastic deformation (Becker, 1998).

Table 2.8 Types of surface defects created during elastic – plastic deformation (Raabe et al., 2003).

Surface phenomenon	Underlying mechanisms
Elastic distortions	Local stress state and Hooke's law
Point defects	Diffusion, mechanics
Creep pores and hills	Diffusion, mechanics, creep
Atomic slip steps	Dislocations penetrating the surface
Larger crystallographic slip steps	Dislocation bands consisting of sets of collectively gliding dislocations on parallel or identical glide planes
Surface twins	Stress-induced orientation dependent twin formation
Athermal transformation phenomena	Stress-induced orientation dependent phase transformations (e.g. martensite)
Non-crystallographic glide traces	Dislocation bands which contain localized and collective slip activity on parallel and non-parallel glide systems; often related to macroscopic strains
Cracks	Fracture mechanics
orange peel	Different crystals produce individual out-of-plane grain-scale surface displacements due to their different orientation factors and resulting shape changes
Surface co-deformation of hard and soft phases	Hard and soft matter assembled in one microstructure
Ridging and roping	Collective deformation of larger sets of grains typically resulting in a banded surface topology

Finite element analysis (FEA) of surface roughness development by Becker was carried out by choosing a suitable crystal constitutive model including experimentally determined parameters such as crystallographic texture and strain hardening for AA6111-T4 with average grain size of 20  $\mu\text{m}$ . The author concluded that there exists a linear relationship

between surface roughness and strain and grain size. Also, a strong relationship was observed between surface roughness and strain localization in which the depth of valleys were controlled. Since strain hardening, crystallographic texture and material inhomogeneities distribution affect strain localization, it is recommended, for surface roughness reduction, to increase strain hardening or modify production process to obtain favorable crystallographic texture or misorientation distribution. However, in this study the effect of precipitates and grain shape were not included. Also, the effect of deformation of grains below surface depth of more than 50  $\mu\text{m}$  was not captured in the analysis.

Texture (or grain orientation distribution) also has a strong effect on the surface roughness (Baczynski et al., 2000; Lee et al., 1998; Zhao et al., 2004). Zhao et al. investigated using a 3D finite element crystal plasticity model the grain scale surface roughening of aluminum sheet subjected to uniaxial and biaxial loading conditions. The authors concluded that surface roughness is controlled by factors such as boundary (loading) conditions, Taylor factor, which is a measure of the ability of specific grain orientations to accommodate plastic flow or grain anisotropic kinematic hardening, shear tendency of individual grains and the spatial distribution of neighbouring grains orientations. It was found that surface roughness for samples deformed in transverse to sheet rolling direction (TD) is more significant than those deformed in rolling direction (RD) due to a lower Taylor factor and can result in plastic flow localization. Also, a combination of soft and hard texture components such as Cube (soft component) and Goss (hard component) can result in ridging formation when the samples is deformed in

the TD direction. Further, spatial distribution of grains may transform a ribbed surface into a corrugated profile. Finally, randomness of different texture component can lead to the development of an orange peel type roughening especially when the grain size of the material is large.

### **2.7.2 Strain hardening and necking characteristics of deformed AA7075 sheet**

Strain hardening due to mechanical working is one of the most important properties that controls the material behavior after yielding and has a significant effect on formability. This phenomenon arises from interaction of mobile dislocations with other immobile and mobile dislocations as well as other microstructure constituents such as precipitates, solute atoms and grain boundaries (Gupta et al., 2015). During deformation strain hardening rate continues to decrease with increase in strain while stress continues to increase to a maximum value. At that point, strain localization (or necking) is initiated due to the onset of plastic instability at the continuum or microstructural level. Sheet metal with high strain hardening coefficient show delay in the onset of strain localization and hence a larger forming limit strains can be obtained. Figure 2.15 shows a schematic diagram of a typical uniaxial tensile load versus displacement curve from Gupta et al. (Gupta et al., 2015) with labeling of various stages of the deformation process starting with elastic loading, yielding, ultimate strength, necking and finally fracture (or separation) of the material.

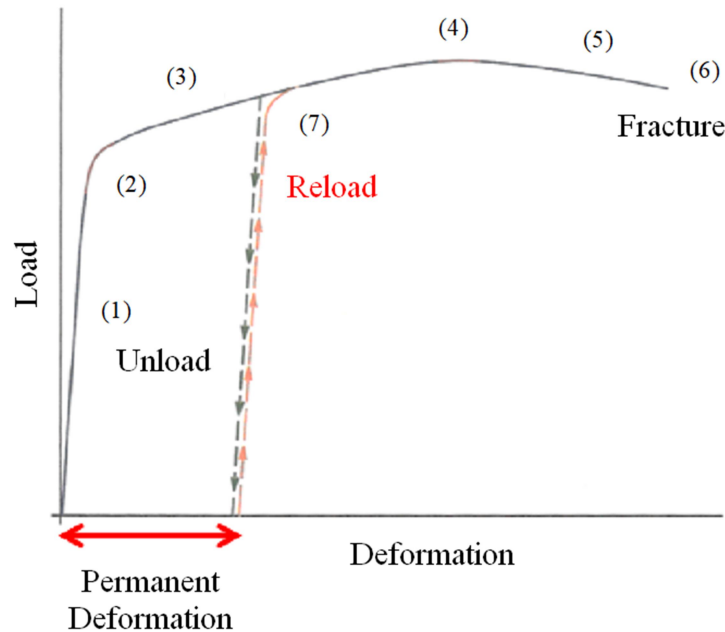


Figure 2.15 Uniaxial tensile test based schematic of load – deformation curve; (1) Linear elastic portion, (2) proportional limit, (3) yielding (strain hardening start point), (4) ultimate strength, (5) plastic instability (necking), (6) fracture point and (7) unload – reload result in strain hardening (Gupta et al., 2015).

Necking (or strain localization) is an important phenomenon that occurs just before fracture and determines forming limit for sheet materials for a specific loading or strain path. It is well known that plastic instability is affected by strain, strain path (or strain state), strain rate and forming temperature. Huo et al. made investigation of warm forming for peak-aged AA7075 sheet metal at a range of temperatures from room temperature to 250°C by studying warm tensile behaviour (Huo et al., 2016). Figure 2.16 taken from the work of Huo et al. shows a set of true stress – true strain curves obtained at different isothermal test temperatures. The author divided each curve into four regions (I-IV) consisting of elastic and yield, uniform deformation, diffused necking and localized necking regions. The range of each of the regions is indeed affected by the test

temperature. For example, the strain hardening (and uniform deformation) stage is quite extensive but the diffuse and localized necking region is substantially smaller at room temperature. On the other hand, at the highest temperature, the opposite is true. The strain hardening (and uniform deformation) stage is relatively small but the diffuse and localized necking region is substantially larger. Similar trends have been observed by others for other material systems (Kumar & Ross, 2016; Venkateswarlu et al., 2010). In general, material softening at elevated temperature leads to improved material formability and delay in the onset of localized necking due to the positive effect of the increased material strain rate sensitivity.

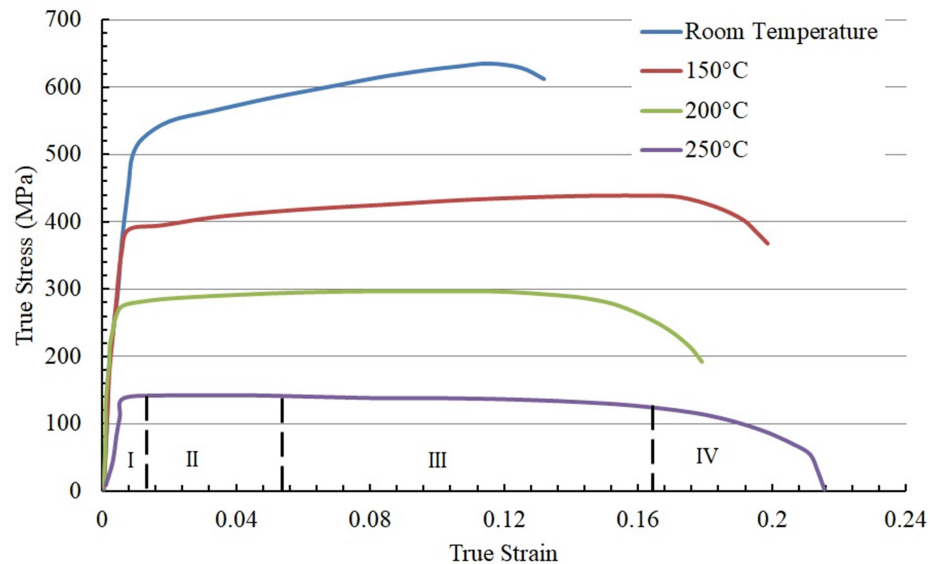


Figure 2.16 Uniaxial tensile true stress – strain curves of AA7075-T6 (Huo et al., 2016).

Another group of researchers, Hui et al. (Hui et al., 2012) studied experimentally warm formability of AA7075-T6 sheet by performing stretch forming, deep drawing and uniaxial tensile tests. The research established uniaxial tensile flow stress curves at



different strain rates of  $0.008 \text{ s}^{-1}$ ,  $0.025 \text{ s}^{-1}$  and  $0.583 \text{ s}^{-1}$  at  $220^\circ\text{C}$  (see Figure 2.17). It was found that as strain rate increased the yield and ultimate strength increased but the total elongation decreased probably due to the a decrease in strain rate sensitivity ( $m$ ) which reduced the diffuse and localized necking regions of the curve at higher strain rate.

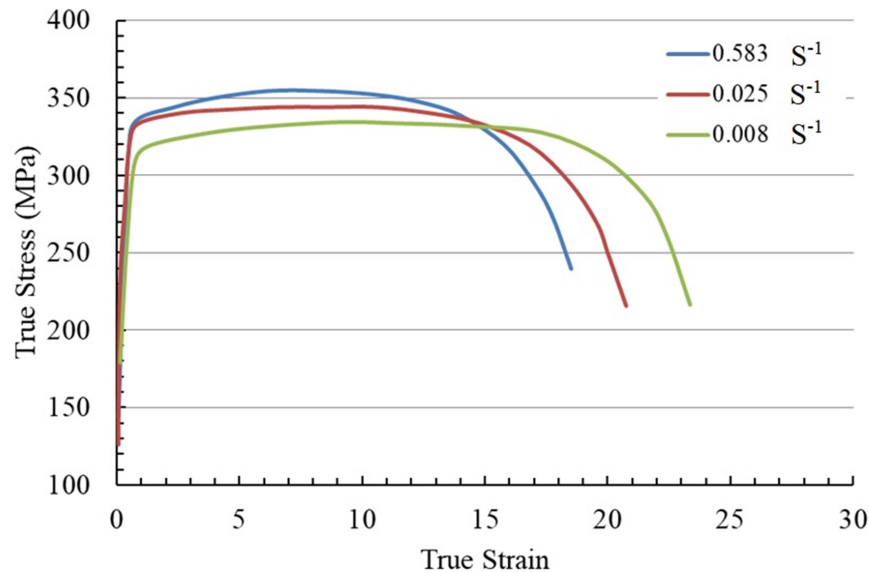


Figure 2.17 Uniaxial tensile true stress-strain curves for AA7075-T6 at  $220^\circ\text{C}$  (Hui et al., 2012).

### 2.7.3 Void-induced damage at room and elevated temperatures in aluminum alloys

Typical ductile fracture mechanisms in metallic materials from literature are illustrated in Figure 2.18 below (Kanvinde & Deierlein, 2007). These mechanisms typically operate at large plastic strains in the diffuse and localized necking regions with micro-void nucleation from either the matrix particle de-cohesion or break-up of particles (Garrison & Moody, 1987) (top left sketch). The micro-voids then grow under the applied stress (top right sketch) and eventually internal necking in the inter-void region is initiated

(bottom left sketch) depending upon the stress state. This leads to so-called void sheeting along a characteristic plane or set of planes. The last stage consists of void coalescence as shown by the linkage of voids in the void sheet plane resulting in the so called dimpled rupture of the specimen. The extent of each of the void development stages is a function of many microstructural parameters such as matrix flow behavior, strengths of the different particles which are often elastic in nature, strength of the interface, particle size shape and distribution etc. Also, the void nucleation and growth process can occur simultaneously in some materials in different regions of the microstructure.

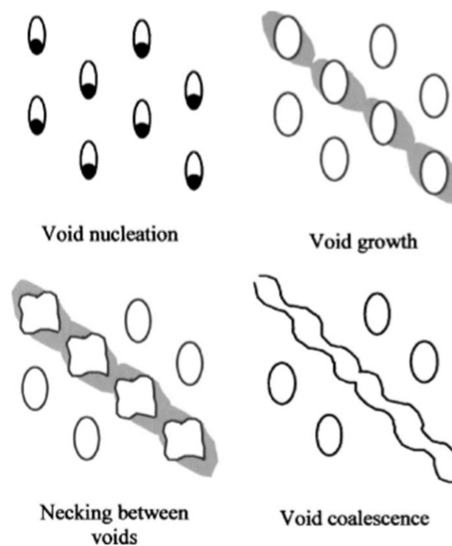


Figure 2.18 Ductile fracture mechanism (Kanvinde & Deierlein, 2007).

Ductile fracture is typically examined in the literature by imaging the nature of micro-void induced damage using SEM. Ductile fracture can be detected via dimples formation

on the fracture surface associated with large-scale void coalescence prior to the fracture process as illustrated by the large magnification SEM fractographic images of a room temperature tensile test for 1 mm thick AA6016-T4 sheet specimen in Figure 2.19 (Thuillier et al., 2012). The authors investigated the ductile damage evolution by using X-ray micro-tomography for a notched AA6016-T4 tensile samples with three different geometries that introduced different stress triaxialities ( $\sigma_m/\bar{\sigma}$ ) in the region of reduced cross-section, as shown in Figure 2.20. The experimental work was complemented with a numerical (FE) simulation of the experimental test specimen by using the well-known GTN ductile void growth model (Chu & Needleman, 1980; Gurson, 1977; Tvergaard, 1981) and void volume fraction evolution with applied strain was predicted. It was concluded that rapid evolution of void volume fraction with strain was more pronounced for samples of 45° direction from rolling while similar results were obtained for samples of LT and TD directions. Also, the greatest void volume fraction was obtained at the highest stress triaxiality state (smallest notch radius, i.e.,  $R = 1$  mm). However, the effect of stress triaxiality on void volume fraction was underestimated in some of the model geometries. Also, void coalescence step was not included in the model to predict void volume fraction and consequently a sudden increase in void volume fraction was observed at strain above 0.6.

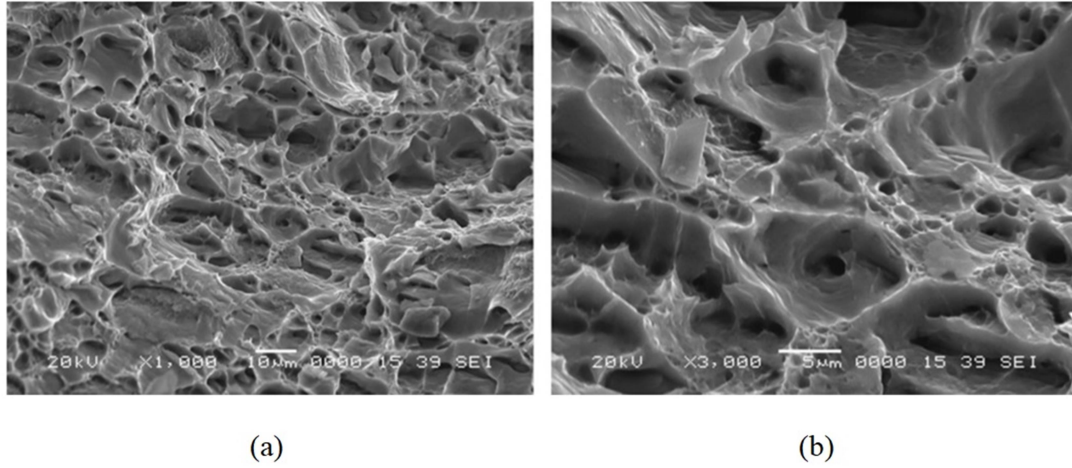


Figure 2.19 SEM images for dimple rupture of AA6016-T4 after tensile test at room temperature; (a) low magnification, and (b) high magnification (Thuillier et al., 2012).

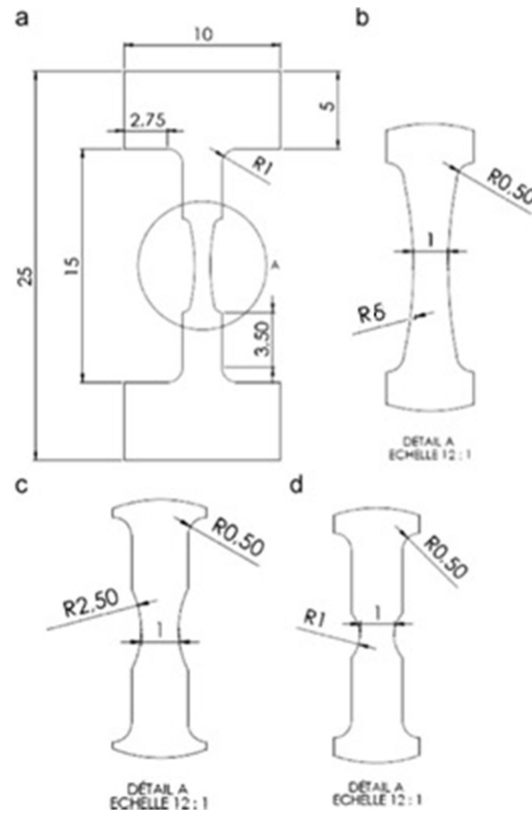


Figure 2.20 AA6016-T4 X-ray tomography sample shape; (a) whole sample, (b) middle zone A with  $R = 6$  mm, (c) middle zone A with  $R = 2.5$  mm and (d) middle zone A with  $R = 1$  mm (Thuillier et al., 2012).

In another study, sheet metal formability was investigated for 2 mm thick AA2024-T3 sheet by performing a series of elevated temperature tensile and cup (deep drawing) tests by using hemispherical and flat punch in the temperature range 350°C to 493°C (Wang et al., 2011). Ductile damage was evaluated by SEM fractographic analysis on fractured tensile samples. These results are presented in Figure 2.21.

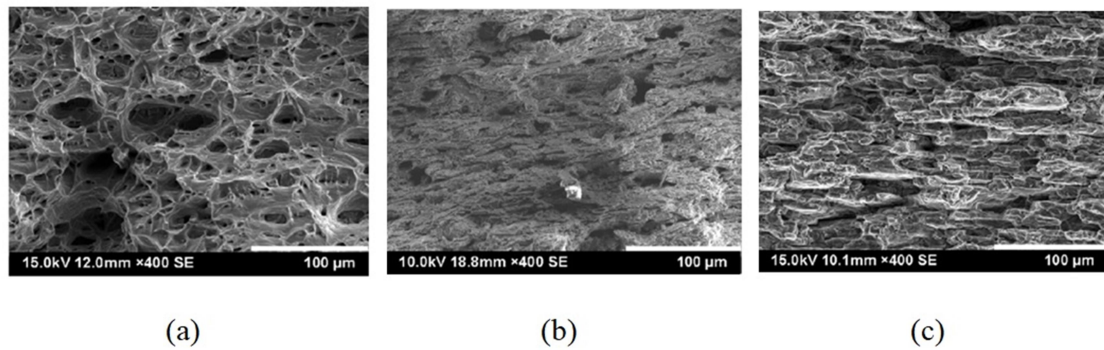


Figure 2.21 SEM fractographic images for AA2024-T3 tensile samples; (a) test temperature of 350°C, (b) test temperature of 450°C and (c) test temperature of 493°C (Wang et al., 2011).

Dimple rupture with clear tear ridges was obtained on the fracture surface of tensile samples deformed at 350°C while intergranular fracture associated with relatively smaller dimples was observed in samples tested at 450°C, and almost no dimples but elongated intergranular fracture occurred in deformed samples at 493°C. After in-situ SEM examinations, the author concluded that as the tensile temperature increases up to 450°C, more grain boundary precipitation and precipitates coarsening takes place due to thermal activation. As a consequence, void formation initiated at the grain boundary through the interface between large precipitates and matrix. Also, due to the existence of small

precipitates, small voids nucleated and grew resulting in relatively smaller dimples at fracture. Lastly, contrary to the general trend of increasing formability with temperature for many aluminum sheet materials, a drop in formability was observed for samples formed at 493°C. This is probably due to the lower strength of grain boundaries at a higher homologous temperature (defined as the ratio between forming temperature and melting temperature of the alloy) of grain boundaries than that of grains interior. Therefore, the stress required for grain boundaries de-cohesion is lower than that of precipitates-matrix de-cohesion, and the fracture mode was intergranular. While this study highlights the competing ductile fracture mechanisms at elevated temperature deformation conditions, more detailed microstructural investigations using SEM and TEM methods are required to support and explain in detail the degradation of formability at 493°C.

#### **2.7.4 Crystallographic texture in aluminum alloys**

Crystallographic slip is by far the most important deformation mechanism in aluminum alloys at room and elevated temperatures. It is responsible for the large plastic strains involved in sheet forming operations. It is normally considered to involve a simple shear plane parallel to specific crystallographic planes and directions. Slip can be analyzed in terms of changes to grain orientation distribution (or crystallographic texture). The latter may also be considered as an important microstructure feature that affects mechanical properties and formability of rolled sheet materials including the rolled FCC aluminum sheet. Figure 2.22 shows a schematic drawing of texture in a plate or sheet material.

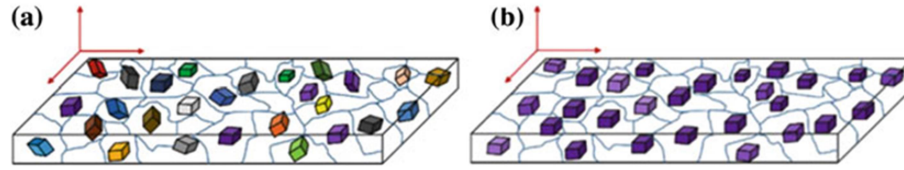


Figure 2.22 A schematic illustration of grain orientation in a plate or sheet of polycrystalline material; (a) random grain orientation, and (b) preferred orientation (Prasad & Wanhill, 2017).

Texture can be analyzed either microscopically from the surface and near surface regions of the sheet by using a SEM fitted with a X-Ray detector (the so-called electron backscattered diffraction or EBSD method) or at a more macroscopic scale with X-ray diffraction (XRD) technique. Both methods can provide statistical data in forms of pole figures (PFs) that can be mathematically transformed to orientation distribution functions (ODFs). The latter can be represented in Euler space by three Euler angles,  $\varphi_1$ ,  $\phi$  and  $\varphi_2$  (Bowen, 1990). This Euler space represents a rotation system that relates sheet metal sample coordinate system to the entire crystal coordinate system in order to specify grain orientation distribution. Figure 2.23 shows both coordinates for sheet metal and entire crystals while Figure 2.24 illustrates the Euler angles rotation system.

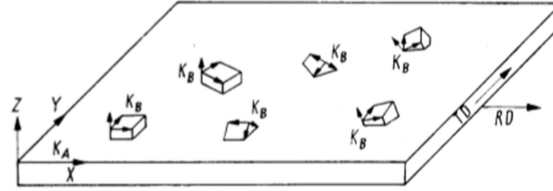


Figure 2.23 Two coordinate systems, one for specific grains ( $K_A$  and  $K_B$ ) in the polycrystalline sheet and the other for the entire sheet specimen ( $X$ ,  $Y$  and  $Z$ ) (H.-J. Bunge, 2013).

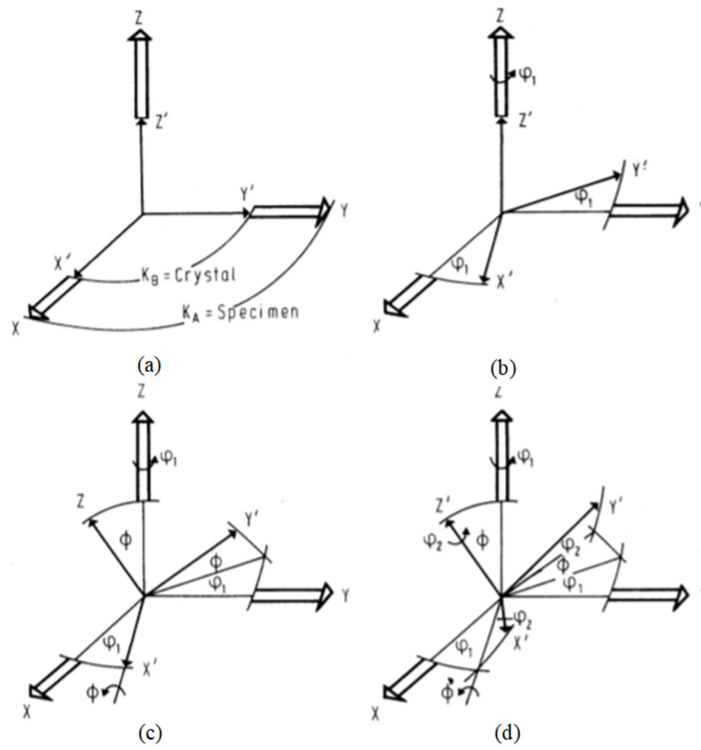


Figure 2.24 Euler space; (a)  $K_A$  and  $K_B$  are parallel, (b) rotation of  $K_B$  around  $Z'$  axis by  $\varphi_1$ , (c) rotation of  $K_B$  around  $X'$  axis by  $\phi$  and (d) rotation of  $K_B$  around  $Z'$  axis by  $\varphi_2$  (H.-J. Bunge, 2013).



Figure 2.25 shows ODF for  $\phi_2 = 0$  and  $45^\circ$  including ideal orientations of face centered cubic (FCC) metals and alloys. Also, Table 2.9 summarizes positions of ideal orientations in Euler space. The main texture components in FCC metals and alloys fall under two main categories; (a) deformation texture, in which sheet metal grains rotate during rolling process and take certain orientation, and represented by Copper  $\{112\}\langle 111 \rangle$ , Brass  $\{011\}\langle 211 \rangle$  and S  $\{123\}\langle 634 \rangle$  orientations, and (b) recrystallization texture, in which recrystallization occurs during hot rolling stage, represented by Cube  $\{001\}\langle 100 \rangle$  and Goss  $\{011\}\langle 100 \rangle$  orientations (Moghaddam et al., 2016). However, the two types of textures may appear at the same time with one texture being strong and the other weak.

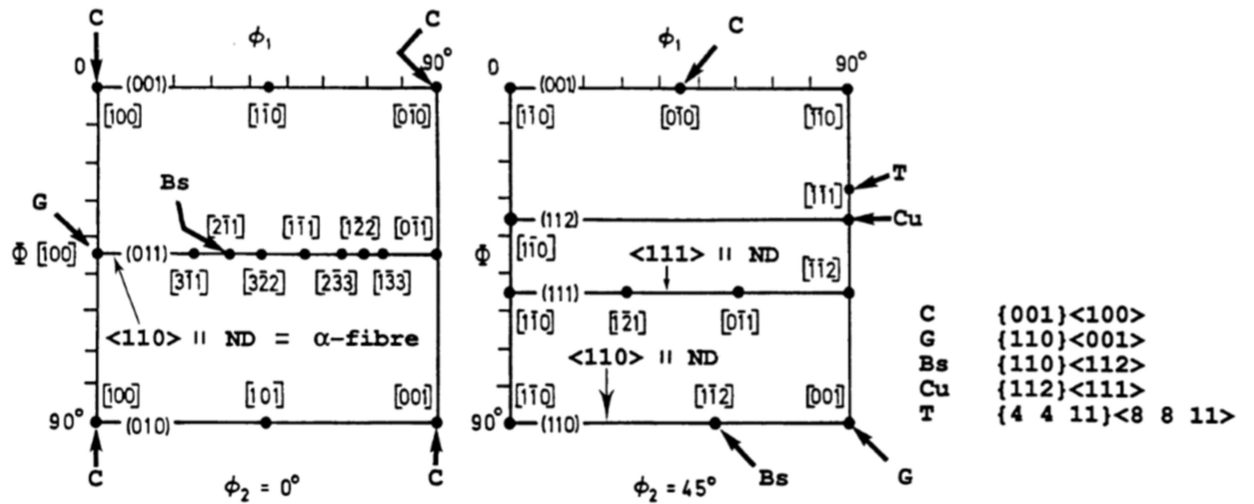


Figure 2.25 ODF show 5 ideal orientations (Cube, Goss, Brass, Copper and T (also called S)) for FCC metals and alloys at  $\phi_2 = 0^\circ$  and  $45^\circ$  (Bowen, 1990).

Table 2.9 FCC ideal texture orientations and its positions in Euler space (Olaf Engler &amp; Hirsch, 2009; O Engler &amp; Lücke, 1992; JR Hirsch, 1990; Suwas &amp; Gurao, 2008).

Texture Type	Texture Designation	Texture Orientation $\{hkl\}\langle uvw \rangle$	Euler Angles $(\varphi_1, \phi \text{ and } \varphi_2)$
Deformation	Copper	$\{112\}\langle 111 \rangle$	$90^\circ, 30^\circ \text{ and } 45^\circ$
	Brass	$\{011\}\langle 211 \rangle$	$35^\circ, 45^\circ \text{ and } 0^\circ/90^\circ$
	S	$\{123\}\langle 634 \rangle$	$59^\circ, 34^\circ \text{ and } 65^\circ$
Recrystallization	Cube	$\{001\}\langle 100 \rangle$	$0^\circ, 0^\circ \text{ and } 0^\circ/90^\circ$
	Goss	$\{011\}\langle 100 \rangle$	$0^\circ, 45^\circ \text{ and } 0^\circ/90^\circ$

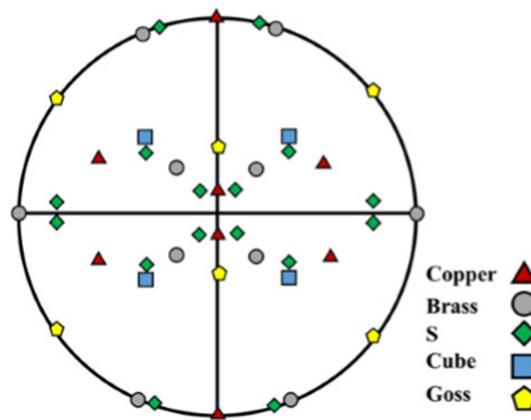


Figure 2.26 A schematic representation of different texture orientations in (111) pole figure for FCC material (Moghaddam et al., 2016).

The formability of two 7xxx extruded aluminum sheet alloys AA7108 and AA7030 with 200 mm width and 3 mm thickness in soft conditions (i.e., water-quenched or W temper and annealed or O temper) were assessed by conducting tensile, compression, plane strain, and in-plane biaxial tension (Marciniak) tests at room temperature by Lademo et al. (Lademo et al., 2008). The extruded sheets were subjected to cold rolling to 50% thickness reduction (1.5 mm) then thermo-mechanically treated before forming (see Table 2.10). The effect of texture and grain structure on formability was assessed.

Table 2.10 TMP conditions of AA7108 and AA7030 sheets prior to mechanical and formability tests (Lademo et al., 2008)

Material	Alloy	Thermo-mechanical processing	Grain structure
A	AA7108	Extruded, cold rolled, solution heat treated at 470°C for 5 min. and water quenched	Elongated, recrystallized
B		Extruded, cold rolled and annealed at low temperature (400°C for 5 min.)	Fibrous, non-recrystallized
C	AA7030	Extruded, cold rolled, solution heat treated at 470°C for 5 min. and water quenched	Equi-axed, recrystallized
D		Extruded, cold rolled and annealed at low temperature (350°C for 5 min.)	Elongated, deformed

Figure 2.27 and Figure 2.28 show the through-thickness microstructures and mid-thickness (111) pole figures for extruded AA7108 and AA7030 respectively. Note that the authors did not specify the observation plane (LT or ST) from where the microstructures were taken. In any case, AA7108 extruded sheet show fibrous grain structure due to Zr (0.15 wt%) based dispersoids, which controls grain size and prevents grain recrystallization, while AA7030 illustrate recrystallized grain structure (with no Zr present). Also, both alloys show surface layers of recrystallized grains which were likely due to surface shear deformation in the extrusion process.

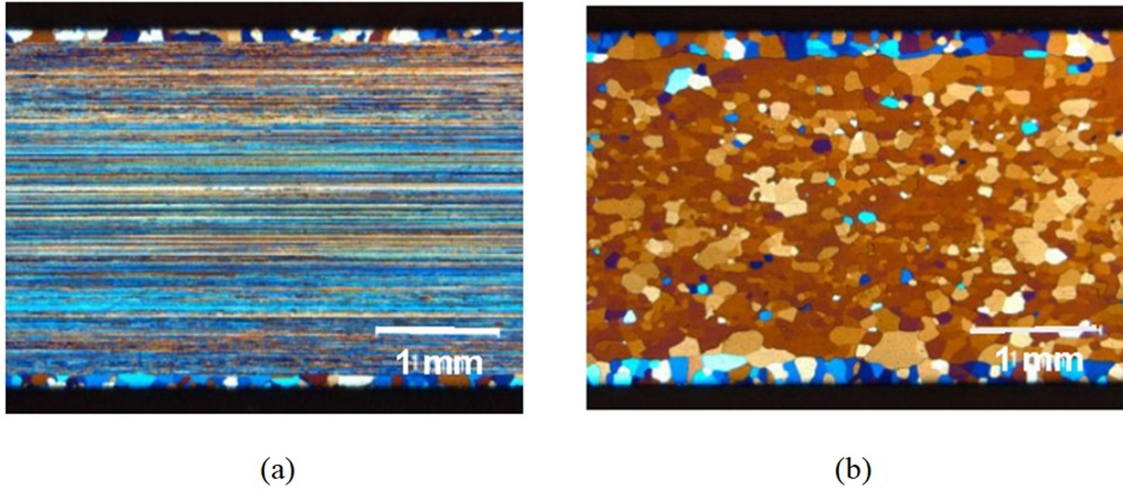


Figure 2.27 Extruded sheet metals microstructure; (a) AA7108 and (b) AA7030 (Lademo et al., 2008).



Figure 2.28 Mid-thickness (111) pole figures of extruded sheet metals; (a) AA7108 and (b) AA7030 (Lademo et al., 2008).

PFs for both alloys show textured materials in which AA7108 show Brass texture component while AA7030 reveal Cube texture component according to the ideal texture orientation in (111) plane (see earlier Figure 2.26). Figure 2.29 show the microstructures of different thermo-mechanical processes combinations for both AA7108 and AA7030

sheet metal. The first microstructure (Figure 2.29 (a)) shows elongated and recrystallized grain structure for AA7108 while equi-axed recrystallized grain structure was obtained for AA7030 subjected to the same thermo-mechanical processing (Figure 2.29(c)). The other two annealed microstructures, annealed at low temperatures, show largely the elongated grain structure (Figure 2.29 (b, d)). The bulk texture after deformation (cold rolling) and heat treatments is shown in Figure 2.30. Near random texture was revealed for both aluminum alloys with conditions A and C (see Figure 2.30 (a, c)) probably due to the annealing temperature which was high enough for recrystallization process to occur while a clear texture components of  $\beta$  – fibre and rotated Cube texture components were obtained for low temperature annealed AA7108 and AA7030 (materials B and D) respectively (see Figure 2.30 (b, d)).

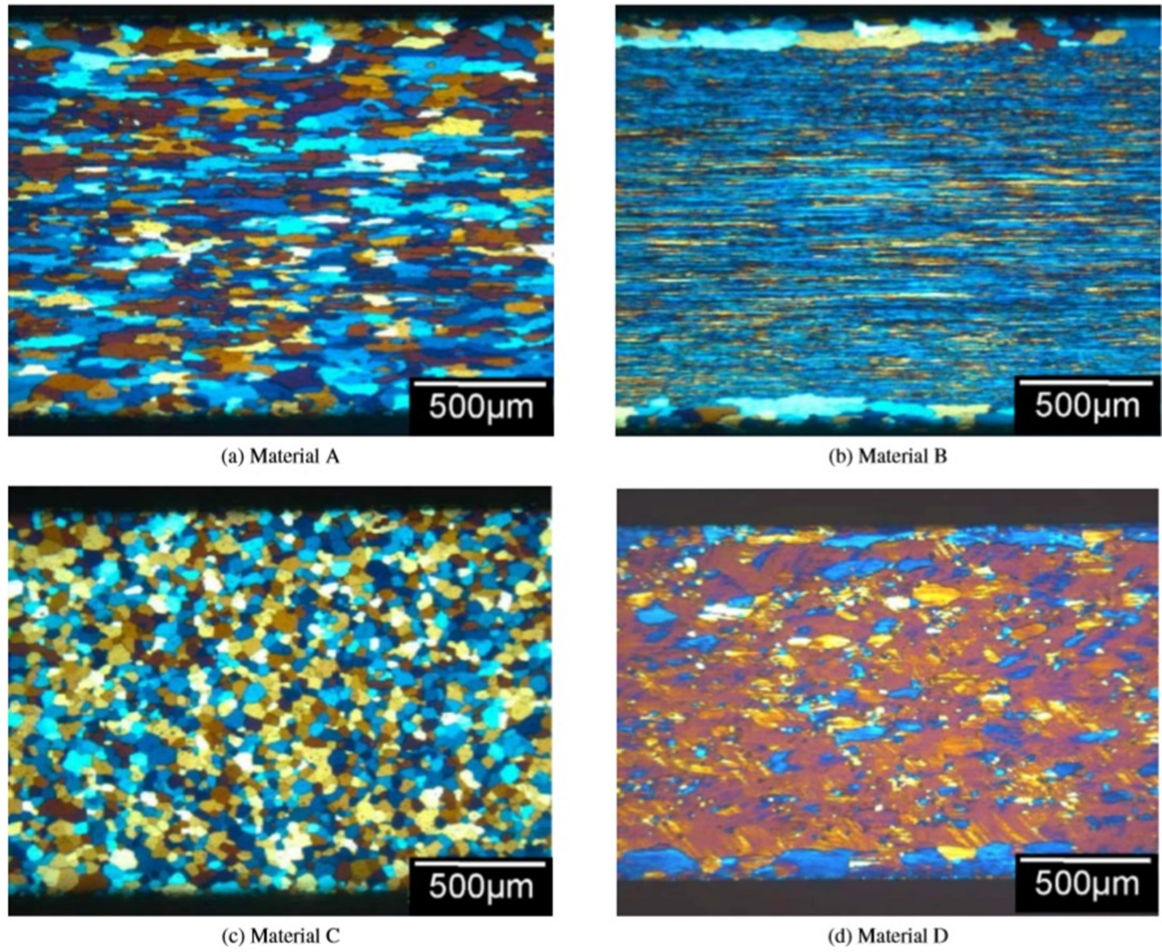


Figure 2.29 Through-thickness microstructure; (a) AA7108 extruded, cold rolled and annealed, (b) AA7108 extruded, cold rolled and annealed at low temperature (400°C for 5 min.), (c) AA7030 extruded, cold rolled and annealed and (d) AA7030 extruded, cold rolled and annealed at low temperature (350°C for 5 min.) (Lademo et al., 2008).

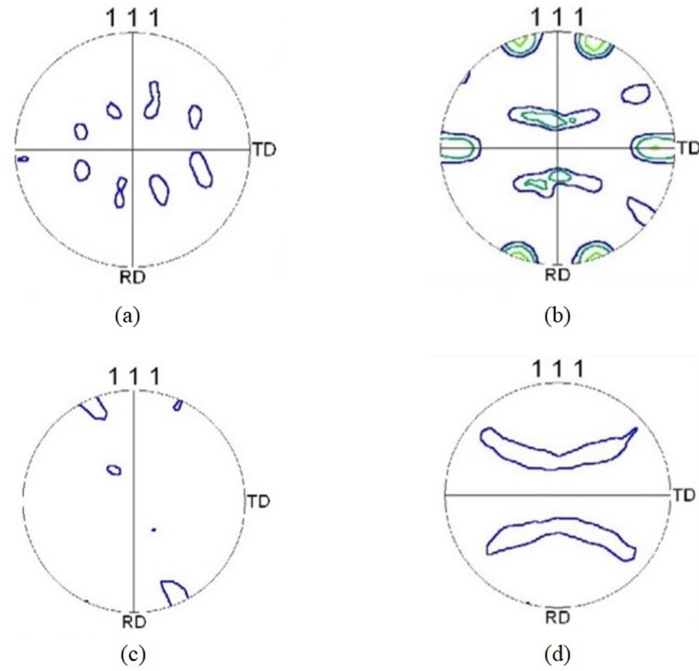


Figure 2.30 (111) pole figure of cold rolled and heat treated sheet metal; (a) Material A, (b) Material B, (c) Material C and (d) Material D (Lademo et al., 2008).

Post-mechanical and formability test microstructures and textures were also investigated using necked and fractured polished and anodised tensile samples. The optical microscopic (OM) through-thickness grain structure images are shown in Figure 2.31. Extensive through-thickness intersecting shear bands were observed in the localized region of all of the specimens. However, for equi-axed grain and near random texture obtained in materials A and C, the evolution in grain orientation led to crack initiation and propagation from the outside (sample surface) towards the inside (mid-thickness region). Material D with less elongated grains also showed trends similar to Materials A and C despite the different heat treatment and grain elongation. Material C, with highly

elongated grains, showed a characteristically sharp shear bands and an early onset of fracture from one of the surfaces. The microstructure of Material B (AA7108 extruded, cold rolled and annealed at low temperature) exhibited no significant change from annealing compared to the starting extruded AA7108 sheet microstructure except the surface layer was recrystallized (see Figure 2.27 (a) and Figure 2.29 (b)). Therefore, the early formation of shear bands, probably attributed to the fibrous grain structure and dispersoids due to Zr content, tended to degrade formability. In conclusion, the near random textured sheet materials (A and C) exhibited good formability compared to the sharp textured Material B and D which exhibited an early onset of fracture and lower formability.



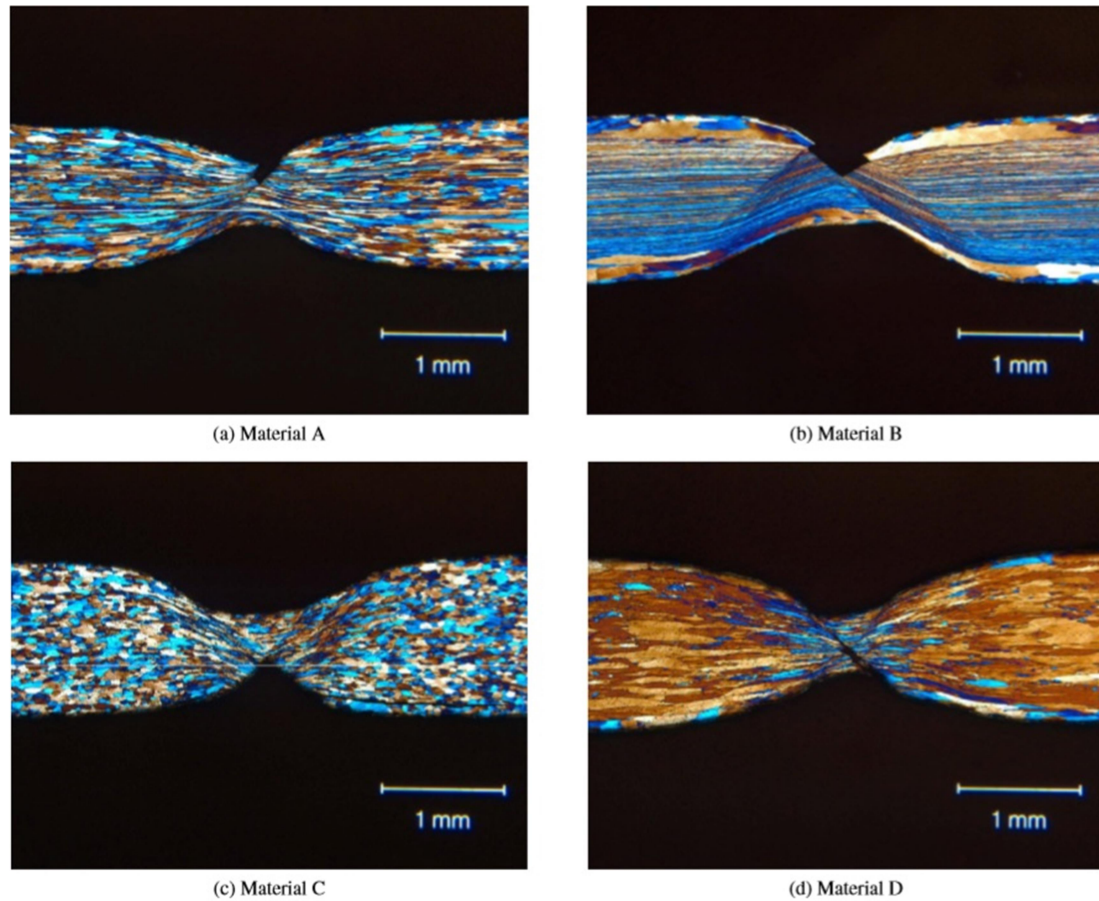


Figure 2.31 Through thickness optical microscope images for room temperature fractured tensile samples; (a) AA7108 extruded, cold rolled and annealed, (b) AA7108 extruded, cold rolled and annealed at low temperature (400°C for 5 min.), (c) AA7030 extruded, cold rolled and annealed and (d) AA7030 extruded, cold rolled and annealed at low temperature (350°C for 5 min.) (Lademo et al., 2008).

Narayanan et al. investigated the evolution of crystallographic texture in cold rolled Al-Zn-Mg aluminum plate and sheet (Narayanan et al., 2012). Two different alloys of AA7075-T7351 (15 mm thick plate) and AA7020-T651 (1.8 mm thick sheet) were investigated at mid-thickness section after artificial aging treatment and 70% cold rolling reduction. Figure 2.32 show PFs of AA7075-T7351 and AA7020-T651 as starting

materials and after artificial ageing treatment and 70% thickness reduction. Texture of starting material of AA7075-T7351 shows a rather weak Cube orientation. After 70% rolling thickness reduction, the grains orientation reveals a sharper Cube orientation. AA7020-T651 has Copper texture as a starting material while Brass and S texture components appear clearly after 70% deformation but with a weak Copper orientation.

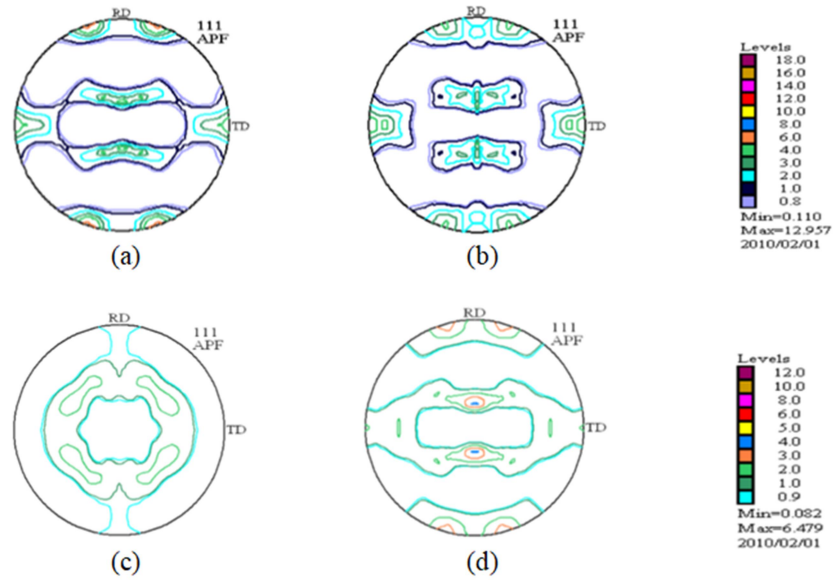


Figure 2.32 (111) pole figures of AA7075 and AA7020; (a) AA7075-T7351 starting material, (b) AA7075 after 70% reduction, (c) AA7020-T651 starting material and (d) AA7020 after 70% reduction (Narayanan et al., 2012).

Figure 2.33 shows the ODFs, with constant  $\varphi_2$  of  $0^\circ$ ,  $45^\circ$  and  $65^\circ$ , for both AA7075-T7351plate and AA7020-T651 sheet after artificial aging treatment and 70% rolled thickness reduction.

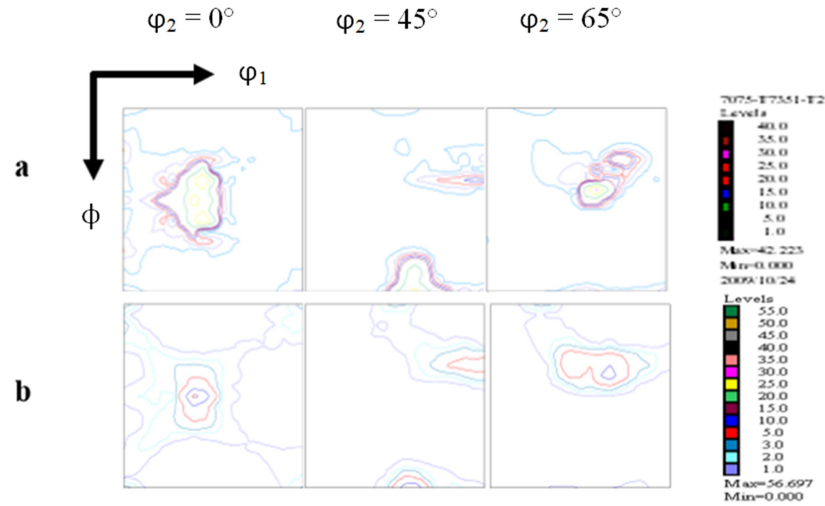


Figure 2.33 Mid-thickness ODFs after 70% thickness reduction; (a) AA7075 and (b) AA7020 (Narayanan et al., 2012).

The authors have obtained ODF results as well that are similar to those from PFs for both aluminum alloys. Copper, Brass and S texture components were obtained clearly while weak Cube texture was observed. After 70% cold rolling reduction, Brass and S components appeared strong but the Cube and Copper textures were weak. It is concluded that as the rolling deformation increases the deformation texture components, Copper, Brass and S, increase in intensity. Also, AA7075 shows S texture orientation clearly while AA7020 reveal sharp Brass texture component than other orientations. Moreover, shear bands (see Figure 2.34) were observed in AA7020 but not in AA7075 probably due to its higher Zn/Mg ratio (about 4).

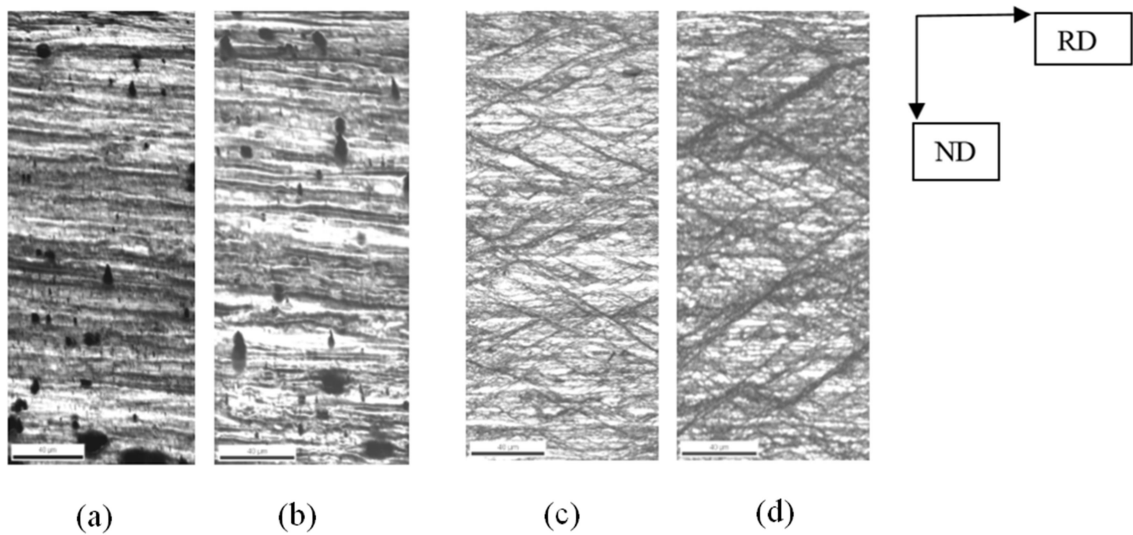


Figure 2.34 Shear bands observed in cold rolled alloys; (a) AA7075 after 50% reduction, (b) AA7075 after 70% reduction, (c) AA7020 after 50% reduction and (d) AA7020 after 70% reduction (Narayanan et al., 2012).

To the best of our knowledge, there are no published studies on surface roughness development, void-induced damage and crystallographic texture development in deformed AA7xxx sheet metal, and specifically for AA7075, after biaxial dome tests under different strain paths at room or elevated temperature.

## 2.8 Summary

It is observed from the above review of literature that there is limited work, if any, that attempts to correlate microstructure, texture and material damage that occur under multi-axial large plastic deformation in AA7xxx series sheet material, in general, at room and elevated temperatures, and specifically for AA7075 sheet materials in different temper conditions (such as O and T6). Although there are a few publications on forming limits of fully annealed (O-temper) and age-hardened (T6-temper) AA7075 at room temperature, no noteworthy publications that provide elevated temperature forming limits of AA7075-O are available. Therefore, there is a need to firstly and clearly establish the elevated temperature forming limit and other material flow and strain development characteristics of AA7075 sheet in O and T6 temper conditions to aid the understanding of the elevated temperature forming process for these tempers. Also, there is a need to correlate the elevated temperature formability to the underlying microstructure, texture, surface and damage characteristics of the rolled AA7075 sheet. All of the above microstructural features evolve with strain, strain path, strain rate and temperature and thus affect sheet formability by contributing to plastic instability (localized necking). With increasing interest in forming of AA7xxx series sheet materials into automotive components, fulfillment of the knowledge gaps in AA7075 sheet metal formability via experimental studies and numerical modeling is critical.

### **3-Experimental Methodology**

The basic research experimental methodology consisted of elevated temperature uniaxial tensile and formability characterization of conventional AA7075-O and AA7075-T6 sheet materials at room and elevated temperatures using uniaxial tensile tests and multi-axial hemispherical dome tests as well as surface, microstructure and crystallographic texture assessment of un-deformed and deformed (i.e., necked and fractured) tensile and dome samples. Isothermal uniaxial tensile experiments were carried out at two different cross-head speeds at various test temperatures to guide the selection of a suitable material constitutive model for AA7075 (model details are provided in Chapter 5). For formability characterization, punch load versus displacement traces for different specimen geometries corresponding to different strains path, strain distribution across the neck for different tensile and dome specimens, and forming limit diagrams (FLDs) were obtained at a range of temperatures. The temperatures utilized for dome tests were same as those utilized for uniaxial tension tests. Further, quantitative microstructural damage characterizations using optical and scanning electron microscopic methods were carried out on un-deformed and deformed (dome samples with neck and fracture) specimens of O and T6 temper materials to correlate formability with microstructure at different test temperatures. Lastly, crystallographic bulk texture of the un-deformed sheet and deformed hemispherical dome samples of AA7075 sheet in O and T6 tempers were analyzed to assess the nature of texture evolution as a function of strain path, local strain, and test temperature.

### **3.1 Material selection and microstructural characterization**

#### **3.1.1 Chemical composition**

Inductively Coupled Plasma – Optical Emission Spectrometer (ICP-OES) was used to analyze the chemical composition of AA7075 sheet metal received from the sheet producer, Novelis, Inc. A photograph of the test equipment and a schematic drawing of ICP system components are shown in Figure 3.1 and Figure 3.2 respectively. The system was capable of analysing 73 elements in the sheet material in about 35 seconds (including sample uptake time of 25 seconds) covering a rather wide wavelength range of 167 nm - 785 nm to minimize the spectral interference. The specimen preparation procedure prior to ICP analysis consisted of; (i) weighing of the sample, and (ii) placement of the sample in the volumetric cylinder and its dissolution in a solution of 3 ml HCL and 5 ml H<sub>2</sub>O and then filling up to the specified volume. The sample was introduced into the device by peristaltic pump into a nebulizer and then into a plasma torch. The nebulizer turned the sample into tiny droplets (Aerosol) in which some of these droplets entered a very hot ionized argon plasma torch of about 2% of sample volume. The sample entered the plasma and the molecules were atomized and excited to a higher state. The excited atoms fell down to the ground state as they emitted light which was a characteristic of the metal in the alloy and each metal in the alloy had its own one or more emission lines. The emitted light produced in the ICP unit then goes through a set of lenses into the OES unit. The different wave lengths of the light were separated by a set of prisms so that they could be distinguished on reaching the detector of OES. The detector measured the light intensity and determined the amount of the element in the alloy.

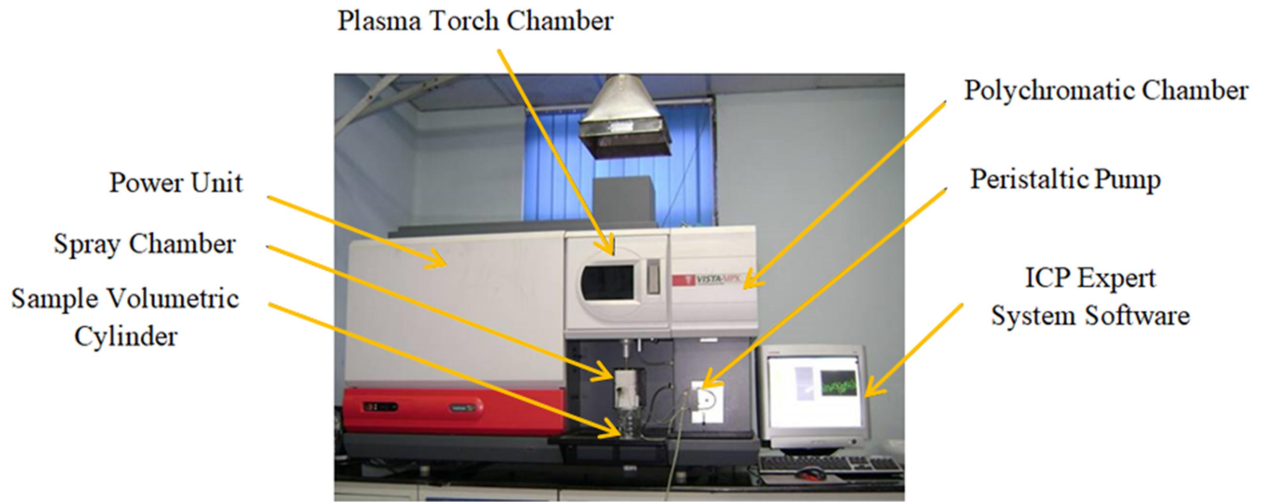


Figure 3.1 Inductively coupled plasma ICP-OES device type VISTA-PRO used for composition analysis of AA7075 sheet.

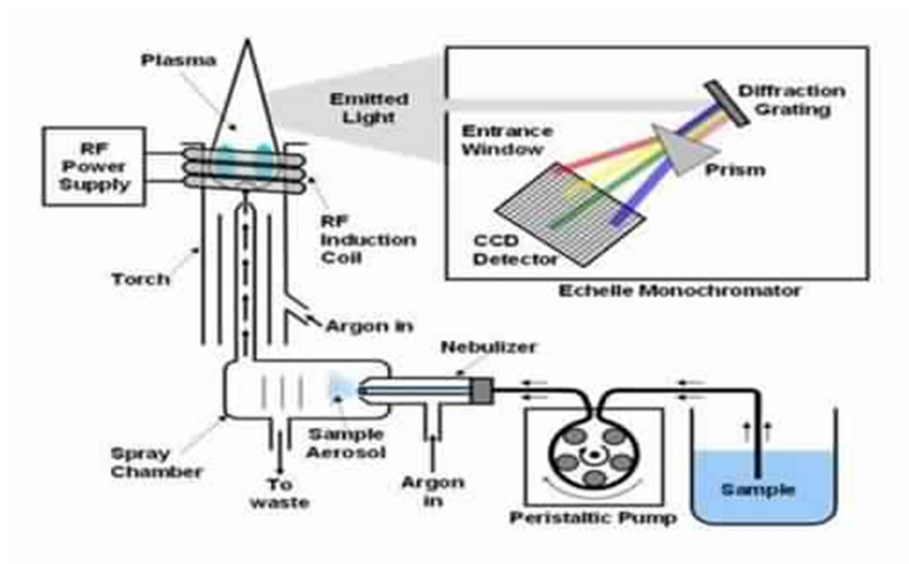


Figure 3.2 A schematic drawing of ICP set-up (Laboratory, 2014).



The ICP testing conditions included an adopted power of 1.2 kW and a plasma flow rate of 15 liters/min with auxiliary and nebulizer flow rates of 1.5 liters/min and 0.7 liters/min respectively. The replicate read and instrumentation stabilization times were 10 seconds and 30 seconds respectively. The pump rate was 10 rpm. The test was typically repeated 3 times and the results analyzed for all of the elements relevant to AA7075 alloy with three different wavelengths used for each element. The minimum detection amount for each alloying element is shown in Table 3.1.

Table 3.1 ICP detection limit of alloying elements in AA7075 sheet.

Alloying Element	Cr	Cu	Fe	Mg	Mn	Si	Ti	Zn
Minimum Detection (PPM)	0.2	0.4	0.1	0.04	0.1	1.0	0.35	0.2

### 3.1.2 Material heat treatment

The commercial AA7075 sheet was heat-treated to fully-annealed (O) and peak-aged (T6) tempers in the ambient air environment in a furnace (model: KF-KILN) with a maximum operating temperature of 1300°C (see Figure 3.3). Full-anneal heat treatment included holding sheet metal in the furnace at  $413^{\circ}\text{C} \pm 5^{\circ}\text{C}$  for 3 hours followed by a furnace cool to room temperature. The T6 temper heat treatment involved two steps. First, the sheet sample was heated to  $480^{\circ}\text{C} \pm 5^{\circ}\text{C}$  for 3 hours in the above furnace followed by water quenching to room temperature. The water quenching step involved vertically dipping the sample in a bath of still cold water for about 10 seconds immediately after heating, to avoid any shape distortion resulting from inhomogeneous cooling rate. Since the as-

quenched sample was in a supersaturated solid solution  $\alpha_{SSSS}$  state with an unstable microstructure, the second step involved immediate artificial aging of the sample in the furnace to stabilize the microstructure and attain the T6 temper properties. Artificial aging was carried out at  $121^{\circ}\text{C} \pm 2^{\circ}\text{C}$  for 24 hours followed by a furnace cool to room temperature. The purpose of this second step was to allow diffusion of material alloying element atoms through the aluminum matrix to compose precipitates that provided higher strength and mechanical properties to the alloy, as per the so called dispersion or precipitation hardening process.

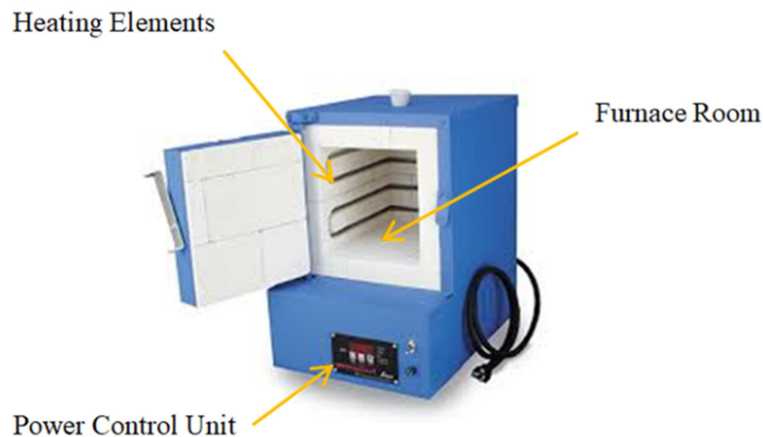


Figure 3.3 Heat treatment furnace type KF-KILN.

### 3.1.3 Specimen preparation for microscopic studies

#### 3.1.3.1 Optical microscopy

AA7075 sheet metal samples were prepared for optical microscopy examination. First, larger flat sheet coupons were cut into 5 mm width and 10 mm length using STRUERS precision saw as shown in Figure 3.4. The samples were then cold mounted to observe

three different planes of ND, LT and ST by using 20 gm to 3 gm mixture of Epoxy and resin respectively and allowed to harden over 24 hour period. The samples were ground and polished by using STRUERS automatic grinder and polisher (see Figure 3.5) as per the sequence of polishing medium and other conditions shown in Table 3.2.

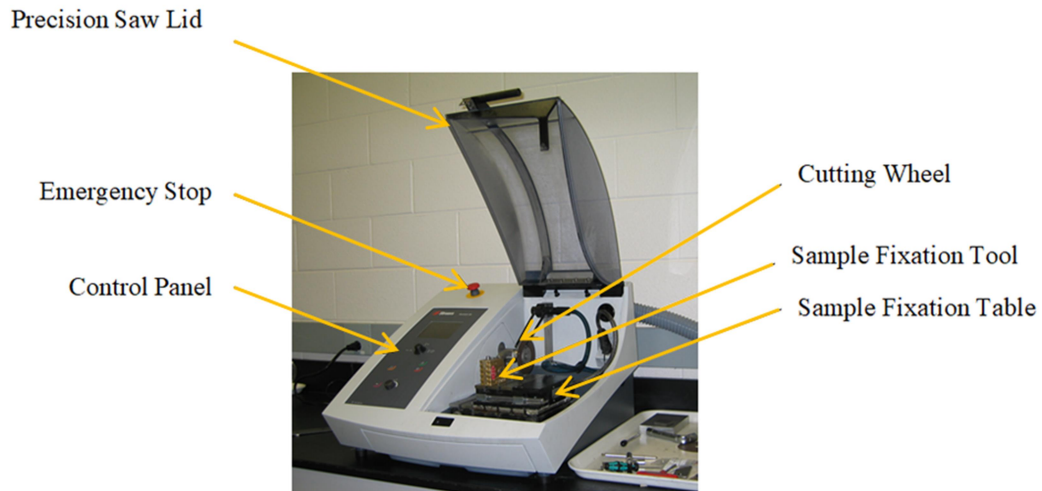


Figure 3.4 STRUERS precision saw device.

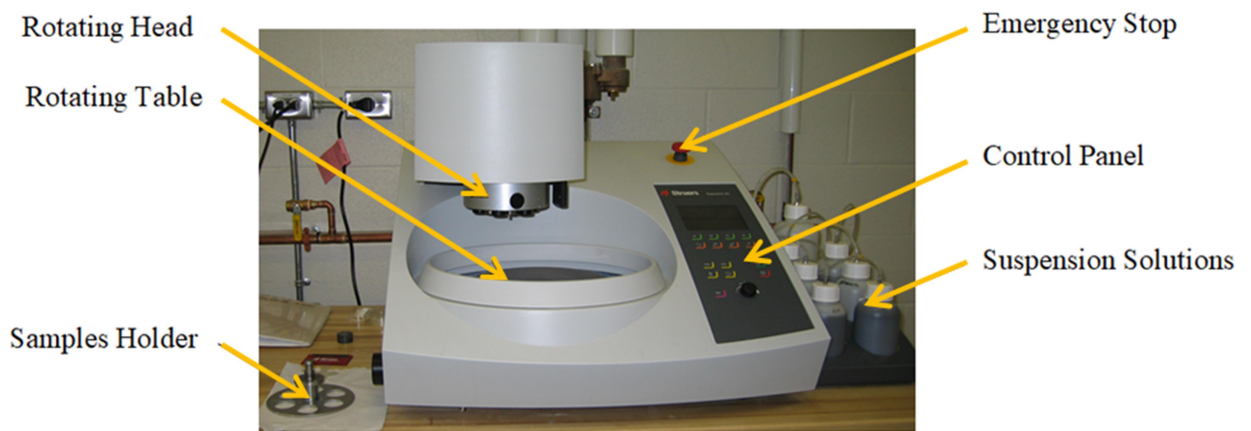


Figure 3.5 STRUERS automatic grinder/polisher device.

Table 3.2 Automatic grinding and polishing processes procedure.

Steps	Abrasive	Coolant	Speed (rpm)	Load per Sample (N)	Time (min.)
1	400-Grit-SiC	Water	150	25	1.5
2	600-Grit-SiC	Water	150	25	1.5
3	800-Grit-SiC	Water	150	25	1.5
4	1200-Grit-SiC	Water	150	25	1.5
5	3 micron	Green Lub.	150	20	6
6	1 micron	Green Lub.	150	20	6
7	0.5 micron	Colloidal Silica	150	15	10

The curved specimens from hemispherical dome samples of similar size to the flat specimens were cut, mounted, ground and polished in a similar manner to flat specimens except that they were cut perpendicular to the localized necking line and mounted through their thickness as shown in Figure 3.6.



Figure 3.6 AA7075 LDH sample preparation for microscopic examination.

To reveal alloy grain structure in the optical micrographs, polished samples were etched by dipping in a sodium hydroxide solution (10 gm NaOH + 90 ml water) in a flask that settled in 60°C hot water bath for about 35 seconds and finally dipping the sample in a

solution of 50% concentrated Nitric acid ( $\text{HNO}_3$ ) to remove the formed demerit layer from the sample surface.

### 3.1.3.2 Scanning electron microscopy

Sample preparation for SEM was similar to that for OM except that samples were coated after polishing by depositing a carbon layer on the polished surface to enhance the secondary electrons emission characteristics of the sample for better microstructural image quality. Figure 3.7 shows photographs of a polished sample before and after carbon coating. Carbon coating left a light brown tinge on the polished specimen surface.



Figure 3.7 Photographs of a mounted AA7075 dome sample; (a) before carbon coating and (b) after carbon coating.

### 3.1.4 Microstructure characterization

Optical microscopy (OM) was performed on un-deformed and deformed samples using digital optical microscope (KEYENCE model VHX-2000), see Figure 3.8. This microscope provided image magnifications up to 2000X, a large depth-of-field, as well as automatic 2D and 3D imaging and measurement capabilities via motorized three axes (X, Y and Z) control, high speed image stitching, a high resolution imaging mode, easy and

automatically adjustable contrast, brightness, and a high dynamic range (HDR). The microscope was utilized to observe the initial grain shape and grain size distribution through the sheet thickness from the three orthogonal sheet planes (long transverse (LT), short transverse (ST) and normal (NP)). In addition, quantitative initial grain size data was obtained from the LT plane.

Microstructures of necked dome specimens were observed by cutting and mounting samples through-thickness from the neck region. A scanning electron microscope (JOEL, model 6610LV), with a resolution of 3 nm at 30 keV and automatically adjustable contrast and brightness capability, was utilized for microstructural studies (see Figure 3.9). The microscope had a large specimen chamber to accommodate specimens up to 200 mm in diameter. It also allowed for simultaneous viewing of secondary electron (SE) and backscattered electron (BEC) images from the same region. The dual observation mode was especially useful for SEM microstructures and fractographic investigations in which SE images represented shallow depth features of about 5 – 10 nm from sample surface (topographic data) while BEC images utilized diffracted electrons emitted from a depth of about 1  $\mu\text{m}$  from sample surface (compositional data). SEM was chosen for fractography image analysis work because of its much larger depth of field and image magnification compared to OM. Moreover, SEM had a very useful sample rotation and tilt capability to allow imaging of fracture surface according to the fracture location in the dome samples. The SEM was used for fractographic examination of fractured uniaxial tensile and dome specimens of different tempers at several different magnifications of interest.

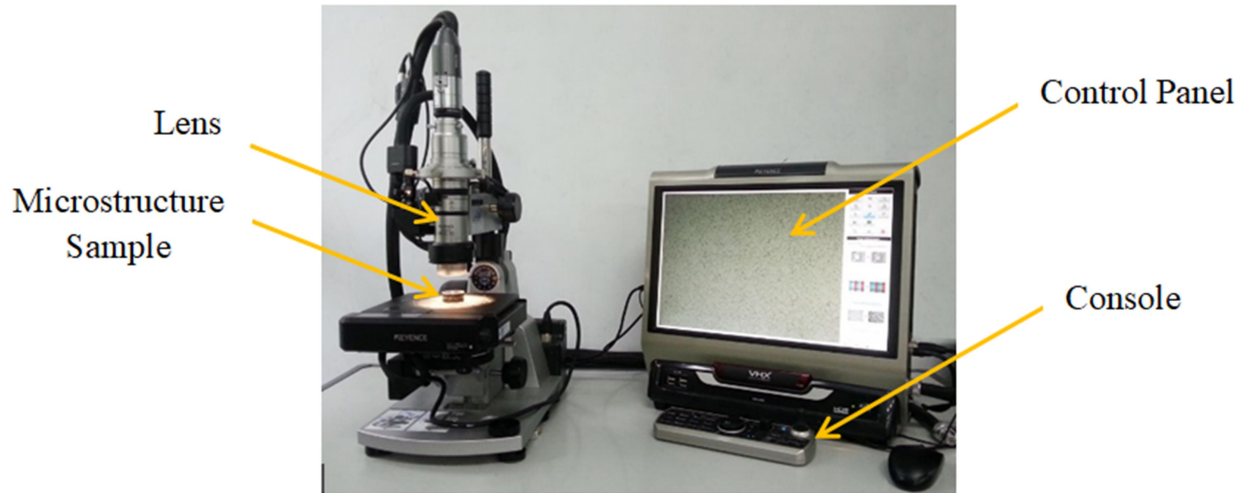


Figure 3.8 A photograph of KEYENCE model VHX-2000 digital optical microscope.

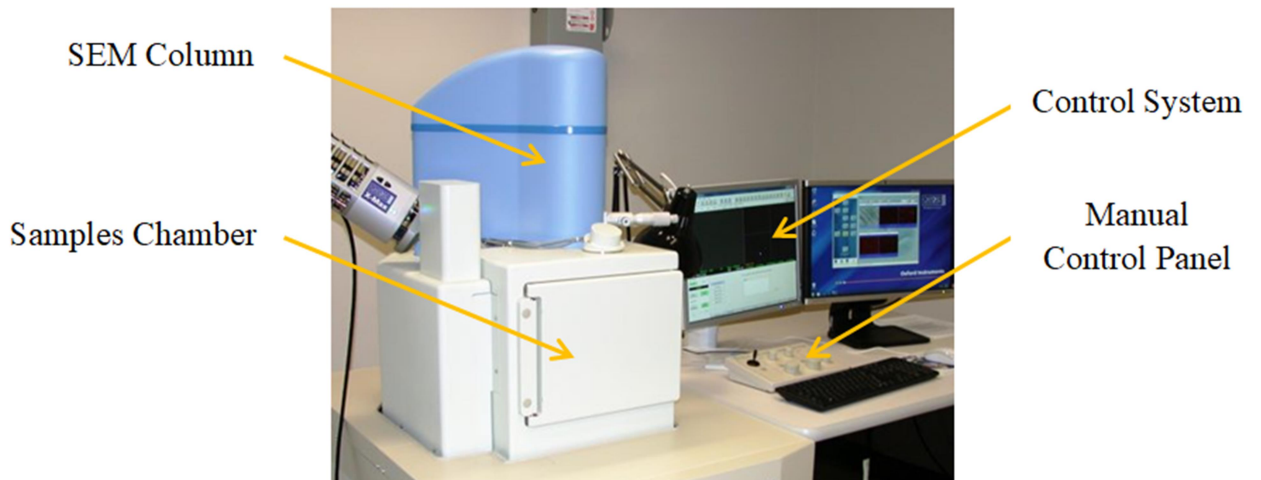


Figure 3.9 A photograph of JOEL 6610LV scanning electron microscope.

#### 3.1.4.1 Microstructural image processing

Microstructural images from optical and scanning electron microscopes were processed by Clemex Vision Lite software (version 8.0). The software enabled microstructure

analysis by establishing a list of operations such as image input, gray level scaling, and thresholding. A calibration step was performed prior to the image analysis in which the software detected the scale bar of the image to calculate image features size accurately. The output from the software for polished and etched specimens consisted of a series of measurements of microstructural features such as precipitates or micro-voids size and distribution. There were two main steps for analysing microstructural features;

(a) Gray image enhancement via a process called delineation in which the image is transformed to a clearer and sharper features as shown in Figure 3.10.

(b) Binarization by thresholding based on gray levels for different phases in the microstructural image. This step is illustrated in Figure 3.11 where various grey levels (including the pure white and pure black) are separate into different colours.

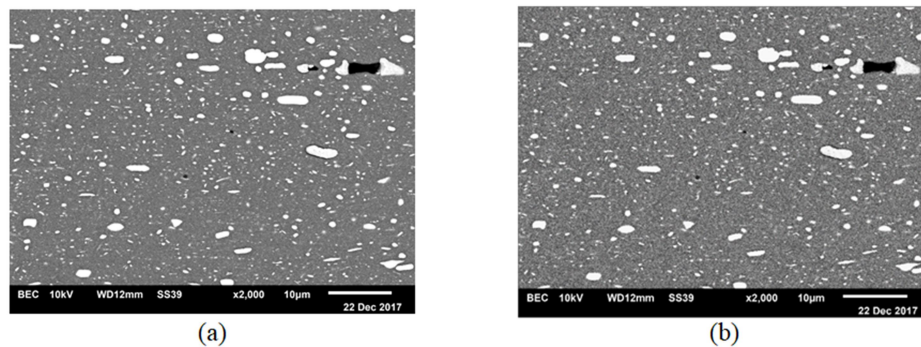


Figure 3.10 Image delineation step; (a) Initial image and (b) post- delineation image.



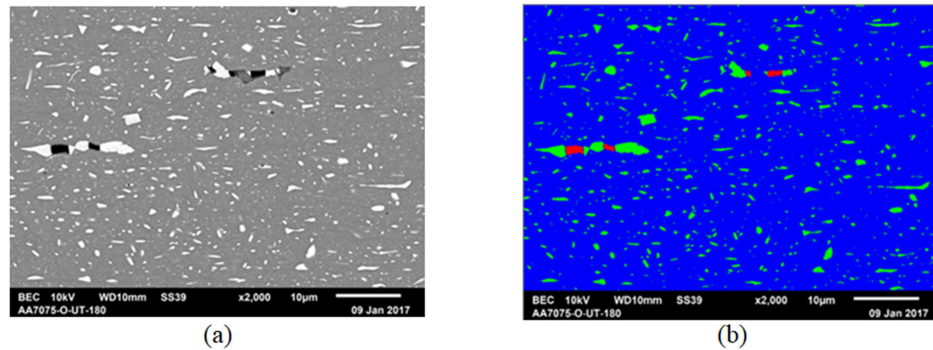


Figure 3.11 Image binarization by thresholding; (a) before thresholding and (b) after thresholding.

#### 3.1.4.2 SEM fractographic image processing

Metallic sheet specimens subjected to uniaxial tensile and dome tests under specific strain paths (such as uniaxial, plane strain and balanced biaxial) often exhibit ductile rupture in the form of dimples or depressions on the fracture surface. The dimples are often associated with precipitates, dispersoids and constituent particles embedded in the matrix that either fracture or delaminate from the matrix, forming voids. The objective was to investigate the relationship between damage features in the image including dimples size and distribution and their relationship to the forming limits and fracture of AA7075 sheet. KEYENCE model VHX-2000 digital optical microscope image processing software was used to analyze the SEM fractographic images of fractured specimens to receive dimple area fraction data under different test conditions such as strain path, test temperature as well as temper of the sheet material. The software was able to distinguish between different gray levels (thresholding) associated with tear ridges between the dimples (shaded in red) while the dimples area was left in gray color (or vice versa) as shown in Figure 3.12. Since contrast of the SEM images affected the quality of the results, SEM

parameters such as working distance, focusing, contrast and brightness were adjusted to bring clarity to the image so that the software could properly threshold the image. All SEM images were captured at a working distance of  $20 \text{ mm} \pm 1 \text{ mm}$  with magnification of  $1000\times$  and applied voltage of 10KV.

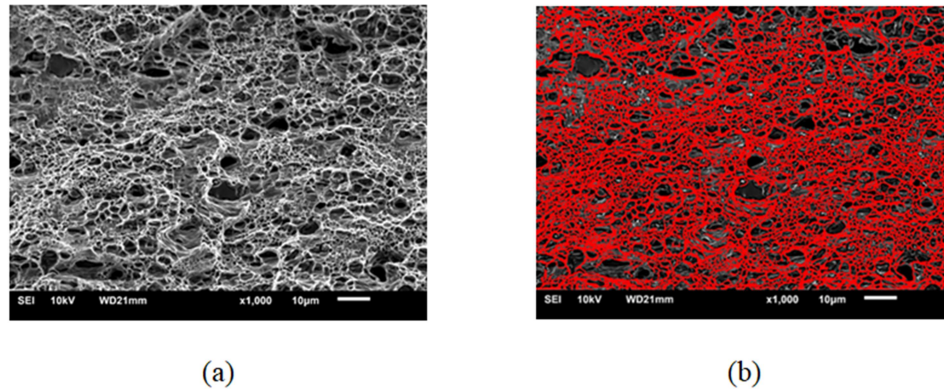


Figure 3.12 Processing of a SEM fractographic image from fracture surface of a uniaxial tension AA7075 test specimen at room temperature using KEYENCE digital optical microscope image processing software; (a) original SEM image and (b) image after processing.

### 3.1.5 Crystallographic texture characterization

#### 3.1.5.1 Specimen preparation

Bulk texture analyses were performed from the surfaces of un-deformed AA7075 sheet and formed domed samples (at pole of the dome and neck locations). The goal of these experiments was to assess the extent of texture evolution from out-of-plane plastic straining process and if there was any association between the texture evolution and forming limit of the sheet material. There was no special sample preparation required for XRD-based texture measurements except ensuring that the scanned areas of the samples

did not comprise of electrochemically etched grid areas on the samples surface. It is to be noted that one of the surfaces of all dome specimens was imprinted with period grids in the form of small circular dots (i.e., solid circles) to measure local strains using the ARGUS strain measurement system (more details about the imprinted grids are provided later in sub-section 3.2.2). Avoidance of etched dots on the dome sample surface during XRD experiments was achieved by placing the X-ray spot between the etched dots.

#### **3.1.5.2 XRD Equipment**

The XRD equipment to determine the sheet metal bulk texture and grain orientation distribution before and after plastic deformation is described below. Bulk texture measurements were carried out by X-Ray diffraction (XRD) equipment model Bruker D8 DISCOVER with DAVINCI diffractometer as shown in Figure 3.13. The device utilized a cobalt sealed tube source of average wave length  $1.79026 \text{ \AA}$ , applied voltage of 35 KV, applied current of 45 mA with parallel focus Goebel Mirror, Vantec 500 area detector, and 1 mm micro-slit and 1 mm short collimator. Also, it utilized a vertical D8  $\theta$ - $\theta$  goniometer, Chi cradle with phi rotation, X, Y, Z translation stage and laser-video sample alignment. These specifications provided a tilt capability (translation and rotation) for dome samples so scans of different samples locations could be carried out.

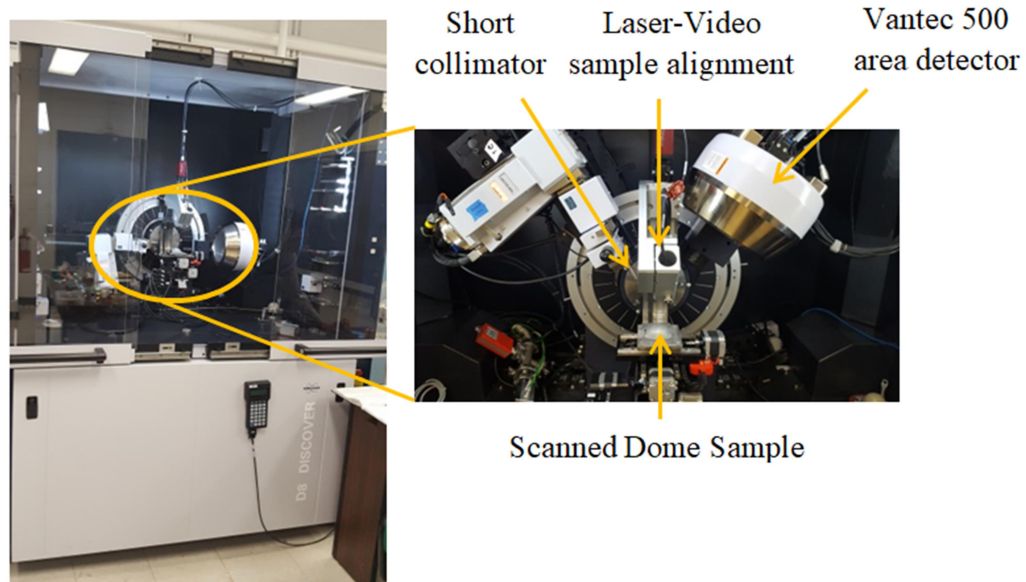


Figure 3.13 A photograph of X-ray equipment type Bruker D8 DISCOVER with DAVINCI diffractometer for bulk texture measurements on AA7075 samples.

### 3.1.5.3 XRD data analysis

XRD data were analysed by General Area Detector Diffraction System (GADDS) to obtain the crystallographic pole figures for flat sheet and dome samples. There were no special considerations for flat sheet specimens. However, dome specimens involving curved surfaces were analyzed for two regions of interest (pole and neck). The pole region could be scanned easily because it was at the top of the dome sample which could be treated as ‘flat’ and X-ray beam scan could easily cover it while rotating the specimen about the axis of the pole. Carrying out X-ray scan from the neck region, however, was challenging because of sample curvature and varying slope. The location of neck itself varied with the sample geometry and lubrication conditions. Therefore, higher angles were used to scan the neck zone to avoid shadowing effect during sample rotation. Three

different scan angles of  $45^\circ$ ,  $52.5^\circ$  and  $77.5^\circ$ , corresponding to three peaks for FCC aluminum alloys, were used for flat samples and pole region in dome samples corresponding to plane families of (111), (200) and (220) while another group of angles of  $77.5^\circ$ ,  $93.5^\circ$  and  $99.5^\circ$  were used for neck region on dome samples to identify the three families of planes of (220), (311) and (222) to determine pole figures. The three output files for each scan from GADDS software were utilised as input data for a module of the MATLAB software called MTEX for determining pole figures and ODFs for each test specimen.

### **3.1.6 Experimental surface roughness data**

It is well known that the surface roughness of metallic sheet materials evolves with plastic deformation. It also depends upon the grain size and crystallographic texture of the sheet. Further, AA7075 sheet surfaces exhibited large undulations at large plastic strain prior to the development of a localized neck. A non-destructive optical surface roughness measurement system was therefore used to obtain surface roughness data for un-deformed and deformed uniaxial tensile and dome samples formed under different test conditions.

#### **3.1.6.1 Surface roughness measurement equipment**

AA7075 sheet surface roughness measurements were carried out using ALICONA surface roughness measurement system (see Figure 3.14). ALICONA is a three-dimensional (3-D) noncontact optical roughness measurement system based on focus variation. The system can create 3-D surface images which capture colour and topographic information that is used to calculate the surface roughness. It is able to carry out surface measurements with high resolution, high repeatability and high accuracy as

noted in Table 3.3 for objective lens magnification of 20X (the image magnification utilized in the present work). Measurement parameter settings are provided automatically. The system has up to six different objectives magnifications of  $2.5 \times$ ,  $5 \times$ ,  $10 \times$ ,  $20 \times$ ,  $50 \times$  and  $100 \times$ .

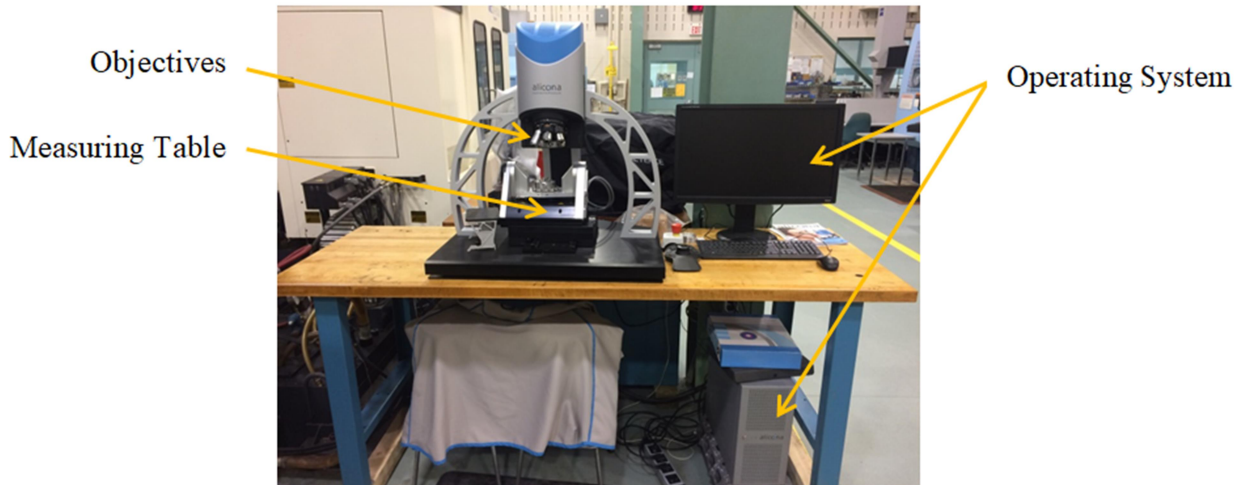


Figure 3.14 ALICONA non-contact optical roughness measurement system.

Table 3.3 ALICONA roughness measurement system technical specifications.

Technical specifications	
objective magnification	20X
working distance	19 mm
lateral measurement range (X,Y)	0.81 mm
(X $\times$ Y)	0.66 mm <sup>2</sup>
vertical resolution	50 nm
height step accuracy	0.05 mm
maximum measurable area	10000 mm <sup>2</sup>
minimum measurable roughness ( $R_a$ )	0.15 $\mu$ m
minimum measurable roughness ( $S_a$ )	0.075 $\mu$ m

### 3.1.6.2 Surface roughness testing and data analysis procedure

ALICONA non-contact optical roughness measurement system utilizes a combination of small depth of focus and vertical scanning to provide 3D topographical and true colour information from focus variation. This technique utilizes coaxial light in roughness measurement. Figure 3.15(a, b) shows surface roughness map of a fully-annealed undeformed (left) and deformed (right) AA7075-O uniaxial tensile test sample. The undeformed sample shows clear horizontal lines indicative of the rolling direction with low height variations in the colour map and an average roughness value ( $R_a$ ) of  $0.36\text{ }\mu\text{m}$  while the deformed uniaxial tension sample provides a much higher  $R_a$  value of  $1.81\text{ }\mu\text{m}$ .

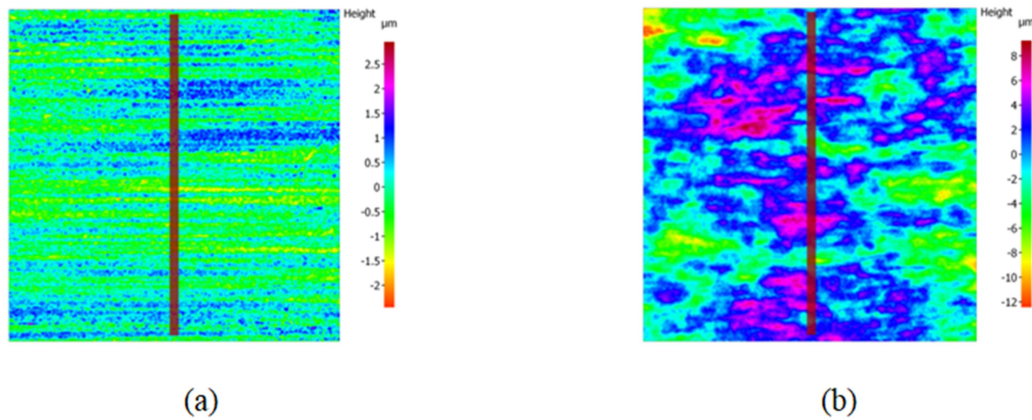


Figure 3.15 Non-contact surface roughness measurements; (a) AA7075-O un-deformed sheet metal and (b) AA7075-O uniaxial tensile sample tested at  $220^{\circ}\text{C}$  with test speed of  $1\text{ mm/min}$ .



### 3.2 Grid imprinting, strain measurement, mechanical properties and sheet formability characterization

Mechanical properties were evaluated by uniaxial tensile tests performed on F, O and T6 temper AA7075 sheet materials tested at different conditions of temperatures (RT, 180°C, 220°C and 260°C) and test speeds (1 and 10 mm/min). The tensile samples were water jet cut as per ASTM E2448 standard, deburred (to remove the worked hardened sharp edge regions) and then heat treated to the desired heat treatment (see sub-section 3.1.2). A random (stochastic) speckle pattern of white and black high temperature paints was applied sequentially with two separate spray guns to the samples gauge length area prior to the test. A light continuous white spray was first applied to sample surface followed by a fine black speckle pattern with an air brush. To ensure good contrast between the white background and the black speckle pattern for continuous strain mapping, sample surface was cleaned to remove any dirt, residual oil or grease from the sheet surface prior to imprinting. The pattern quality characteristics are described in Figure 3.16.

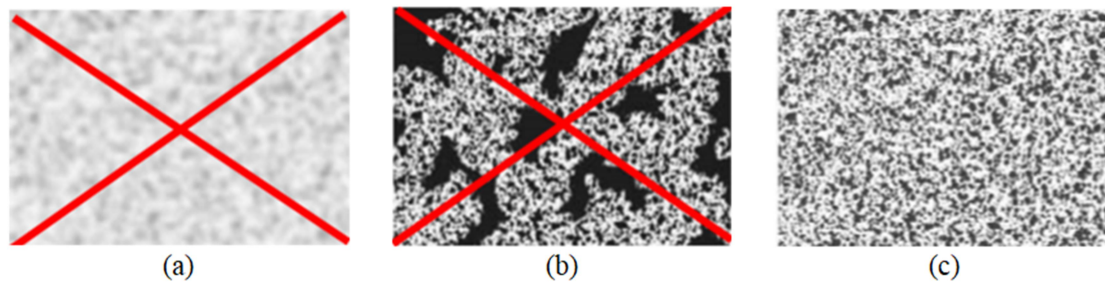


Figure 3.16 Illustrations showing speckle patterns of different quality and contrast; (a) low contrast, (b) high contrast with disturbed large spots and (c) good high contrast pattern (ARAMIS, 2007).



The stochastic pattern was utilized for assigning the camera images pixels (facets). The pixel area in the first Image (i.e., reference image) could be allocated to the corresponding pixel area in the target image. The speckle pattern remained adherent to the sheet surface and deformable with the sheet substrate during large strain mechanical and formability testing of the sheet specimens. After grid imprinting, the sample was mounted in the grips of the mechanical test system and a non-contact online optical 3D strain measurement system ARAMIS, based on digital image correlation (or DIC) technique, was used for field strain measurements (see Figure 3.17).

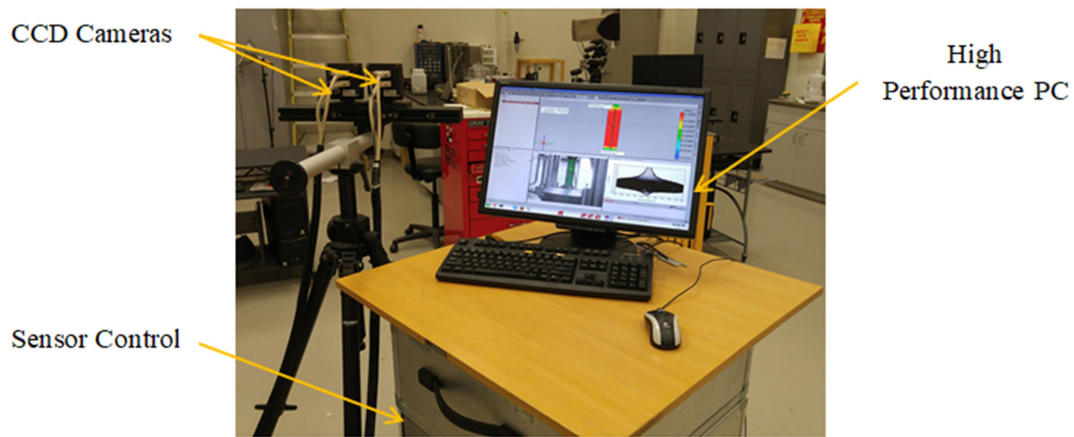


Figure 3.17 ARAMIS online strain measurement system.

The DIC technique utilizes a sequence of recorded digital images of continuously deforming speckle pattern on sample surface and allocates their position to a predetermined coordinate system. The first image of measurement region of the test

specimen is considered as a reference image that typically represents the un-deformed state of the sheet metal specimen. As the sample deforms, there are changes in the intensity of the pixels and also the configuration of the pixels within the facets that provides the displacement field data between the two subsequent images. Comparing images pixels (facets) for each image with the previous one results in the determination of shift, rotation and distortion of the facet from which the local and global (macroscopic) strain field can be obtained. Figure 3.18 shows the various general steps involved in the DIC process for strain field measurements (Lagattu et al., 2004). These steps are similar to the procedure employed in the ARAMIS DIC software. In addition, ARAMIS 3D system, used in the present work on hemispherical punch stretched dome specimens, utilizes the principle of photogrammetry to take into account in the strain mapping algorithm the evolving spherical curvature of the specimen as it deforms. The photogrammetry method in the ARAMIS 3D system is based on simultaneous acquisition of a pair of images from the same region of the deforming specimen from two different cameras oriented at different angle to one another. More details of the ARAMIS 3D system are available in ARAMIS user manual (ARAMIS, 2007).

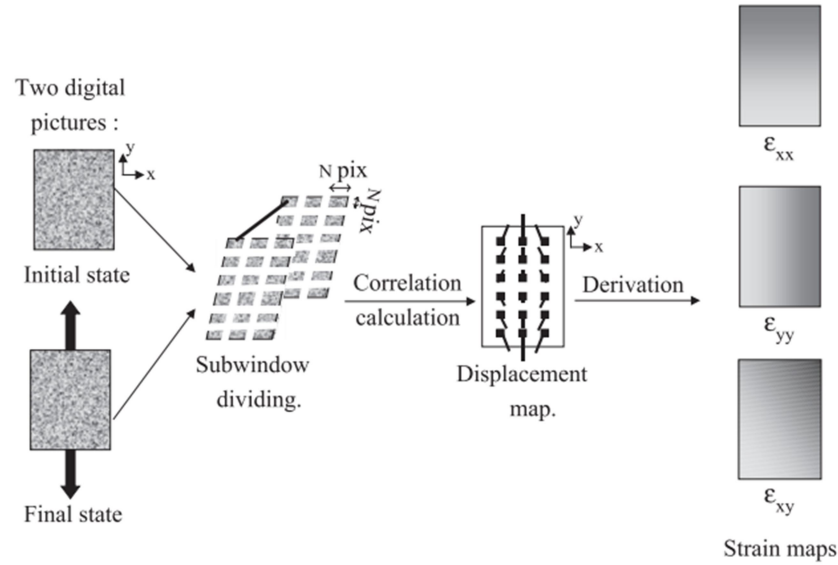


Figure 3.18 A schematic of DIC methodology for strain measurements (Lagattu et al., 2004).

### 3.2.1 Specimen machining, periodic grid imprinting and off-line strain measurement

LDH test samples were machined by computer numerical controlled (CNC) milling machine which resulted in smooth, chatter marks free edges and did not require any deburring of the edges after machining. The machined test specimen geometries for achieving different strain paths are presented later in sub-section 3.2.3.1.2. A useful electrochemical etching procedure, also called electrolytic marking or gridding, was developed to apply a periodic grid pattern of solid circular dots to AA7075 sheet samples surface for post-deformed sample strain measurements using the ARGUS optical strain measurement system. Figure 3.19 shows a schematic drawing of the electrochemical etching process where the electrode wheel and the AA7075 blank were separated by a felt pad saturated with etching solution placed on a stencil to complete the electric circuit. A

suitable stencil with a highly accurate pattern (or mask) of grid circles of 1 mm diameter and centre-to-centre distance of 2 mm, supplied by the ARAMIS system manufacturer (GOM), was utilized. The deformed dome samples were imaged with the ARGUS system to obtain post-test, off-line, surface strain maps of a large majority of dome test specimens for FLD determination. For ARGUS-based strain mapping, dome samples were placed on a rotating stage to provide 360° rotation angle and surrounded by magnetic position markers and a scale bar as shown in Figure 3.20. A camera mounted on a tripod was utilized to image deformed samples by rotating samples to one complete 360° rotation for three different tilt angles of 30°, 45° and 60°. In total, 18 images were taken for each camera tilting angle corresponding to every 20° rotation angle to cover the entire sample area by capturing as much information as possible. Since illumination of the measured dome samples had a critical influence on the measurements, the light sources were placed in a manner to achieve as uniform an illumination of the dome sample surface as possible and to limit sample surface reflections which cause data loss during the strain calculation process. Two unique markers that had a known and fixed distance were also utilized for the imaging camera to recognise the position coordinate of the dots on the samples surface.

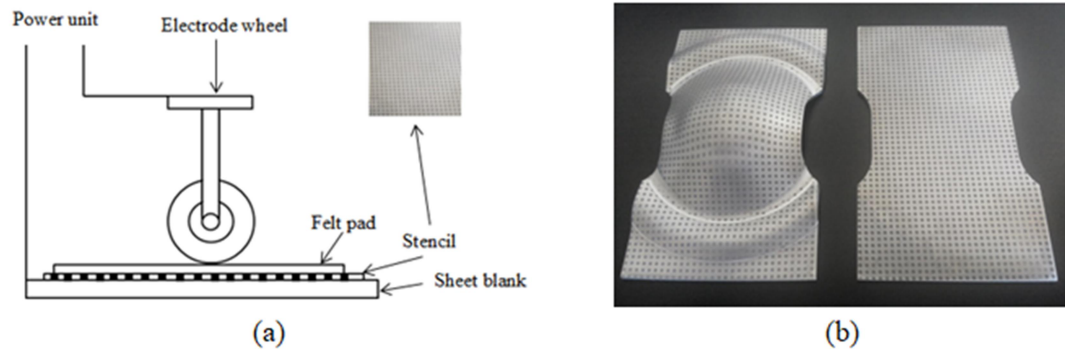


Figure 3.19 Electrochemical etching process; (a) schematic of device setup (Ozturk et al., 2009) and (b) photographs of deformed (dome) and un-deformed test samples of one specific strain path applied with a periodic grid pattern.



Figure 3.20 ARGUS offline strain measurement system.

The processing of the photographic data by ARGUS software consisted of two steps. First, the ARGUS software was made to recognise the deformed circular dots, now ellipses in the deformed state on the dome surface and the position markers, and then compute the camera positions. Second, the software converted the ellipses in to 3D points which were subsequently used to create grid pattern. This grid pattern was a connection

between 3D points to form elements. Finally, software computed the deformation of these elements over the entire imaged dome surface and obtained major and minor strain map of the surface. The software also enabled extraction of major and minor strain along a specific line segment (or line section) of interest. In the present work, three line segments perpendicular to the neck region were typically utilized to characterize the local strain gradient in the neck and to classify grids for the purpose of determining the FLD of the materials. This last step is discussed in more detail in a later sub-section 3.2.3.1.4 on FLD determination procedure.

### **3.2.2 Uniaxial tensile testing**

#### **3.2.2.1 Tensile test grips and specimen design**

Uniaxial tension test samples of 2 mm thick AA7075 sheet metal in F, O and T6 tempers were machined as per ASTM E2448 standard, with gauge length of 22 mm and gauge width of 6 mm as shown in Figure 3.21. Inconel (a nickel base alloy used in high temperature applications) grips, shown in Figure 3.22, were designed and used to perform all room and elevated temperatures tensile tests.

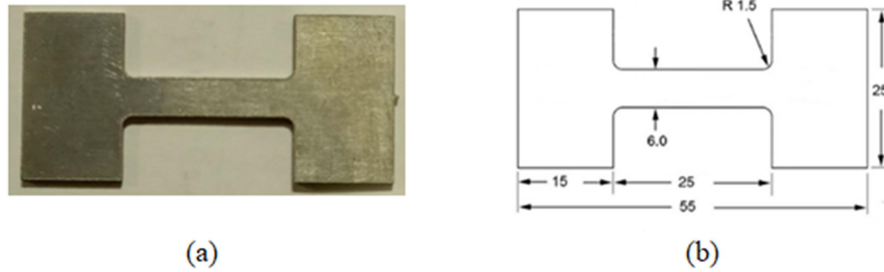


Figure 3.21 Uniaxial tensile test sample; (a) photograph of the test sample and (d) sample drawing with dimensions (Comley, 2007) (all sample dimensions are in mm).

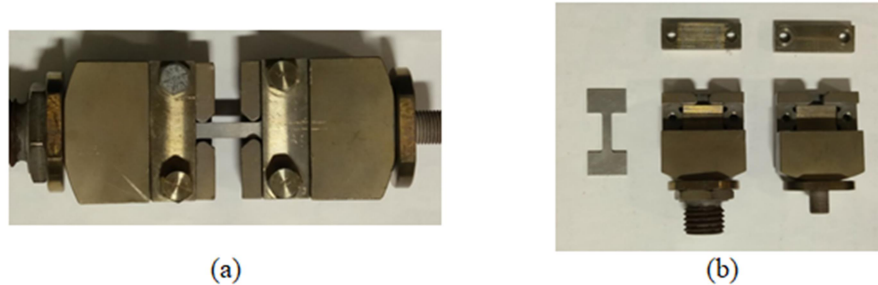


Figure 3.22 Grips utilized for tensile testing; (a) grips and tensile test sample assembly, and (b) disassembled grips and test sample.

### 3.2.2.2 Room temperature tests

Uniaxial tensile tests at room and elevated temperatures were carried out using a computer-controlled servo-hydraulic MTS uniaxial tensile test machine of 250 kN load capacity which was fitted with an environmental chamber (see Figure 3.23).

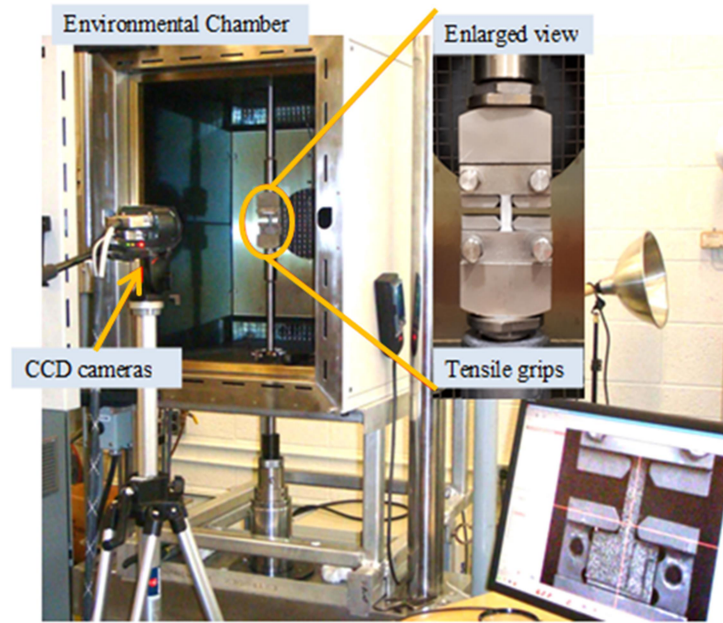


Figure 3.23 Servo-hydraulic MTS uniaxial tensile test machine equipped with INSTRON environmental chamber for elevated temperatures tests. Strain measurement system, ARAMIS-2D with a single CCD camera, mounted on a tripod was used to record images of the deforming test specimens.

Test speeds of 1 and 10 mm/min (corresponding to initial strain rates of  $0.001 \text{ s}^{-1}$  and  $0.01 \text{ s}^{-1}$  respectively) were utilized for all tensile tests. For the room temperature tests, camera images for ARAMIS-based strain data from the uniaxial tensile samples gauge region could be obtained while the INSTRON environmental chamber door was kept open. For setting up the experiment, the test sample was first installed in the grips, and then the test parameters such as data acquisition rate (1 Hz) and test speed were input via the MTS test system interface. Also, ARAMIS system parameters such as camera magnification, frame (1 frame/sec) and shutter time were set to obtain an optimum image quality from the sample gauge length region. Both mechanical testing and ARAMIS camera form images



capture were triggered simultaneously to begin testing. The MTS system software continuously recorded the axial loading forces and displacements while ARAMIS software recorded the sample images during the test until the onset of fracture of the specimen. ARAMIS test data were analysed by applying a virtual strain gauge on the sample gauge length and acquiring the macroscopic axial (major) strain data from the virtual gauge length region to obtain true strain. The corresponding true stress data was obtained from force data from the MTS system software, initial gauge area of cross-section and ARAMIS strain data. The two set of data were then used to construct the true stress versus true strain curves.

### **3.2.2.3 Elevated temperature tests**

Elevated temperature uniaxial tensile tests were carried out by using the same MTS tensile test system as for the room temperature tests except that the INSTRON environmental chamber (with a maximum temperature capacity of 600°C) was utilized in the sample loading arm and grip region to control the specimen test temperature. The environmental chamber had a fan in the centre of the back wall of the furnace to ensure uniform temperature distribution within the chamber. A thermocouple was placed at the center of the furnace for an independent verification of the temperature. The environmental chamber was set at the desired test temperature (180°C, 220°C and 260°C). The chamber door was opened and the sample was inserted in the grips, and the door was then closed and the sample allowed to reach the test temperature (about 10 minutes) prior to testing. During sample heat-up step, sample expansion was taken in to consideration by observing the changes in the force being registered by the specimen and

manually adjusting the system parameters. Test speeds for all elevated temperature tests were taken to be the same as for the room temperature tests. Finally, test specimen illumination was also adjusted for ARAMIS-based strain measurements, since the furnace door was closed and the camera images were captured through the glass window in the environmental chamber. Other aspects of the test procedure were identical to the room temperature tests.

### **3.2.3 Formability testing**

#### **3.2.3.1 Formability testing using MTS test system**

MTS test system was also utilized for formability tests using a dome stretching tooling that employed a smaller 50.8 mm diameter hemispherical punch than the standard diameter of 101.6 mm, associated dies, and a set of customized specimen geometries to cover various strain paths. The tests were conducted on O-temper sheet at room temperature as well as at several elevated temperatures. For the T6 sheet, however, only elevated temperature test at 220°C and above could be carried out with the MTS system but not below this test temperature. This was because at lower temperatures this system did not provide enough clamping force for the test specimen due to its much higher strength in T6 condition that exceed the system capacity. Consequently, another higher capacity press had to be used as discussed in sub-section 3.2.3.2.

##### **3.2.3.1.1 Test tooling**

The hemispherical punch test jig was mounted to the above noted MTS frame and placed within the INSTRON environmental chamber as shown in Figure 3.24. The main features of this test jig were two circular dies (upper and lower) with a coinciding circular hole at

the centre of each die and a stationary hemispherical punch placed directly above the upper die. The AA7075 test specimen was clamped between the two dies prior to the test. The entire test jig, mounted to the bottom actuator, moved upwards at a desired speed to contact the punch and subsequently deform sheet in to a dome shape. The test was typically stopped at onset of localized necking of the test specimen. The onset of necking was detected indirectly by observing the image of the specimen with unaided eye through a mirror placed inside the test chamber at  $45^\circ$  to the vertical axis of the dome specimen.

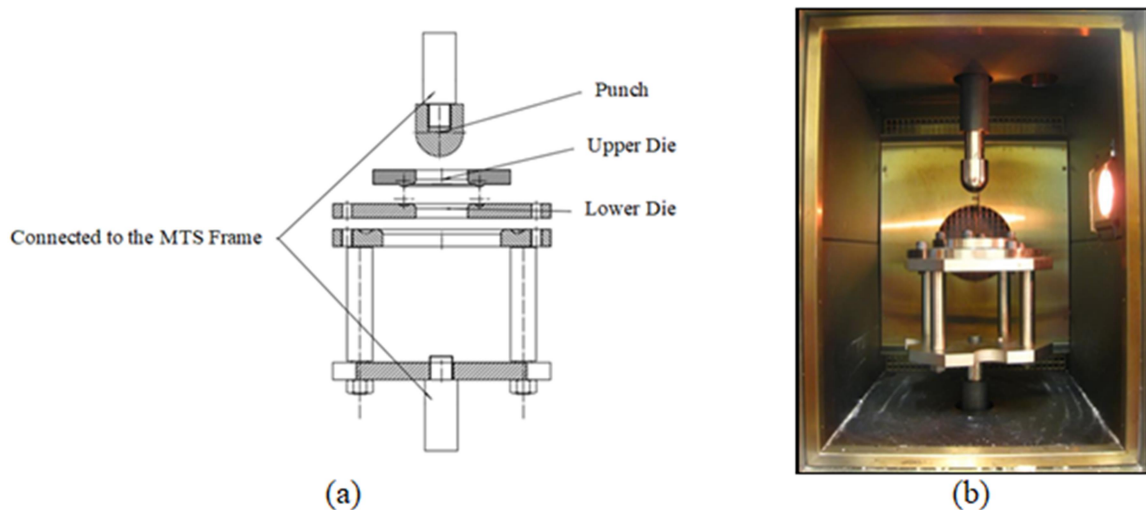


Figure 3.24 Photograph of the elevated temperature FLD tooling; (a) detail drawing and (b) actual tooling.

#### 3.2.3.1.2 Test specimen geometries for attaining different strain paths

FLD determination requires hemispherical punch (i.e., out-of-plane) loading of specific specimen geometries to cover different strain paths ranging from uniaxial tension to equibiaxial tension. However, these geometries can be material dependent, and therefore, some trial experimentation was needed to optimize the specimen geometries of AA7075

sheet (see Figure 3.25 for various final specimen geometries). Tension-compression side of FLD from uniaxial strain path to plane strain path were constructed by utilizing narrow width specimens whereas tension-tension side of the FLD was obtained by implementing various full size specimens and by utilizing three different friction conditions; (i) dry punch (i.e., no lubrication between the hemispherical punch and the test blank), (ii) a thermoplastic polymer film PTFE (or Teflon) between punch and sheet specimen contacting surface (where PTFE film acts as a lubricant), and (iii) a combination of PTFE film and vacuum grease between the punch and sheet.

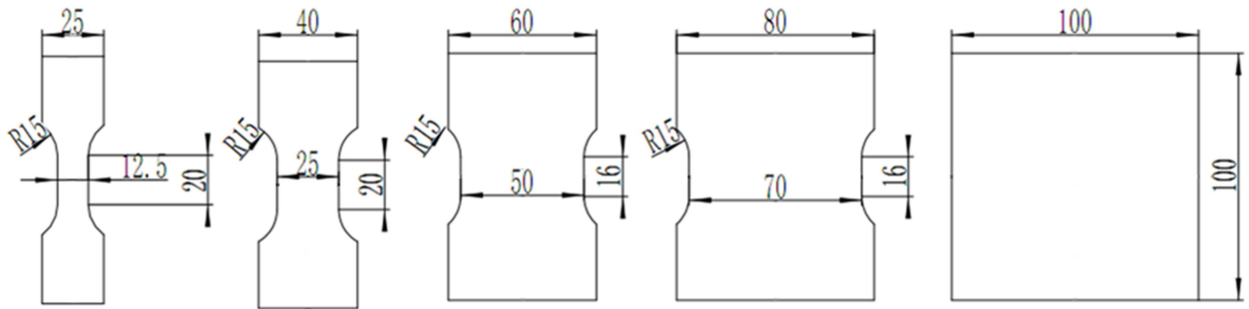


Figure 3.25 Test specimen geometries for obtaining experimental FLDs using small punch tooling (all dimensions in mm) (Guowei Zhou, 2015).

### 3.2.3.1.3 Test procedure

The FLD determination at room temperature has been standardized in ISO 12004-2:2008.

This procedure was largely followed to determine FLD for AA7075 at room temperature.

For elevated temperatures, because no standards are available in the literature, a new methodology for FLD determination was developed based on existing high temperature hemispherical stretching test tooling available at McMaster University.

The test samples, after electrochemically imprinting with periodic dot pattern, were clamped between upper and lower dies in the environmental chamber where clamping force ranged from 22 kN to 45 kN, depending on sample geometry, to ensure complete lock-bead clamping (i.e., no draw-in of the test specimen at the bead during the test). The punch was first brought in contact with the sheet by slowly moving the dies with the clamped test specimen upward until a very small contact force was detected. The punch was kept in fixed position throughout the test. The data acquisition and further upward movement of the die to deform the sheet specimens to a dome shape were simultaneously triggered to initiate the test. On visually observing a formed localized neck on the dome surface, the test was stopped manually by pushing a stop button of MTS operating software. Punch force and displacement data were continuously recorded during the test.

#### **3.2.3.1.4 FLD determination procedure**

ARGUS strain data was utilized to construct forming limit curve (FLC) by analyzing major and minor strain field in the localized neck on dome specimens and its vicinity from deformed periodic circular grids. A strain gradient was developed in the neck region of each of the specimen geometries. To capture this strain gradient using the ARGUS system and to determine the limit strain values, a position-dependent methodology was used in which three parallel lines perpendicular to the localized neck length for each specimen geometry were drawn and analyzed (see Figure 3.26 which shows ARGUS strain map of uniaxial strain path specimen tested at 180°C; (a) actual deformed sample and (b) ARGUS strain map). These lines were used to calculate major and minor strains in the necking region which represented grids that lie within the neck itself as well as

outside of neck region. The latter were considered safe grids that lie under the FLC. This strain gradient was approximated by means of a grid classification scheme. According to this scheme, grids were classified by different symbols according to their proximity to the deepest neck region. After determination of both major and minor strains from three equally spaced parallel lines passing through neck region for 2 to 3 samples for each strain path, the data was plotted in the FLD space with different symbols representing major and minor strain pairs from grids in the neck and its vicinity. FLC was manually constructed based on lowest bound representing the locus of necked grids. FLC was taken as a measure of formability for material at each temperature.

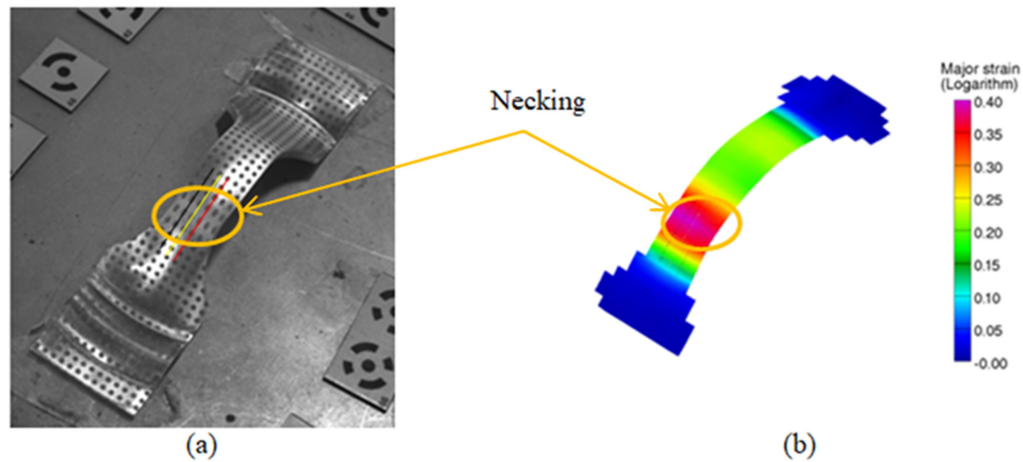


Figure 3.26 ARGUS strain map of uniaxial strain path specimen tested at 180°C; (a) actual deformed sample and (b) ARGUS strain map.

### 3.2.3.2 Formability testing using MACRODYNE press

As mentioned earlier, dome tests for FLD determination for peak-aged AA7075-T6 alloy at room temperature required the use of a higher capacity (150 Ton) MACRODYNE

press. This press was a servo-hydraulic, down-stroking, 4-column press with two double-acting hydraulic cylinders, one actuating the press slide and the other actuating the press bed (see Figure 3.27). The press was designed for high temperature sheet metal forming up to maximum temperature of 700°C. The maximum pressing forces for blank-holding and punching were 150 Ton each, thus making it suitable for forming high strength AA7075-T6 sheet at room temperature. Also, a two-camera ARAMIS on-line strain measurement system, and integrated to the MACRODYNE press, was utilized for FLD determination for both peak-aged and fully-annealed dome samples at room temperature. The two CCD cameras were mounted on the top of the press environmental chamber (see Figure 3.28). A standard 101.6 mm punch diameter Nakazima FLD test tooling was utilized for FLD determination. The dies consisted of lower die with die insert of male lock-bead and upper die with a die insert of female lock-bead.

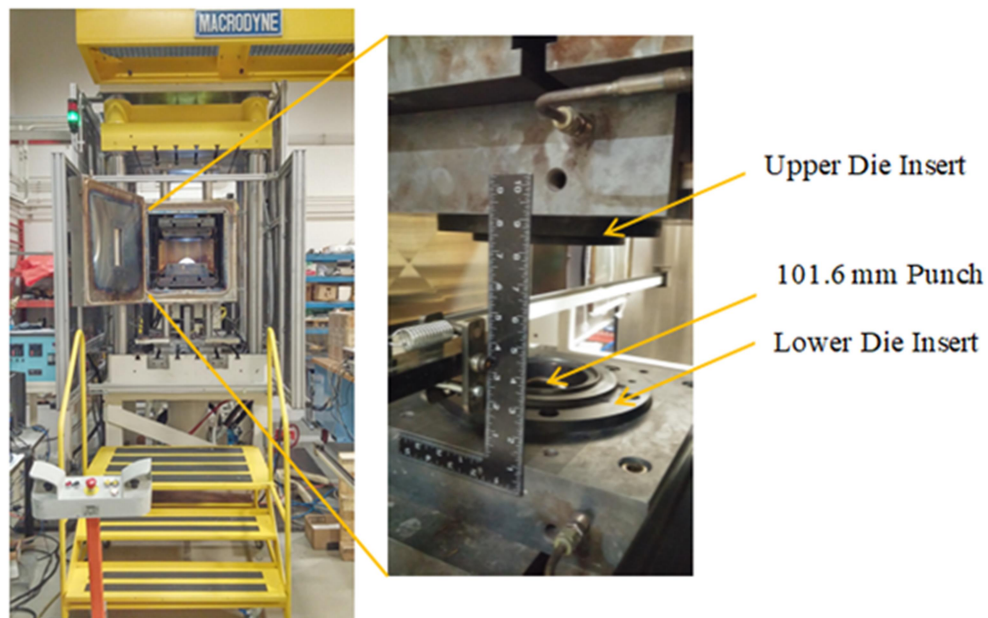


Figure 3.27 MACRODYNE 150 Ton hydraulic press equipped with 101.6 mm punch diameter dome test tooling.

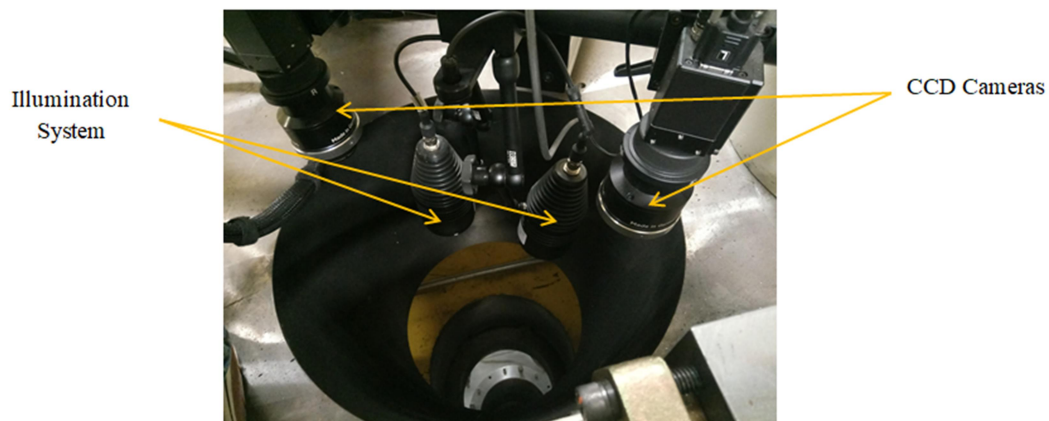


Figure 3.28 ARAMIS online strain measurement system CCD cameras attached to MACRODYNE 150 Ton hydraulic press and located directly above the deforming dome specimen.



### 3.2.3.2.1 Test specimen geometries for attaining different strain paths

Nakazima dome test samples with different geometries were water jet cut to achieve different strain paths (see Figure 3.29). Test samples with widths of 12.7 mm, 50.8 mm and 76.2 mm were utilized to achieve strain paths on tension – compression side of FLD while sample of 127 mm width was utilized for plane strain tension path. Round disk samples of 177.8 mm diameter with different punch-sheet lubrication conditions were utilized for attaining tension – tension strain paths. Water jet cut samples were first sprayed with a fine speckle pattern on the side exposed to the camera for ARAMIS online strain measurements during testing as described earlier. The samples were then clamped between upper and lower dies while punch was moved up to be in touch with the lower surface of the forming blank. Lastly, punch was moved upward to deform the test specimen up to the onset of necking while simultaneously acquiring ARAMIS camera images for strain measurements.

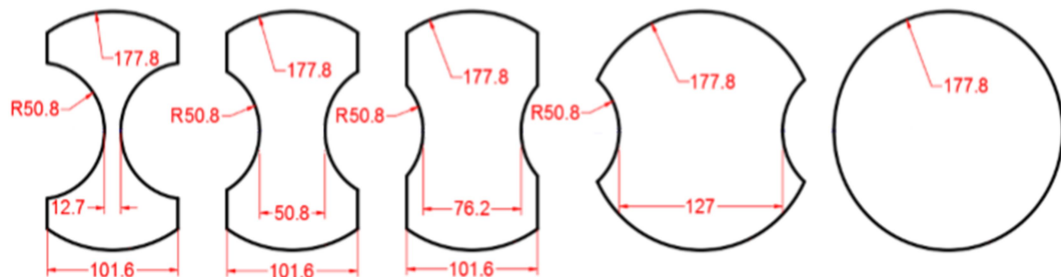


Figure 3.29 Test specimen drawings for attaining different strain paths deformed with 101.6 mm diameter hemispherical punch during dome tests (all dimensions are in mm).

### 3.2.3.2.2 Limit strain determination methodology

As discussed in the Literature review chapter, there are different approaches available in the literature towards determining limit strain from continuously acquired strain data from dome tests specimens. A recent approach called the time – dependent method (Martínez-Donaire et al., 2014) was used in the present work to obtain limit strains. ARAMIS images were utilized to obtain the entire major strain, and corresponding minor strain, history from the neck region of the deforming dome surface until the onset of fracture. The major limit strain at neck (point B in Figure 3.30) was defined as the major strain inside the neck region until fracture occurred at point B while the major strain increased outside of this region (point A) until it reached saturation (last point on the red line). At this time, the major strain rate at point A reached a maximum value (highest point on the green line) while the major strain at point B reaches saturation and becomes the major limit strain value,  $\epsilon_{1,lim}$  at fracture. The major strain and corresponding minor strain values at point A corresponding to peak major strain rate at point A,  $\dot{\epsilon}_{1A,max}$ , were then taken as a pair of limit strain points at the onset of necking and placed on the FLD. This procedure was applied to the entire set of test samples corresponding to the different specimen geometries (i.e., all strain paths) to obtain a set of points in the FLD space. The locus of this set of points was defined as the FLC of the sheet material.

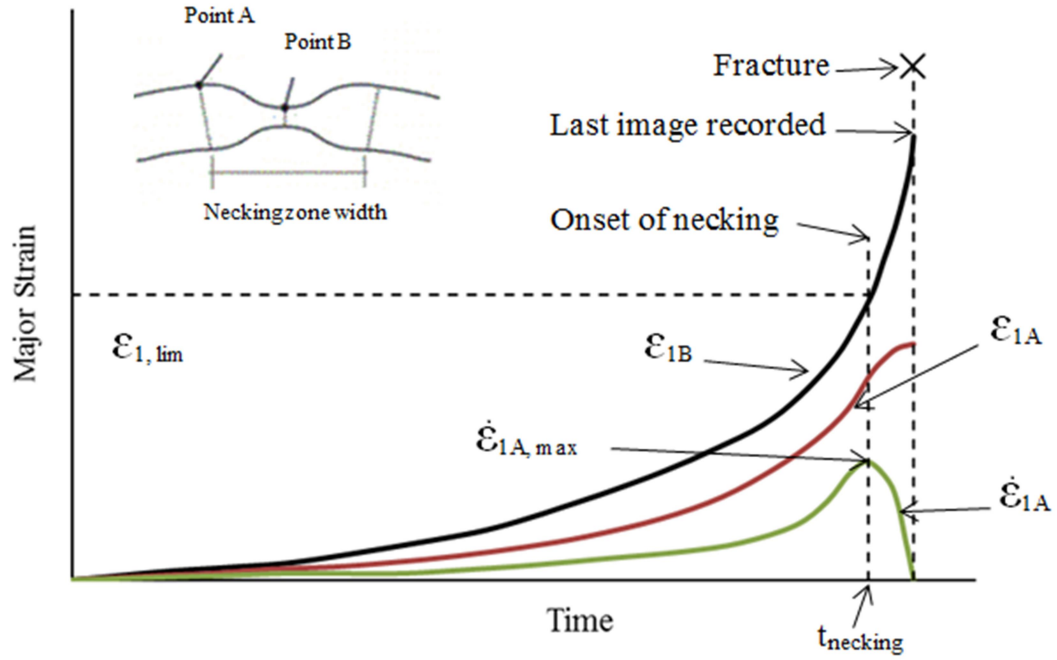


Figure 3.30 Schematic illustration of time-dependent approach for obtaining the FLD of sheet material from continuous strain map data for each strain path from the literature (Martínez-Donaire et al., 2014).

### 3.3 Summary

The research methodology presented in this chapter described critical aspects of material composition, heat-treatment, microstructure characterisation, mechanical properties and sheet metal formability characterisation methodologies to investigate formability of AA7075 sheet and its microstructure before and after deformation. DIC technique was used to evaluate both mechanical properties (i.e., flow stress for all tempers of F, O and T6) by using one CCD camera with servo-hydraulic MTS uniaxial tensile test machine and sheet metal formability (i.e., FLDs for O and T6 tempers at room temperature with 101.6 mm diameter hemispherical punch tooling and FLDs for O temper at elevated temperatures with 50.8 mm diameter hemispherical punch tooling) by using on-line two CCD cameras equipped with 150 Ton MACRODYNE press. Also, ALICONA non-contact surface roughness measurement system was utilized to measure surface roughness for both uniaxial tensile test samples and dome samples. Moreover, a quantitative fractographic tool (KEYENCE digital optical microscope and image processing software) was used to analyse microstructural features (i.e., dimple size and dimple area fraction) in SEM fractographic images for fractured uniaxial tensile samples as well as fractured dome samples. Finally, bulk texture measurements were made on un-deformed and deformed AA7075 for different heat treatment samples, by using X-ray equipment type Bruker D8 DISCOVER with DAVINCI diffractometer. The results from the above test methodologies are presented in the next chapter.

## 4-Experimental Results and Discussion

This chapter presents the results of experiments related to material characterization, mechanical properties, formability, crystallographic texture and fracture characteristics of heat-treated AA7075 aluminum sheets in fully annealed (O) and peak aged (T6) conditions. The sheet material was subjected to uniaxial and biaxial loading conditions to large plastic strains at room and elevated temperatures. A discussion of all experimental results is also included in this Chapter.

### 4.1 Material characterization

#### 4.1.1 Chemical composition, material processing and initial microstructure

Chemical composition of O and T6 temper, 2 mm thick, AA7075 sheet, and a standard composition of the same alloy according to ASTM B 209 - 96, is given in Table 4.1. It is to be noted that the percentages of Iron (Fe) and Silicon (Si), which cause the formation of intermetallic particles that degrade mechanical properties, were lower in the experimental sheet (medium purity AA7075) compared to the standard composition from literature for AA7075 aluminum alloy. The Zinc (Zn) content on the other hand was closer to the upper limit in the standard composition range.

Table 4.1 Chemical composition of AA7075 (in weight %).

	Cr	Cu	Fe	Mg	Mn	Si	Ti	Zn	Al
Research Alloy	0.192	1.662	0.163	2.605	0.02	0.02	0.022	5.829	Balance
Standard Alloy	0.18-0.28	1.2-2.0	0.5	2.1-2.9	0.3	0.4	0.2	5.1-6.1	Balance

Processing of research alloy AA7075 was carried out by Novelis Solatens Group. A schematic of material processing steps from the literature is shown in Figure 4.1. The first step consisted of direct chill (DC) ingot casting in which the molten metal was poured into a mold until it was solidified. This was followed by stress relieving of the cast ingot to prevent cracking. The front and back sides of the ingot were then trimmed off and upper and lower faces were scalped to achieve a final thickness of 65 mm. Second step included homogenization (or preheating) to reduce chemical segregation of cast structure and improve its workability. Homogenization was implemented in two steps; the ingot was first heated to 460°C at a heating rate of 50°C/hour and held for 3 hours, and then heated from 460°C to 485°C and soaked for 6 hours followed by air cooling. Hot rolling of the ingot was then carried out at pre-heat temperature of 420°C where a reduction in thickness from 65 mm to 8 mm was achieved over certain multiple passes. The edges of resulting thick sheets were then trimmed off to avoid edge cracking. Subsequent cold rolling of the 8 mm thick sheet was carried out over multiple passes to achieve a final thickness of 2 mm.

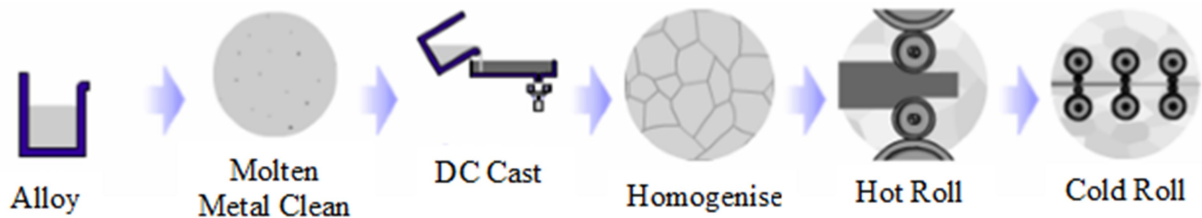


Figure 4.1 A schematic of AA7075 processing steps (Fribourg, 2009).

Various optical micrographs in Figure 4.2 and Figure 4.3 illustrate the initial microstructures of O and T6 temper sheets respectively in the form of 3D volumetric representations by stitching images from 3 orthogonal sheet planes (LT, ST and ND). In general, the grains were equi-axed or pancake shape in normal direction plane (ND) while the grains in the other two planes, longitudinal (LT) and short transverse (ST) were elongated due to the rolling process. Table 4.2 gives quantitative grain data in terms of average grain lengths, widths and aspect ratios for the two sheet tempers (O and T6). The data shows that the average grain size of fully annealed sheet (O temper) is significantly larger than that of the peak aged (T6) sheet. Also, the grain size measurements from mid-thickness layer of sheet in both LT and ST planes for both O and T6 tempers resulted in a higher grain aspect ratio in the O-temper sheet compared to the top surface layers. This was possibly due to increased work hardening and grain recrystallization of the surface layers during multiple stages of hot and cold rolling processes.

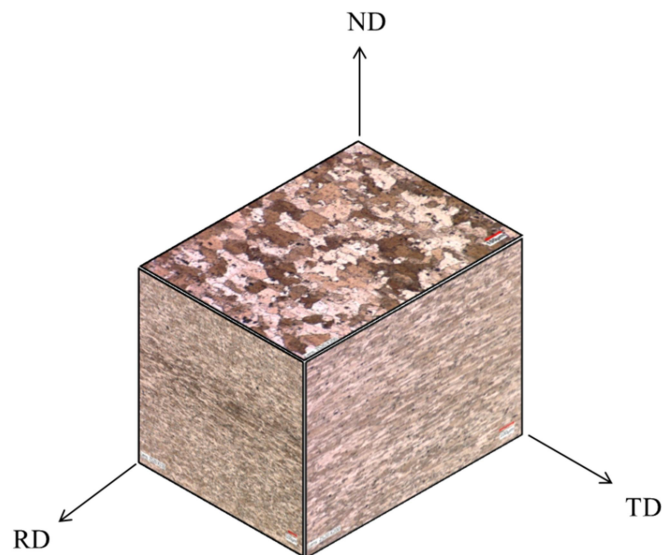


Figure 4.2 A collage of optical micrographs of un-deformed AA7075-O sheet representing 3D microstructure from LT, ST and ND planes (Mag. 200 X).

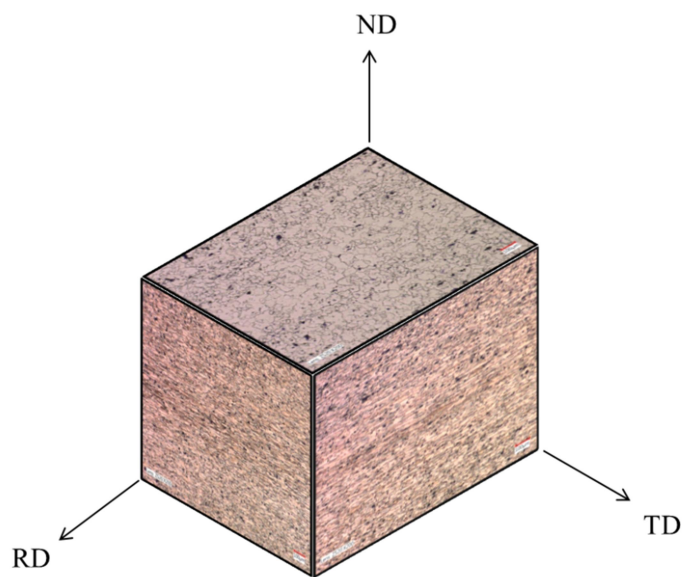


Figure 4.3 A collage of optical micrographs of un-deformed AA7075-T6 sheet representing 3D microstructure from LT, ST and ND planes (Mag. 200 X).



Table 4.2 Average grain length, width and aspect ratios for un-deformed O and T6 tempers.

Temper	Plane	Grain Length (μm)	Grain Width (μm)	Aspect Ratio	
O	ND	97.19	62.66	1.55	
	LT	Top Layer	79.62	16.56	4.81
		Middle Layer	152.77	17.74	8.61
	ST	Top Layer	67.2	13.64	4.93
		Middle Layer	134.89	17.84	7.56
	T6	ND	23.985	14.024	1.71
LT		Top Layer	18.534	5.615	3.3
		Middle Layer	22.697	5.754	3.94
ST		Top Layer	19.297	6	3.22
		Middle Layer	18.636	4.935	3.78

The initial crystallographic texture of AA7075 sheet in O and T6 tempers was also obtained from SEM-based electron backscatter diffraction (or EBSD) experiments and subsequent analysis of data. The EBSD analysis provided spatial crystallographic texture information from diffraction patterns from a region 20-100 nm below the sheet surface.

Figure 4.4 and Figure 4.5 show EBSD-based 3D volumetric representations of grain structure from the three orthogonal sheet planes for O and T6 temper materials respectively. The grain structures for both fully annealed and peak aged tempers show similar grain shapes and aspect ratio to the earlier optical micrographs. The quantitative grain data from ND is presented in Table 4.3. A comparison of Table 4.2 and Table 4.3 reveals that OM images analysis resulted in a larger grain size for O temper sheet compared to the T6 temper. This is perhaps because EBSD measurement area was very small ( $400 \times 400 \mu\text{m}$ ) in comparison with OM area and not as representative of the material.

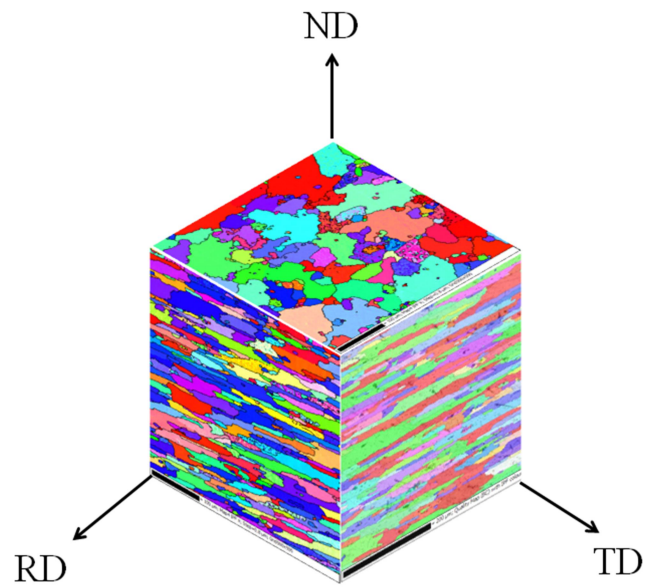


Figure 4.4 A collage of EBSD pattern from three orthogonal planes for AA7075-O sheet.

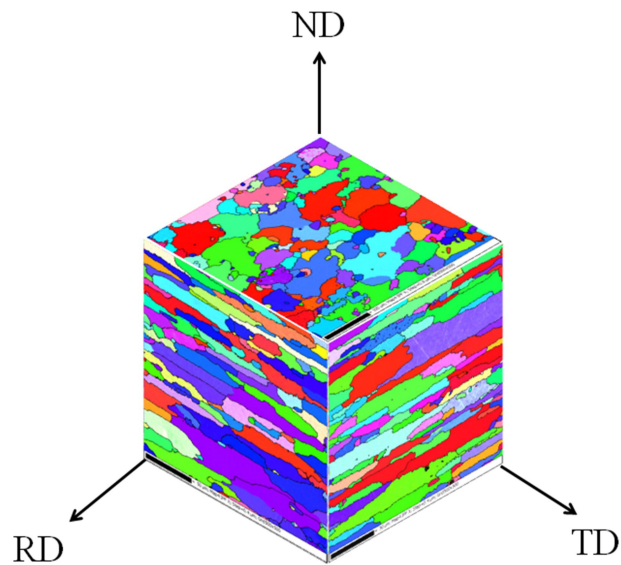


Figure 4.5 3D volumetric representations of EBSD for AA7075-T6 sheet.

Table 4.3 EBSD-based measurements of average grain length, width and aspect ratio from ND plane for AA7075-O and T6 sheet samples.

Temper	Plane	Grain Length ( $\mu\text{m}$ )	Grain Width ( $\mu\text{m}$ )	Aspect Ratio
O	ND	47.04	28.64	1.64
T6	ND	52.72	31.62	1.67

## 4.2 Uniaxial tensile stress-strain curves

### 4.2.1 Room temperature uniaxial tensile test results

Figure 4.6 shows typical room temperature uniaxial tensile flow stress-strain curves for as-received AA7075 sheet in rolling direction tested at speeds of 1 and 10 mm/min (the test speeds correspond to initial strain rates of  $0.00076 \text{ s}^{-1}$  and  $0.0076 \text{ s}^{-1}$  respectively). The material shows rapid work hardening to stress saturation. There was no significant difference in the shapes of the curves and saturation flow stress values at the two test speeds. However, a slight reduction in the terminal strain was observed at the higher speed. This could be attributed to a slight reduction in the strain rate sensitivity (or  $m$  value) at the higher strain rate which can lead to slight reduction in the strain to failure. Similar test data for the O-temper, on the other hand, exhibited much lower yield strength; a larger work hardening range, continued hardening up to fracture, and almost no dependence of stress-strain response on strain rate (see Figure 4.7). The lower yield strength of O-temper sheet compared to F-temper due to fully annealed heat treatment that result in large grain size and reduction in dislocation density, and consequently an increase in work hardening capacity of the material and increased ductility on the expense of strength.

Lastly, tests on T6-temper sheet exhibited stress-strain curves of significantly higher yield strength, a largely linear plastic work hardening range, and a significantly lower strain to fracture compared to the O temper sheets (see Figure 4.8). Also, no marked effect of test speed (i.e., strain rate) was observed on the flow behaviour, as in the case of F and O-temper sheets. The reduction in strain to fracture in T6 compared to O temper sheet is attributed to significantly higher yield and tensile strengths and increased damage development in T6 (peak-aged condition) due to precipitates formation. The plastic deformation consists mainly of dislocation motion and their interaction with the precipitate field. The size, shape and distribution of the precipitate varies with the specific heat treatment with a well-known precipitation sequence consisting of supersaturated solid solution  $\alpha_{ssss}$  – GP zones – metastable coherent  $\eta'$  - stable non-coherent  $\eta$  precipitates (Mukhopadhyay & Prasad, 2011). This precipitation sequence is responsible for the increase in yield and tensile strengths in T6 temper compared to fully annealed specimens.

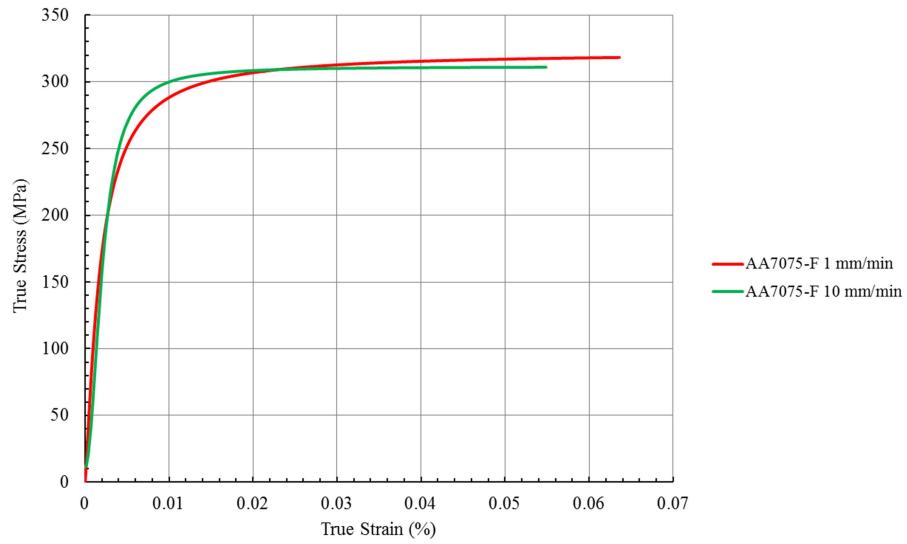


Figure 4.6 Flow stress-strain curves for AA7075-F in rolling direction. Tests conducted at speeds of 1 and 10 mm/min at room temperature.

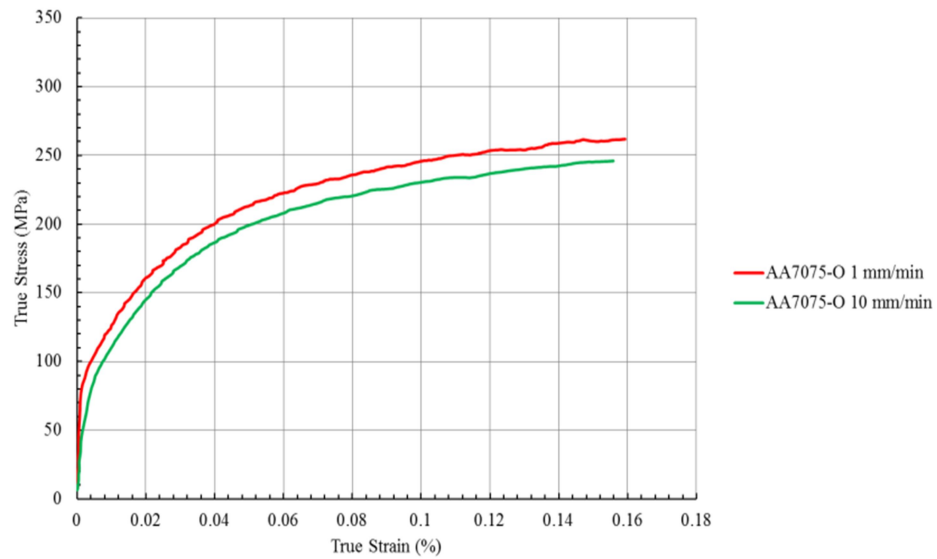


Figure 4.7 Flow stress-strain curves for AA7075-O in rolling direction. Tests conducted at speeds of 1 and 10 mm/min at room temperature.

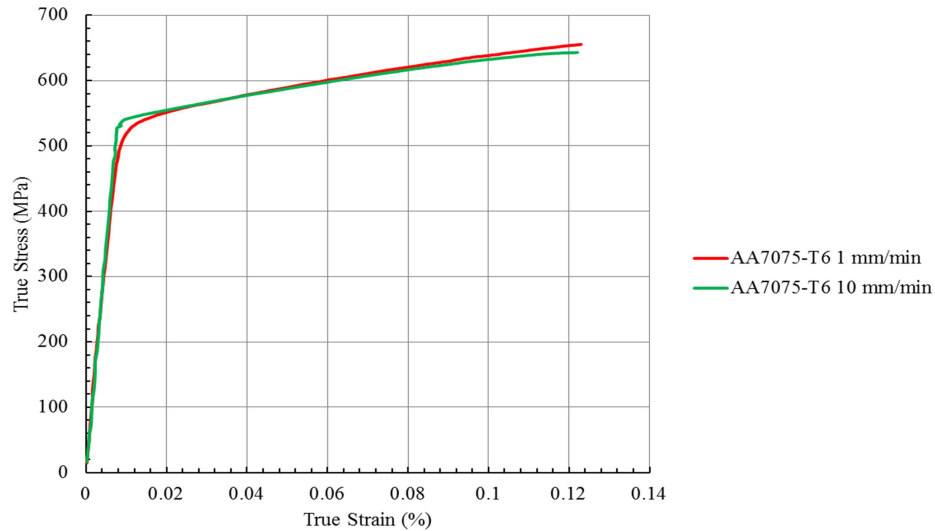


Figure 4.8 Flow stress-strain curves for AA7075-T6 in rolling direction. Tests conducted at speeds of 1 and 10 mm/min at room temperature.

#### 4.2.2 Elevated temperature uniaxial tensile test results

The results for tests at three elevated temperatures and two test speeds, in the same temper sequence as for the room temperature tests earlier, are shown in Figure 4.10 – 4.14. As expected, the flow stresses were reduced with increase in the test temperature for all tempers and this is probably due to material softening from dynamic recovery. Dynamic recovery softening mechanism, which can be activated at elevated deformation temperature, reduces dislocation density by cross-slip of screw dislocations and climb of edge dislocations (Totten & MacKenzie, 2003). Also, the strains to fracture increased for all temper sheets with the increase in test temperature. The F temper sheets exhibited immediate softening in the plastic deformation range at low temperatures but saturation at 260°C (see Figure 4.10). Also, the strain to fracture was reduced and yield strength increased at higher test speeds as shown in Figure 4.11. This material behaviour may be

attributed to a reduction in strain rate sensitivity (or  $m$  value) at high test speed which leads to decrease in strain to fracture. The O temper sheet exhibited significant work hardening though out the deformation process at all temperatures. The rate of work hardening was, however, reduced, as the temperature was increased. In fact, the material exhibited stress saturation at 260°C. The stress-strain curves moved to higher stress and strain values with increased speed, possibly from the positive effect of increased strain rate sensitivity at elevated temperature (see Figure 4.12 and Figure 4.13). All elevated temperature flow stress curves at 180°C, 220°C and 260°C for AA7075-O sheet from tests at 1 and 10 mm/min show evidence of work hardening up to fracture with work hardening rate decreasing progressively with the increase in temperature as shown in Figure 4.9. There are also indications of non-uniformity of flow in the stress-strain curves of O-temper sheet at room temperature and at the lower end of the elevated temperature (such as at 180°C) possibly due to dynamic strain ageing. However, the effect is reduced at higher temperatures (220°C and 260°C) as shown in Figure 4.12 and Figure 4.13. Lastly, the T6-temper sheet exhibited a different elastic response compared to the other two tempers. In addition, the plastic flow behaviour exhibited strain softening (i.e., post-uniform straining) after initial strain hardening (uniform straining) at 220°C and 260°C, and a significant reduction in plastic strain to fracture compared to the O-temper sheet, as shown in Figure 4.14 and Figure 4.15. The increase in the post-uniform strain with increasing temperature more than compensated for the decrease in uniform strain. The reduction in strain to fracture compared to the O-temper sheet is due to dislocation-precipitates interaction and ductile damage development which led to an early onset of

fracture in the T6 sheet. The material exhibited slight work hardening at 180°C compared to the room temperature response of the material. The T6 sheet exhibited near saturation in flow stress at 220°C and significant softening at 260°C. This result may be explained in terms of partial dissolution of GP zones and  $\eta'$  precipitates, which act as barriers to dislocation motion, and lead to higher ductility and softening behavior in T6 temper sheet at 260°C (see sub-section 2.6 in Literature Review Chapter). The strain to fracture was slightly higher at 10 mm/min compared to the test speed of 1 mm/min.

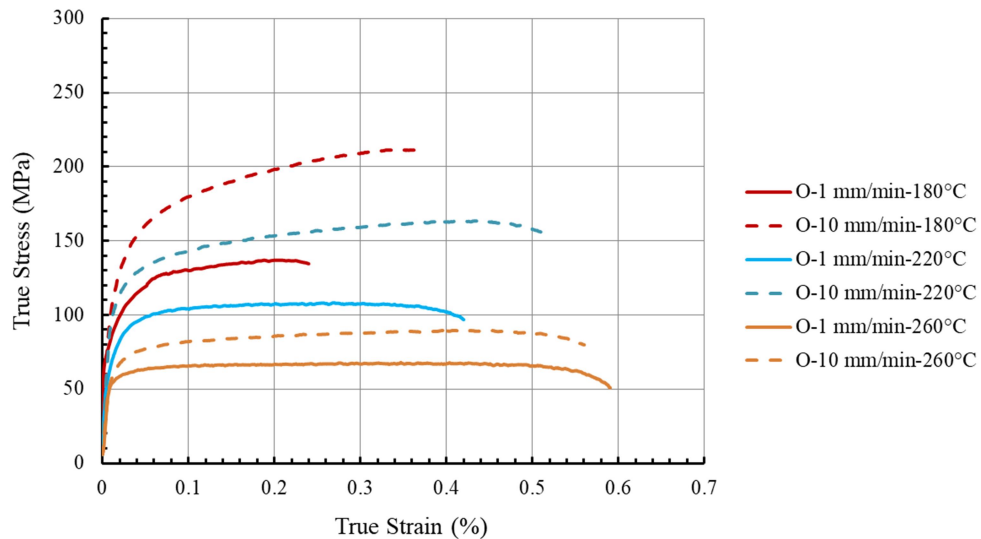


Figure 4.9 Flow stress-strain curves for AA7075-O in rolling direction. Tests conducted at speeds of 1 and 10 mm/min at three elevated temperatures.



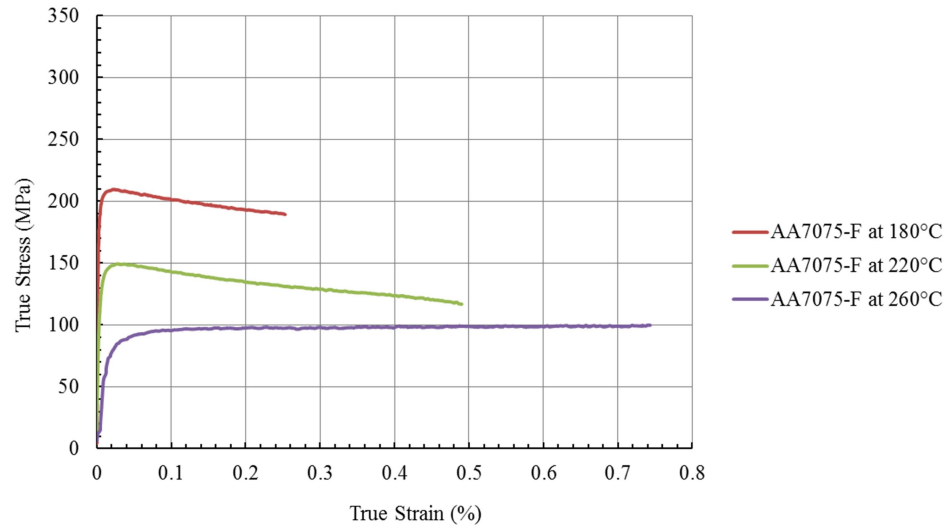


Figure 4.10 Flow stress-strain curves for AA7075-F in rolling direction. Tests conducted at a speed of 1 mm/min at three elevated temperatures.

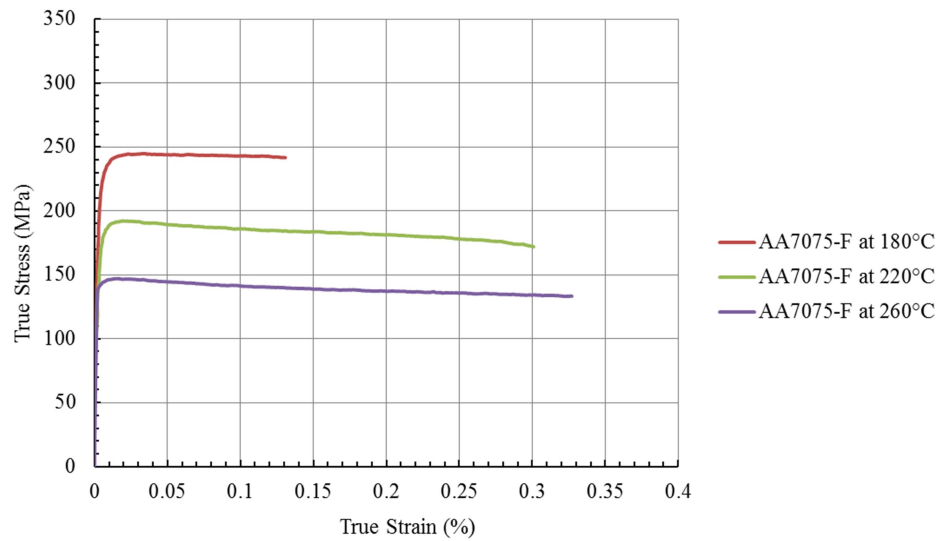


Figure 4.11 Flow stress-strain curves for AA7075-F in rolling direction. Tests conducted at a speed of 10 mm/min at three elevated temperatures.

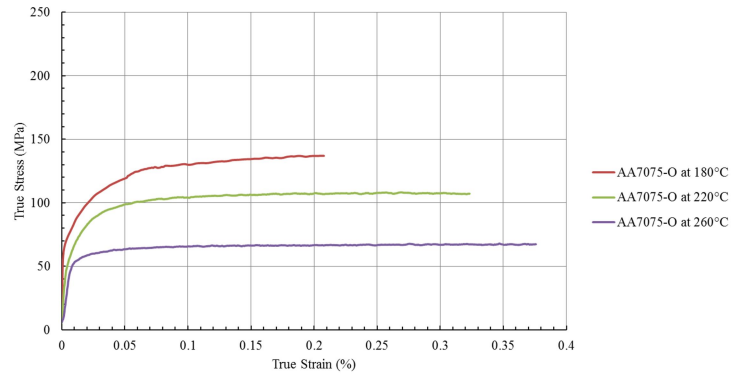


Figure 4.12 Flow stress-strain curves for AA7075-O in rolling direction. Tests conducted at a speed of 1 mm/min at three elevated temperatures.

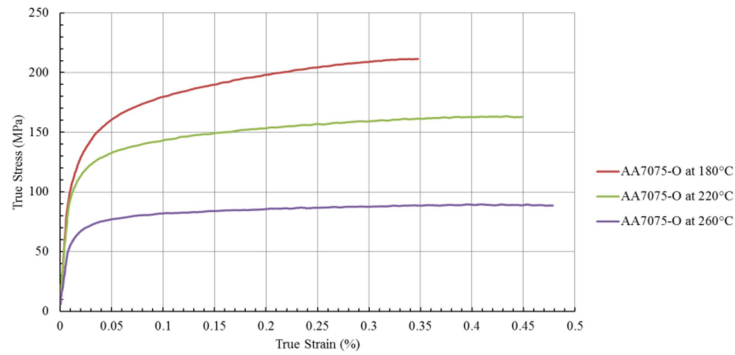


Figure 4.13 Flow stress-strain curves for AA7075-O in rolling direction. Tests conducted at a speed of 10 mm/min at three elevated temperatures.

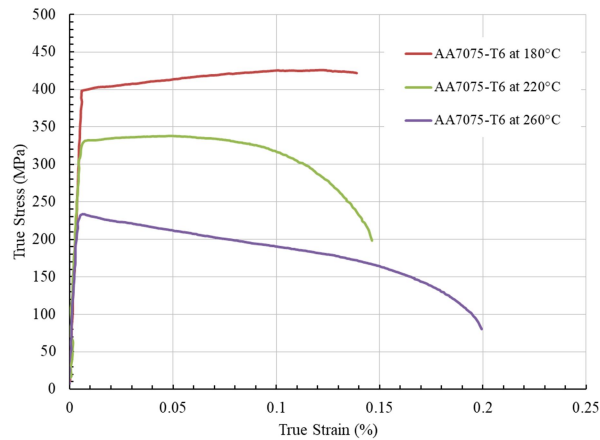


Figure 4.14 Flow stress-strain curves for AA7075-T6 in rolling direction. Tests conducted at a speed of 1 mm/min at three elevated temperatures.

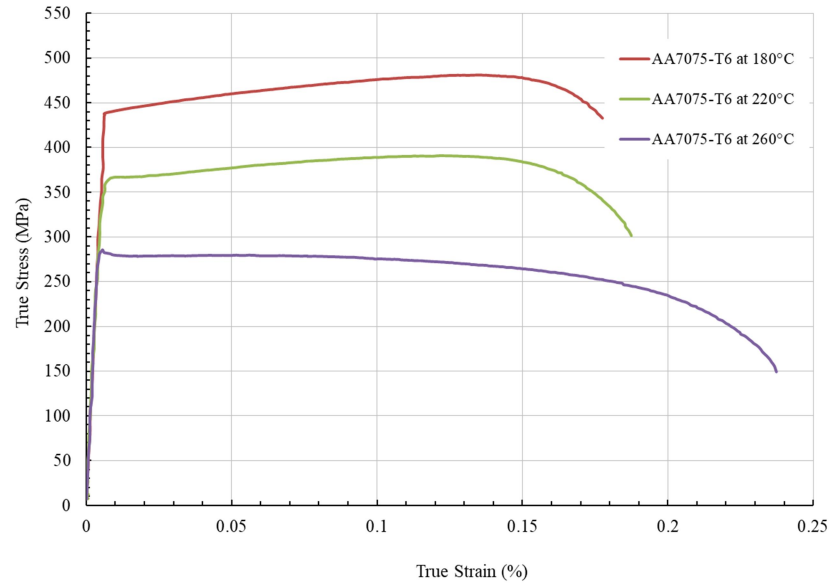


Figure 4.15 Flow stress-strain curves for AA7075-T6 in rolling direction. Tests conducted at a speed of 10 mm/min at three elevated temperatures.

The material property data from room and elevated temperature stress-strain curves for all three tempers are summarized in Table 4.4 below. This data is also plotted as graphs in Figure 4.16 and Figure 4.17 to show yield strength dependence on temperature and test speed for the three tempers. At a test speed of 1 mm/min, as the tensile test temperature increased from room temperature to 260°C the yield stress decreased by 69.42%, 41.19% and 54.13% for F, O and T6 tempers respectively. Similarly, at a test speed of 10 mm/min, as the tensile test temperature increased from room temperature to 260°C the yield stress decreased by 53.55%, 19.9% and 51.56% for F, O and T6 tempers respectively. The lowest reduction in yield strength was observed in the most stable fully annealed temper and it was dependent on the microstructure resulting from the heat treatment. Annealing heat treatment for sheet metal includes recrystallization stage which

means that new grains, with reduced dislocation density, were formed and led to increase in ductility and reduction in yield strength. Moreover, higher yield strength was obtained in peak-aged (T6) condition due to the presence of coherent and non-coherent precipitates ( $\eta'$  and  $\eta$ ) in the microstructure that impeded the dislocations motion.

Table 4.4 Material property data from the room and elevated temperature uniaxial tensile tests.

Temper	Temperature (°C)	Test Speed (mm/min)	Yield Strength (MPa)	Tensile Strength (MPa)	Elongation
F	Room Temperature	1	230.17	322.58	0.064
		10	280.74	315.89	0.055
	180	1	190.06	189.34	0.25
		10	218.06	241.67	0.13
	220	1	121.17	116.89	0.49
		10	163.15	171.98	0.3
	260	1	70.38	99.83	0.74
		10	130.39	133.28	0.33
O	Room Temperature	1	88.1	261.8	0.16
		10	75.82	245.97	0.156
	180	1	77.84	136.95	0.21
		10	83.73	211.48	0.35
	220	1	61.23	107.17	0.32
		10	77.97	162.97	0.45
	260	1	51.81	67.35	0.37
		10	60.73	88.65	0.48
T6	Room Temperature	1	481.7	655.36	0.123
		10	540.38	642.98	0.122
	180	1	400.2	425.99	0.14
		10	440.44	480.79	0.177
	220	1	320.11	341.08	0.146
		10	361.2	375.57	0.187
	260	1	220.96	216.42	0.2
		10	261.73	278.04	0.24

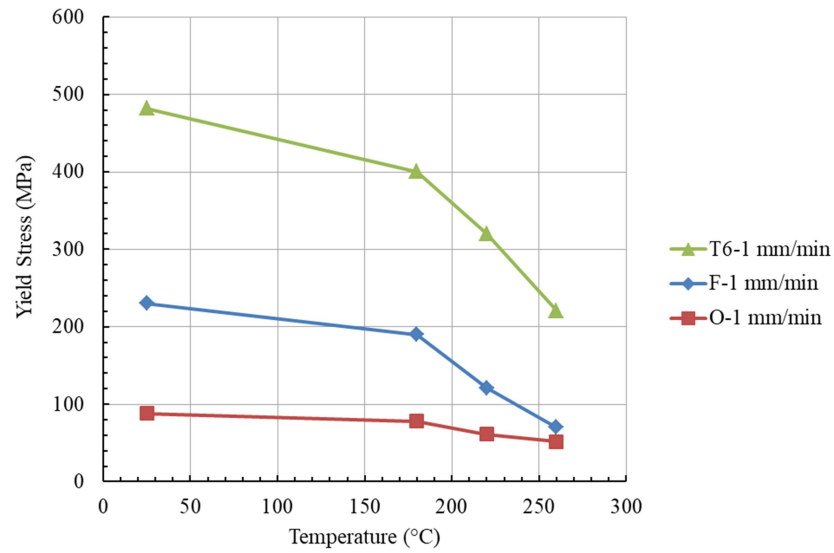


Figure 4.16 A plot of yield stress versus test temperature for the sheet material in three temper states tested at a test speed of 1 mm/min.

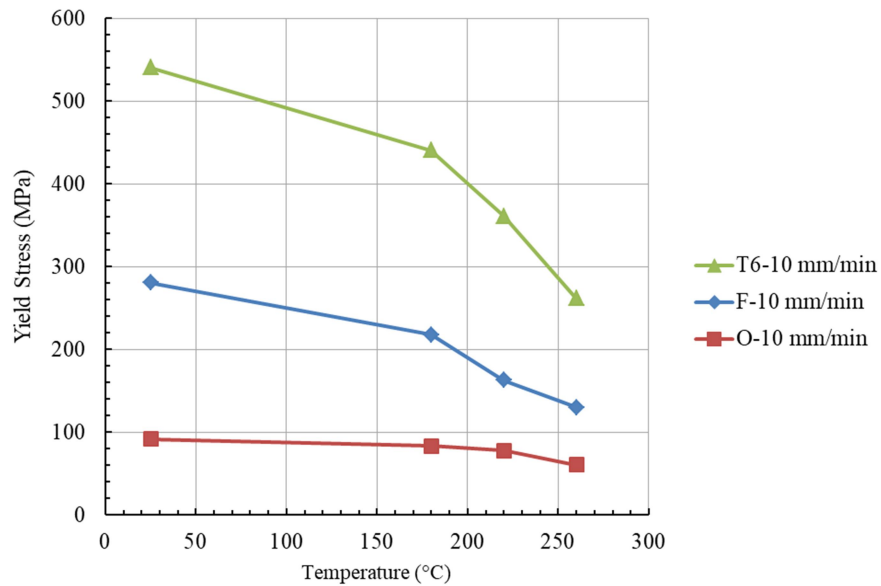


Figure 4.17 A plot of yield stress versus test temperature for the sheet material in three temper states tested at a test speed of 10 mm/min.

The strain hardening exponent ( $n$ ) and strength coefficient ( $K$ ) values were obtained from power law fit to the O-temper stress-strain data (see Table 4.5). As shown, the higher values of  $n$  and  $K$  resulted from higher test speed of 10 mm/min for all testing temperatures, likely due to positive strain rate sensitivity of AA7075-O sheet. Also, as the test temperature increased, the strain hardening and strength coefficient were decreased. It is to be noted that, for as-fabricated (F temper) and peak-aged (T6 temper) samples, the  $n$  and  $K$  values could not be obtained in many instances via the power law fit due to their decreasing flow stress with strain (or softening behaviour). Also, O temper samples tested at room temperature show the highest values of strength coefficient and strain hardening exponent but rather poor power law fit to the experimental data as shown in Figure 4.18.

Table 4.5 Strain hardening exponent and strength coefficient for AA7075-O at room and elevated temperatures.

Temper	Temperature (°C)	Test Speed (mm/min)	Strain Hardening Exponent ( $n$ )	Strength Coefficient ( $K$ )	quality of fit ( $R^2$ )
O	RT	1	0.254	437.4	0.98
		10	0.286	443	0.97
	180	1	0.185	197.5	0.91
		10	0.195	270.48	0.93
	220	1	0.138	134.86	0.82
		10	0.146	191.45	0.88
	260	1	0.102	78.42	0.67
		10	0.123	102.5	0.82

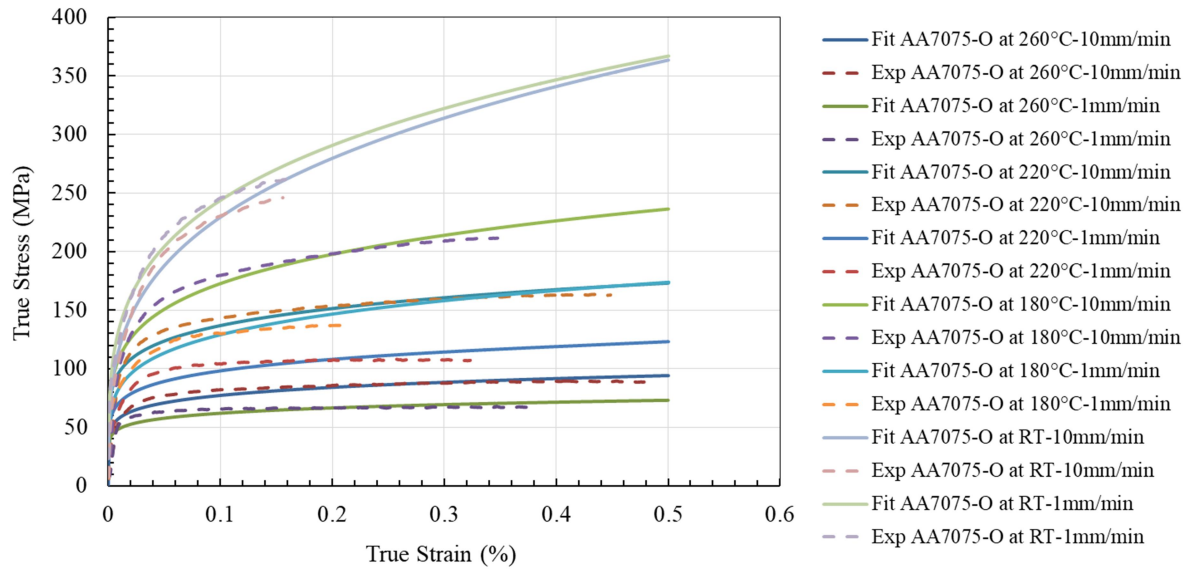


Figure 4.18 Experimental and power law fitted flow stress-strain curves of AA7075-O. Tests conducted at speeds of 1 and 10 mm/min at room temperature and three elevated temperatures.

Figure 4.19 and Figure 4.20 present onset of diffused necking for AA7075-O tensile test samples at different testing conditions of temperature and strain rate based on Considère criterion (corresponding to the black diamond symbol placed on the stress-strain curves). This criterion establishes the onset of diffused necking when strain is equal to strain hardening exponent (i.e.,  $\epsilon_{\text{diffuse}} = n$ ). Table 4.6 summarizes the strain and stress values at the onset of diffused necking for the O-temper sheet.

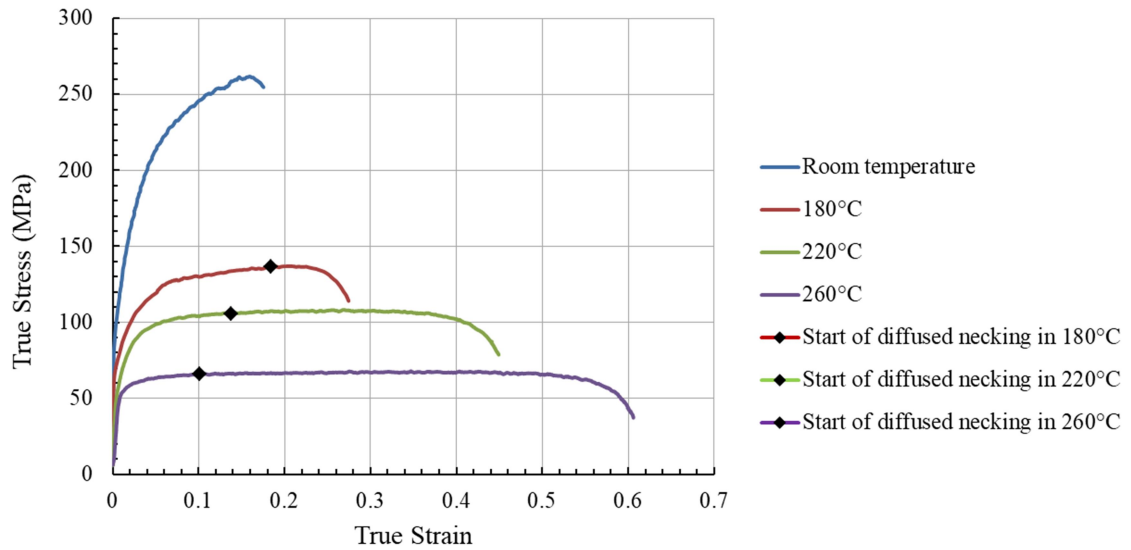


Figure 4.19 Onset of diffused necking for AA7075-O tensile test samples tested at speed of 1 mm/min.

Table 4.6 Onset of diffused necking initiation conditions for O temper at elevated temperatures.

Temper	Temperature (°C)	Test Speed (mm/min)	Strain at Diffused Neck Initiation ( $\epsilon = n$ )	Stress at Diffused Neck Initiation (MPa)
O	180	1	0.185	136.47
		10	0.195	197.26
	220	1	0.138	105.65
		10	0.146	148.51
	260	1	0.102	65.59
		10	0.123	82.74

Results from Table 4.6 demonstrate that as the tensile test temperature increases the stress corresponding to onset of diffused necking decreases. Also, as the strain rate or test speed



is increased the stress at the onset of diffused necking is also increased. These conclusions are consistent with the shape of flow stress curves.

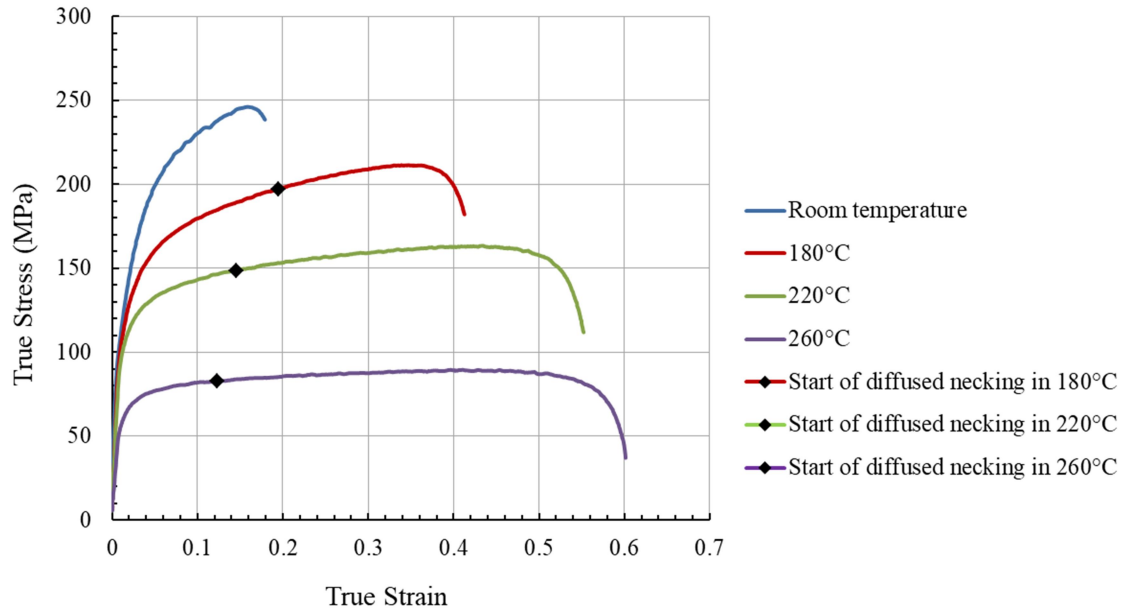


Figure 4.20 Onset of diffused necking for AA7075-O tensile test samples tested at speed of 10 mm/min.

### 4.3 AA7075 formability test results

In this sub-section, formability test results for AA7075-O and AA7075-T6 sheets are presented. Two different hemispherical punch stretching (HPS) tool sets based on 50.8 mm and 101.6 mm diameter punches mounted on two different forming test systems were used for O and T6 tempers respectively due to experimental limitations as described earlier in the Experimental Methodology Chapter. FLDs for fully annealed samples were established at room temperature, 180°C, 220°C, and 260°C by using 50.8 mm punch diameter while the FLDs for peak-aged temper were obtained using 101.6 mm HPS tool set. The data in this sub-section is organized in the following order; (i) punch load –

displacement characteristics for 50.8 mm punch based HPS tests, (ii) strain distribution maps from deformed dome specimen from ARGUS offline optical strain measurement system, (iii) experimental FLDs for O temper sheet formed in the temperature of RT - 220°C and T6 temper at 220°, and (iv) strain distribution maps and FLDs from 101.6 mm punch based HPS tests and using ARAMIS online optical strain measurement system for O and T6 deformed at room temperature.

#### **4.3.1 Punch load versus displacement characteristics from dome tests**

Each specimen geometry and lubrication condition provided a ‘signature’ load versus displacement trace during hemispherical punch stretching (i.e., dome testing) of specimens. In general, the load applied by the hemispherical punch increased non-linearly as the specimens deformed plastically in the form of a dome. A curvature reversal in the shape of the curve (the so called inflection) occurred for each specimen geometry. Figure 4.21 (a-d) shows a set of load versus displacement traces for O temper material corresponding to different test specimen geometries deformed by 50.8 mm diameter punch at room and three elevated temperatures, 180°C, 220°C and 260°C respectively. As shown, the inflection point varied with the specimen geometry and physically represents the location of the punch-dome specimen surface contact boundary. Further, the load and displacement at neck or fracture typically increased with specimen width for the narrow width specimens and with better lubrication between the punch and sheet for the full size dome specimens. Also, the load at fracture decreased, and the displacement at fracture increased, for each strain path with an increase in temperature. This was generally consistent with the trends in the uniaxial stress-strain curves reported earlier in sub-

sections 4.2.1 and 4.2.2. The largest displacements at fracture (i.e., maximum dome height) of about 25 mm were obtained at 220°C using lubricated punch. The average limiting dome height (LDH) data for all AA7075-O sheet specimens tested at different temperatures are presented below in Table 4.7.

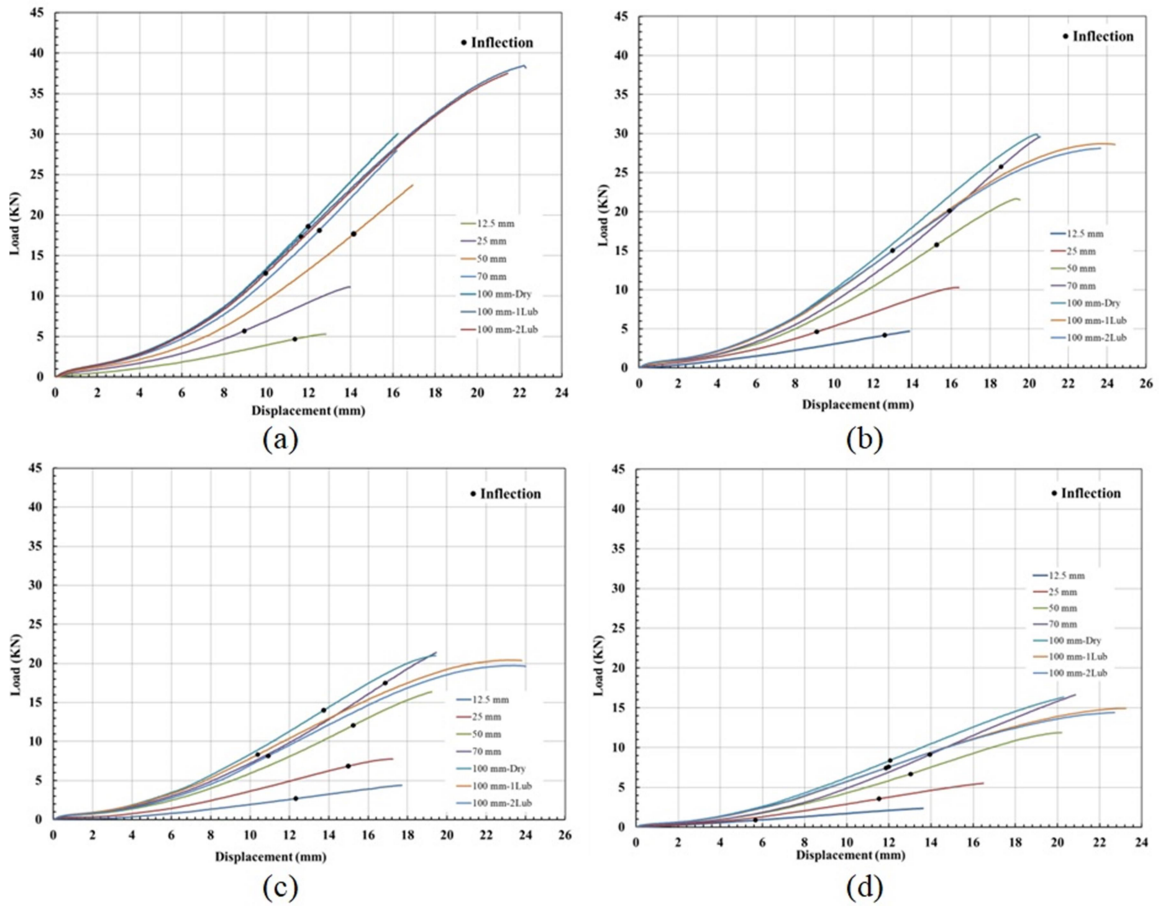


Figure 4.21 Punch load versus displacement curves from hemispherical dome stretching tests for AA7075-O sheet. The graphs correspond to test at, (a) room temperature, (b) 180°C, (c) 220°C, and (d) 260°C.

Table 4.7 Average LDH data and standard deviation of AA7075-O for dome specimens tested at room temperature, 180°C, 220°C, and 260°C. All data are in mm.

Specimen Type (in terms of min. width in mm)	Room Temperature		180°C		220°C		260°C	
	Avg.	SD	Avg.	SD	Avg.	SD	Avg.	SD
12.5	14.5	0.16	17.67	0.48	18.6	0.82	17.59	0.64
25	15.5	0.16	18.3	0.37	19.64	0.21	19.54	1.01
50	18.05	0.37	21.18	0.016	21.78	0.18	22.26	0.11
70	17.85	0.37	21.87	0.24	21.97	0.19	22.26	0.016
100-Dry	17.5	0.16	21.38	0.26	21.54	0.13	22.53	0.38
100-1, Lubricant	21.2	0.16	24.77	0.47	25.08	0.016	24.3	0.08
100-2, Lubricants	22.1	0.082	24.44	0.21	25.07	0.057	23.7	0.29

#### 4.3.2 Strain distributions in dome test specimens

Figure 4.22 below shows the post-test strain maps of O-temper necked specimens of 7 different geometries deformed by using 50.8 mm diameter punch tooling at 220°C. As shown, for the narrow width specimens (of widths of 12.5 mm, 25 mm, 50 mm and 70 mm), strains were concentrated in two different regions on opposite sides of the pole. For the full dome samples (100 mm diameter round blanks), formed under 3 different lubrication conditions, the necks moved towards the pole with improved lubrication conditions. This was attributed to a reduction in friction between the punch and blank and increased sliding of the blank over the punch surface prior to necking causing a change in strain path of the critical necking region towards increased biaxial tension and higher limit strains. The latter is discussed in more detail in a later sub-section 4.3.4.

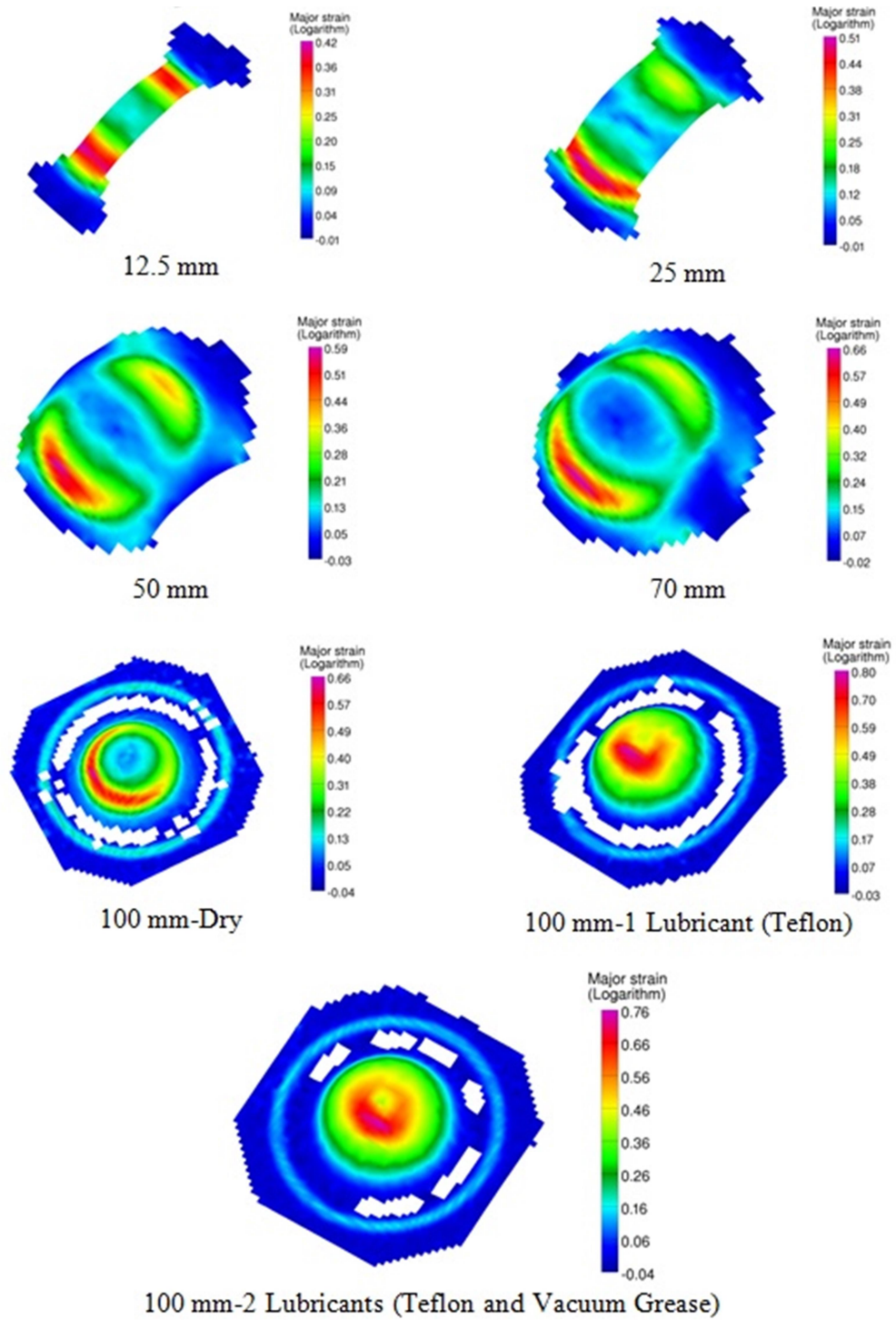


Figure 4.22 ARGUS strain maps of various specimen geometries tested for AA7075-O at 220°C. White areas in the strain maps are regions where strain calculations could not be completed due to poor image quality.

For each of the hemispherical dome specimen geometries corresponding to a specific strain path, the major strain distribution along a section line from the pole, and passing through the middle of the neck line, to the base of the hemisphere was obtained from post-test strain field data, as explained earlier in the Experimental Methodology Chapter. For brevity, only the major strains for uniaxial strain (UT), plane strain (PST) and balanced biaxial strain (BBT) paths for O temper specimens tested at room temperature and 220°C are shown in Figure 4.23 to Figure 4.25. In general, dome samples formed at 220°C exhibited a larger major limit strain value (i.e., peak strain) than those formed at room temperature. The increase in the major strain value in the neck at elevated temperatures is consistent with the general increase in dome height with temperature. Also, the location of the neck with respect to the pole of the dome (i.e., necking distance) varied as a function of strain path, temperature and friction conditions. A comparison of the necking distance between room and elevated temperatures is shown in Table 4.8. This difference was the largest for plane strain test specimens. The neck distance from the pole was smallest in BBT samples indicating a low friction state between the punch and the blank due to better lubrication provided by a combination of Teflon sheet and grease between the punch and test blank.

Similar strain distributions to O temper were also obtained for T6 temper necked dome specimens deformed by 50.8 mm diameter punch tooling but only at 220°C since room temperature test specimens often failed prematurely and it was difficult to stop the tests at neck. The results for O and T6 temper dome specimens are compared for the UT, PST and BBT strain paths in Figure 4.26 - Figure 4.28. The PST sample strain distribution

(Figure 4.27) shows the largest necking distance for T6 sheet, a result similar to the O temper sheet. Also, major strain for T6 PST sample has a smaller value compared to the O temper sheet due to its much higher strength and considerably lower ductility (see earlier Figure 4.7 and Figure 4.8). Moreover, BBT sample in T6 temper show zero distance from pole which means that the necking occurred at the pole whereas it was shift by about 5.6 mm from the pole for the O-temper sample (see Figure 4.28). In general, the strain gradients leading to the peak strain in the neck were higher for the T6 temper samples compared to the O-temper at all temperatures and strain paths. This is indicative of more rapid localization evident in the T6 material, and likely a result of its lower strain rate sensitivity.

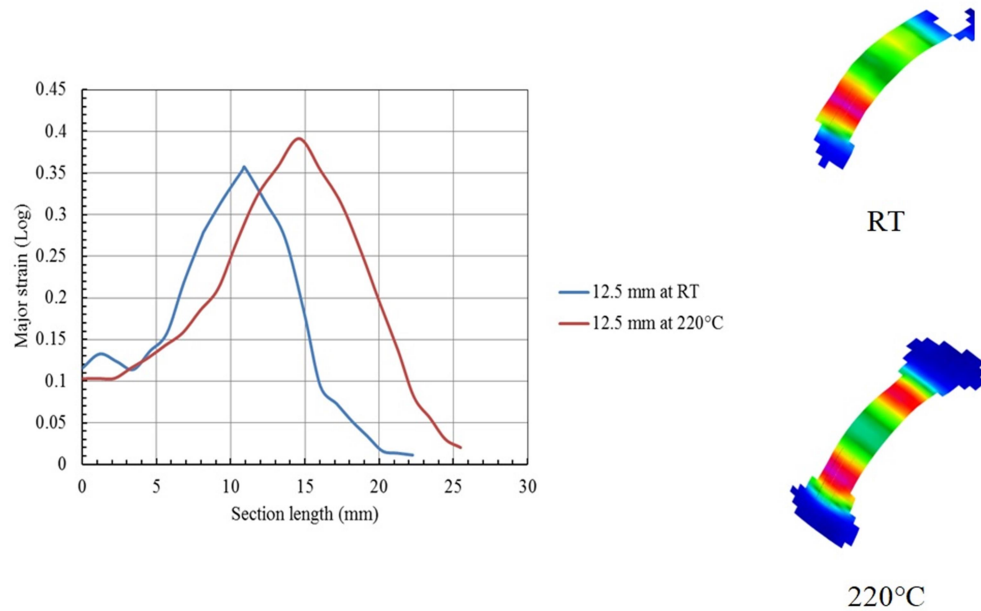


Figure 4.23 Major strain distributions for 12.5 mm width dome specimens (UT) in O temper formed at room temperature and 220°C.

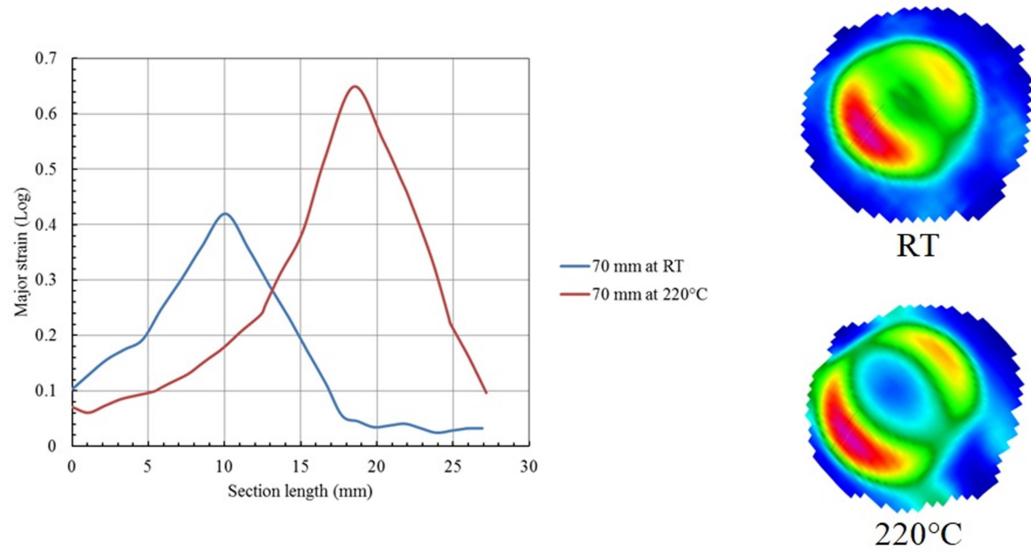


Figure 4.24 Major strain distributions for 70 mm width dome specimens (PST) in O temper formed at room temperature and 220°C.

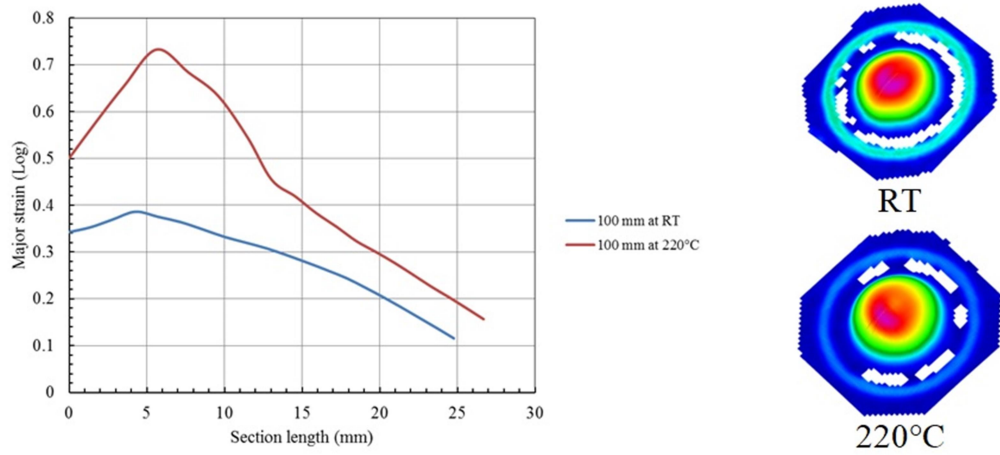


Figure 4.25 Major strain distributions for 100 mm width dome specimens (BBT) in O temper formed at room temperature and 220°C.



Table 4.8 Distance from pole to the neck in O and T6 temper hemispherical dome specimens formed by using 50.8 mm diameter punch tooling at room temperature and 220°C.

Temper	Forming Temperature (°C)	Strain Path	Neck distance (measured horizontally from sample pole) (mm)
O	Room Temperature	UT	10.93
		PST	10.06
		BBT	4.27
	220°C	UT	14.61
		PST	18.48
		BBT	5.63
T6	220°C	UT	9.56
		PST	10.07
		BBT	0 (neck at the pole)

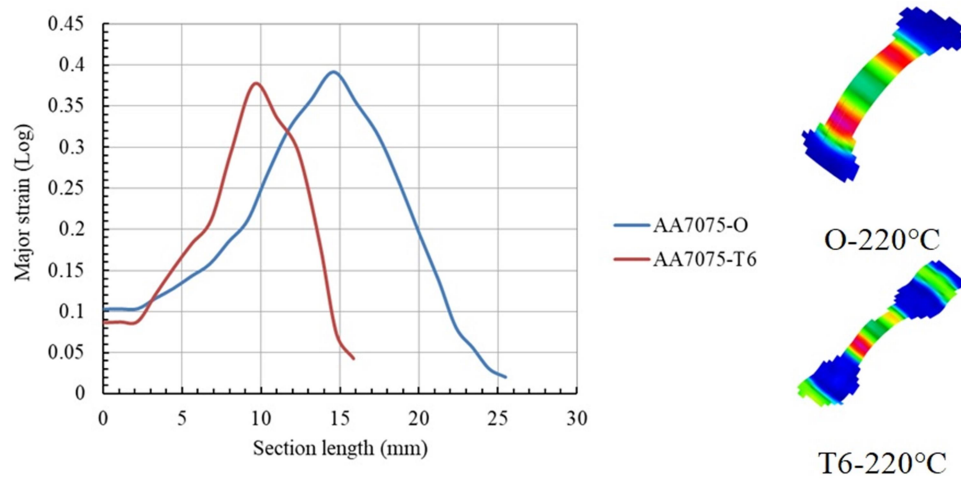


Figure 4.26 A comparison of major strain distributions for 12.5 mm width dome specimens (UT) in O and T6 tempers formed at 220°C.

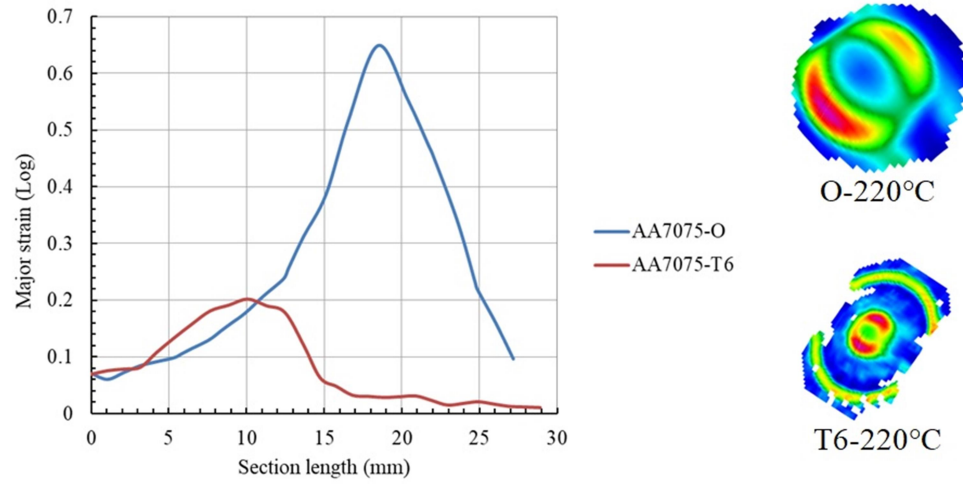


Figure 4.27 A comparison of major strain distributions for 70 mm width dome specimens (PST) in O and T6 tempers formed at 220°C.

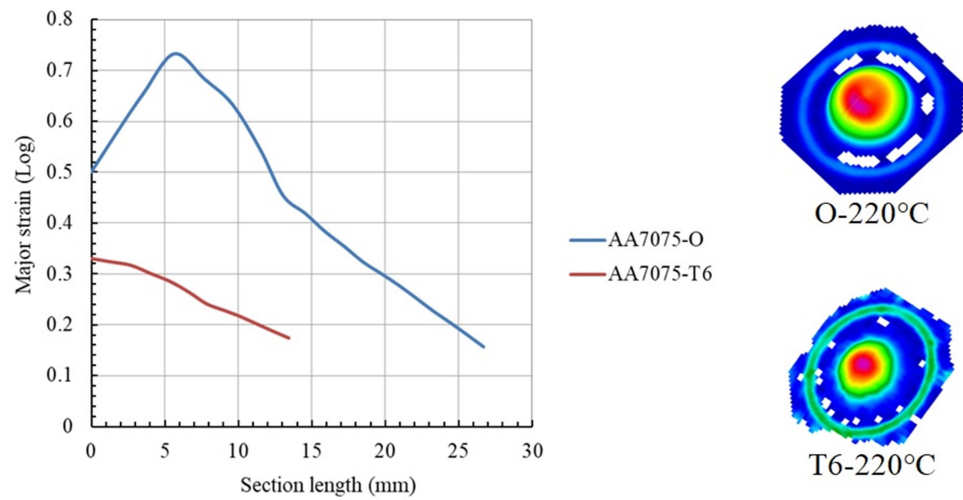


Figure 4.28 A comparison of major strain distributions for 100 mm width dome specimens (BBT) in O and T6 tempers formed at 220°C.

As earlier for O-temper dome samples, Figure 4.29 shows strain maps for different AA7075-T6 dome samples formed at 220°C. The measured major strain range is considerably lower than that for the fully-annealed sheet due to its significantly lower ductility resulting from age hardening heat treatment. The dispersion hardening mechanism leads to strengthening of the T6 sheet by forming precipitates that act as obstacles to dislocation motion. The strengthening of the material results in increased forming force and reduced dome height prior to localized necking and fracture compared to the fully annealed sheet. Additionally, at test temperature of 220°C, partial dissolution of precipitates may occur and consequently cause increased solid solution strengthening of the matrix (Kumar & Ross, 2016; Kumar et al., 2014; Nicolas & Deschamps, 2003). It was stated in the above papers that extent of second phase dissolution for 7xxx series mainly depend on temperature. The dissolution temperature range for GP zones,  $\eta'$  and  $\eta$  precipitates are typically 50 - 150°C, 200 - 250°C and 300 - 350°C respectively (Kumar & Ross, 2016; Kumar et al., 2014; Löffler et al., 1983). Also, it is clear, from strain maps legends, that the major strain range for T6 FLD deformed samples is significantly lower compared to the major strain range for O temper samples (see Figure 4.22 earlier).

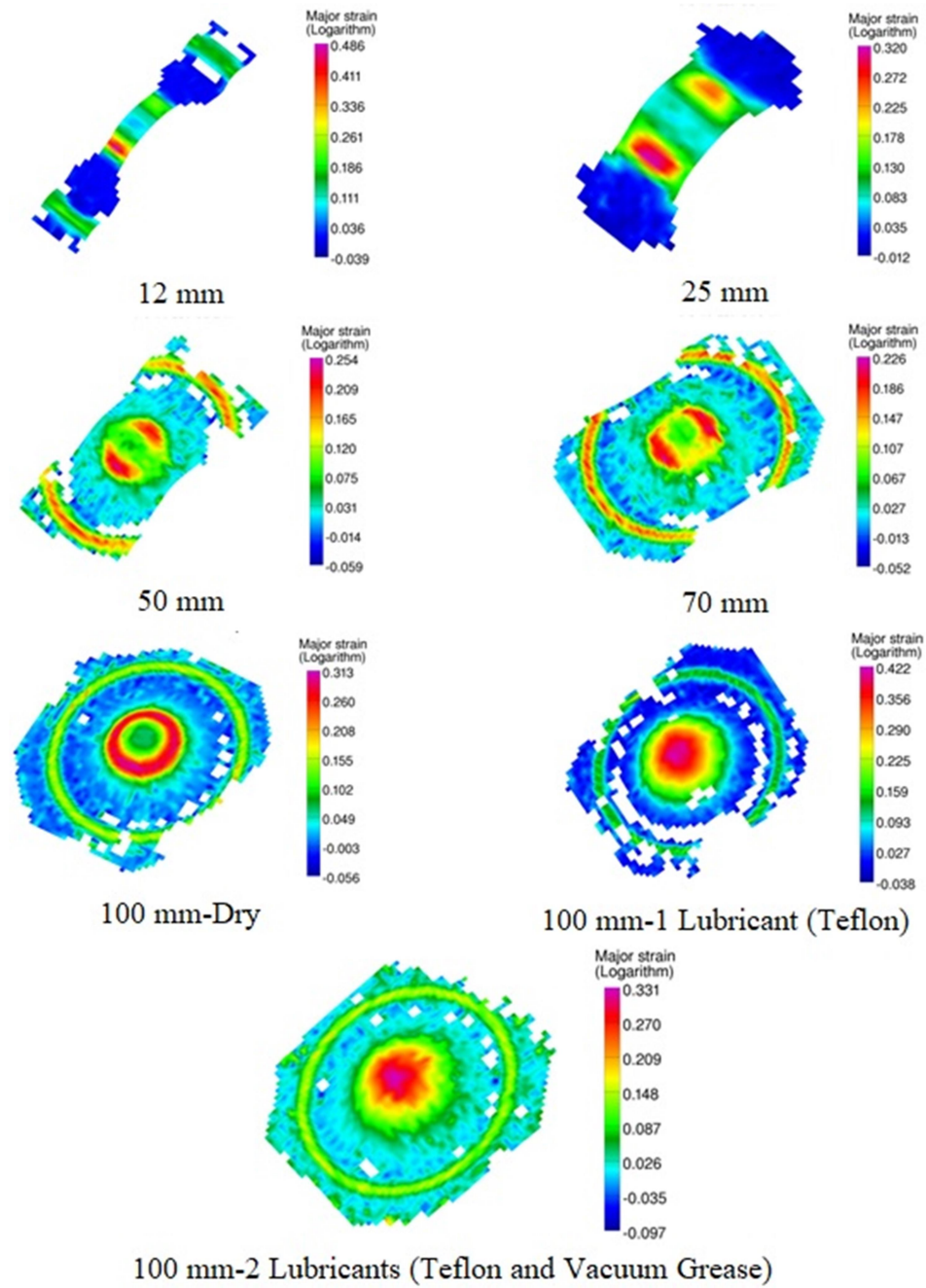


Figure 4.29 ARGUS strain maps from various specimen geometries of AA7075-T6 dome specimens tested at 220°C.

### 4.3.3 Experimental FLDs

As noted earlier in Chapter 3 on Experimental Methodology, two different methodologies were adopted for obtaining the experimental FLDs due to experimental equipment limitations. This sub-section presents the FLDs obtained from 50.8 mm diameter punch based HPS tests with strains measured post-test from periodic grids on the test blank surface.

The various FLDs for O-temper sheet, with corresponding forming limit curve (FLC) superimposed on each FLD, are presented in Figure 4.30 - Figure 4.33 for room and three elevated test temperatures. All temperature dependent FLCs are then compared in Figure 4.34 in terms of their relative shapes and locations on the same graph. The FLCs moved upwards along the major strain axis as the test temperature was increased from room temperature to 260°C due to thermal softening and enhanced ductility. As the forming temperature increased, the limit strains increased for all strain paths (UT, PST and BBT). However, there seems to be very small upward movement in the position of FLD when the temperature was raised from 220°C to 260°C. This is may be attributed to a slowdown in the dynamic recovery (DRV) softening and its transition to dynamic recrystallization (DRX). Such a transition typically occurs at elevated temperatures with relatively long times. As a result, only a minor upward shift in the FLC was observed at 260°C compared to 220°C (Shi et al., 2014).

It is to be noted that the FLCs on tension – compression side did not extend to larger compressive minor strains under all forming conditions and for all tempers. This may be attributed to the specific samples geometries selected for dome tests. Perhaps, some non-

standard tests such as a hole expansion test could be utilized in the future to improve this side of the FLD. Also, there is a strain path ‘gap’ in the data for the tension – tension side of the FLDs. Perhaps a new combination of lubricants and a polymer film could be utilized to achieve strain paths that will fill the gap in the biaxial tension side strain limit data. In spite of these limitations, to the best of our knowledge, the literature lacks experimental FLDs of AA7075-O sheet metal at room and elevated temperatures. This is the first time that a systematic and detailed procedure was followed as part of this work to obtain the experimental FLDs for fully annealed AA7075 sheet metal at a range of temperatures.

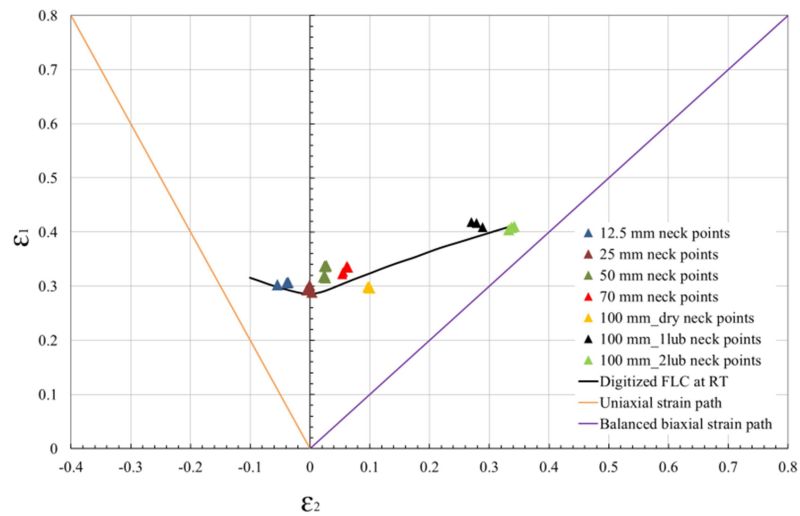


Figure 4.30 FLD of AA7075-O sheet at room temperature ( $FLD_0 = 0.28$ ).

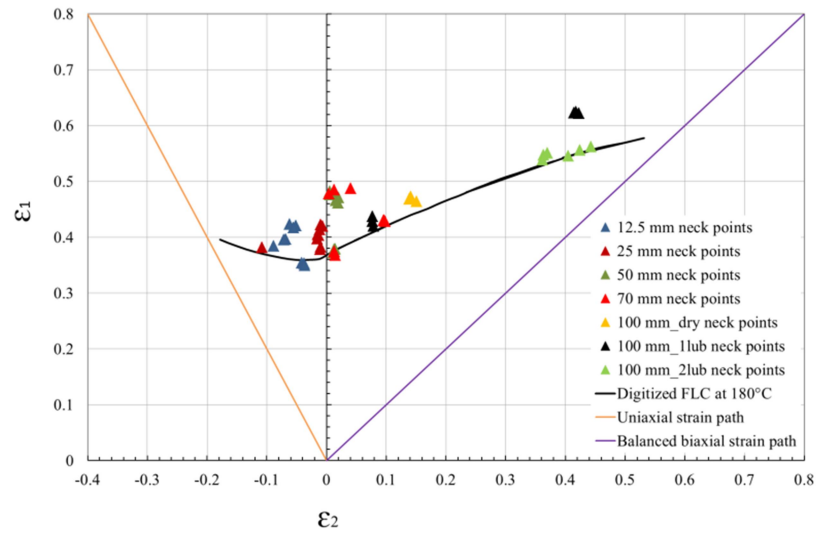


Figure 4.31 FLD of AA7075-O sheet at 180°C ( $FLD_0 = 0.37$ ).

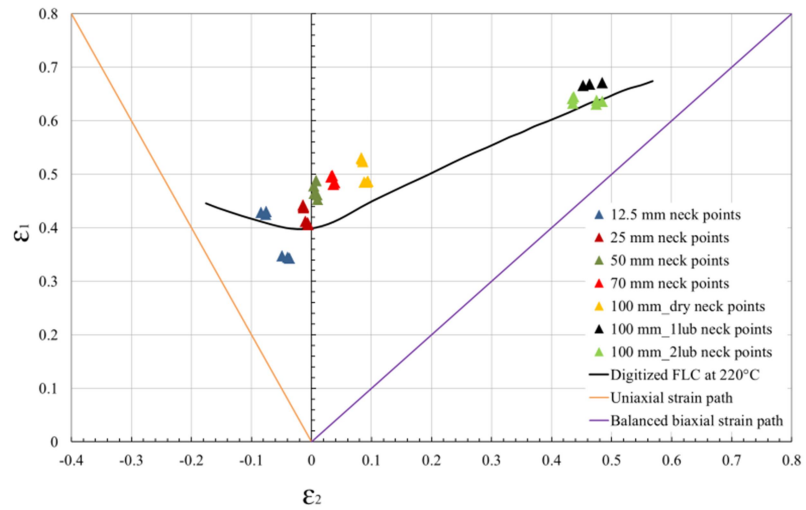


Figure 4.32 FLD of AA7075-O sheet at 220°C ( $FLD_0 = 0.4$ ).

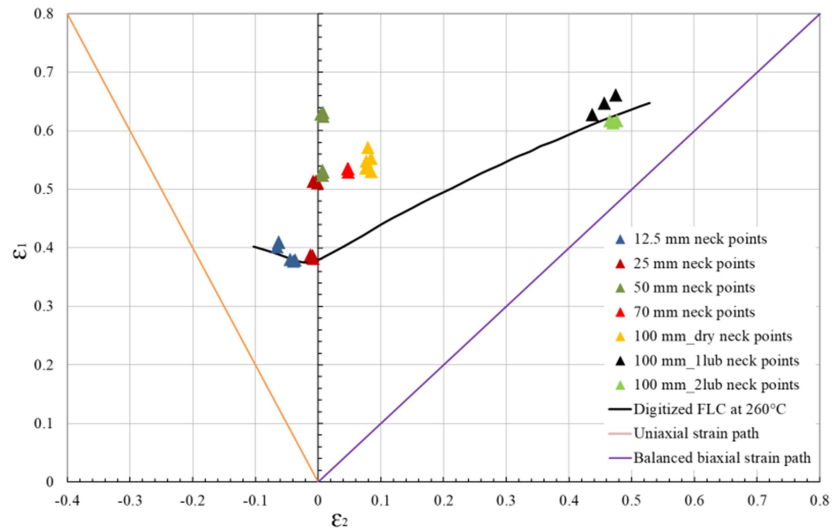


Figure 4.33 FLD of AA7075-O sheet at 260°C ( $FLD_0 = 0.38$ ).

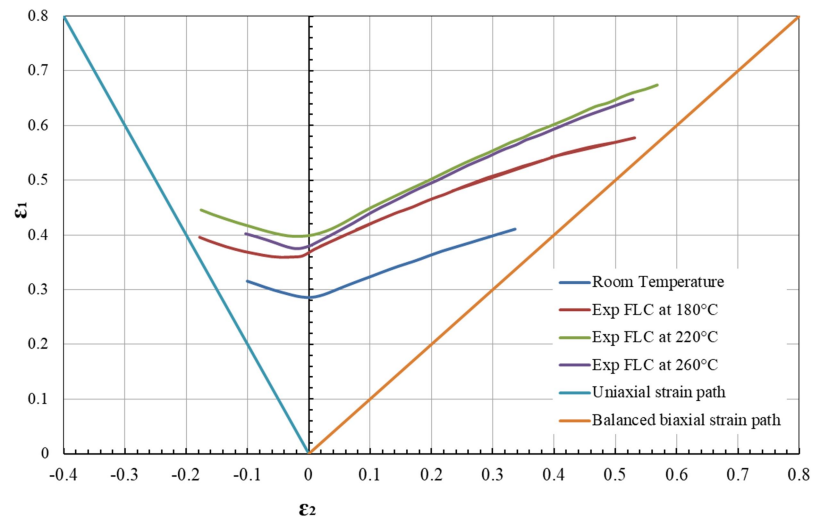


Figure 4.34 A comparison of FLCs of AA7075-O sheet at different forming temperatures.

Experimental FLDs of AA7075-T6 sheet at 220°C is presented in Figure 4.35. A  $FLD_0$  value of about 0.2 for this case is considerably lower than even the room temperature  $FLD_0$  value of 0.28 for O temper sheet. This could be attributed to significantly higher strength of AA7075-T6 sheet due to its microstructure of dispersed precipitates which



provides effective barrier to dislocation gliding and more extensive ductile void damage development (to be discussed later). It is to be noted that the microstructure has an influence on the material work hardening behavior as noted earlier while discussing the tensile test results. The precipitate microstructure can also caused ductile void damage early in the deformation process for the T6 temper sheet, as noted in subsequent sub-section, and thus contributed to the damage-induced earlier onset of localized necking and reduced limit strains. As noted by other researchers, increased particle volume fraction also leads to early void initiation, growth and coalescence prior to onset of strain localization (Pedersen et al., 2011). This is discussed in more detail after presenting the results of microstructural damage development in fractured test specimens in Sub-section 4.4.3. Figure 4.36 shows a comparison of FLCs for O and T6 at 220°C where the T6 temper FLC is significantly lower than for the O temper sheet. There exists a shift in T6 FLC towards right side of the major strain axis and this is likely the result of pre-strain that occurred due to increased lock-bead clamping of the T6 sheet material before forming into dome shape. While the amount of pre-strain from lock-bead clamping is expected to be the same for the T6 and O temper materials, their relative effect is expected to be more pronounced in T6 sheet due to its significantly lower FLC compared to the O-temper sheet. In addition, due to the larger shift in the FLC of T6 sheet towards the biaxial tension quadrant, its exhibits a lesser minor strain value on the tension-compression quadrant compared to the O-temper sheet.

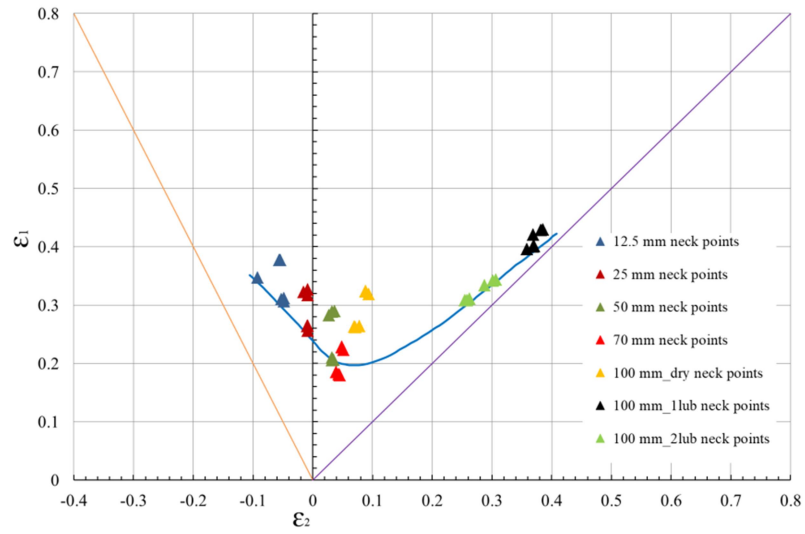


Figure 4.35 FLD of AA7075-T6 sheet at 220°C (FLD<sub>0</sub>=0.2).

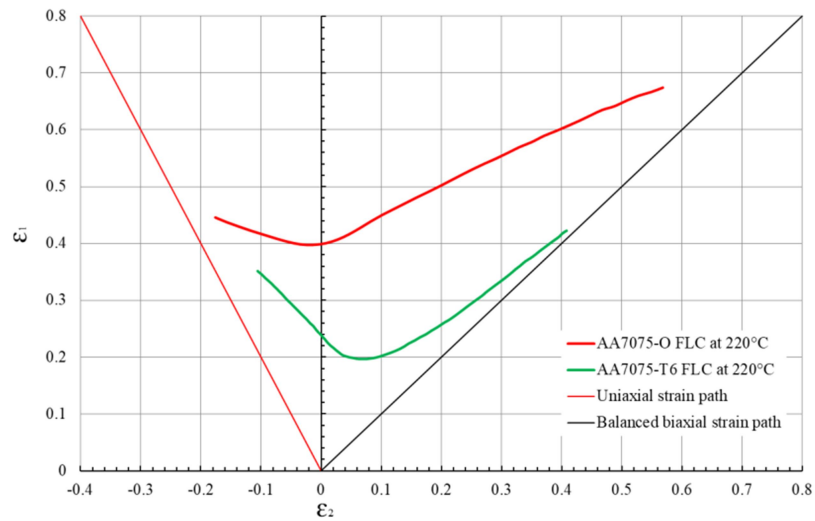


Figure 4.36 A comparison of FLDs of AA7075-O and T6 sheets at 220°C.

#### 4.3.4 Continuous strain distributions over the dome surface in room temperature tests

This sub-section presents results of spatial and temporal major strain distributions from on-line ARAMIS strain measurement system during the test. Unlike the previous post-test strain measurements on 50.8 mm dome specimens, these measurements were made on

larger dome specimens of different widths as well as full dome specimens formed with 101.6 mm punch diameter HPS tooling. As noted earlier, the measurements were carried out along a section line passing through the pole of the dome and across the neck of the specimen, as shown in Figure 4.37 for a full dome specimen. The section line is shown in black as a series of points traversing the pole of the dome, for each of the strain paths.

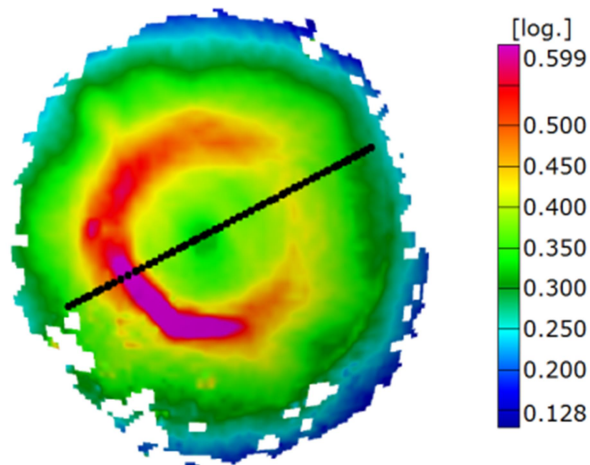


Figure 4.37 A typical major strain map of a full dome specimen from a continuously recorded ARAMIS data set during the test.

As earlier, the major strains distributions are presented for UT, PST and BBT strain paths only and for specimens of O and T6 tempers tested at room temperature. The results are shown in Figure 4.38 (a-c) –Figure 4.39 (a-c) for O and T6 temper specimens respectively. Each section line, for major strain (in blue) and minor strain (in red), was obtained from a set of recorded camera images of the evolving dome specimen. The section lines moved upward to larger strain values as the dome height (or macroscopic

strain) increased during the test. In general, the O-temper dome specimens exhibited higher major strains compared to the corresponding samples in the T6 temper state. For the narrow UT path specimen geometry, the strain were homogeneous across the specimen in the early stages of forming but began to concentrate to form a single neck region as the dome height increased (see Figure 4.38 (a) and Figure 4.39 (a)). In contrast, for PST path specimen geometry, the strains were lower and two distinct strain peaks developed quite early leading to two localized necks on opposite sides of the pole of the dome (see Figure 4.38 (b) and Figure 4.39 (b)). The two peaks were closer to the pole in the case of O-temper sheet compared to the T6 sheet. The BBT path specimen geometry started with a more homogeneous deformation of the dome specimen but exhibited two peaks on both sides of the pole towards the end of the test (see Figure 4.38 (c) and Figure 4.39 (c)). The location of the two peaks, however, were much closer to the pole than in the case of PST samples. One of the two peaks became the site of the localized neck and subsequent fracture of the specimen.

Marked undulations in strains were observed in the strain profiles for PST and BBT specimens for both O and T6 tempers, and especially for the BBT samples. These undulations exhibited a clear pattern that was established in the early stage of the deformation. The pattern was relatively more smooth in O temper BBT dome sample compared to the T6 sample. The undulations in strain distribution for T6 temper dome specimens may be explained based on microstructure of age-hardening sheet metal in which solute atoms interact with dislocations during deformation resulting in serration in plastic flow during deformation. This interaction is often referred to as dynamic strain

aging (DSA) in the literature (Hörnqvist & Karlsson, 2006; Robinson, 1994). The strain undulations were consistent with very faint surface markings on the dome surface indicative of localized plastic flow.

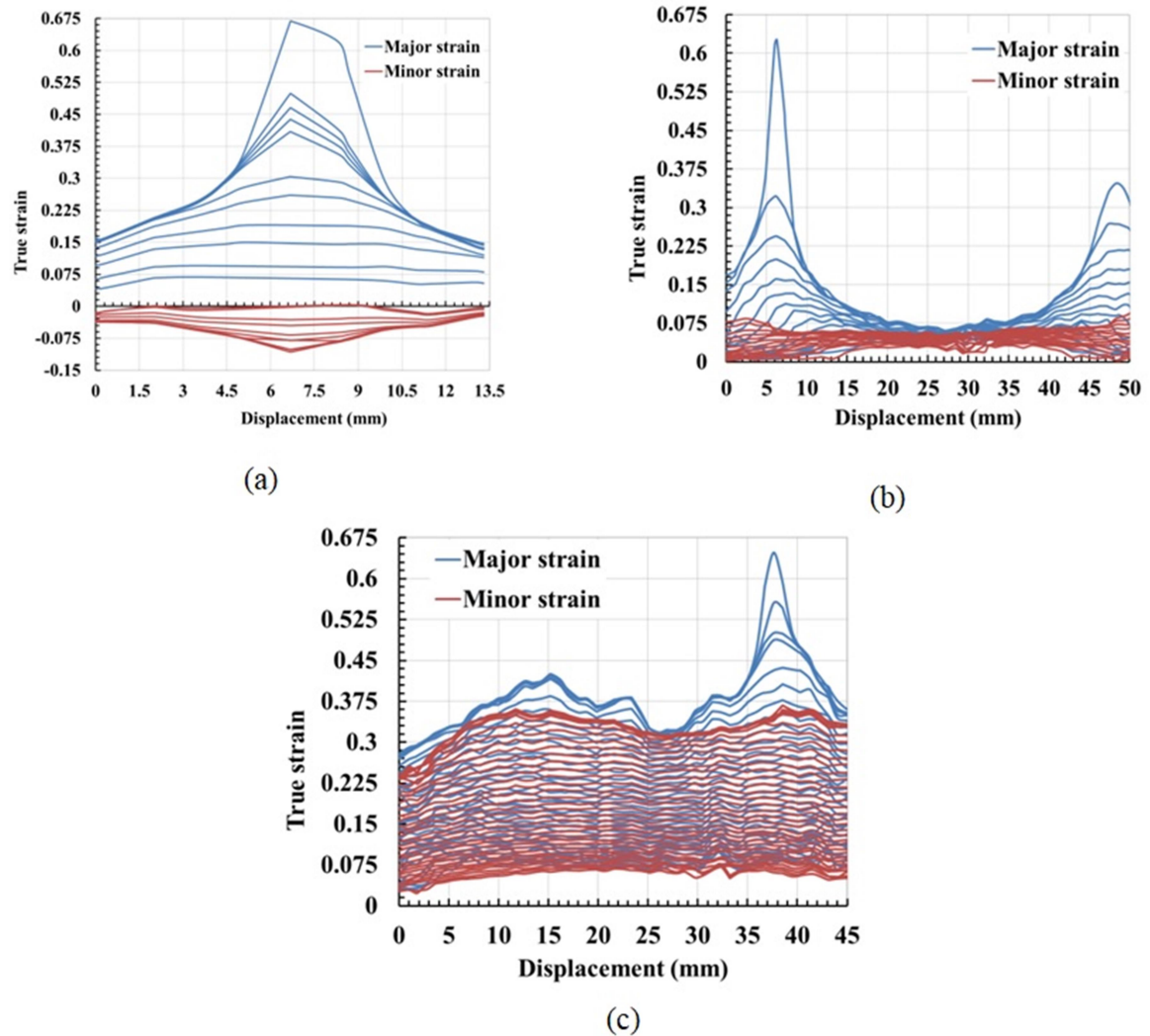


Figure 4.38 Major and minor strain distributions for AA7075-O dome specimens of different specimen width tested by using 101.6 mm diameter punch tooling at room temperature, (a) width 12.7 mm (UT), (b) width 127 mm (PST), and (c) width 177.8 mm (BBT).

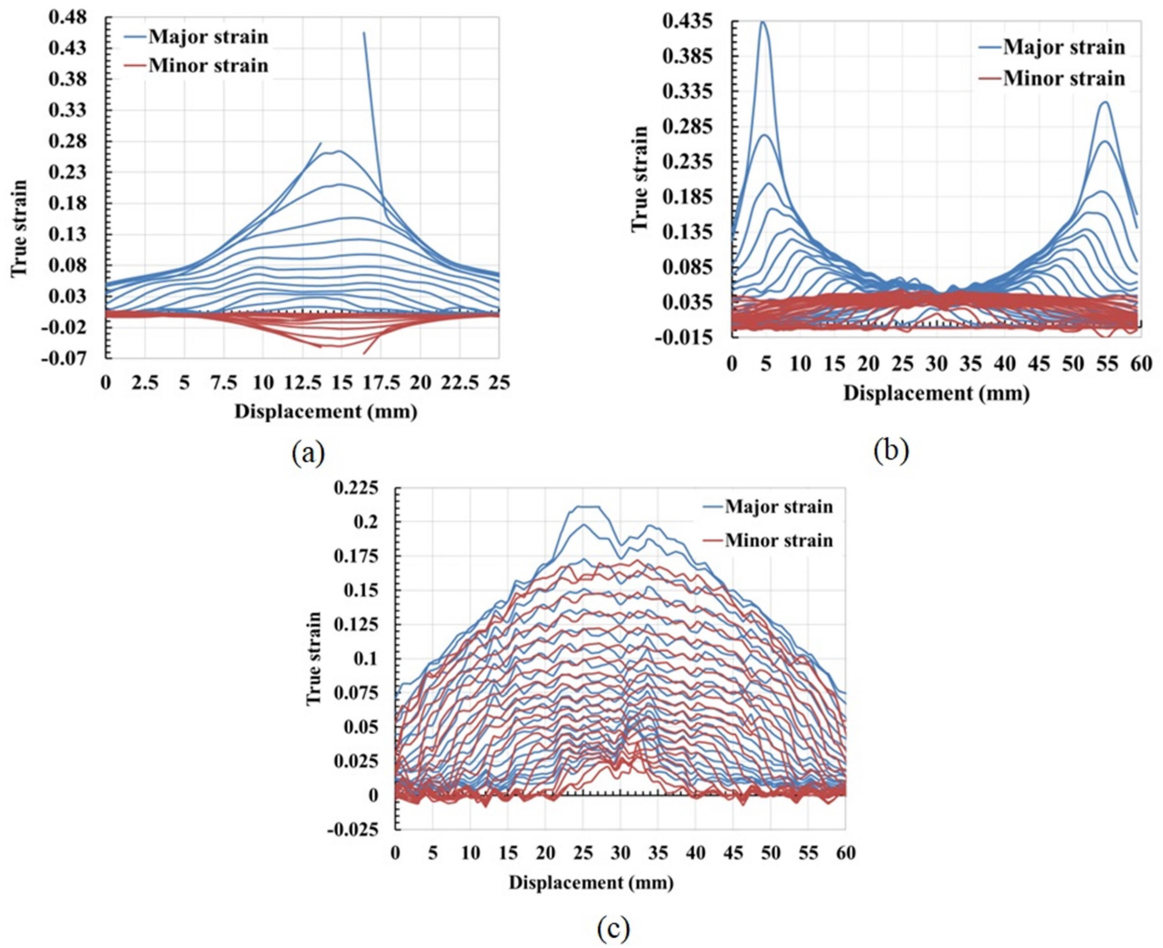


Figure 4.39 Major and minor strain distributions for AA7075-T6 dome specimens of different specimen width tested by using 101.6 mm diameter punch tooling at room temperature, (a) width 12.7 mm (UT), (b) width 127 mm (PST), and (c) width 177.8 mm (BBT).

The strain paths of the prominent localized neck point for each specimen geometry and temper state were extracted from major and minor strain history data for O and T6 temper dome test specimens. The results for UT, PST and BBT strain path are shown in the FLD co-ordinate space in Figure 4.40 and Figure 4.41 for the O and T6 tempers dome samples respectively. The strain paths are continuous but non-linear for the most part. The non-

linearity arises from both the hemispherical shape of the punch in contact with the sheet as well as the extent of punch-sheet sliding (i.e., friction at the punch-sheet contact surface). In fact, for the UT path geometry, the strain path starts off closer to the plane strain state but soon moves away from it and towards the tension-compression side as the dome height is increased (see the blue curve in Figure 4.40 and Figure 4.41). On the other hand, the intended plane strain specimen geometry did not quite result in a PST path but a strain path slightly towards tension – tension side in FLD space (red curve in Figure 4.40 and Figure 4.41). The vertical slope of this curve, after an initial transient, indicates that the specimen remained in the plane strain state for most of the deformation process until the onset of fracture. This result is consistent with the shift in the lowest limit strain point (i.e.,  $FLD_0$ ) to the tension-tension side as observed earlier for T6 temper specimens.

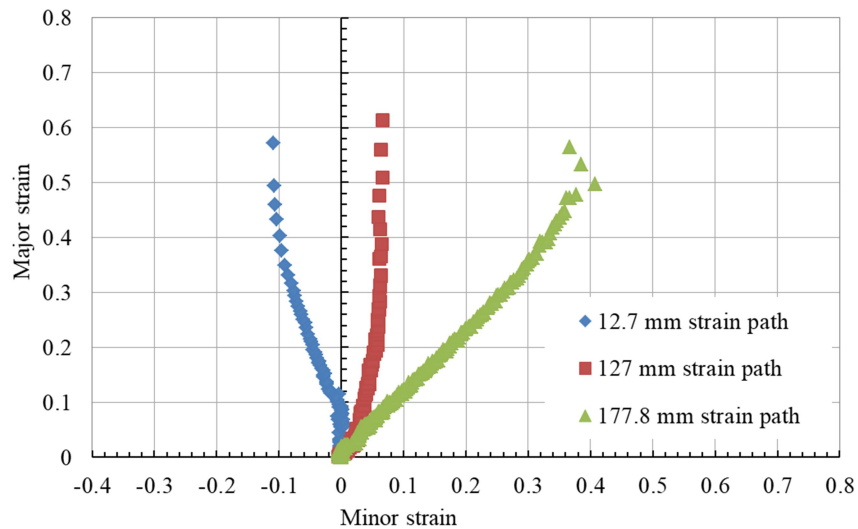


Figure 4.40 UT, PST and BBT path for dome specimens in the O-temper specimens tested by using 101.6 mm diameter punch tooling at room temperature.

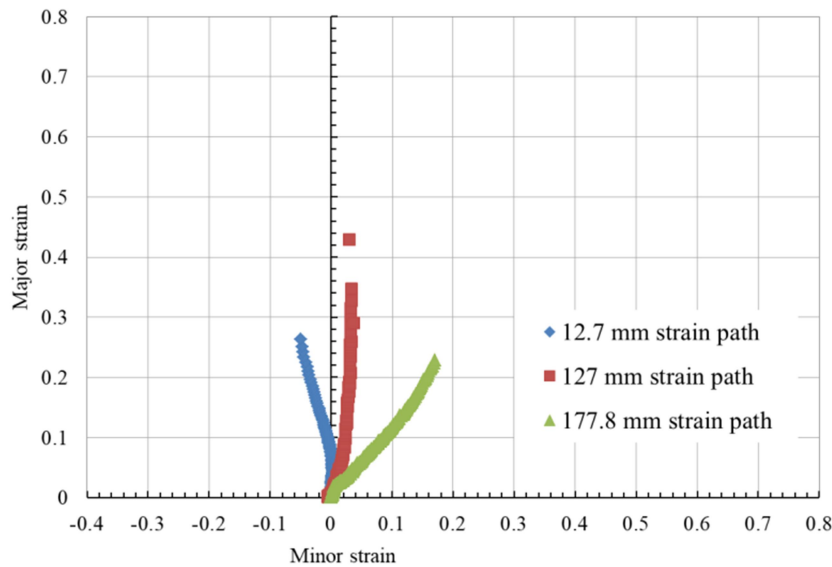


Figure 4.41 UT, PST and BBT path for dome specimens in the T6-temper specimens tested by using 101.6 mm diameter punch tooling at room temperature.

#### 4.3.5 Comparison of room temperature FLDs of O and T6 temper AA7075 sheets

FLCs at room temperature were also constructed from 101.6 mm diameter hemispherical punch stretching tests on O and T6 temper sheets using various specimen geometries and continuous strain field data from ARAMIS online strain measurement system. A time-dependent procedure for establishing the onset of localized necking based on continuous strain field data and its time derivative was followed as described earlier in the Experimental Methodology Chapter. Figure 4.42 shows two FLCs at room temperature for O and T6 temper sheets. The FLC for T6 temper is significantly lower than for the O temper sheet. This trend was more pronounced in terms of the FLC positions of the two tempers but consistent with the uniaxial tensile stress-strain curves and uniaxial tensile ductility at room temperature. The difference in forming limits is attributed to the



previously mentioned microstructural characteristics of the two tempers and their effect on material work hardening. The work hardening is higher for the O-temper sheet in uniaxial tension than for the T6 sheet probably due to Mg, Cu and Zn in solid solution leading to a softer matrix flow stress compared to the T6 sheet. In plane strain tension and biaxial tension, the forming limit depends mainly on the work hardening and on the degree of heterogeneity in the material. The latter is likely to be smaller for the O-temper sheet compared to the T6 sheet and thus lead to more uniform and higher limit strains. Also, the shapes of FLCs were quite different where the biaxial tensile side of FLC of O-temper sheet was more gradual whereas it was rather sharp for T6 temper sheet. This is attributed to increased damage in the T6 temper sheet under biaxial tensile loading conditions where more shear-like fracture and less ductile void growth was observed. As earlier at elevated temperature, the  $FLD_0$  is shifted towards the tension – tension side for the T6 temper state. These results are consistent with the data reported in the previous section on strain distributions and strain paths. Additionally, the lock-bead clamping procedure applied to T6 temper specimens, possibly resulted in increased biaxial tensile pre-straining of the specimen. Such pre-straining can also cause a shift in the  $FLD_0$  position to the biaxial tensile side. While all dome tests were conducted using the lock bead to fully clamp the specimens, as required in the Nakazima test, the tests on T6 specimens at room temperature especially required a deeper lock-bead as the clamping requirement was more severe due to its higher strength which resulted in considerably larger pre-strain in the test specimen prior to the dome test.

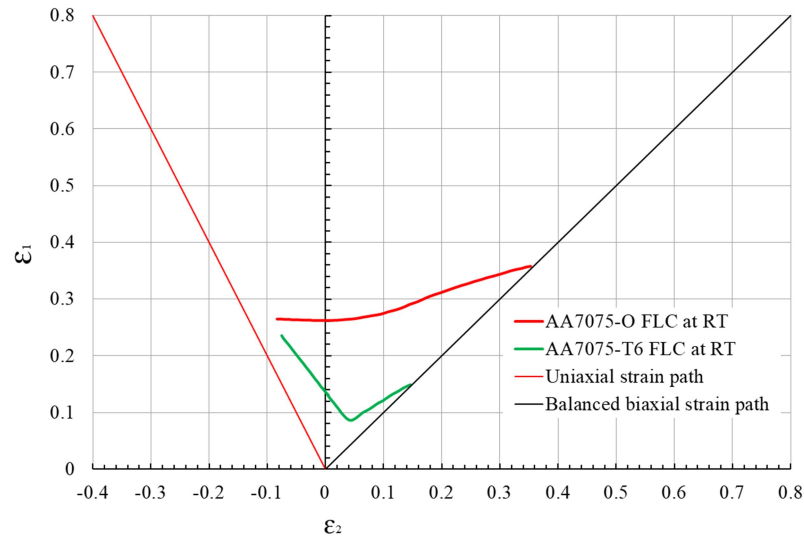


Figure 4.42 FLCs of AA7075-O and AA7075-T6 temper sheets at room temperature using 101.6 mm diameter hemispherical punch.

#### 4.3.6 Effect of punch radius on FLDs of O temper AA7075 sheet

Figure 4.43 shows a comparison between two FLCs for AA7075-O at room temperature using 50.8 mm and 101.6 mm punch diameter based HPS tool sets and strain measurement methods (post-test ARGUS and on-line ARAMIS respectively). It was observed that the FLC from the 50.8 mm diameter punch resulted in a higher FLC than the one obtained using the 101.6 mm diameter punch (assuming that the strain measurement methods did not affect the result). The results can be interpreted in terms of increased bending effect in the dome specimens from the smaller punch of 50.8 mm diameter compared to 101.6 mm punch. As reported in the literature (Charpentier, 1975; A. K. Ghosh & Hecker, 1974), a strain gradient results from punch curvature and friction. The limit strains increase as the punch curvature ( $1/R$ ) increases, where  $R$  is the punch radius. However, the bending effect on upward FLD shift is still relatively small, and of

the order of about 0.03 change in the plane strain limit for the two test-setups while the shape of the two curves remains largely unaffected.

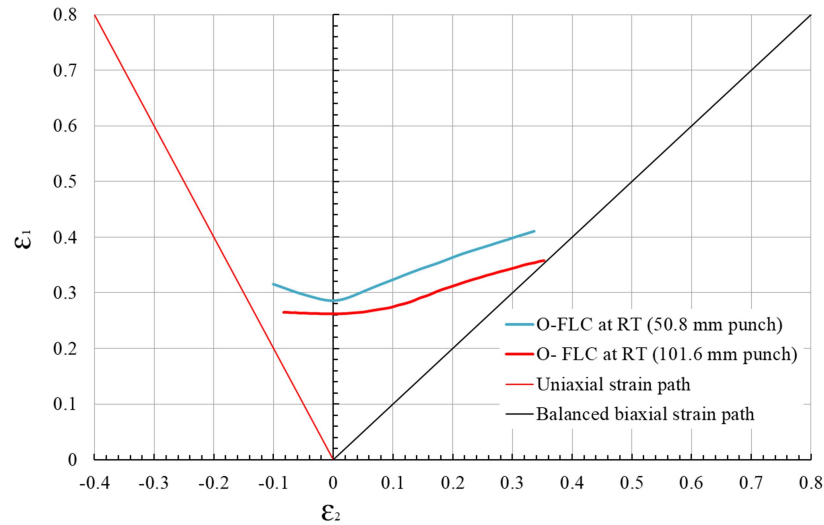


Figure 4.43 FLCs of AA7075-O sheet at room temperature from two different NAKAZIMA test tool set-ups.

## 4.4 Microstructure studies

### 4.4.1 Initial sheet surface roughness and its evolution

Surface roughness is considered as a useful characteristics of rolled sheet materials and a component of their surface texture. A mill-finish surface of a rolled sheet manifests itself as roll lines to the un-aided eye on a smooth sheet surface. However, this surface at higher magnifications exhibits peaks (asperities) and valleys transverse to the rolling direction. Also, the initial sheet surface roughness evolves with applied plastic strain and strain path during sheet forming as well as with microstructural parameters of the sheet such as grain size and crystallographic texture components (Becker, 1998). At large plastic strains, the increased surface roughness can lead to unstable contact between the punch and

deforming dome specimen resulting in non-uniform plastic flow and in some cases initiate localized necking and fracture of sheet materials in the predominant groove region of the sheet during deformation (Becker, 1998; Jain et al., 1996). In this sub-section, results related to initial surface roughness and its evolution in deformed in-plane uniaxial tensile test specimens as well as in out-of-plane (hemispherical dome) test specimens of AA7075-O and AA7075-T6 sheet materials are presented. As described earlier, the uniaxial in-plane and hemispherical dome specimens were deformed at room and elevated temperature. The latter specimens were also subjected to different strain paths corresponding to UT, PST and BBT. Details of the test equipment and surface roughness measurement procedure were provided earlier in the Experimental Methodology Chapter.

#### **4.4.1.1 Surface roughness evolution in uniaxial tension test samples**

Table 4.9 summarizes the surface roughness values of undeformed and deformed O and T6 temper sheets under different test conditions. All surface roughness values were measured in areas located at a distance of 5 mm away from fracture zone to avoid any influence of damage which could affect the surface roughness measurements. Also, all surface areas imaged in uniaxial tension samples were of the same size.

Table 4.9 Average surface roughness  $R_a$  and average area surface roughness  $S_a$  for un-deformed and uniaxially deformed (5 mm from fracture) AA7075-O and AA7075-T6 sheet materials.

Temper	Deformation State	Temperature (°C)	Test Speed (mm/min)	$R_a$ (μm)	$S_a$ (μm)
F	Un-deformed	RT	-	0.319	0.389
O		RT		0.358	0.394
T6		RT		0.247	0.329
O	deformed	RT	1	0.606	0.768
		180		1.106	1.612
		220		1.807	1.708
		260		1.026	1.507
		RT	10	0.539	0.752
		180		1.155	1.252
		220		1.796	1.682
		260		1.439	1.822
		RT	1	0.655	0.814
		180		0.806	1.114
T6	deformed	220		0.457	0.562
		260		0.578	0.789
		RT	10	0.632	0.842
		180		0.823	0.87
		220		0.721	1.095
		260		0.876	0.982

For T6 temper, the roughness for un-deformed sample is slightly lower than the other two tempers (F and O) possibly due to a long holding time of three hours at solutionizing temperature of  $480^{\circ}\text{C} \pm 5^{\circ}\text{C}$  and perhaps from local melting of the high peaks. Also, the average surface roughness values increased with increase in temperature as well as with applied strain. There was about 2 to 5 fold increase in O-temper surface roughness at room and elevated temperature deformations respectively. However, the effects of temperature and strain may be interrelated in that the higher temperature tests led to high strains to fracture. In contrast, the effect of test speeds (or strain rate) on surface

roughness evolution appears to be relatively minor. Figure 4.44 shows two-dimensional surface roughness maps of un-deformed F, O and T6 temper sheets. Similar data for samples deformed in uniaxial tension are shown in Figure 4.45 (a-d). The linear pattern of roll lines in the un-deformed condition is clearly transformed by plastic straining to a superimposed patchy morphology of dome and crater-like features arising from grain re-orientation and their emergence on the surface of the sheet as shown in Figure 4.45. Similar results for the deformed uniaxial tensile specimen surfaces at two temperatures (RT and 220°C) and two tempers (O and T6) are shown in Figure 4.45 (a-d). The surface roughness evolution at elevated temperature was significantly larger for the O-temper sheet compared to the T6 temper sheet. One possible explanation is the presence of second phase particles on the grain boundaries of T6 sheet which suppress the grain boundary sliding (GBS) during the deformation process. Sliding occurs only in the particle free area of the grain boundary and does not penetrate through the particles (Suzuki et al., 1985).

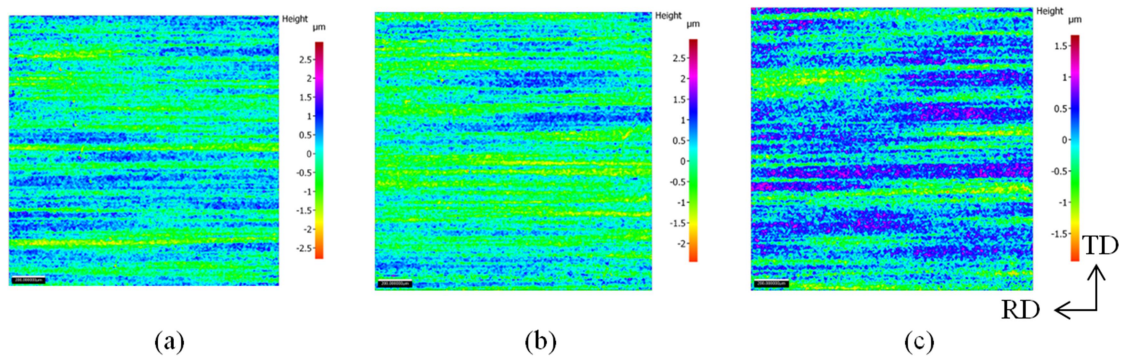


Figure 4.44 2D surface roughness maps (NP plane) of un-deformed sample in the; (a) as-fabricated (F), (b) fully- annealed (O) and (c) peak-aged (T6) temper conditions. The scanned sample surface area is 1.6 mm x 1.6 mm.

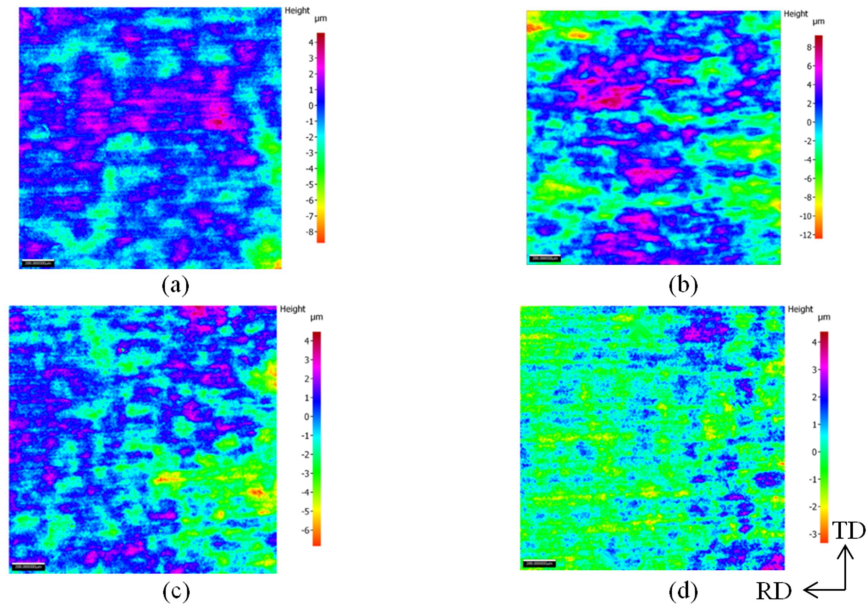


Figure 4.45 2D surface roughness maps (NP plane) of deformed samples under the following tempers and test conditions; (a) O-temper tested with test speed of 1 mm/min at room temperature, (b) O-temper tested with test speed of 1 mm/min at 220°C, (c) T6-temper tested with test speed of 1 mm/min at room temperature, and (d) T6-temper tested with test speed of 1 mm/min at 220°C.

#### 4.4.1.2 Surface roughness evolution in forming limit (dome) test samples

As noted earlier in sub-section 4.3, two different punch diameters were utilized in the dome tests. Consequently, the contribution of the bending component to the surface strain as well as the surface roughness evolution on the dome surface was expected to be larger for the smaller punch diameter of 50 mm. Figure 4.46 to Figure 4.49 show three-dimensional surface roughness maps of deformed O and T6 temper dome samples for different punch diameter dome tests at room temperature and 220°C. The line and area surface roughness values ( $R_a$  and  $S_a$ ) for the 3 different strain paths, various temperatures and two tempers are also summarized in Table 4.10. In general, the surface roughness values are larger in the neck region compared to the values at the pole except for the BBT

samples where the two locations, pole and neck, were quite close to each other due to very low friction value at the sheet/punch contact surface. Also, in general, surface roughness values obtained for dome samples deformed by using 50.8 mm punch were indeed higher than those deformed by 101.6 mm punch possibly due to increased bending strains for the smaller diameter punch and possibly more grain rotations. Further, surface roughness in the neck region were generally higher in the RD direction compared to the TD direction for both tempers (O and T6) as well as at all temperatures, and this was consistent with the TD orientation of fracture line on the dome sample surface, for UT and PST strain paths as shown in Figure 4.50. The BBT strain path, on the other hand, did not show any clear trend in terms of surface roughness anisotropy.

Surface roughness values based on more reliable pole data, in general, is less for PST paths compared to the UT and BBT strain paths for both sheet tempers and at RT and 220°C. This could be explained in terms of reduced effective strain value under PST strain path compared to the UT and BBT strain paths. For the O-temper sheet, the surface roughness values are larger compared to the T6 sheet at RT and 220°C deformation conditions. This could be explained in terms of reduced grain boundary sliding (and hence lower roughness) due to the presence of second phase particles at the grain boundaries in the T6 sheet, as I have explained earlier when discussing the surface roughness evolution of uniaxial tensile test samples. Second reason is simply that the applied strains are lower in the T6 dome samples compared to the O temper dome samples, so, the surface roughness, being proportional to the applied strain, will also be lower for the T6 dome samples. The third reason is that the grain size of the O-temper



sheet is larger than the T6 sheet, and this should also lead to larger surface roughness of the O-temper sheet compared to the T6 temper sheet.

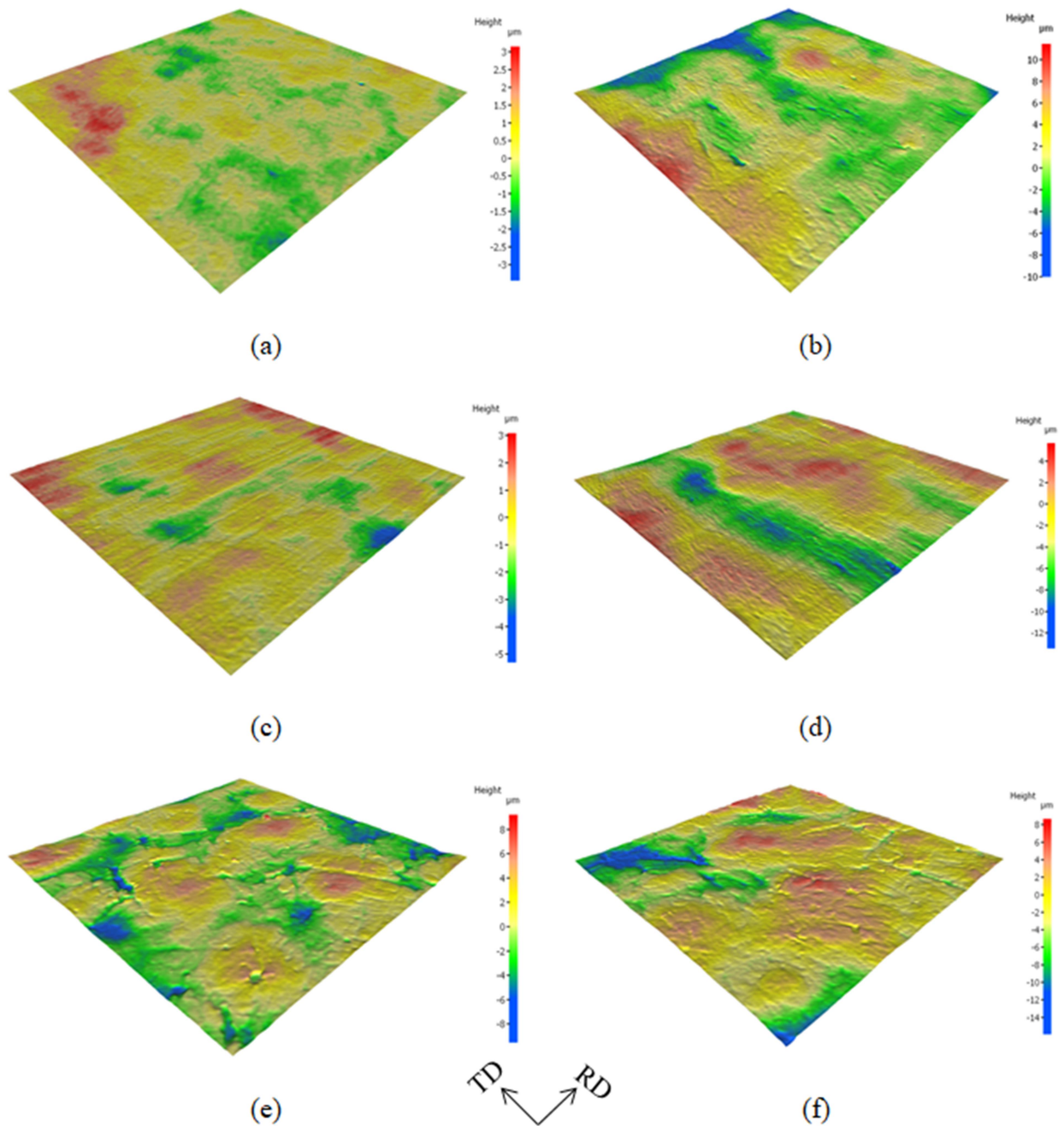


Figure 4.46 3D surface roughness maps of deformed O-temper samples obtained using 50.8 mm punch at room temperature corresponding to; (a) UT at the pole and (b) UT in the neck region, (c) PST at the pole, (d) PST in the neck region, (e) BBT at the pole, and (f) BBT in the neck region.

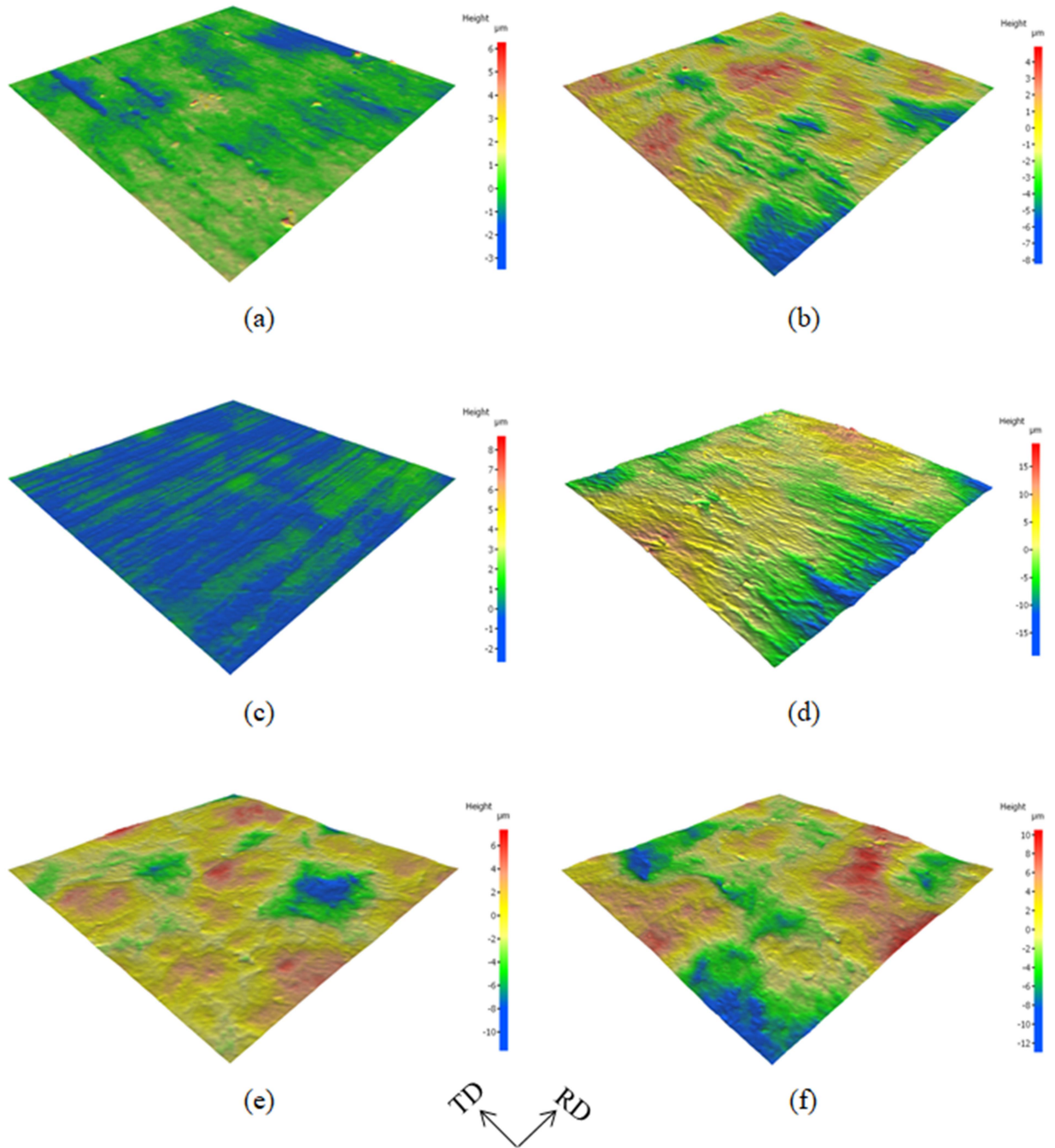


Figure 4.47 3D surface roughness maps of deformed O-temper samples obtained using 50.8 mm punch at 220°C corresponding to; (a) UT at the pole and (b) UT in the neck region, (c) PST at the pole, (d) PST in the neck region, (e) BBT at the pole, and (f) BBT in the neck region.

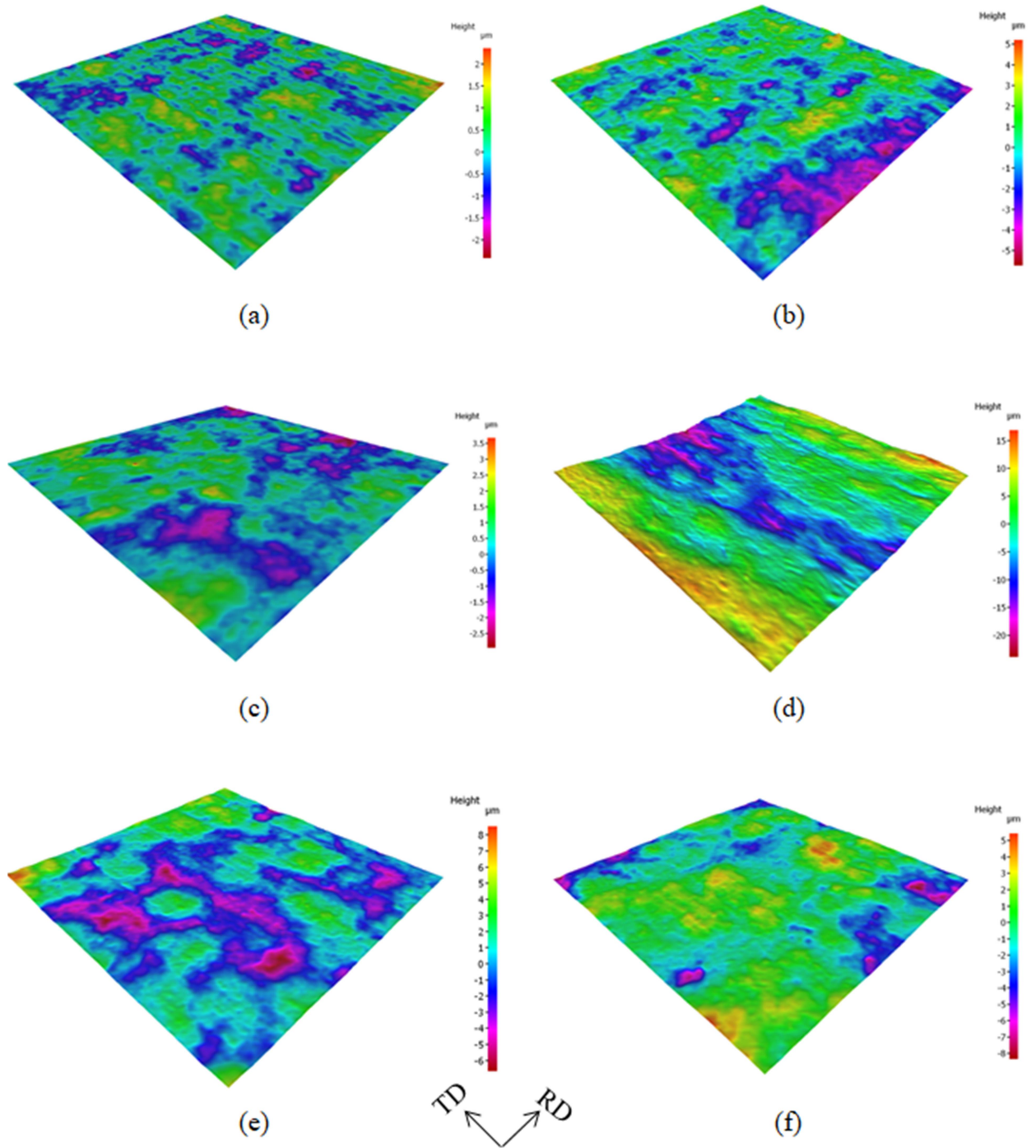


Figure 4.48 3D surface roughness maps of deformed T6-temper samples obtained using 101.6 mm punch at room temperature corresponding to; (a) UT at the pole and (b) UT in the neck region, (c) PST at the pole, (d) PST in the neck region, (e) BBT at the pole, and (f) BBT in the neck region.



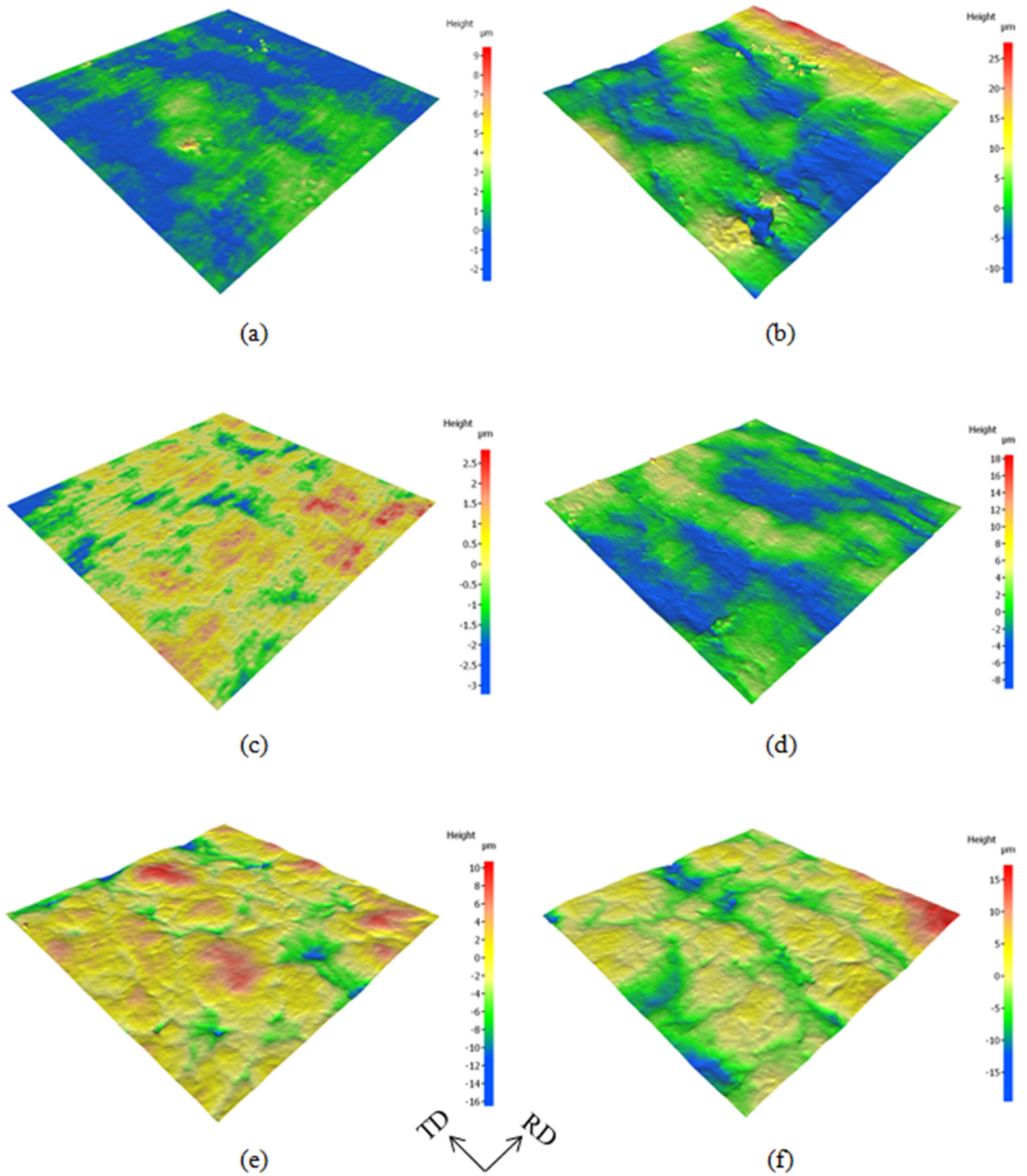


Figure 4.49 3D surface roughness maps of deformed T6-temper samples obtained using 50.8 mm punch at 220°C corresponding to; (a) UT at the pole and (b) UT in the neck region, (c) PST at the pole, (d) PST in the neck region, (e) BBT at the pole, and (f) BBT in the neck region.

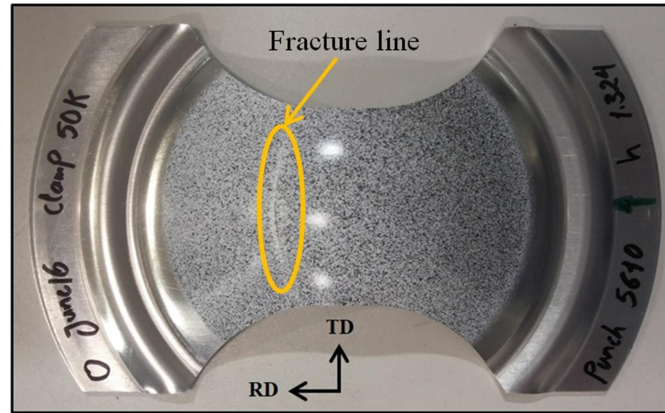


Figure 4.50 A photograph of fractured UT sample of AA7075-O formed by using 101.6 mm diameter hemispherical punch tooling at room temperature.

Table 4.10 Surface roughness measurements for AA7075 dome samples.

Temper	Temperature (°C)	Strain path	Measurement at the pole			Measurement in the neck		
			R <sub>a</sub> (μm) (RD)	R <sub>a</sub> (μm) (TD)	S <sub>a</sub> (μm)	R <sub>a</sub> (μm) (RD)	R <sub>a</sub> (μm) (TD)	S <sub>a</sub> (μm)
O	RT (50.8 mm punch)	UT	0.287	0.33	0.409	1.43	0.868	1.376
		PST	0.474	0.629	0.598	1.715	1.013	1.877
		BBT	1.346	1.712	1.766	2.079	1.597	2.118
	RT (101.6 mm punch)	UT	0.387	0.417	0.513	1.029	0.907	1.177
		PST	0.371	0.413	0.484	2.572	1.014	1.8
		BBT	1.383	1.752	1.557	3.681	2.857	2.619
	180	UT	0.483	0.462	0.618	1.156	0.697	1.283
		PST	0.51	0.544	0.562	1.574	1.165	1.874
		BBT	0.707	1.506	1.712	2.267	2.064	2.199
	220	UT	0.522	0.278	0.474	0.871	0.814	1.157
		PST	0.353	0.432	0.463	2.177	1.378	1.962
		BBT	1.468	1.701	1.643	1.484	1.468	1.921
	260	UT	0.479	0.407	0.515	1.768	1.329	1.402
		PST	0.277	0.496	0.458	2.777	2.088	2.621
		BBT	1.748	1.042	1.922	1.821	2.182	2.061
T6	RT (101.6 mm punch)	UT	0.316	0.289	0.451	0.925	0.74	0.933
		PST	0.45	0.487	0.529	2.526	1.324	2.508
		BBT	1.018	0.25	1.383	0.676	1.108	1.089
	220	UT	0.696	0.386	0.587	2.139	2.123	2.501
		PST	0.563	0.509	0.588	1.826	1.089	1.608
		BBT	1.881	1.883	2.303	1.829	2.422	2.689

#### 4.4.2 Necking and fracture characteristics of uniaxial tensile test samples

As mentioned earlier in the Experimental Methodology chapter, the fractured uniaxial tensile test samples from the necked region were cut perpendicular to the neck length, in the rolling direction, and mating surfaces were mounted in a metallurgical mount to microscopically observe the LT cross-sections of the necked or fractured specimens. Samples in both O and T6 temper conditions were observed at room and elevated temperatures and two test speeds. Figure 4.51 shows a typical through-thickness section of a fractured specimen tested at room temperature at a speed of 1 mm/min. Table 4.11 presents a summary of AA7075-O sheet sample thickness values at fracture and thickness reduction under different test conditions. As shown, there is a steady increase in the thickness strain at fracture as the test temperature is increased from room temperature to 260°C. This result is consistent with the earlier forming limit strain values for the uniaxial strain path in the FLC curves (see Figure 4.34).

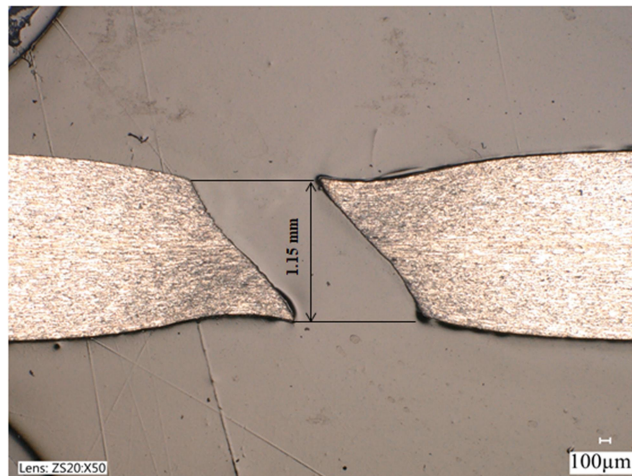


Figure 4.51 Through-thickness section from LT plane of etched AA7075-O uniaxial tension test sample tested at a speed of 1 mm/min at room temperature.

Table 4.11 Fracture thickness and thickness strain at fracture for 2 mm thick AA7075-O tensile test specimens.

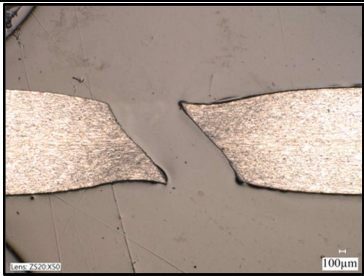
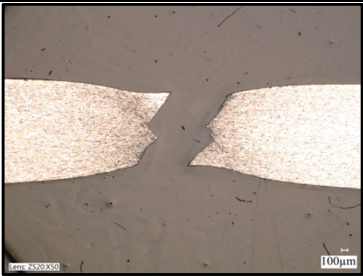
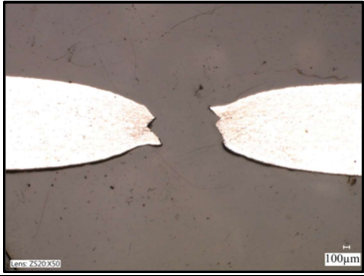
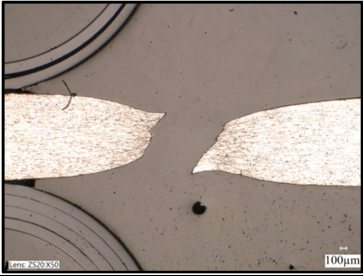
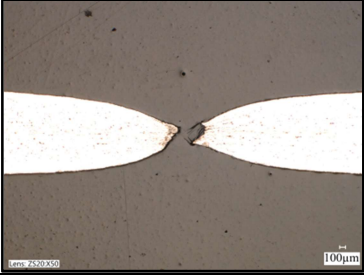
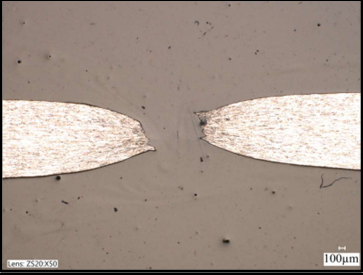
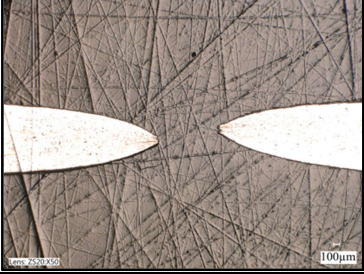
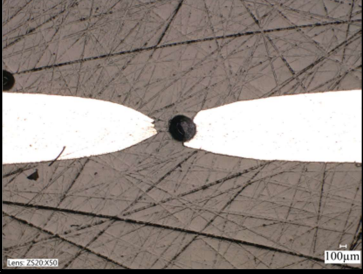
Temper	Temperature (°C)	Test Speed (mm/min)	Fracture Thickness (mm)	Thickness Strain
O	Room temperature	1	1.15	-0.425
		10	1	-0.5
	180	1	0.625	-0.687
		10	0.75	-0.625
	220	1	0.325	-0.837
		10	0.4	-0.8
	260	1	0.125	-0.937
		10	0.2	-0.9

Table 4.12 presents a set of OM images of neck and fracture profiles of O temper tensile samples from the LT plane corresponding to different temperatures and test speeds. The necking and fracture characteristics were rather similar at the slow and faster test speeds but the extent of necking prior to fracture was typically lower at the higher speed of 10 mm/min. It is well known that strain rate hardening ( $m$ ) controls post-uniform elongation during deformation and affect the sheet metal resistance to necking (Mahmudi, 1997). At relatively higher test speeds (or strain rates) the strain rate sensitivity is decreased and then the tensile test sample resistance to thinning (or necking) is also decreases resulting in early onset of localized necking and a decreased thickness reduction prior to fracture. In contrast, at low test speed (strain rate), the strain rate sensitivity is higher for many higher strength aluminum alloys, which leads to increased resistance to localized necking (or to more diffuse necking) which results in a larger reduction of sample thickness at fracture. Also, the extent of necking was larger as the temperatures increased from RT to 260°C (See Table 4.11, Table 4.12, and Figure 4.53). This thinning behaviour was due to



increased temperature dependent ductility at elevated temperatures from thermally activated dislocation slip activity on multiple slip planes. Further, the nature of fracture changed from through-thickness shear fracture at room temperature where fracture plane was inclined from the sheet normal by about  $45^\circ$  to a cup-and-cone type fracture at elevated temperatures. At room temperature, the fractures typically occurred along one of the two intersecting through-thickness shear planes. In some cases, the through-thickness crack changed direction from one to the other shear plane typically at the mid-thickness location, especially at lower temperatures, for example, see Table 4.12,  $180^\circ\text{C}$ , 1 mm/minute sample.

Table 4.12 Through-thickness OM images of fractured AA7075-O tensile test specimens tested under different test conditions.

Temper	Temperature (°C)	Test Speed (mm/min)	
		1	10
O	RT		
	180		
	220		
	260		

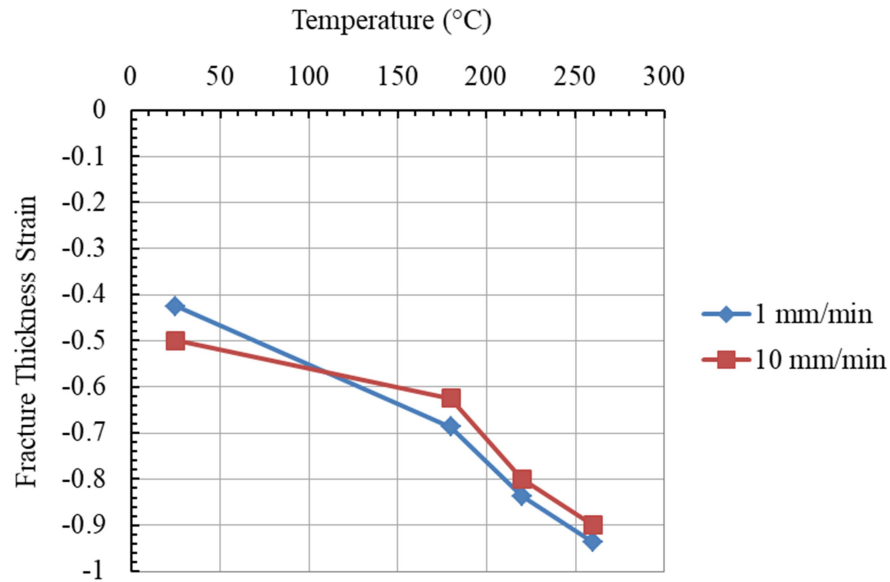


Figure 4.52 Uniaxial tensile test fracture thickness strain versus test temperature for O-temper sheet.

The grains in the LT plane were considerably elongated in the principal stress (i.e., loading) direction, and especially in the neck region, prior to fracture (see Figure 4.53). In general, the fracture mode in AA7xxx series aluminum alloys is ductile fracture (or dimple rupture) in which voids nucleation, growth and coalescence occur with increasing strain prior to failure (Broek, 1973). Voids were observed in the vicinity of the fracture in the polished LT sections as well as on fracture surfaces when observed via SEM. Fractographic data from SEM is presented and discussed later in sub-section 4.4.4.

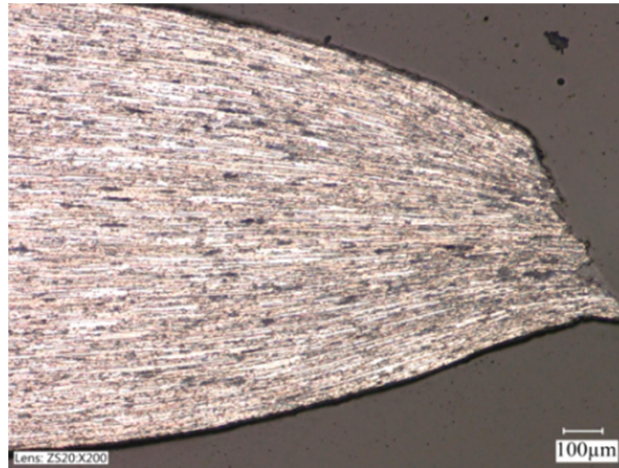


Figure 4.53 Optical micrograph of through-thickness section of an etched AA7075-O uniaxial tensile sample tested at 10 mm/min and 220°C showing highly elongated grains.

Uniaxial tensile test results for T6 temper sheet are presented in Table 4.13 and Table 4.14 and Figure 4.54 and Figure 4.55. Results in Table 4.13 and Figure 4.55 show that as the test speed increased the sheet thickness at fracture is also increased, i.e., the fractional reduction in thickness decreased. In other words, the amount of necking prior to fracture is decreased with an increase in test speed. This trend is similar to the earlier O-temper sheet.

Also, similar to the O-temper sheet, the nature of fracture in T6 sheets changed from through-thickness shear at room temperature to cup and cone type of fracture at 260°C. There appears to be very little evidence of sheet necking prior to fracture for sample tested at room temperature (see Table 4.14, top row). At intermediate temperatures of 180°C and 220°C, the through-thickness shear failure is similar to the room temperature tensile tests but there is localized necking prior to fracture. The fractured and etched T6 tensile test sample tested at 10 mm/min and 220°C reveals elongated grains in the neck

region, intergranular failure and presence of voids in the vicinity of fractured edge, similar to the case of O-temper fractured specimen (compare Figure 4.53 and Figure 4.55). However, the fractured edge appear to be distinctly more jagged in the T6 temper compared to the O temper perhaps due to increased precipitation at the grain boundaries in the T6 sheet and a through-thickness fracture path through the grain boundaries.

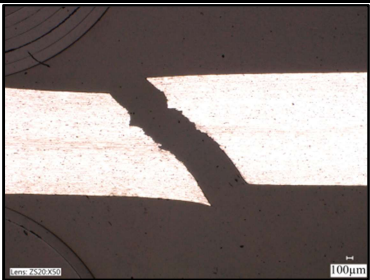

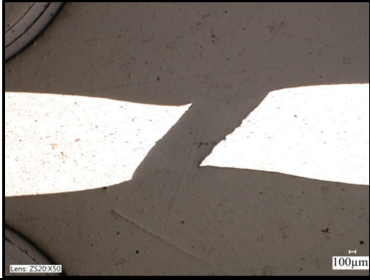

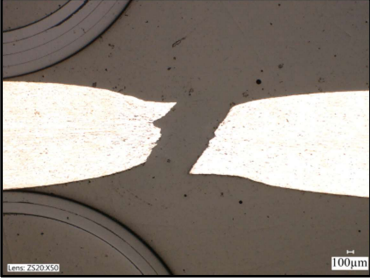
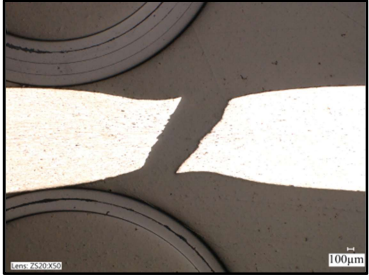
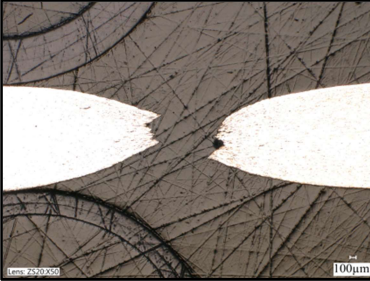
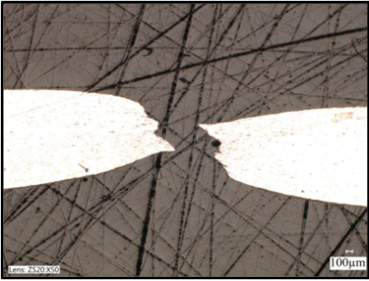
Table 4.13 AA7075-T6 uniaxial test specimen thickness at fracture and thickness strain at fracture from under different test conditions.

Temper	Temperature (°C)	Test Speed (mm/min)	Fracture Thickness (mm)	Thickness Strain
T6	Room temperature	1	1.375	-0.312
		10	1.375	-0.312
	180	1	1	-0.5
		10	1.075	-0.462
	220	1	0.85	-0.575
		10	1	-0.5
	260	1	0.375	-0.812
		10	0.625	-0.687

The earlier onset of necking in the T6 temper is due to the extensive presence of secondary phase particles (or hardening precipitates) from the precipitation hardening process which affect both the strain localization and ductile void damage processes. These will be discussed in more detail once the quantitative fractographic results from the fractured specimens have been compared for O and T6 temper test specimens. Lastly, the extent of necking in O-temper specimens is considerably larger compared to the T6 sheet. This pronounced necking in O-temper samples is due to its microstructure of large grain size, low dislocation density and absence of hardening precipitates as a result of fully annealed heat treatment which increase sheet metal uniaxial tensile ductility and general

formability. The results are consistent with the earlier forming limit data for the two tempers in Section 4.3 (also see Figure 4.36 and Figure 4.42).

Table 4.14 OM images of through-thickness fractured AA7075-T6 tensile test specimens tested under different test conditions.

Temper	Temperature (°C)	Test Speed (mm/min)	
		1	10
T6	RT		
	180		
	220		
	260		



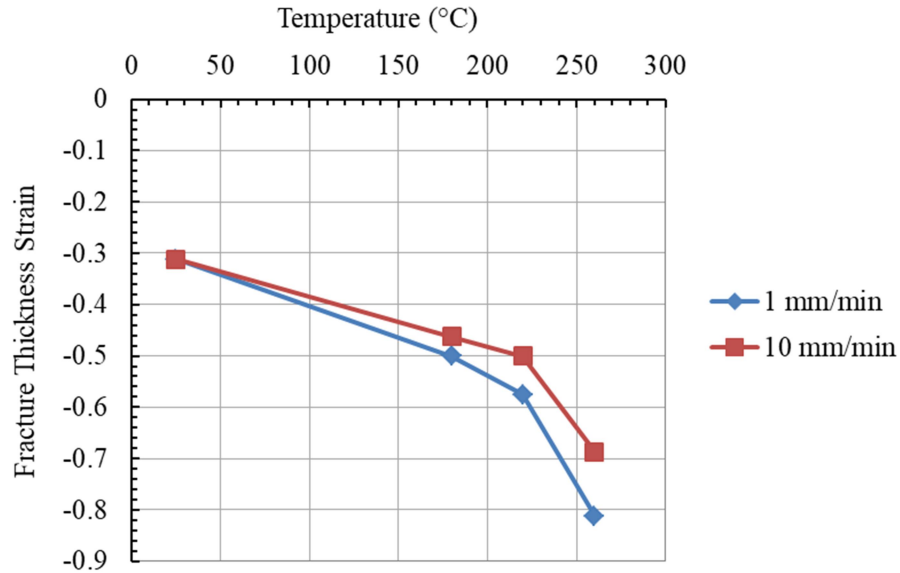


Figure 4.54 Uniaxial tensile test fracture thickness strain versus test temperature for T6 temper sheet.

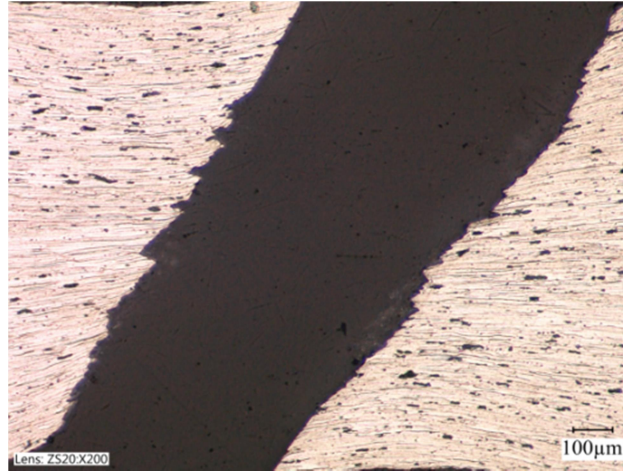


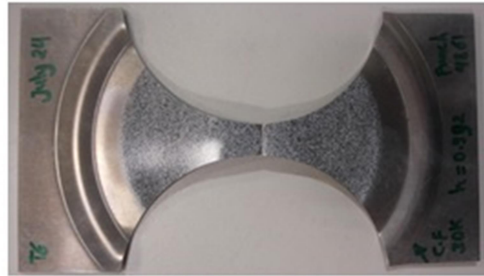
Figure 4.55 A close-up view of through-thickness fractured region of etched T6 temper tensile test specimen tested at 10 mm/min and 220°C showing intergranular fracture.

#### 4.4.3 Necking and microstructural characteristics of dome test samples

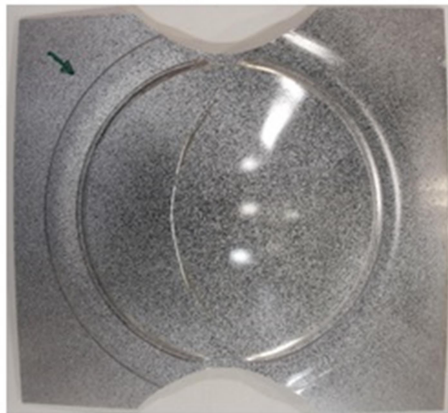
Necking and microstructural characteristics of O temper and T6 temper dome specimens tested at room temperature and 220°C were also examined from LT plane (and

perpendicular to the neck direction) for different strain paths. Figure 4.57 shows through-thickness SEM micrographs for O and T6 temper polished specimens. Similar results from polished and etched specimens observed with OM are presented in Figure 4.58. It is to be noted that the tests were stopped at the onset of necking, and the necking process had just initiated in many of the specimens so it is difficult to compare the neck characteristics of dome specimens with the fracture characteristics of the uniaxial tensile test specimens presented earlier. However, it is clear that O-temper dome samples exhibited local curvature development and necking for all strain paths and at RT and 220°C test temperatures (see Figure 4.57 (a-f)). Localized necking initiated from both upper and lower sample surfaces (the latter surface was in contact with the punch) and grains were elongated in the neck region, especially along the through-thickness shear region (see Figure 4.58 (a, d)). The shear fracture propagated along the macro-shear band through the thickness leading to final failure. T6 temper dome specimens, on the other hand, exhibited no visual necking at room temperature for all strain paths (see Figure 4.56) and necking only for the UT at 220°C (see Figure 4.58 (g)). For the T6 PST and the BBT at 220°C, it was not possible to visually detect any necking and stop the test (see Figure 4.57 (g-i) and Figure 4.58 (g-i)). In other words, all T6 temper dome tests under PST and BBT loading conditions led to a catastrophic fracture of the dome. The results of the UT out-of-plane dome tests are consistent with the in-plane uniaxial test results presented earlier. However, the increased biaxiality of the PST and BBT seemed to promote extensive damage development that likely preceded the onset of localized necking.





(a)



(d)



(c)

Figure 4.56 AA7075-T6 fractured dome samples deformed by 101.6 mm diameter punch tooling set at room temperature; (a) UT, (b) PST, and (c) BBT.

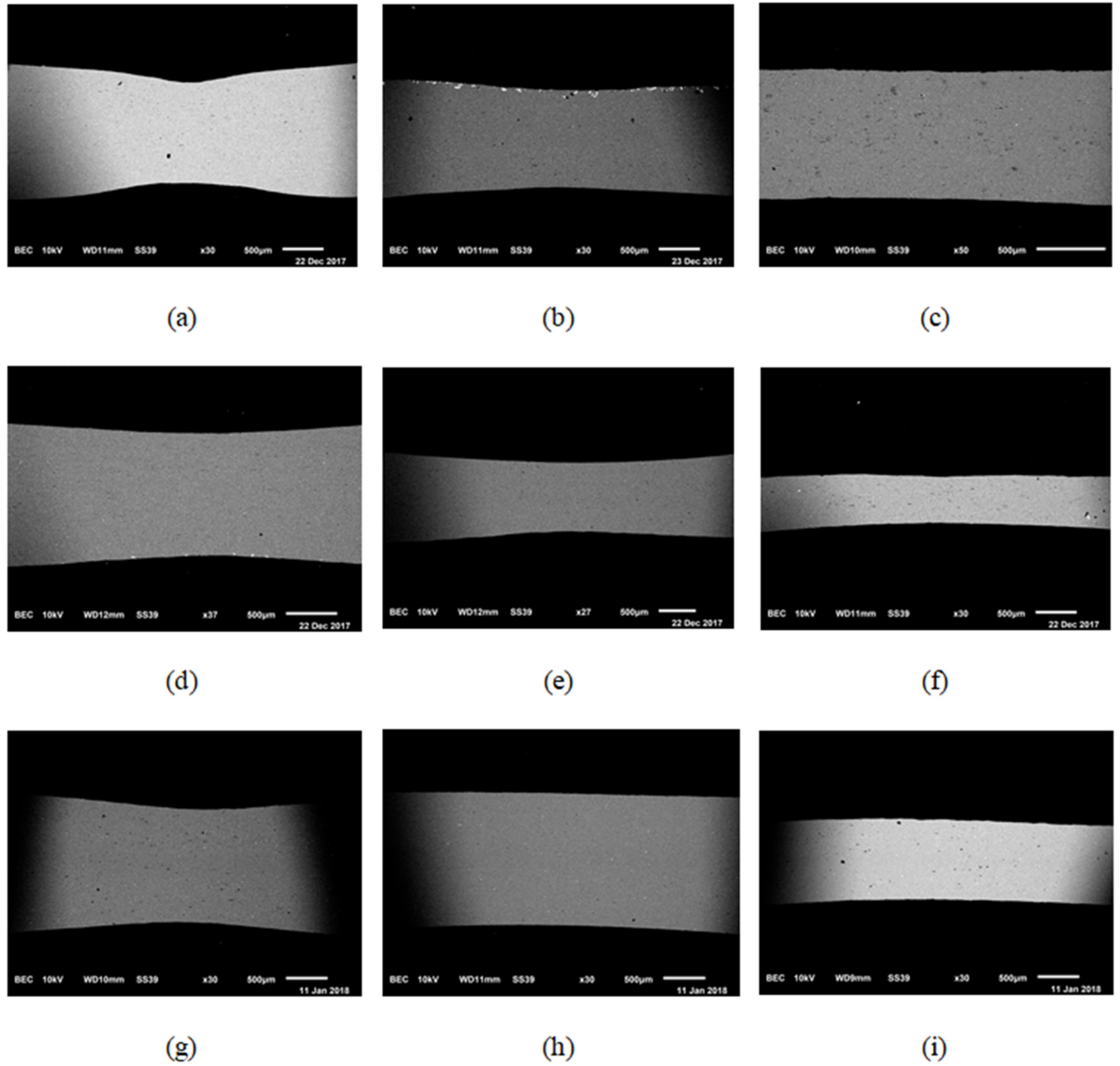


Figure 4.57 Low magnification SEM images of the necked region (LT plane) of dome test samples from various test conditions; (a-c) O-temper UT, PST and BBT specimens tested at RT with thickness strain of -0.425, -0.45 and -0.55 respectively, (d-f) O-temper UT, PST and BBT specimens tested at 220°C with thickness strain of -0.415, -0.555 and -0.725 respectively, and (g-i) T6-temper UT, PST and BBT specimens tested at 220°C with thickness strain of -0.35, -0.25 and -0.525 respectively.

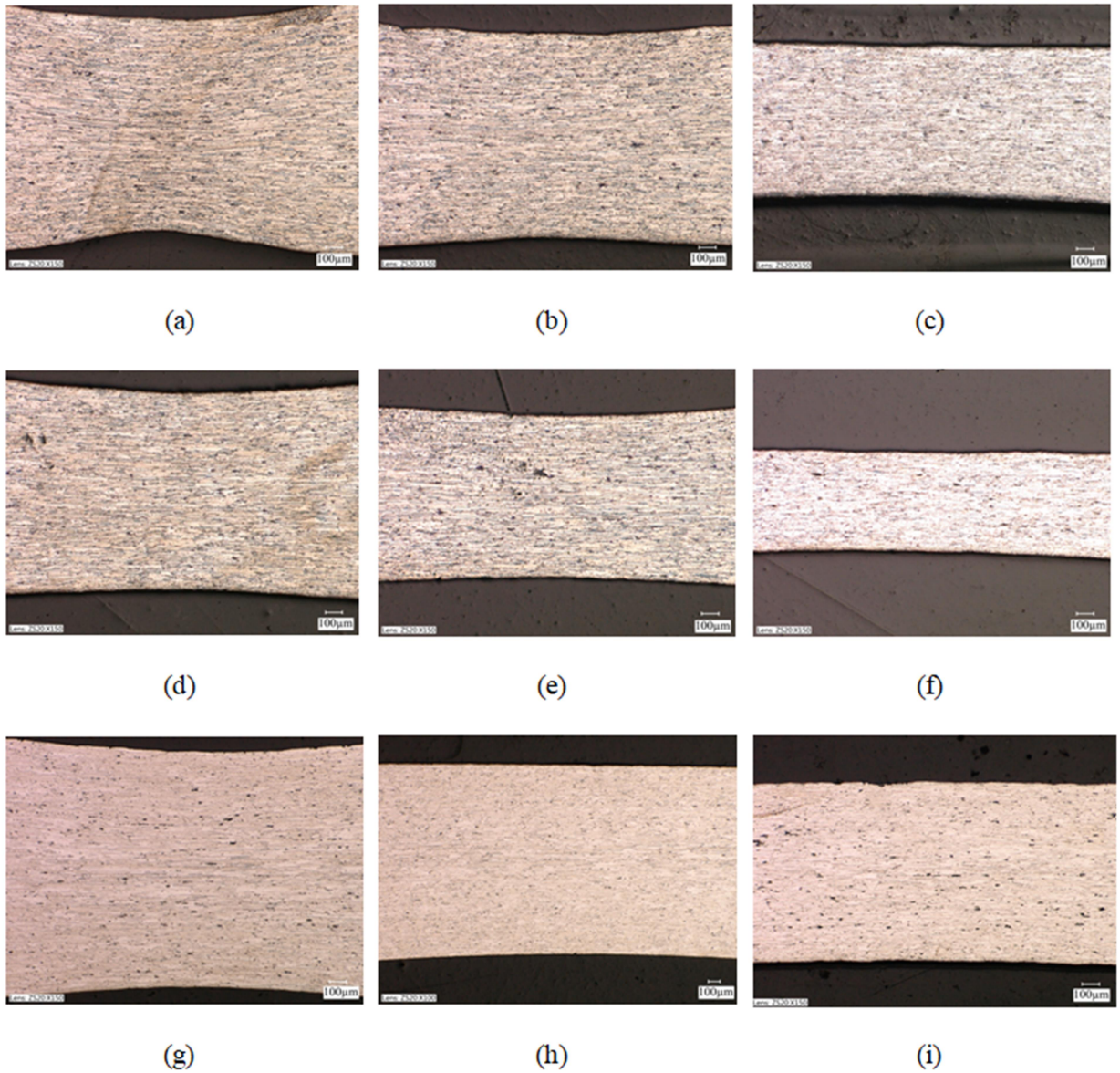


Figure 4.58 Low magnification OM images of the necked region of dome test samples (LT plane) from various test conditions; (a-c) O-temper UT, PST and BBT specimens tested at RT with thickness strain of -0.425, -0.45 and -0.55 respectively, (d-f) O-temper UT, PST and BBT specimens tested at 220°C with thickness strain of -0.415, -0.555 and -0.725 respectively, and (g-i) T6-temper UT, PST and BBT specimens tested at 220°C with thickness strain of -0.35, -0.25 and -0.525 respectively.

Statistical void and precipitate area data was obtained by carrying out a large number of SEM-based field measurements from the polished LT plane of deformed O and T6 temper dome specimens subjected to UT, PST and BBT strain paths. These results for voids and precipitates area data are shown in Figure 4.59 and Figure 4.60 respectively where each field number (or 'FldNo') on the x-axis represents an SEM image with magnification of  $2000\times$ . The images were taken from the neck region of the specimen. Table 4.15 presents a summary of this data for O and T6 sheet temper necked dome samples. The data for O temper sheet shows a higher average void area in PST compared to the UT and BBT at both room temperature and  $220^{\circ}\text{C}$  test condition. These results may be explained as higher elongation of voids in LT direction (or major strain direction) for PST sample than UT and BBT strain paths due to its geometry with almost zero minor strain ( $\epsilon_2$ ) in ST direction as shown in Figure 4.61. For T6 temper, the higher void area was found in UT at  $220^{\circ}\text{C}$  prehab due to increased elongation of voids in LT plane. Also, thickness reduction for UT sample ( $\epsilon_t = -0.324$ ) is higher than that of PST sample ( $\epsilon_t = -0.214$ ) which means more elongation in LT direction (volume constancy) leading to void elongation in LT plane as shown in Figure 4.62. It is known that void growth is controlled by two main factors of stress triaxiality and plastic strain as discribed analytically for perfect plastic material contains a spherical void (Rice & Tracey, 1969) or cylindrical void (McClintock, 1968).

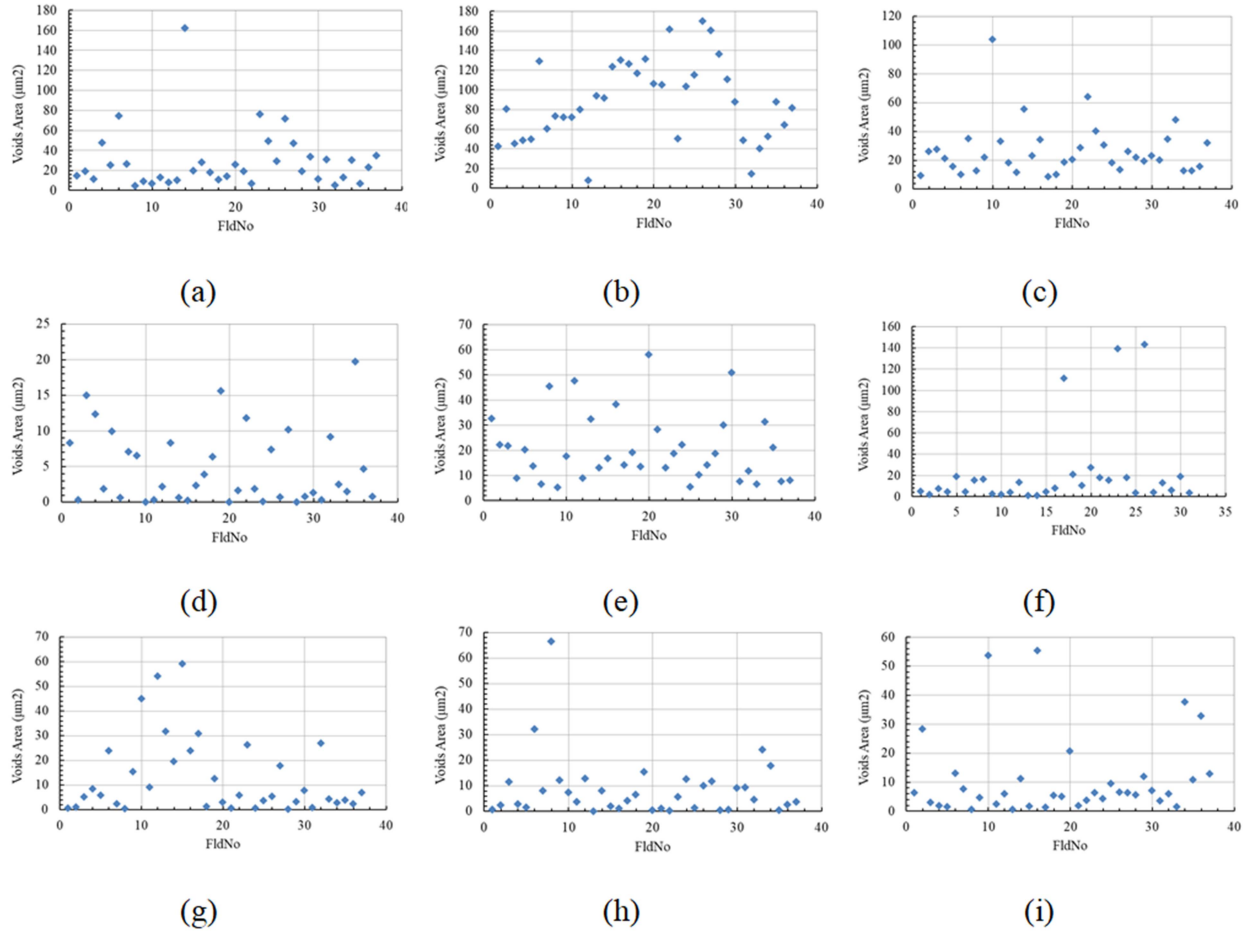


Figure 4.59 Field measurements of void area from necked dome samples tested under different test conditions; (a-c) O-temper UT, PST and BBT specimens tested at RT, (d-f) UT, PST and BBT specimens tested at 220°C, and (g-i) T6-temper UT, PST and BBT specimens tested at 220°C.

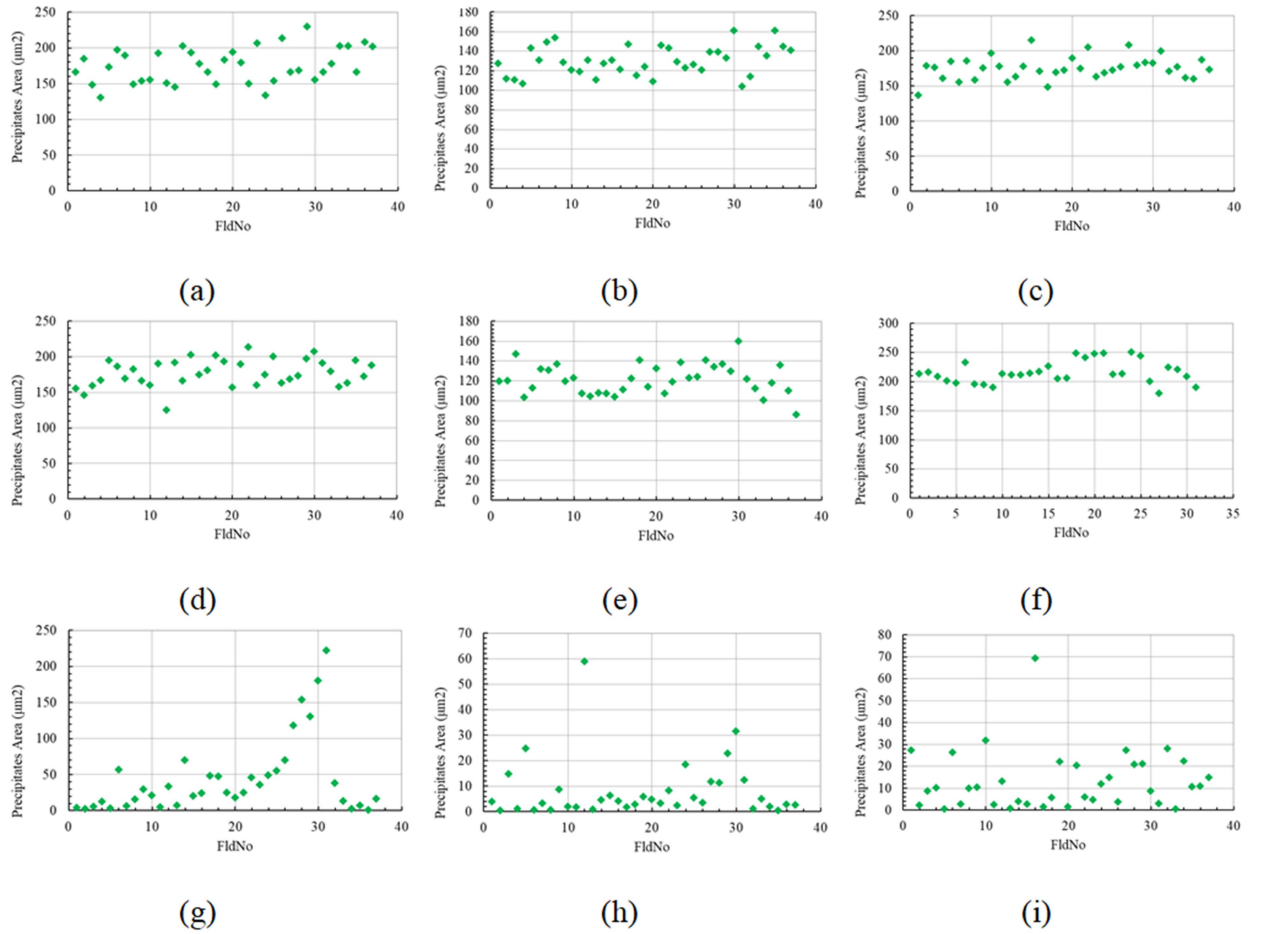
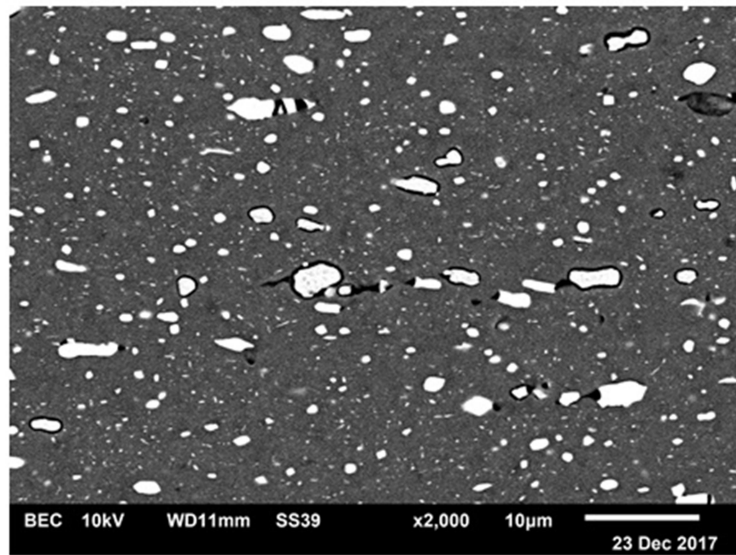
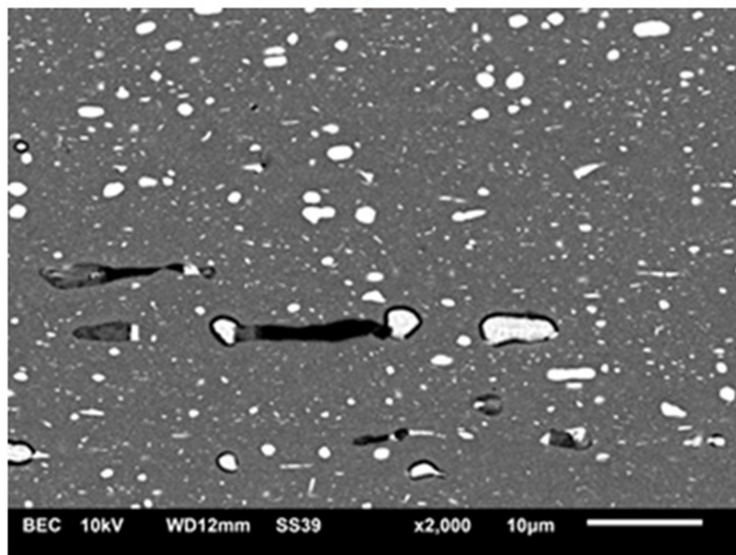


Figure 4.60 Field measurements of precipitate area from necked dome samples tested under different test conditions; (a-c) O-temper UT, PST and BBT specimens tested at RT, (d-f) UT, PST and BBT specimens tested at 220°C, and (g-i) T6-temper UT, PST and BBT specimens tested at 220°C.



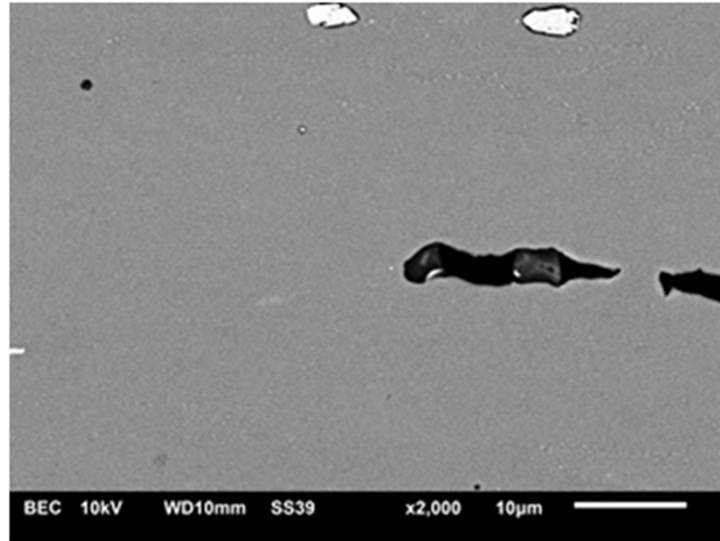


(a)

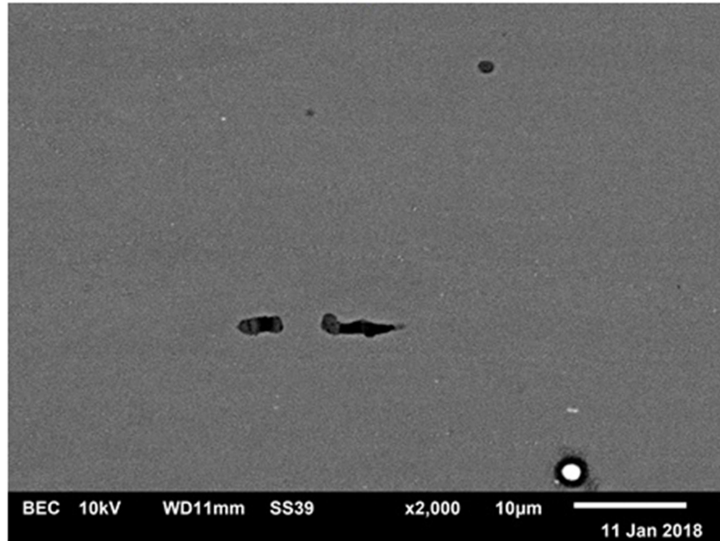


(b)

Figure 4.61 SEM image of through thickness neck region of polished PST dome sample of AA7075-O; (a) deformed at RT, and (b) deformed at 220°C.



(a)



(b)

Figure 4.62 SEM image of through thickness neck region of polished dome sample of AA7075-T6 deformed at 220°C; (a) UT, and (b) PST.

The voids and precipitates area analyzed from field measurements for peak-aged dome samples is much lower than that for fully annealed specimens. This may be explained as the precipitates were partially dissolved during solution treatment and hence the solute



atoms dispersed through the aluminum matrix and strengthen the alloy (Nicolas & Deschamps, 2003). Also, many of the precipitates deposit on the grain boundaries during the T6 ageing treatment where void induced damage is initiated. While precipitate rich grain boundary sites offer good opportunity for void initiation and linkage, there is considerably less void growth prior to fracture. As a result, void area/volume fraction tends to be lower in T6 deformed samples than in the fully annealed test samples.

Table 4.15 Void and precipitate areas from field measurements for AA7075-O and T6 dome specimens in uniaxial, plane and biaxial strain paths at room temperature and 220°C.

Temper	Temperature (°C)	Microstructural Feature	Field No.	Area (μm <sup>2</sup> )				Counts	Thickness Strain (ε <sub>t</sub> )
				Min.	Max.	Mean	Sum		
O	RT	UT							
		Voids	37	4.34	162.23	28.41	1051.09	1500	-0.384
		Precipitates	37	130.04	229.52	175.04	6476.35	26433	
		PST							
		Voids	37	7.71	169.99	88.37	3269.75	45988	-0.411
		Precipitates	37	103.66	161.02	130.27	4819.84	16406	
		BBT							
		Voids	37	8.46	103.95	26.41	977.2	1332	-0.494
		Precipitates	37	136.3	214.74	175.23	6483.35	29434	
	220	UT							
		Voids	37	0	19.67	4.75	175.67	292	-0.414
		Precipitates	37	125.05	213.18	177.25	6558.31	36786	
		PST							
		Voids	37	5.14	57.94	20.55	760.22	1193	-0.53
		Precipitates	37	85.85	159.73	121.43	4492.79	19962	
		BBT							
		Voids	31	0.81	142.82	21.3	660.27	749	-0.719
		Precipitates	31	179.53	250.32	215.47	6679.58	507922	
T6	220	UT							
		Voids	37	0.18	59.11	12.77	472.34	335	-0.324
		Precipitates	37	0.5	221.52	43.51	1610.01	21195	
		PST							
		Voids	37	0.03	66.47	8.48	313.64	340	-0.214
		Precipitates	37	0.36	58.76	8	295.85	302	
		BBT							
		Voids	37	0.46	55.21	10.74	397.56	391	-0.526
		Precipitates	37	0.47	69.36	13.06	483.33	449	

#### 4.4.4 Fractographic analysis of damage in deformed uniaxial tensile test samples

Figure 4.63 and Figure 4.64 show SEM images of fracture surfaces for deformed AA7075-O uniaxial tensile test samples at two different test speeds and test temperatures.

The first 2 images in each figure (images (a,b)) correspond to a low magnification view of the entire fracture cross-section whereas the rest of the images were obtained at larger magnifications from a small representative region in the middle of the specimen. The large magnification images in Figure 4.63 (c,d) and Figure 4.64 (c,d) were acquired in secondary electron imaging (SEI) mode to show the typical dimpled rupture characteristic of ductile failure of metallic materials at the centre region of the fracture cross-sections. The edges of the cross-section indicate more faceted or shear-like fracture initiation from the surface region of the specimen. As shown, the crack initiation area is relatively small and smooth but the topography of the middle region is quite rough. As the test temperature is increased to 220°C, the outer peripheral shear region is increased but the overall fractured area is decreased. Also, the dimples sizes in the central region are increased. The large magnification images in Figure 4.63 (e,f) and Figure 4.64 (e,f) are from the same region of the specimen as the images (c,d) but acquired in the back-scattered electron (BEC) mode to reveal the location of the precipitate or constituent particles in the microstructure which appear as small white ‘dots’ in the images (e,f). The BEC mode also revealed the grain boundaries although they were not always well defined. A comparison of the images (c,e) and (d,f) in Figure 4.63 and Figure 4.64 reveals that voids are typically associated with the particles and the void size is closely related to the particle size. At room temperature, an increase in the test speed from 1 mm/min to 10 mm/min leads to a decrease in the average dimple size, with no marked change in the peripheral shear region (compare Figure 4.63 (c,d) and Figure 4.63 (a,b)). This suggests that at higher test speeds (or strain rates), the void growth process is reduced and fracture

occurs earlier. At 220°C, however, the higher test speed results in larger void sizes and increased peripheral shear fracture region perhaps due to increase in strain rate sensitivity of the sheet (see earlier Figure 2.5 from (Hui et al., 2012)) which delayed the onset of localized necking and enhanced void growth at elevated temperature deformation (compare Figure 4.64 (c and d) and Figure 4.64 (a and b)).

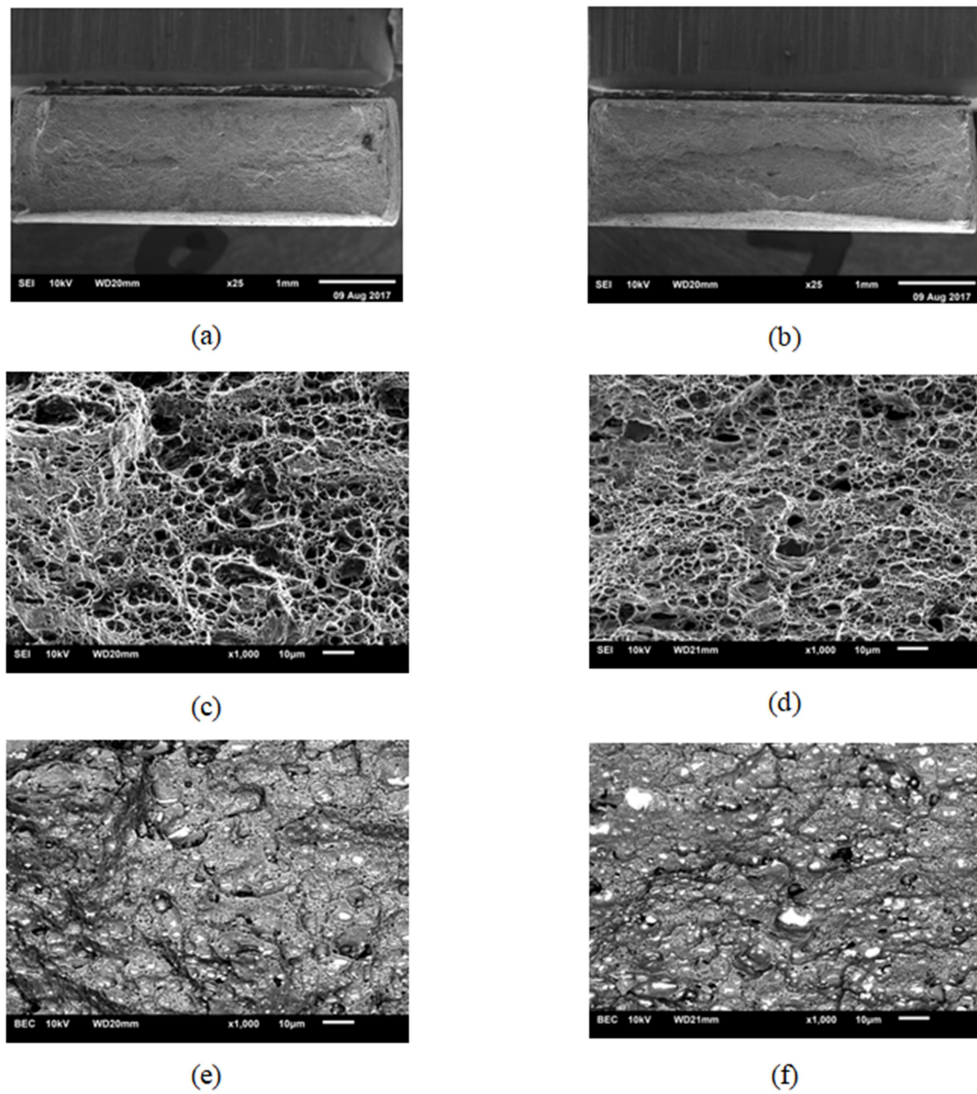


Figure 4.63 SEM fractographic images of fracture surfaces of AA7075-O uniaxial tension samples tested at room temperature corresponding to test speeds; (a, c and e) 1 mm/min, and (b, d and f) 10 mm/min.

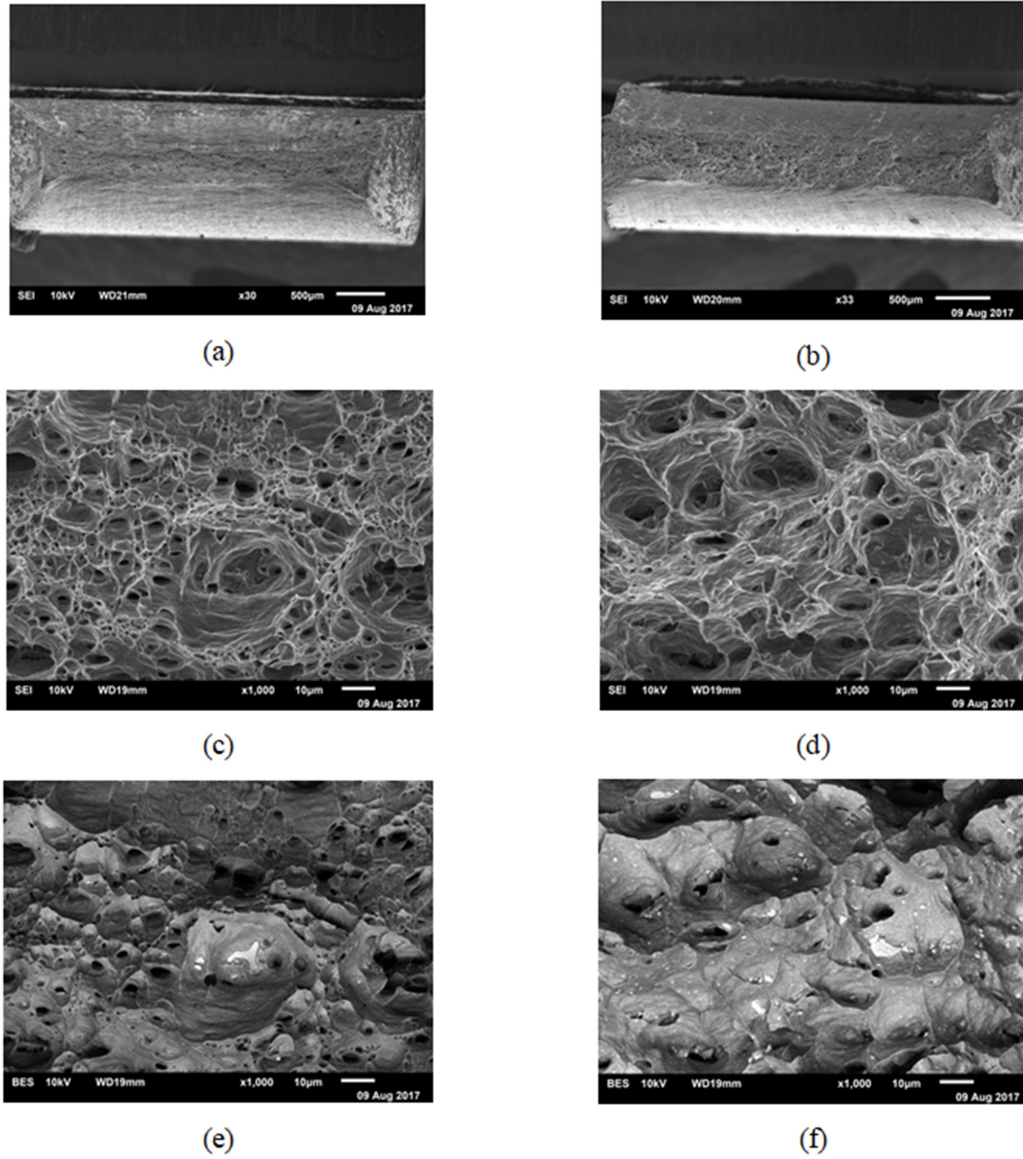


Figure 4.64 SEM fractographic images of fracture surfaces for AA7075-O uniaxial tension sample tested at 220°C corresponding to test speeds; (a, c and e) 1 mm/min, and (b, d and f) 10 mm/min.

The SEM fractographic images under different test conditions were further analyzed to obtain dimple area fraction using a quantitative image analysis software associated with a

digital optical microscope (see earlier sub-section 3.1.4.2 in the Experimental Methodology Chapter for details regarding the measurements). Figure 4.65 shows, as an illustration, the processing of earlier images representing the dimpled rupture at room temperature and 220°C from tensile tests at 10 mm/min (see Figure 4.63 (d) and Figure 4.64 (d)). The dimple area fraction, represented by black and gray area, for room temperature test sample is about 59% while it is about 69% for the sample tested at 220°C, keeping all other test and imaging conditions the same. In other words, elevated temperatures enhance sheet metal ductility by enabling the aluminum matrix material to flow more extensively around hard particles. In addition, the final fracture is delayed due to more extensive void growth in the matrix surrounding the particles. The voids are larger and form clear ridges (or contours) represented by white area. In comparison, at room temperature, there is reduced matrix material flow and consequently earlier and less extensive void growth (i.e., small fractured void size) prior to rupture.

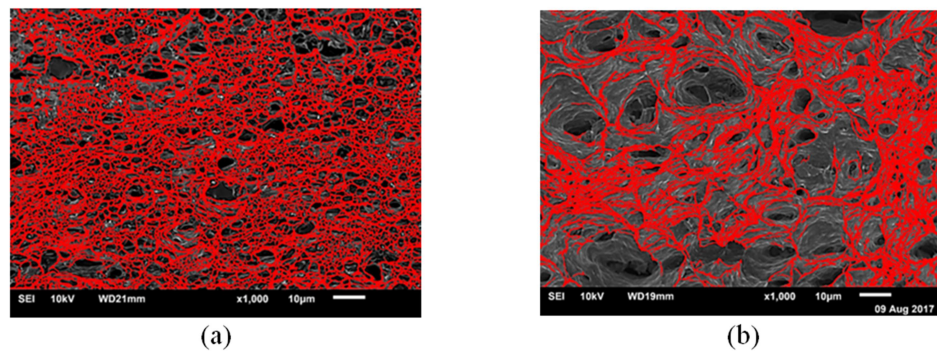


Figure 4.65 SEM fractographic images after image processing of fractured AA7075-O uniaxial tension sample tested at 10 mm/min; (a) room temperature test, and (b) 220°C test.

Fractographic results for the T6 temper failed tensile samples tested under two different speeds and temperatures, similar to the O-temper sheet, are shown in Figure 4.66 and

Figure 4.67. A different fracture mechanism in T6 temper specimens compared to the O-temper can be observed at room temperature. The peripheral shear regions persists in T6 temper but the transition between the shear and the dimpled rupture regions is sharper and exhibits delamination or crack-like feature along the specimen width direction. Also, a combination of limited plastic deformation and cleavage-like (flat facets) fracture can be observed in Figure 4.66 (c,d). This cleavage-like transgranular fracture is also referred to as quasi-cleavage fracture in the literature (Committee, 1987). A quasi-cleavage fracture (or cleavage-like) fracture is a fracture mode that combines both cleavage fracture and dimple rupture (Committee, 1987). Similar cleavage-like (and less ductile rupture) features are noticeable at the higher test speed of 10 mm/min (compare images in Figure 4.66 (c,d)). These results appear consistent with reduced thickness strain at fracture for the T6 temper material compared to the O-temper as shown in Table 4.11 and Table 4.13 respectively. The results are also consistent with the uniaxial stress – strain response of O and T6 temper materials as presented earlier in Figure 4.7 and Figure 4.8 respectively where the macroscopic strains to fracture are 0.16 and 0.12 for O and T6 temper materials.



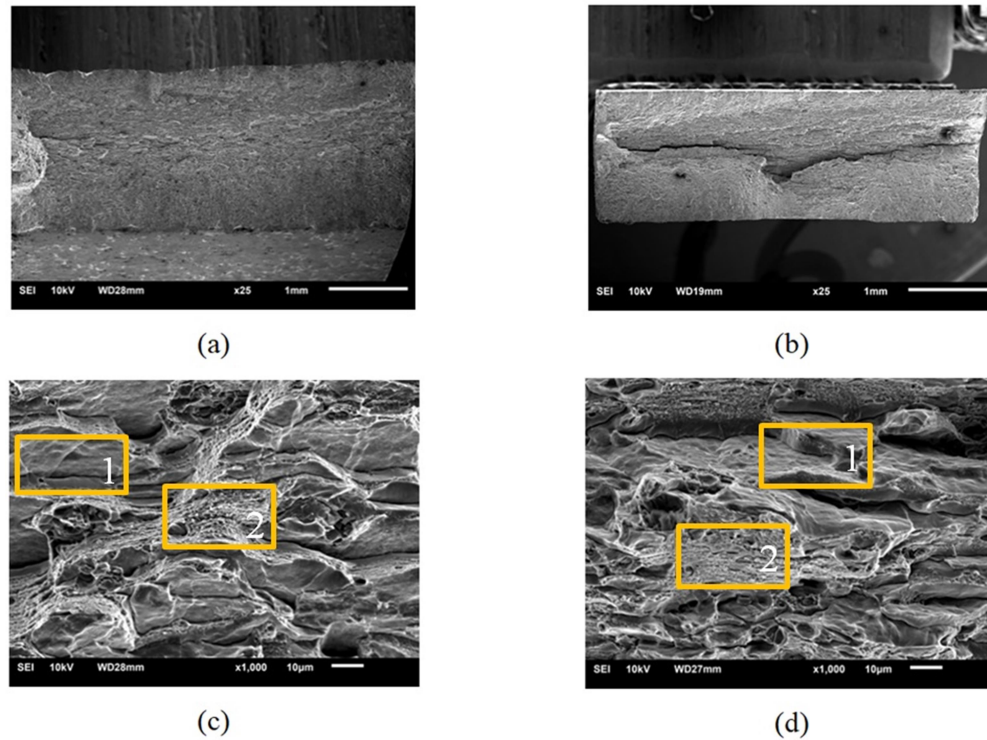


Figure 4.66 SEM fractographic images of fracture surfaces of failed T6 uniaxial tension samples tested at room temperature corresponding to test speeds; (a, c) 1 mm/min, and (b, d) 10 mm/min where zone (1) presents cleavage-like while zone (2) shows micro-void coalescence.

Figure 4.67 shows similar fractographic images of failed T6 tensile samples tested at 220°C. A transition from quasi-cleavage towards more ductile rupture of O-temper sheet can be noted at both test speeds. In fact, Figure 4.67 (c,d) suggests a mixed fracture mechanism involving micro-void coalescence and cleavage-like fracture in T6 samples. The microvoid coalescence appears smaller in size and with a higher number density at the higher test speed of 10 mm/min. As earlier, a quantitative measurement of dimple area fraction from the fractographic images revealed values of about 7% and 9% for sample tested at room temperature and 220°C respectively, for tests at 10 mm/min, as in shown Figure 4.68.



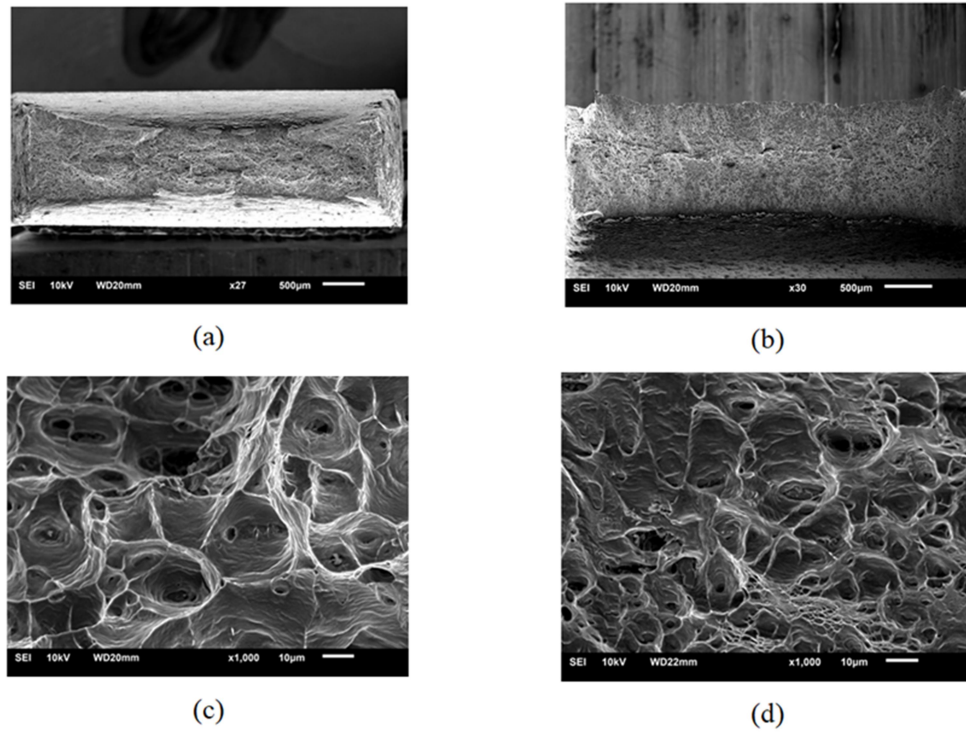


Figure 4.67 SEM fractographic images of fracture surfaces of AA7075-T6 uniaxial tension samples tested at 220°C corresponding to test speeds; (a, c) 1 mm/min, and (b, d) 10 mm/min.

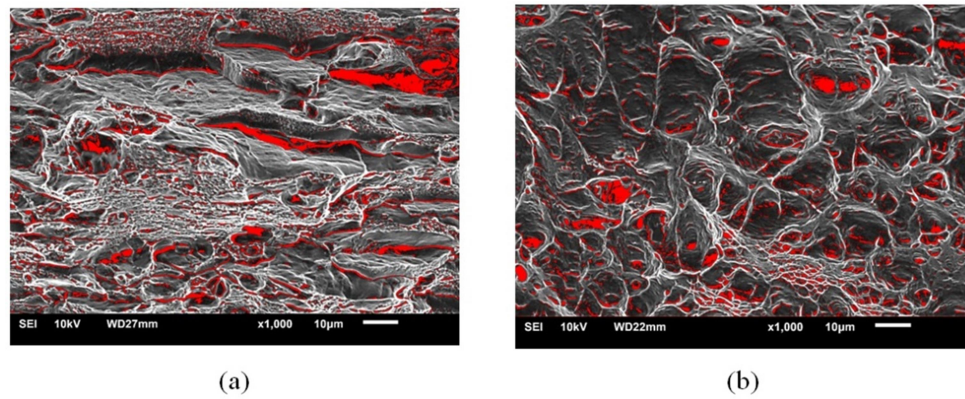


Figure 4.68 SEM fractographic images after image processing of fractured AA7075-T6 uniaxial tension sample tested at 10 mm/min; (a) room temperature test, and (b) 220°C test.

#### **4.4.5 Fractographic analysis of void damage in dome test samples**

Results from fractographic analysis of failed dome test samples corresponding to two tempers (O and T6), two temperatures (room and 220°C) and three strain paths (UT, PST, BBT) are reported in this sub-section in a manner similar to the results presented earlier for the failed in-plane uniaxial tensile test specimens. Figure 4.69 shows SEM fractographic images of through-thickness fracture surfaces of failed O-temper dome test samples for the three strain paths in O temper tested at room temperature. Again, a pair of images for each strain path are presented corresponding to SEI and BEC modes of observation, and arranged horizontally, to reveal the voids and dimpled rupture features in the left image and precipitate or constituent shapes and sizes associated with the voids in the right image. SEM images show numerous relatively small size dimples, likely associated with precipitate particles, for all strain paths. Also, for the BBT sample, the dimple sizes are larger perhaps due to larger stress triaxiality which promotes increased void growth. Nearly all of the voids are shown to be initiated at the particles with larger voids corresponding to larger particles. In general, there was no widespread evidence of break-up of particles for the three strain paths. Similar results for the O-temper domes samples at 220°C are shown in Figure 4.70 where the dimples are clearly larger than at room temperature due to increased matrix material flow in the vicinity of the precipitates/particles and delay in the onset of diffuse and localized necking and perhaps slower neck growth due to increased rate sensitivity of the material at 220°C. This trend is consistent with the earlier SEM fractographic data on O-temper uniaxial tensile specimens in the previous sub-section. It is to be noted that particles are not as clearly

visible in the BEC images due to extensive growth of the voids around them which causes deterioration in the BEC image contrast. Results for T6-temper failed domes at 220°C are shown in Figure 4.71 where fracture surfaces show large flat facets around dimple void cores arising from limited matrix material flow around the precipitates, and unlike the much softer O temper matrix at 220°C.

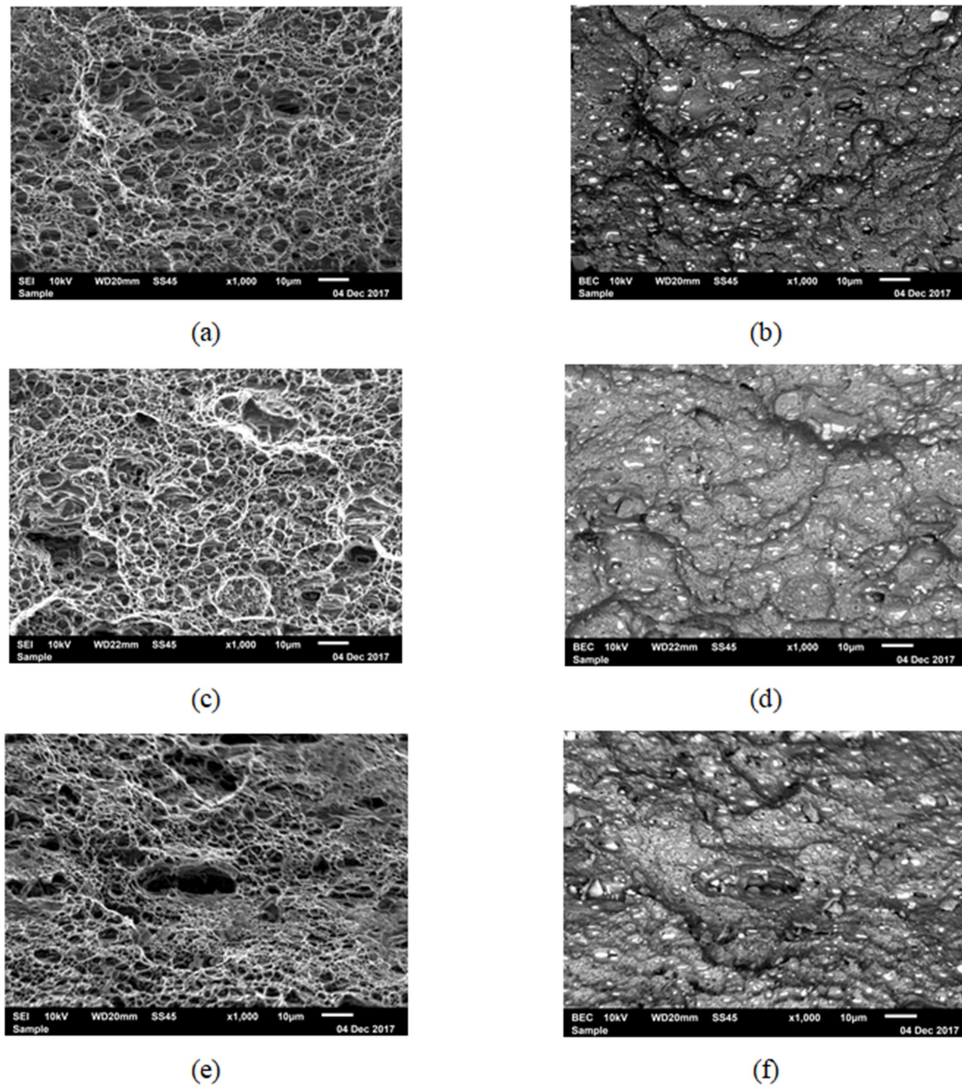


Figure 4.69 SEM fractographic images from the mid-thickness region of failed O-temper dome samples tested at room temperature for the following strain paths; (a, b) UT sample, (c, d) PST sample, and (e, f) BBT sample.

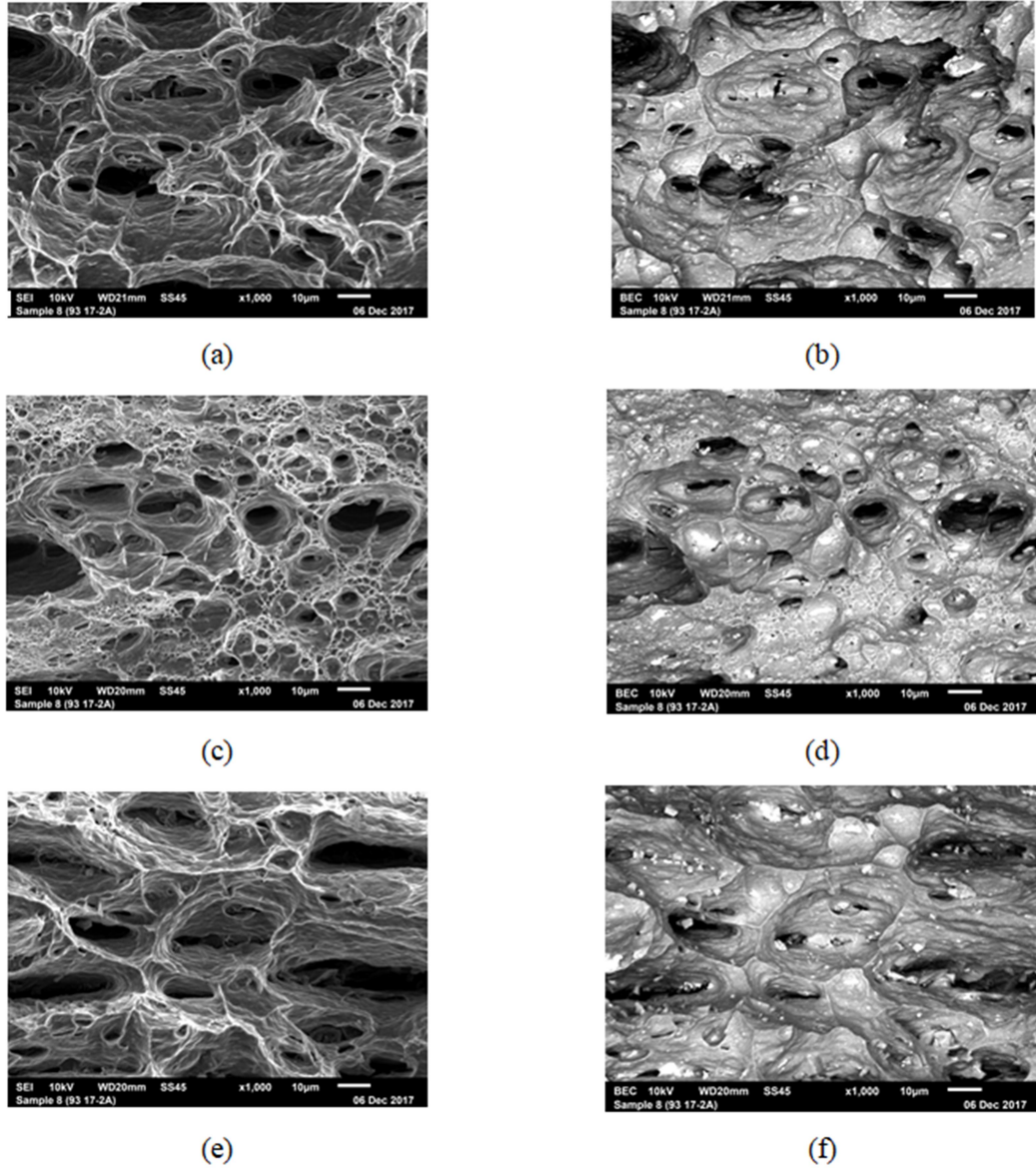


Figure 4.70 SEM fractographic images from the mid-thickness region of failed O-temper dome samples tested at 220°C for the following strain paths; (a, b) UT sample, (c, d) PST sample, and (e, f) BBT sample.



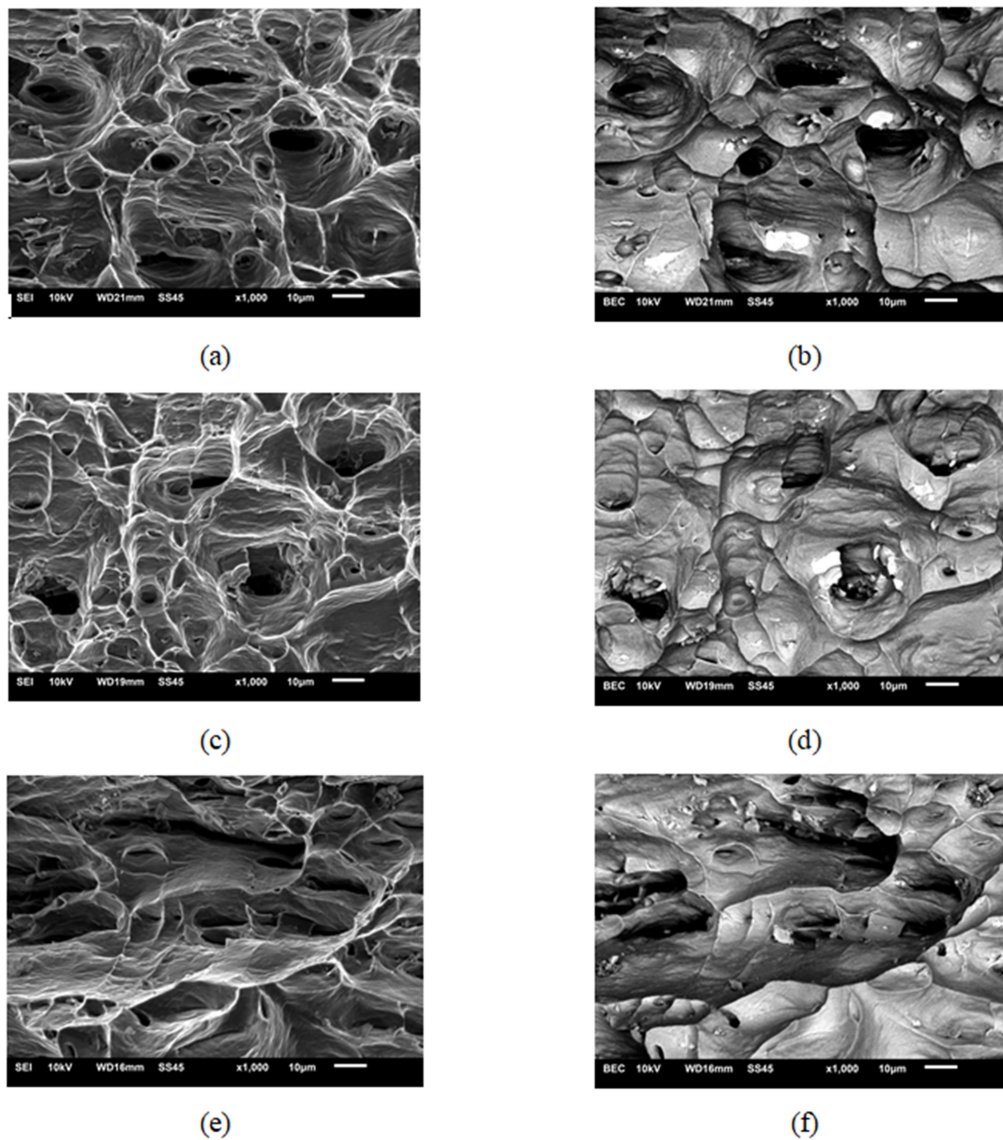


Figure 4.71 SEM fractographic images from the mid-thickness region for AA7075-T6 dome samples formed at 220°C; (a) and (b) UT sample, (c) and (d) PST sample and (e) and (f) BBT sample.

As earlier, for the failed tensile test specimens, dimpled fracture average area fraction data was also obtained for failed dome test samples corresponding to two tempers (O and T6), two temperatures (room and 220°C) and three strain paths (UT, PST, BBT) by processing the fractographic images. This data is presented in Table 4.16 below. For O-temper dome samples tested at 220°C, average dimples area percentage is considerably larger than at room temperature for all strain paths. Also, T6 temper samples formed at 220°C reveal relatively large average dimple area fraction from the flat faceted region in the image compared with O-temper samples. This is perhaps an artifact of the image analysis software which was not able to distinguish between the dimpled (void) and flat faceted regions.

Table 4.16 Average dimples area percentage of AA7075-O and T6 fractured dome samples deformed to fracture by using 50.8 mm diameter punch at room temperature and 220°C.

Temper	Temperature (°C)	Strain Path	Average Dimples Area (%)
O	RT	UT	56.26
		PST	54.06
		BBT	52.33
	220	UT	64.4
		PST	58.86
		BBT	63.7
T6	220	UT	63.9
		PST	67.18
		BBT	62.95

#### **4.4.6 XRD texture analysis**

X-ray diffraction (XRD) measurements and analyses were first carried out on undeformed AA7075 sheet metal in three different sheet tempers; F, O and T6 to determine the bulk sheet texture prior to forming. Also, the bulk texture evolution measurements in O and T6 temper samples subjected to straining along three different strain paths, UT, PST and BBT, were carried out to analyze its role in controlling plastic flow and formability, especially at elevated temperatures. The texture evolution was assessed by measuring grain orientation intensities of ideal texture components namely, Copper (Cu), Brass (Bs), S, Cube (C) and Goss (G) via 2D stereographic projection pole figures (PFs) and orientation distribution functions (ODFs). The XRD experimental and analysis details were provided earlier in the Experimental Methodology chapter (see earlier Sub-section 3.1.5.3).

##### **4.4.6.1 Un-deformed textures**

Texture data from XRD experiments and subsequent analysis for undeformed AA7075 F, O and T6 temper sheet materials in the form of PFs are shown in Figure 4.72. For each of the tempers, three PFs from  $\{111\}$ ,  $\{200\}$  and  $\{220\}$  families of planes were measured from the surface of the specimens and then ODFs were calculated from these three PFs and represented graphically. All ideal texture components of Cu, Bs, S, C and G and their positions in PFs and ODFs were illustrated in the Literature Review chapter (see Sub-section 2.6). The  $\{111\}$  PF for F-temper material showed a strong Brass $\{011\}\langle 211\rangle$  deformation texture from commercial AA7075 sheet processing which included thickness reduction during hot and cold rolling (see earlier Sub-section 4.1.1). In contrast, the O-

temper sheet showed strong Copper  $\{112\}\langle111\rangle$  and Cube  $\{001\}\langle100\rangle$  orientation components while T6-temper sample revealed somewhat weak Copper  $\{112\}\langle111\rangle$  and S  $\{123\}\langle634\rangle$  components from recrystallization during the heat treatment process.

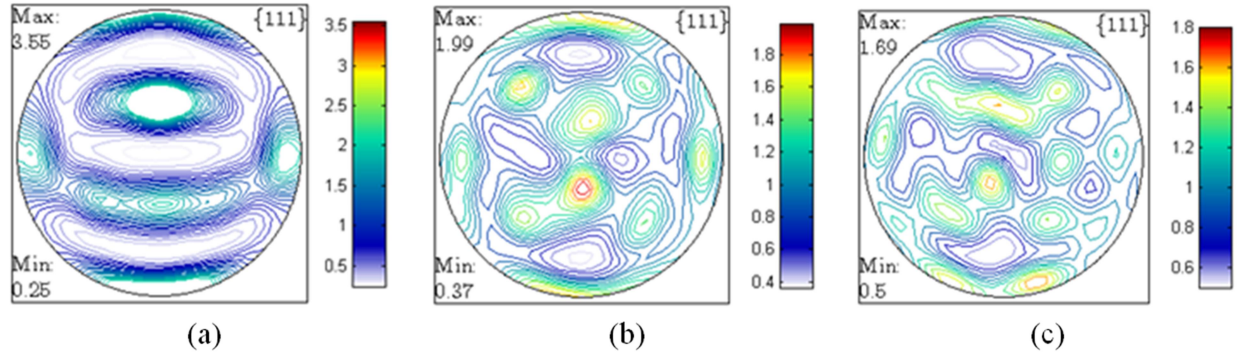


Figure 4.72  $\{111\}$  PFs for un-deformed AA7075 sheets; (a) as fabricated (or F temper), (b) fully-annealed (or O temper) and (c) peak-aged (or T6 temper).

The measured PFs were converted into ODFs that provided the volume fraction of grains with a certain orientation in 3D Euler space defined by three Euler angles ( $\varphi_1$ ,  $\phi$ ,  $\varphi_2$ ) (H. Bunge, 1987). It is to be noted that ODFs for the different tempers were calculated from PFs at constant Euler angle  $\varphi_2$  of  $0^\circ$  up to  $85^\circ$  with  $5^\circ$  increment ( $\varphi_2$  located at the upper right corner in each ODF Figure). Together, they represent three-dimensional data that describes the crystal orientation distribution more comprehensively than the two-dimensional PF representation which is a stereographic projection. Figure 4.73, Figure 4.74 and Figure 4.75 show the ODFs for F, O and T6 un-deformed sheet materials respectively. ODF of un-deformed F-temper sheet metal (Figure 4.73) shows a deformation texture of Brass  $\{011\}\langle211\rangle$ , marked with symbol (Bs) in ODF for  $\varphi_2$  of  $0^\circ$ . In contrast, ODF of O-temper sheet (Figure 4.74) shows a Copper  $\{112\}\langle111\rangle$  component



(see ODF for  $\varphi_2$  of  $0^\circ$ ), strong Cube  $\{001\}\langle 100 \rangle$  (see ODF for  $\varphi_2$  of  $45^\circ$ ) and Brass  $\{011\}\langle 211 \rangle$  (see ODF for  $\varphi_2$  of  $0^\circ$ ) textures. Lastly, undeformed T6 temper ODF in Figure 4.75 represents weak Copper  $\{112\}\langle 111 \rangle$  component (see ODF for  $\varphi_2$  of  $45^\circ$ ) and strong S  $\{123\}\langle 634 \rangle$  component (see ODF for  $\varphi_2$  of  $65^\circ$ ). Table 4.17 summarize texture data from PFs and ODFs for un-deformed sheet metal in three different temper conditions.

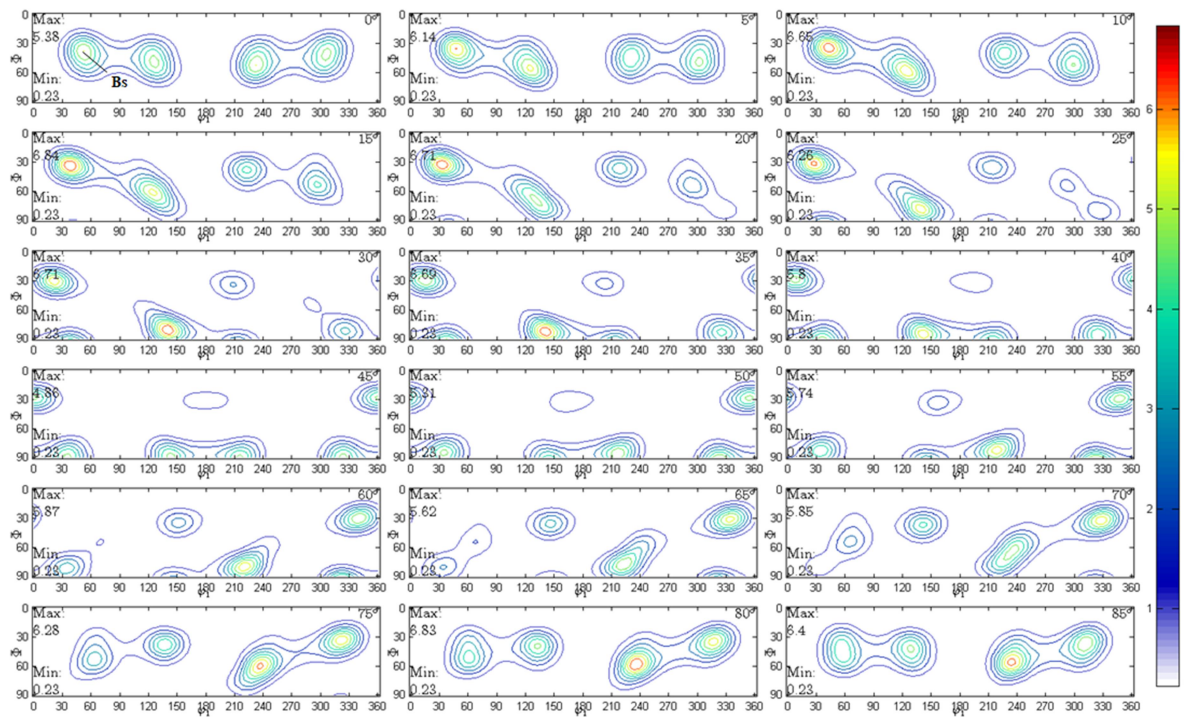


Figure 4.73 ODFs for AA7075-F un-deformed sheet material.

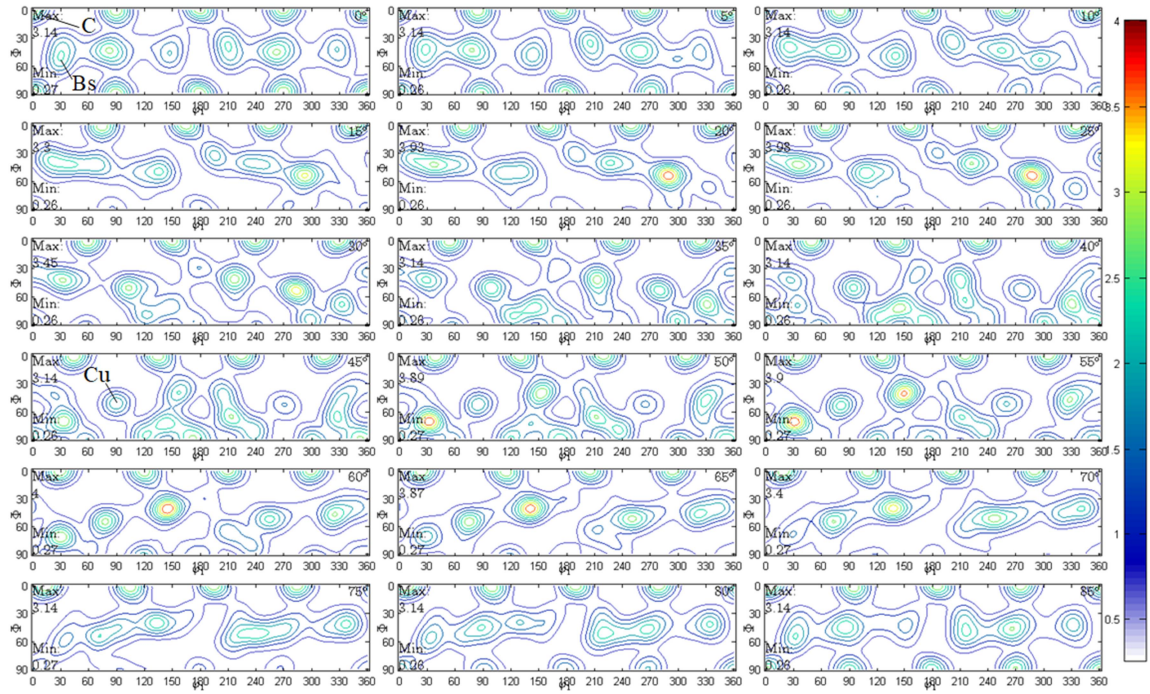


Figure 4.74 ODFs for AA7075-O un-deformed sheet.

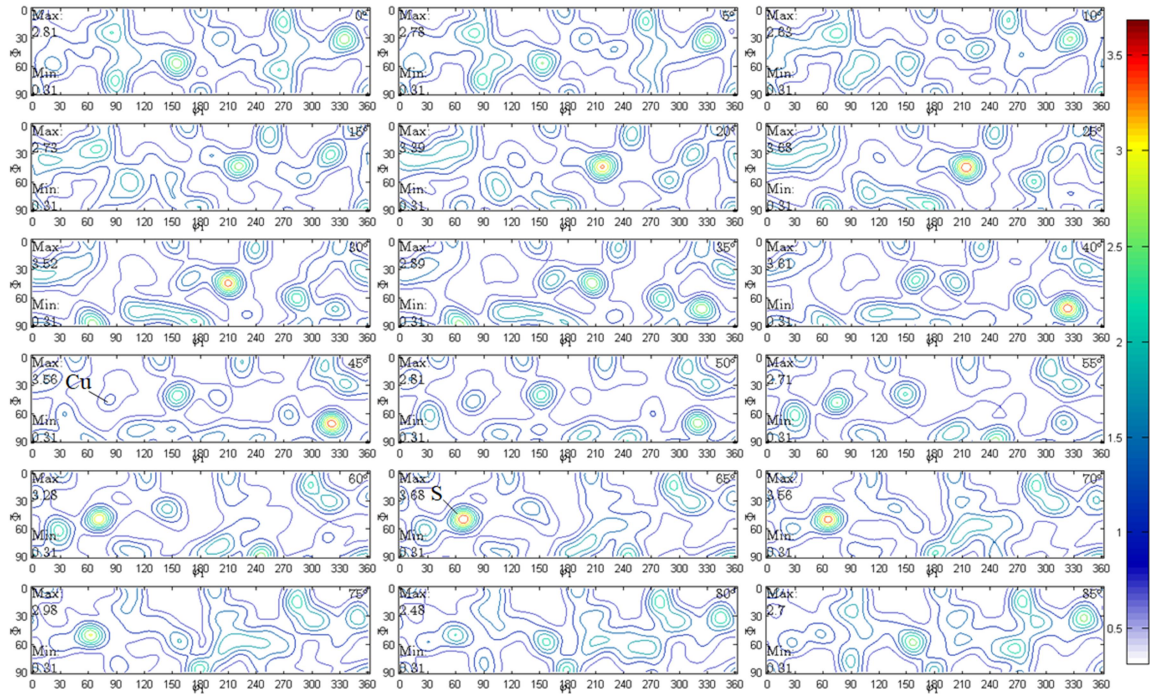


Figure 4.75 ODFs for AA7075-T6 un-deformed sheet.

Table 4.17 Un-deformed sheet metal texture data from PFs and ODFs for {111} family of planes.

Temper	Temperature (°C)	Texture Type (from ODFs)	Euler Angles ( $\phi_1$ , $\phi$ and $\phi_2$ )
F	RT	Brass	35°, 45° and 0°
O		Cube	0°, 0° and 0°
		Brass	35°, 45° and 0°
		Copper	90°, 30° and 45°
T6		Copper	90°, 30° and 45°
		S	59°, 34° and 65°

#### 4.4.6.2 Deformed textures from dome test samples

PFs and ODFs were obtained for three different strain paths, namely UT, PST and BBT, from deformed O temper dome specimens at room temperature and 220°C while PFs and ODFs for T6 temper were analysed for samples deformed at 220°C. Figure 4.76 and Figure 4.77 show {111} PFs for O temper dome samples at the pole and neck respectively after deformation at room temperature. PFs of pole region for UT and PST exhibited strong Cube {001}<100> texture orientation, whereas, for BBT, a strong Brass {011}<211> was revealed. The PFs of neck region for UT and PST samples showed weak Copper {112}<111> component whereas neck region of BBT sample showed predominantly Brass {011}<211> and S {123}<634> components. It is to be noted that there was a small deviation in the Copper orientation of neck region for {111} PF in UT and PST (see Figure 4.77 (a,b)). Such a small deviation may be attributed to the curvature of the neck region that may broaden (or disperse) the original rolling texture in different directions during the X-ray scanning process. This small deviation was minimized by



using high scanning angles of 93.5° and 99.5° and removing any unclear frames during GADDS software PFs analysis.

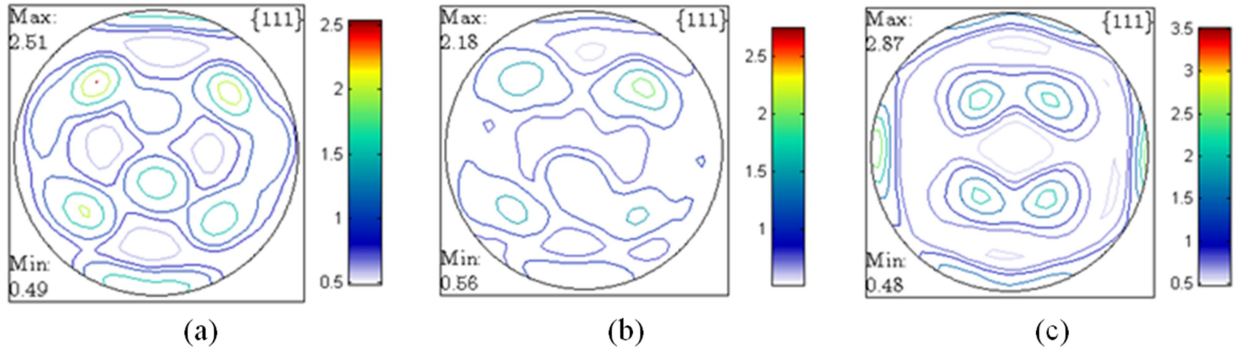


Figure 4.76  $\{111\}$  PFs at the pole of dome in O-temper material deformed at room temperature; (a) UT sample, (b) PST sample and (c) BBT sample.

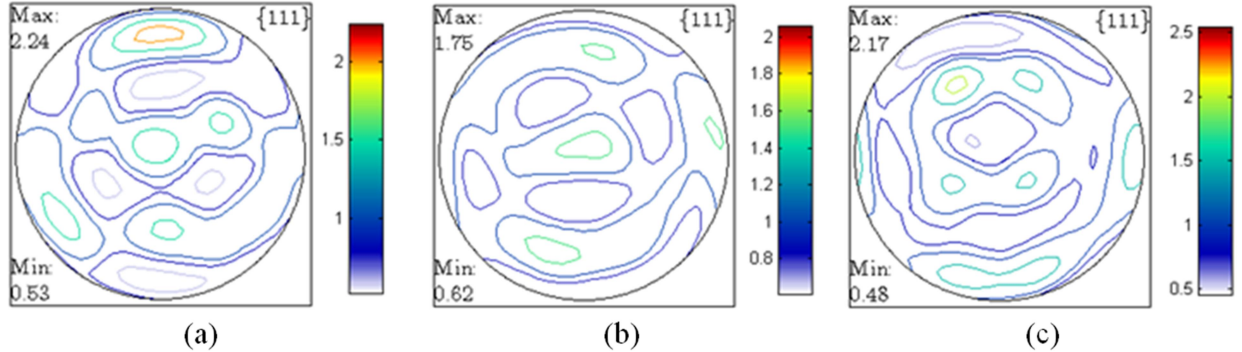


Figure 4.77  $\{111\}$  PFs in the neck region of dome in O-temper material deformed at room temperature in; (a) UT sample, (b) PST sample, and (c) BBT sample.

Figure 4.78 to Figure 4.83 show the ODFs extracted from the PFs data for AA7075-O samples deformed at room temperature for various strain paths. Pole region of UT and PST samples have a strong Cube  $\{001\}\langle 100 \rangle$  texture component probably due to lack of material rotations at the pole when the dome is formed while BBT sample show Brass

$\{011\}\langle 211 \rangle$  component because of the occurrence of the neck, and consequent material rotations, in the pole region. Neck region for both UT and PST paths show weak Copper  $\{112\}\langle 111 \rangle$  texture while ODF of BBT strain path shows strong Brass  $\{011\}\langle 211 \rangle$  component similar to pole region. In addition to the Brass component, S  $\{123\}\langle 634 \rangle$  component is also present in the neck region. Table 4.18 summarize texture data from PFs and ODFs for O temper dome samples deformed at room temperature.

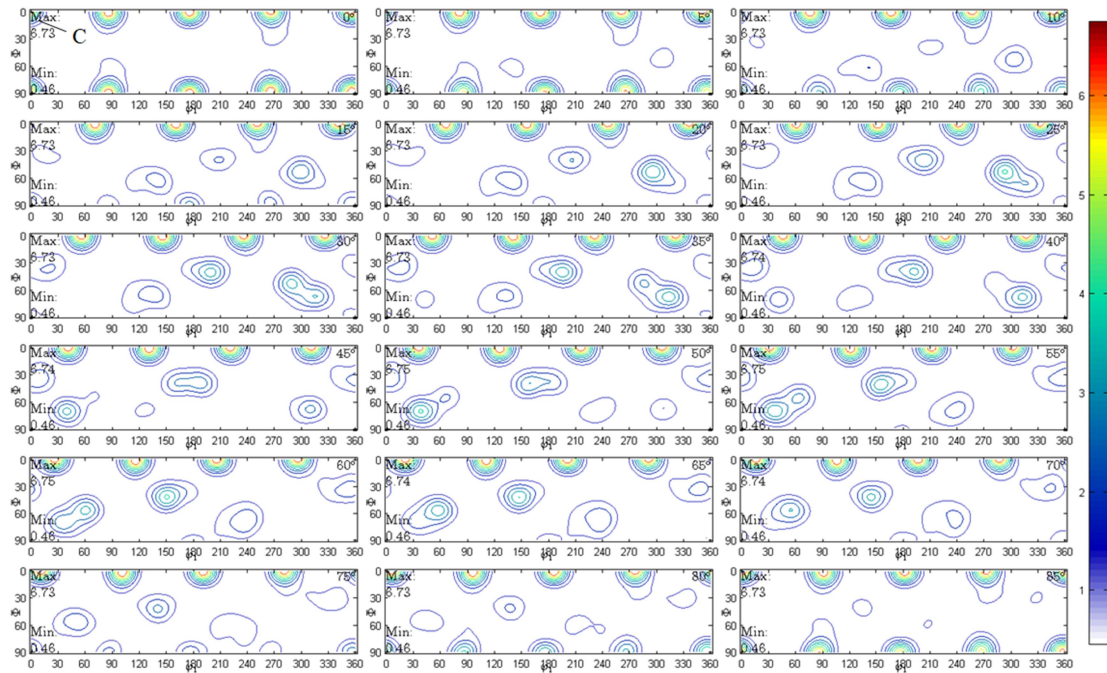


Figure 4.78 ODFs at the pole of AA7075-O UT strain path dome sample deformed at room temperature.

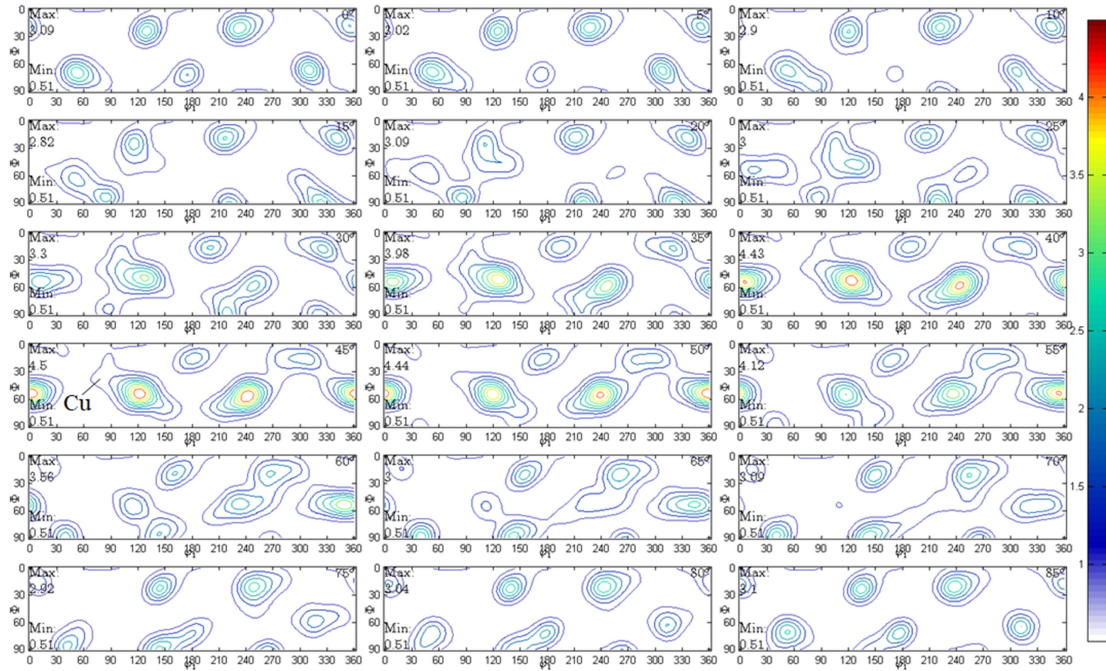


Figure 4.79 ODFs in the neck of AA7075-O UT strain path dome sample deformed at room temperature.

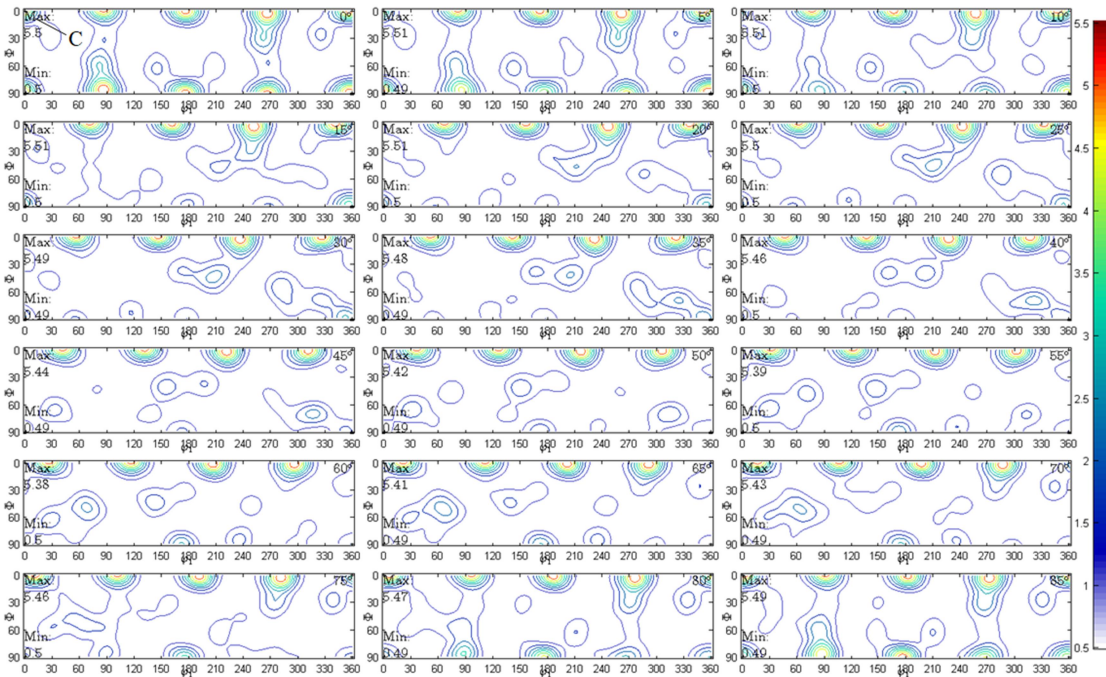


Figure 4.80 ODFs at the pole of AA7075-O PST strain path dome sample deformed at room temperature.



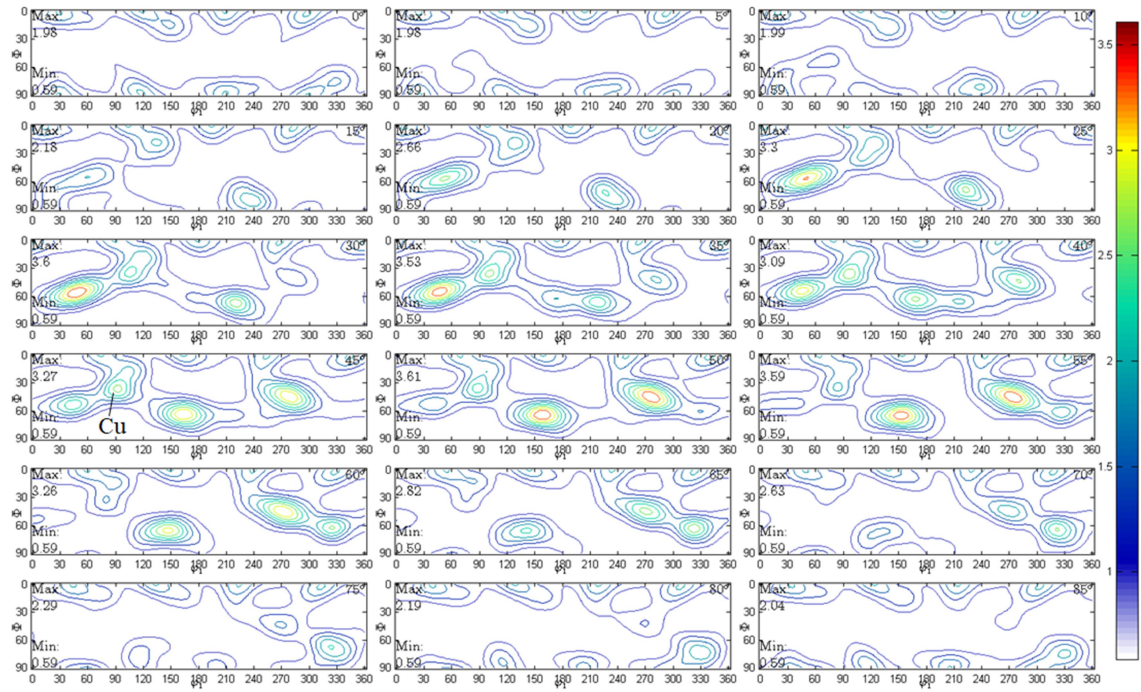


Figure 4.81 ODFs in the neck of AA7075-O PST strain path dome sample deformed at room temperature.

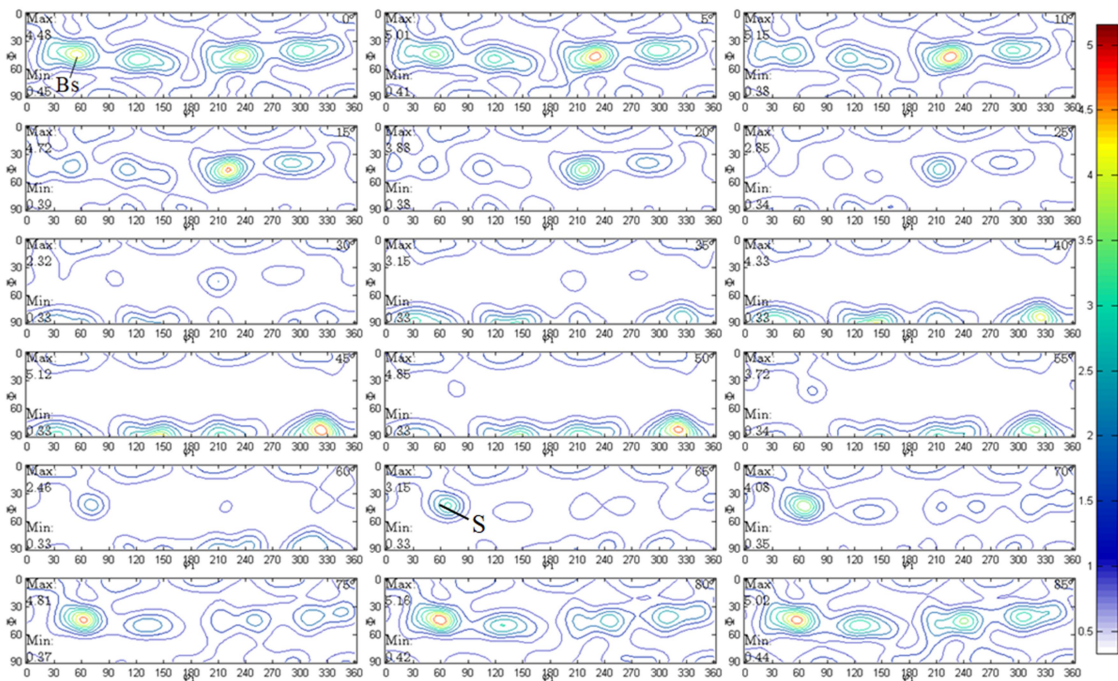


Figure 4.82 ODFs at the pole of AA7075-O BBT strain path dome sample deformed at room temperature.

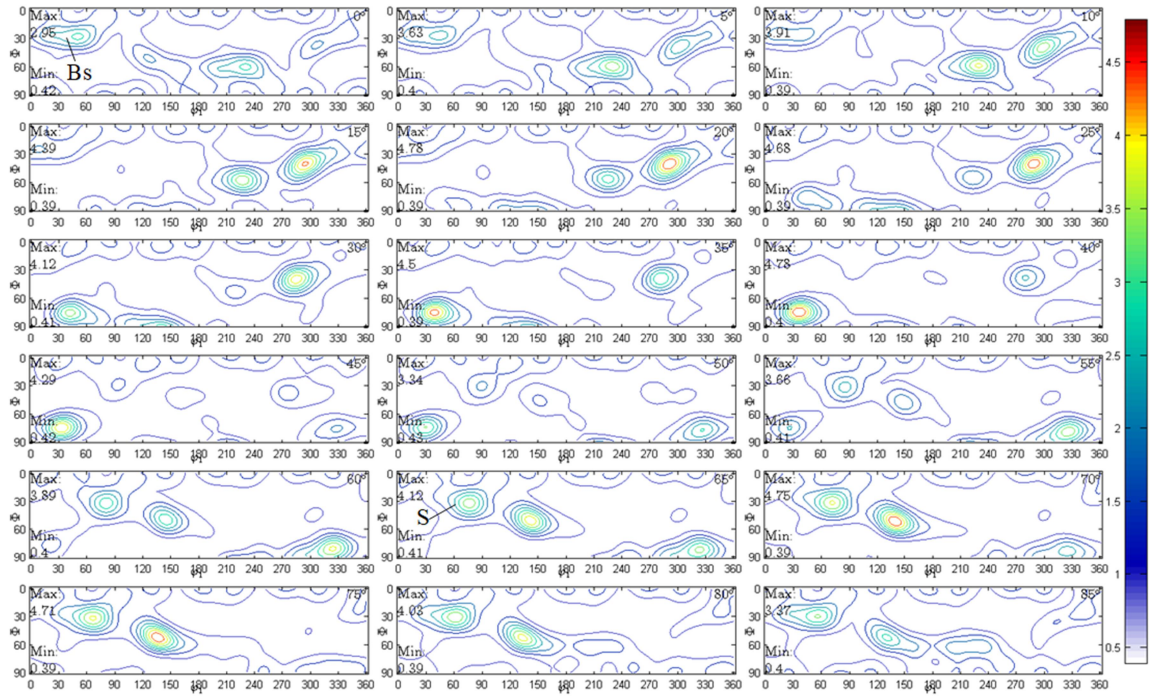


Figure 4.83 ODFs in the neck of AA7075-O BBT strain path dome sample deformed at room temperature.

Table 4.18 Texture data in the form of PFs and ODFs for  $\{111\}$  family of planes deformed at room temperature for O-temper dome samples.

Temper	Temperature (°C)	Scanned Region	Strain Path	Texture Type (from ODFs)	Euler Angles ( $\phi_1$ , $\phi$ and $\phi_2$ )
O	RT	Pole	UT	Cube	$0^\circ$ , $0^\circ$ and $0^\circ$
			PST	Cube	$0^\circ$ , $0^\circ$ and $0^\circ$
			BBT	Brass	$35^\circ$ , $45^\circ$ and $0^\circ$
				S	$59^\circ$ , $34^\circ$ and $65^\circ$
		Neck	UT	Weak Copper	$90^\circ$ , $30^\circ$ and $45^\circ$
			PST	Copper	$90^\circ$ , $30^\circ$ and $45^\circ$
			BBT	Brass	$35^\circ$ , $45^\circ$ and $0^\circ$
				S	$59^\circ$ , $34^\circ$ and $65^\circ$

Figure 4.84 and Figure 4.85 show PFs of  $\{111\}$  family of planes for O temper samples deformed at  $220^\circ\text{C}$  from the pole and neck regions of dome specimens respectively. The



PFs for both pole and neck regions exhibit texture orientations similar to those of O temper deformed at room temperature for all strain paths except for the neck region of BBT samples that show weak Brass, Copper and S components instead of strong Brass and S components. In fact, the maximum intensities for samples formed at 220°C are higher than those deformed at room temperature except for the pole region of BBT sample which gives a value closer to the room temperature value. This result may be explained in terms of occurrence of dynamic recrystallization during elevated temperature deformation, in which new grains are created and grain orientation is changed by high angle grain boundary migration that also leads to a change in crystallographic texture (A. Ghosh, 2018). The new grains with low dislocation density offer additional strain hardening potential and a prospect of improved sheet metal formability.

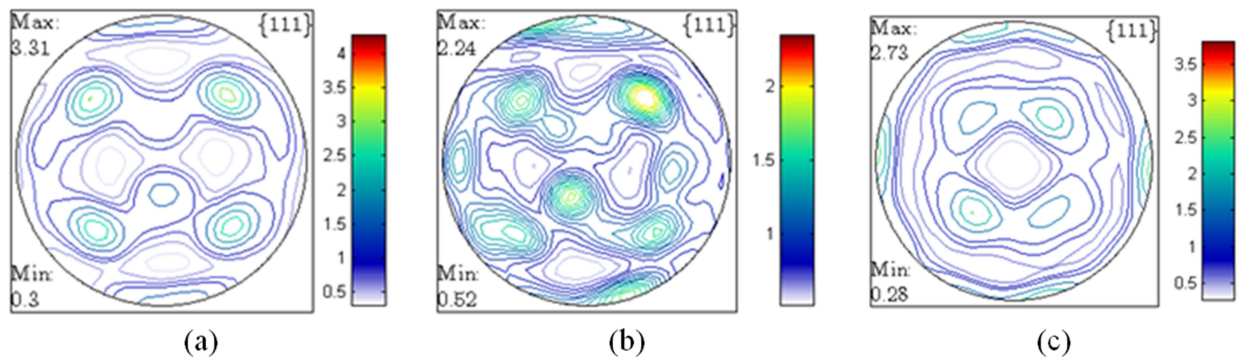


Figure 4.84  $\{111\}$  PFs from the pole region for O-temper dome samples deformed at 220°C corresponding to strain paths; (a) UT sample, (b) PST sample, and (c) BBT sample.

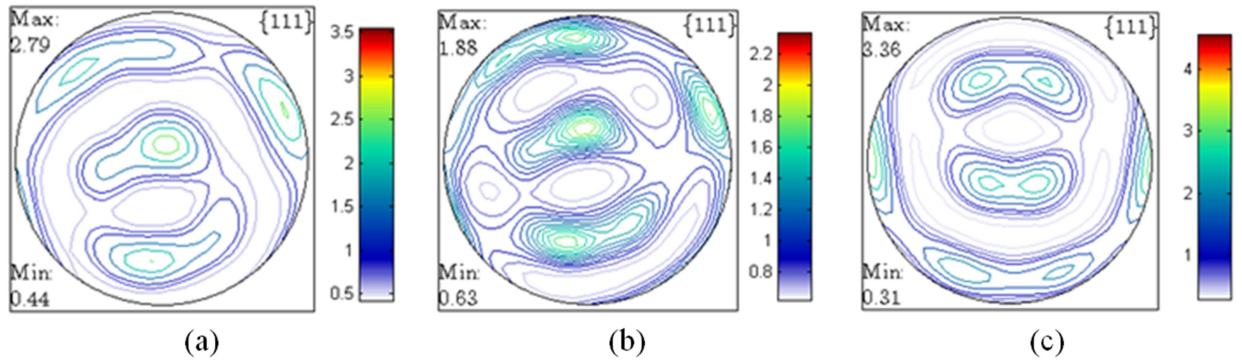


Figure 4.85  $\{111\}$  PFs from the neck region for O-temper dome samples deformed at 220°C corresponding to strain paths; (a) UT sample, (b) PST sample, and (c) BBT sample.

Figure 4.86 to Figure 4.91 show ODFs for AA7075-O deformed at 220°C for UT, PST and BBT strain paths respectively from the pole and neck regions of the dome samples. Pole regions of dome samples for UT and PST strain paths have a strong Cube  $\{001\}\langle 100 \rangle$  texture component while BBT show a strong Brass  $\{011\}\langle 211 \rangle$  orientation. In contrast, the neck region of the dome samples shows weak Copper  $\{112\}\langle 111 \rangle$  component for UT and PST strain paths. BBT strain path sample on the other hand shows weak Brass  $\{011\}\langle 211 \rangle$ , Copper  $\{112\}\langle 111 \rangle$  and S  $\{123\}\langle 634 \rangle$  components. Table 4.19 summarizes the texture data from PFs and ODFs for O temper dome samples deformed at 220°C.

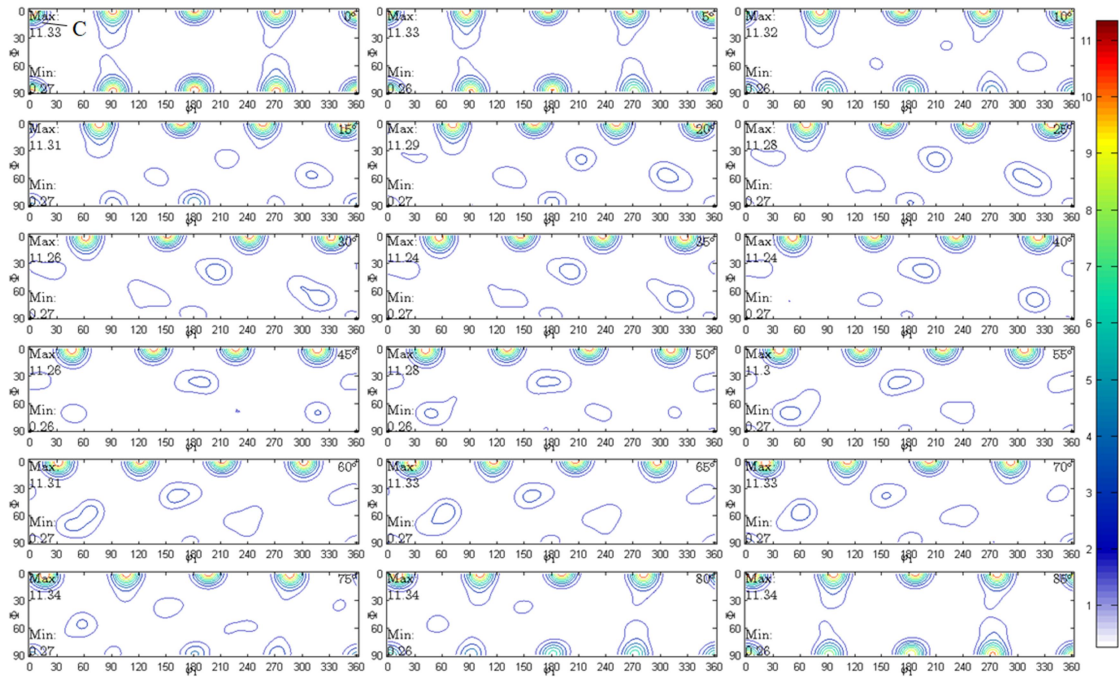


Figure 4.86 ODFs at the pole of AA7075-O UT strain path dome sample deformed at 220°C.

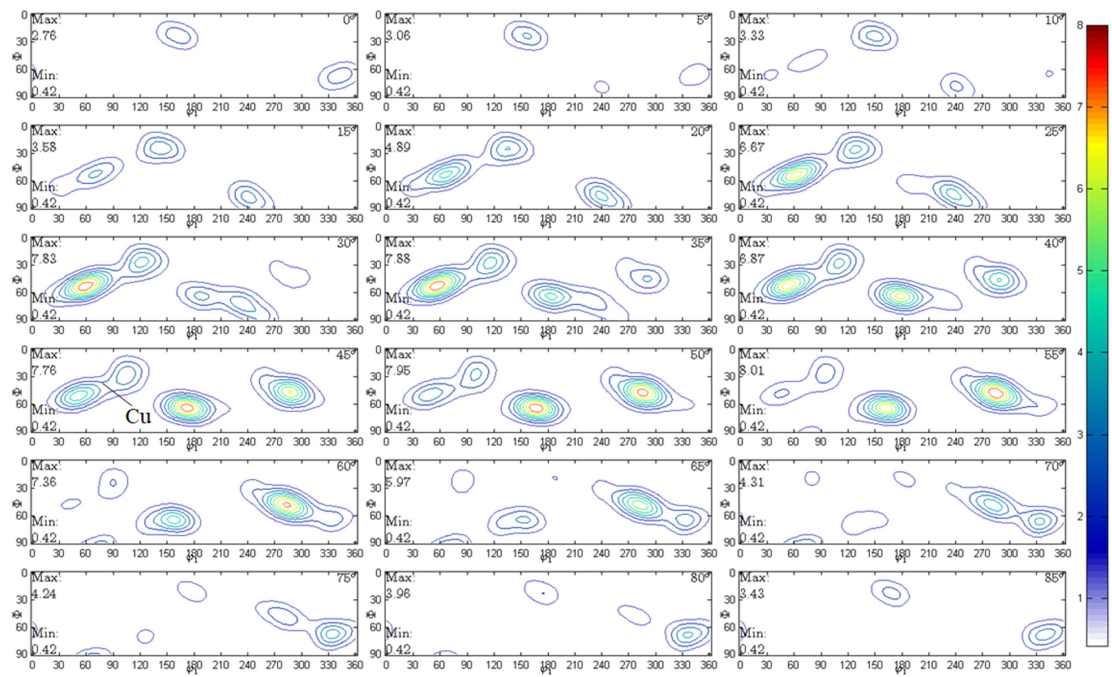


Figure 4.87 ODFs in the neck of AA7075-O UT strain path dome sample deformed at 220°C.



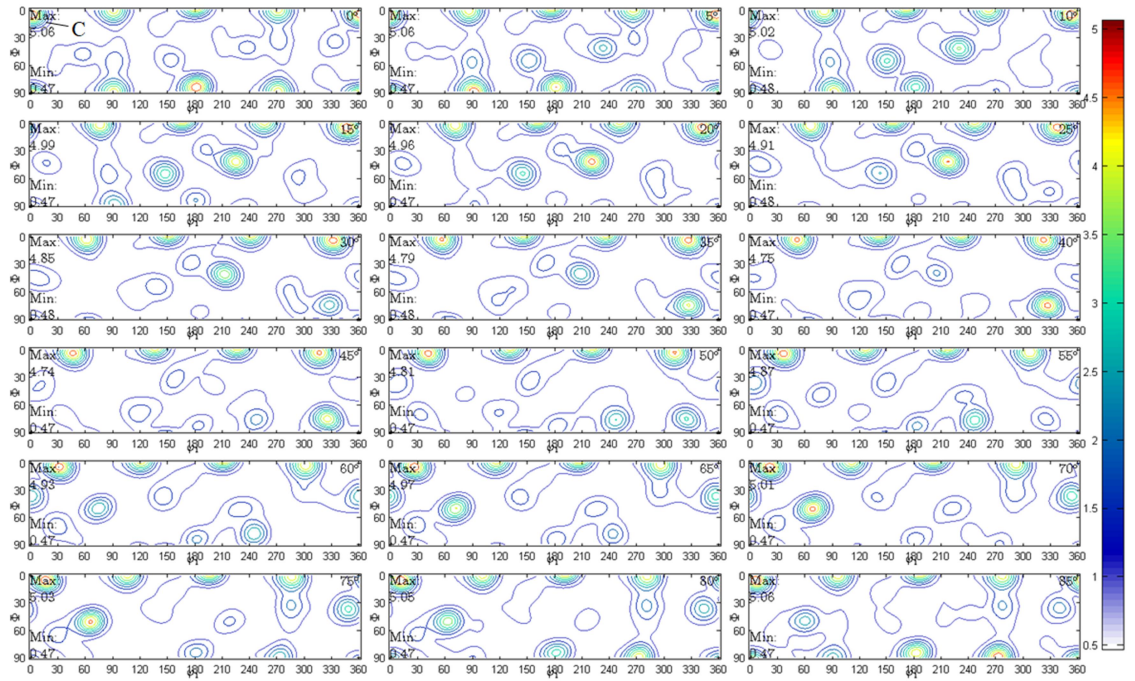


Figure 4.88 ODFs at the pole of AA7075-O PST strain path dome sample deformed at 220°C.

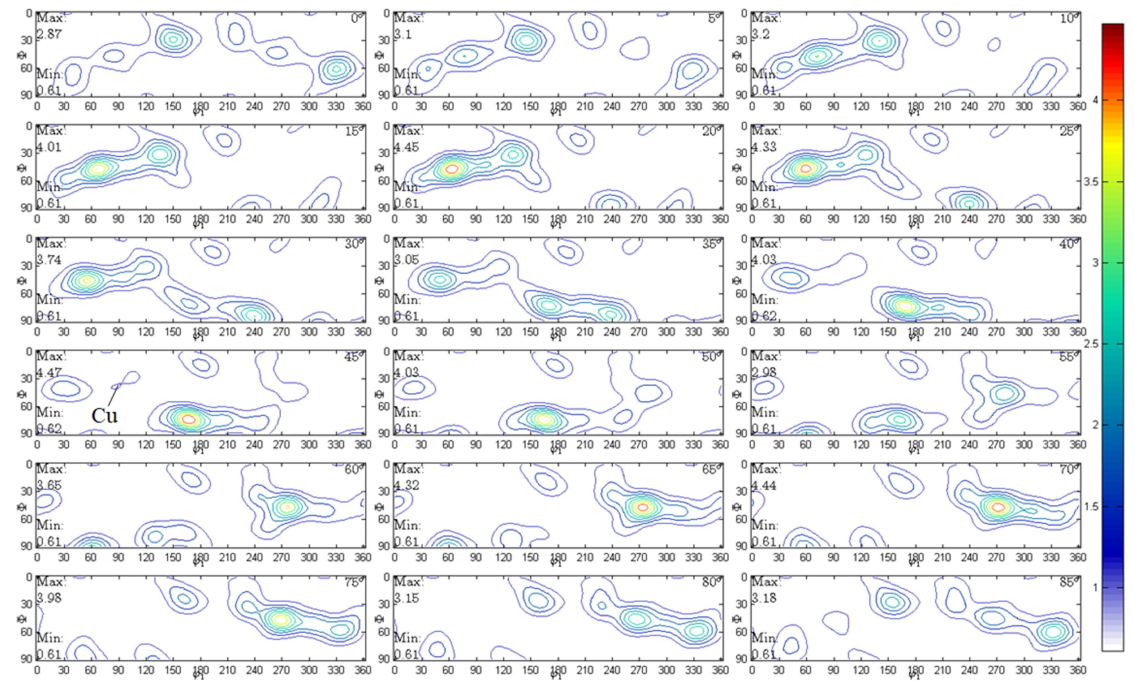


Figure 4.89 ODFs in the neck of AA7075-O PST strain path dome sample deformed at 220°C.

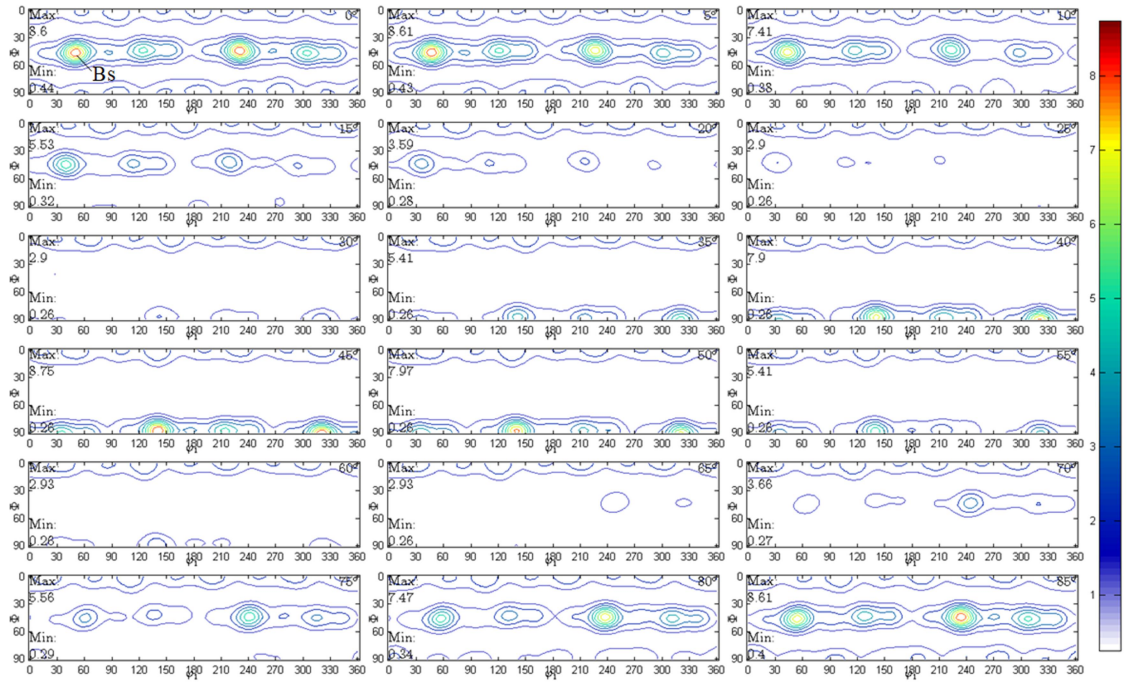


Figure 4.90 ODFs at the pole of AA7075-O BBT strain path dome sample deformed at 220°C.

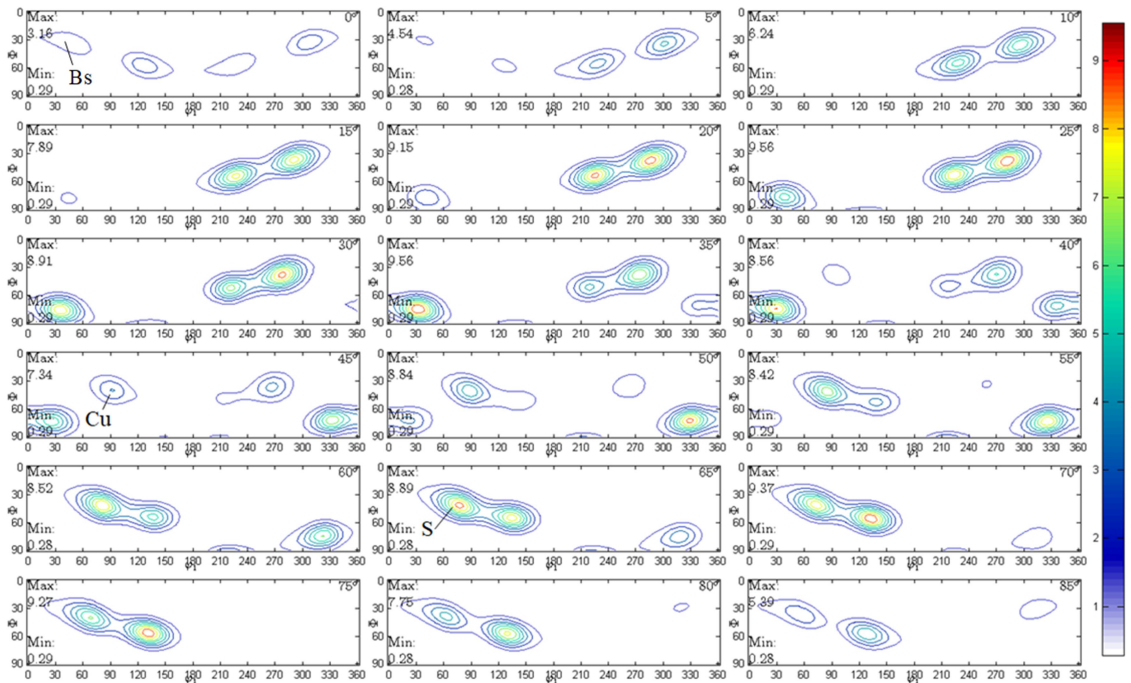


Figure 4.91 ODFs in the neck of AA7075-O BBT strain path dome sample deformed at 220°C.

Table 4.19 Texture data in the form of PFs and ODFs for {111} family of planes deformed at 220°C for O-temper dome samples.

Temper	Temperature (°C)	Scanned Region	Strain Path	Texture Type (from ODFs)	Euler Angles ( $\phi_1$ , $\phi$ and $\phi_2$ )
O	220°C	Pole	UT	Cube	0°, 0° and 0°
			PST	Cube	0°, 0° and 0°
			BBT	Brass	35°, 45° and 0°
		Neck	UT	Weak Copper	90°, 30° and 45°
			PST	Weak Copper	90°, 30° and 45°
				Weak Brass	35°, 45° and 0°
			BBT	Copper S	90°, 30° and 45° 59°, 34° and 65°

Figure 4.92 and Figure 4.93 show PFs from the pole and neck regions respectively for T6 dome samples deformed at 220°C. Cube {001}{100} texture component appears in both regions for UT and PST strain paths. In contrast, the BBT strain path sample shows a higher Brass {011}{211} texture component. These variations in texture components are probably due to the shift of the neck towards the pole region in samples that have low friction with punch. It is to be noted that texture orientation for PST from pole region in PFs is not very clear. However, ODFs for this sample shows clear orientation components. The low intensity of grain orientation for T6 samples may be attributed to the precipitation hardening, in which precipitate-dislocation interactions or solute atoms affect grain boundary migration (O Engler & Lücke, 1992) that leads to high strength and relatively low formability even at 220°C compared to O temper samples deformed at room and elevated temperature of 220°C.

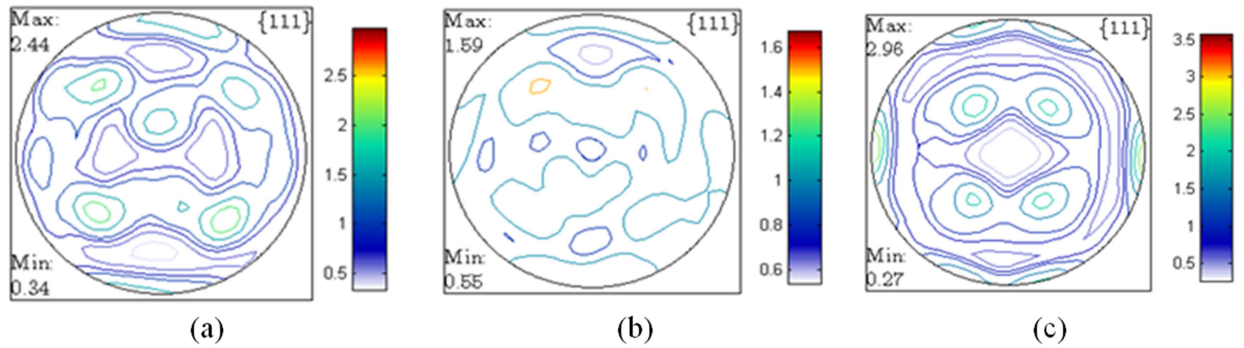


Figure 4.92  $\{111\}$  PFs from the pole region of the T6-temper dome sample deformed at 220°C corresponding to strain paths, (a) UT sample, (b) PST sample, and (c) BBT sample.

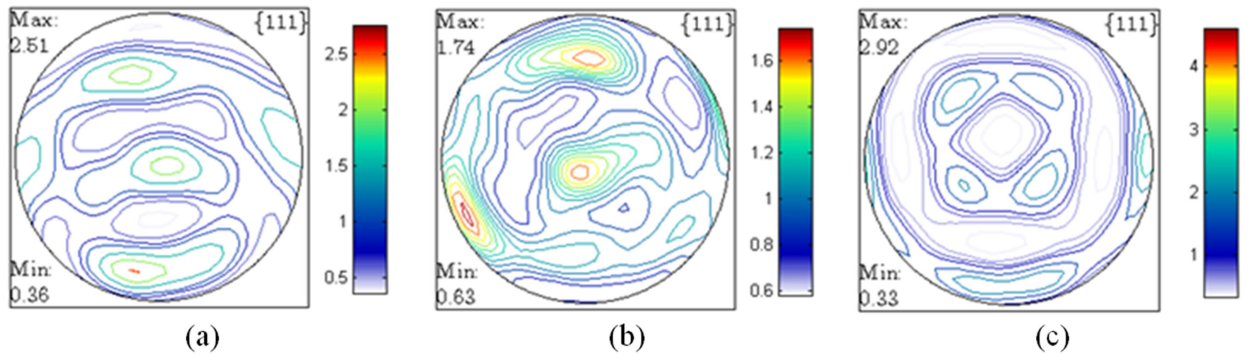


Figure 4.93  $\{111\}$  PFs from the neck region of the T6-temper dome sample deformed at 220°C corresponding to strain paths, (a) UT sample, (b) PST sample, and (c) BBT sample.

Figure 4.94 to Figure 4.99 show ODFs from pole and neck regions for T6 temper dome samples deformed at 220°C under UT, PST and BBT strain paths. The UT strain path reveals Cube  $\{001\}\langle 100 \rangle$  component in pole region but shows Brass and S orientations in the neck region. PST sample, on the other hand, shows strong Cube and S components with weak Copper component in pole region while neck region exhibits Copper and S components with no presence of Cube orientation. In contrast to UT and PST dome



samples, BBT strain path sample shows Brass component in the pole region but Brass and S components in the neck region. All texture orientation components in the neck region reveal deformation components of Copper  $\{112\}\langle 111 \rangle$  and/or Brass  $\{011\}\langle 211 \rangle$  and/or S  $\{123\}\langle 634 \rangle$  due to large plastic deformation in the neck region for all strain paths. BBT sample shows Brass  $\{011\}\langle 211 \rangle$  texture component in the pole region from shift in the neck location to the pole position due to lower friction contact conditions between the punch and sheet (see Figure 4.100). As a consequence, the resulting shear band moves towards sample pole creating neck region and the texture orientation changes to deformed texture. Table 4.20 summarize texture data from PFs and ODFs for T6 temper dome samples deformed at 220°C.

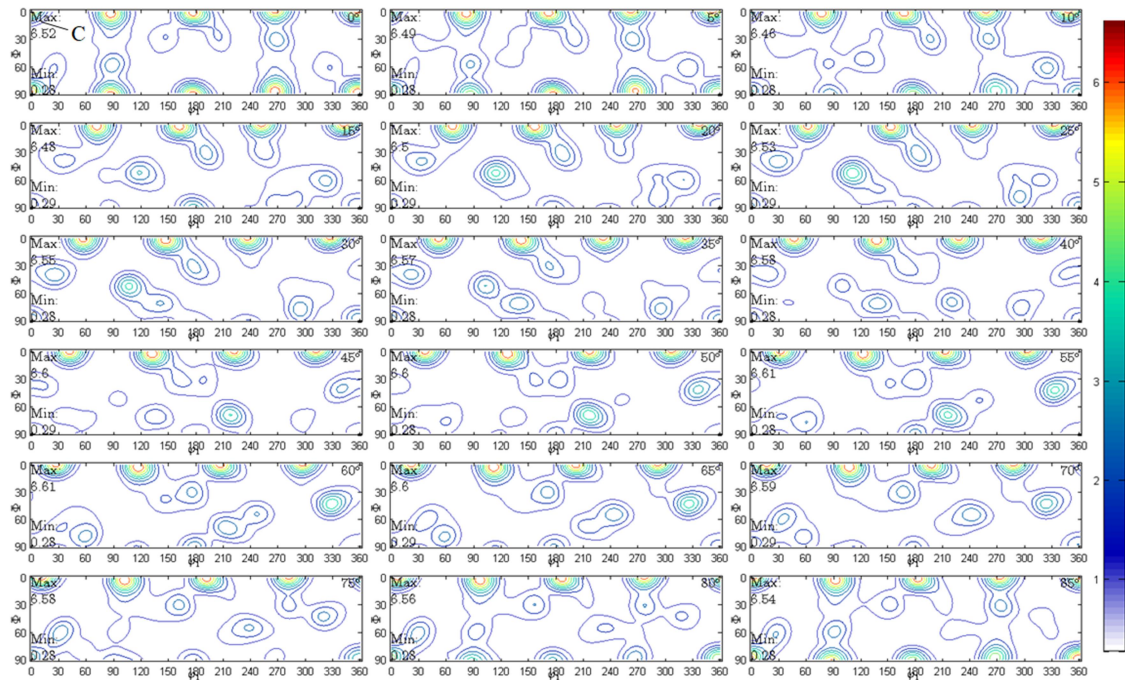


Figure 4.94 ODFs at the pole of AA7075-T6 UT strain path dome sample deformed at 220°C.



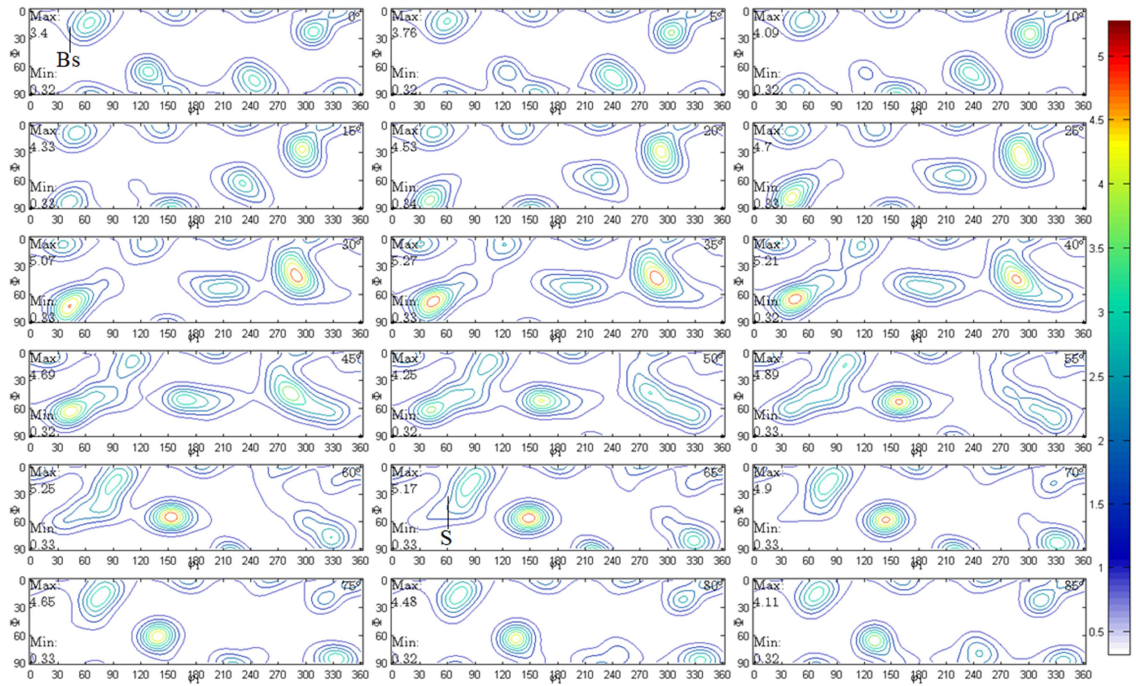


Figure 4.95 ODFs in the neck of AA7075-T6 UT strain path dome sample deformed at 220°C.

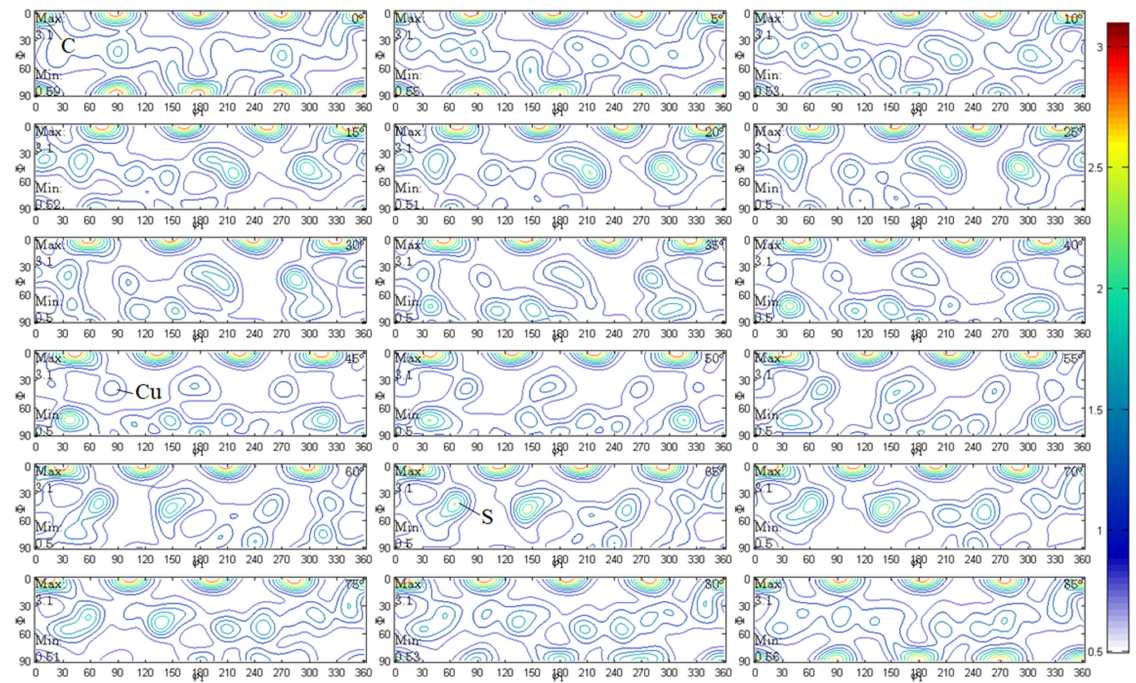


Figure 4.96 ODFs at the pole of AA7075-T6 PST strain path dome sample deformed at 220°C.

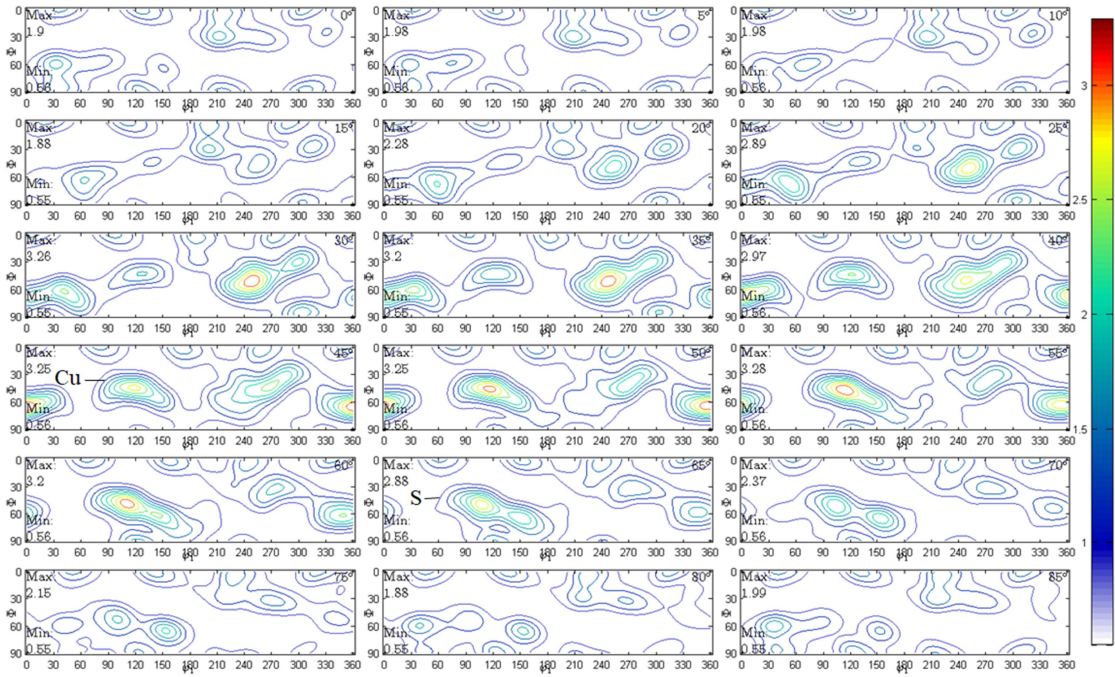


Figure 4.97 ODFs in the neck of AA7075-T6 PST strain path dome sample deformed at 220°C.

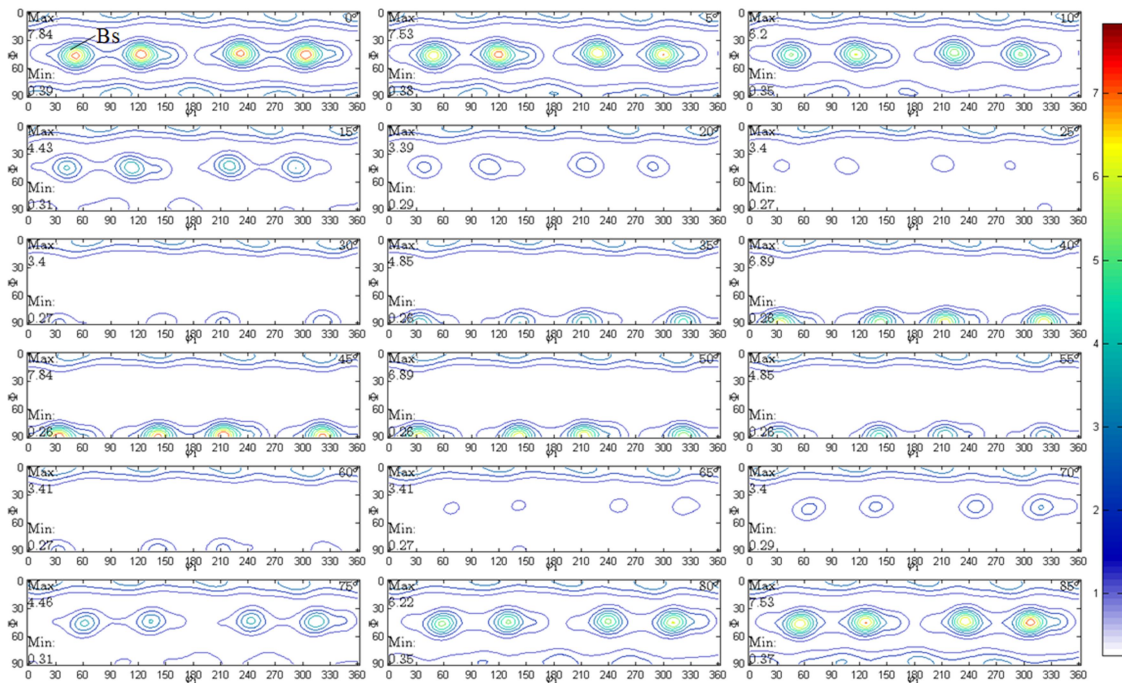


Figure 4.98 ODFs at the pole of AA7075-T6 BBT strain path dome sample deformed at 220°C.



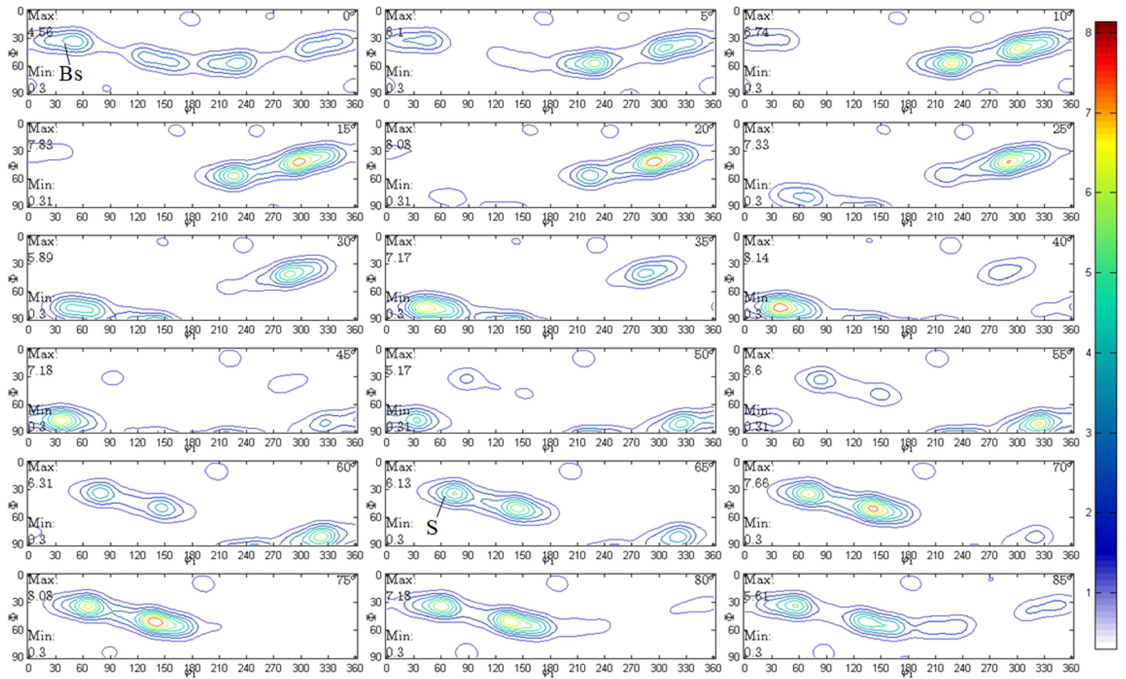


Figure 4.99 ODFs in the neck of AA7075-T6 BBT strain path dome sample deformed at 220°C.

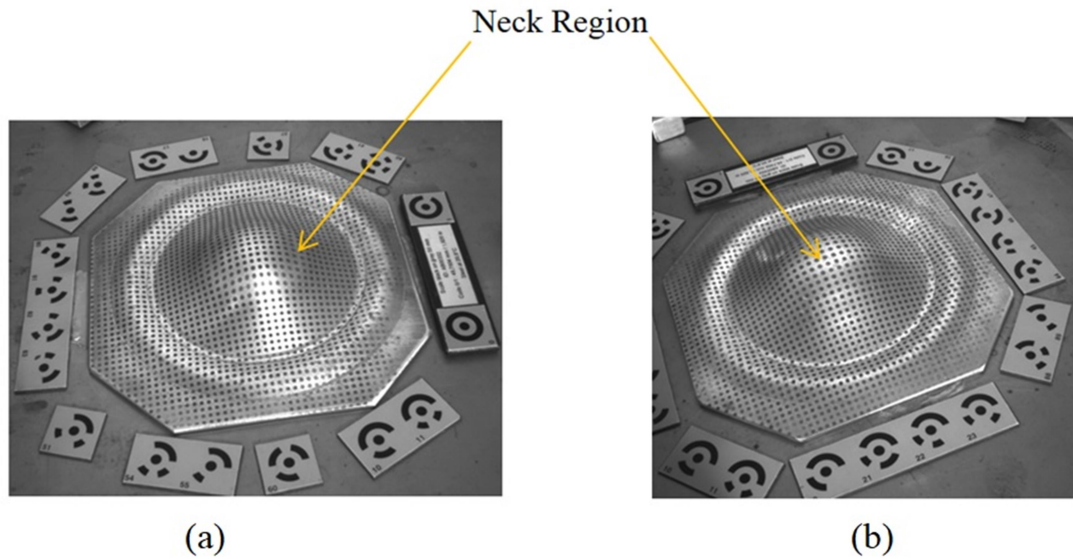


Figure 4.100 Effect of punch-sheet contact lubrication conditions on neck region location for AA7075-T6 full sample deformed at 220°C; (a) punch-sheet dry contact and (b) 1.5 mm thick silicon rubber sheet located between punch and sheet metal during deformation.

Table 4.20 Texture data in the form of PFs and ODFs for {111} family of planes deformed at 220°C for T6-temper dome samples.

Temper	Temperature (°C)	Scanned Region	Strain Path	Texture Type (from ODFs)	Euler Angles ( $\phi_1$ , $\phi$ and $\phi_2$ )
T6	220	Pole	UT	Cube	0°, 0° & 0°
				Cube	0°, 0° & 0°
			PST	Weak Copper S	90°, 30° & 45° 59°, 34° & 65°
			BBT	Brass	35°, 45° & 0°
		Neck	UT	Brass Weak S	35°, 45° & 0° 59°, 34° & 65°
			PST	Weak Copper Weak S	90°, 30° & 45° 59°, 34° & 65°
			BBT	Brass S	35°, 45° & 0° 59°, 34° & 65°

## **5-Analytical Prediction of FLD for AA7075-O Sheet**

This chapter presents results of analytical predictions of isothermal forming limit diagrams (FLDs) of AA7075-O (full annealed) aluminum sheet at room and several elevated temperatures based on well-known Marciniak-Kuczynski (or M-K) model. Two different strain rate and temperature dependent constitutive material models available in the literature have been utilized within the M-K method to carry out room and elevated temperature FLD predictions. The predicted FLDs are compared with the experimental FLDs presented earlier in Chapter 4.

This chapter is arranged as follows. First, a brief introduction to the original M-K methodology is provided where a through-thickness groove perpendicular to the major stress axis is considered. Second, a well-known Hutchinson-Neale (H-N) model that considers various groove orientations in the M-K analysis is described and its basic features discussed. Third, two different constitutive materials laws proposed by Field-Backofen (F-B) (Hua et al., 2014) and Voce-Kocks (V-K) (Kocks, 1976) are presented for their use in Hutchinson-Neale model based M-K analysis for FLD prediction of AA7075-O sheet.

### **5.1 M-K methodology**

As mentioned in the Literature Review Chapter, sub-section 2.5, the experimental FLD determination is often expensive and time consuming especially at elevated temperature and at higher strain rates (or test speeds). Therefore, much effort has been devoted towards development of numerical models for FLD prediction over the years. While

several numerical models are available in the literature, there are very few that encompass the entire range of material parameters and characteristics, specimen geometry and forming test parameters and predict suitable shapes and magnitudes of FLCs. The attempt towards reliable prediction of FLCs is still continuing, especially with respect to elevated temperature and strain rate dependent FLDs of complex material systems such as high strength aluminum alloys.

One of the most acceptable general approaches towards FLD prediction was proposed by Marciniak and Kuczynski (or M-K) in the 1970s (Banabic, 2010; Z Marciniak, 1965; Zdzislaw Marciniak & Kuczyński, 1967; Zdzisław Marciniak et al., 1973). The power of the method lies in its physical basis, and its ease of use in term of measurements of the model input parameters. In this section, a brief review of the M-K method is presented.

M-K method is an analytical method for determination of FLD based on theory of plasticity and mechanics of sheet forming. It assumes a small geometric imperfection factor (or f-value) in the form of a thickness inhomogeneity in the sheet in the original model (see Figure 5.1 below). This inhomogeneity factor is useful but difficult to determine quantitatively. It is useful because its incorporation in the M-K method gives realistic FLD shapes. However, it is difficult to quantify because it treats inhomogeneity of the material in its simplest form (a thickness inhomogeneity) whereas in reality there are multiple sources of inhomogeneity in the material at various microstructural scales (for example from surface roughness and its evolution, texture and its evolution, material damage and its evolution etc.). There is no guidance available in the literature for its

specific value. However, most researchers have used this inhomogeneity factor as a fit parameter to the experimental obtained limit strain values along a specific strain path.

By assuming a state of plane stress, proportional straining, and comparing strains inside and outside the assumed thickness imperfection, a limit strain for a desired strain path is obtained. The method allows for determining a locus of such limit strains covering a range of strain paths from tension-compression to tension-tension region in the 2D principle strain space (same as the experimental FLD). This locus is essentially an analytical FLD for the sheet material. The M-K model has been extended over the years to include new constitutive equations with new anisotropic yield functions and hardening laws, strain rate and temperature dependency, crystallographic texture parameters, ductile damage parameters and others. It has many advantages such as prediction of the effect of uniaxial tensile material parameters and material anisotropy on limit strains. While it has good general capability for predicting the shape of the FLD from easily measurable material parameters, it does suffer from inaccurate quantitative predictions in many material systems. The results tend to be sensitive to choice of the imperfection factor (or  $f$ -value), and many researchers have chosen rather arbitrary values of imperfection to match M-K based FLD to the experimental FLD. In some cases, the model is calibrated with a point on the experimental FLD in order to obtain the value of the imperfection parameter. There are very few studies (Jain et al., 1996; Kim & Kim, 1983; Nurcheshmeh & Green, 2011; Parmar et al., 1977) where a judicious choice of imperfection factor has been made based on material considerations such as material surface roughness or the internal inhomogeneity (such as voids).

In fact, such imperfection is often physically present in most rolled sheet materials in the form of roll lines. This imperfection was represented by an imperfection factor  $f_0$  defined as a ratio of the initial thickness in the imperfection (or groove)  $t_0^B$  and nominal thickness away from the groove (i. e., in the homogeneous region),  $t_0^A$ . Imperfection factor can be written as:

$$f_0 = t_0^B / t_0^A \quad (1)$$

Since  $t_0^B$  is less than  $t_0^A$ , the imperfection factor is less than 1. In the original M-K analysis, the groove is considered perpendicular to the major principal stress axis, as shown in Figure 5.1.

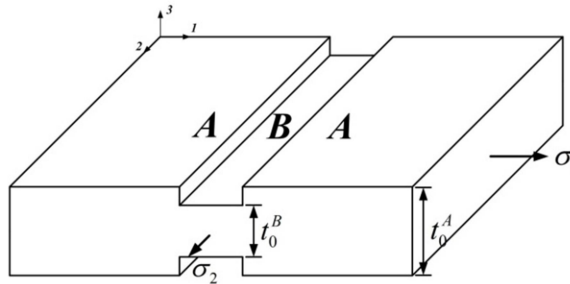


Figure 5.1 A schematic drawing of sheet geometry with an imperfection band B in the thickness direction and perpendicular to the major stress axis from the original M-K model.

The original M-K analysis assumed in-plane deformation and a plane stress state (i.e., through-thickness normal stress  $\sigma_3$  is assumed to be zero) in the loaded sheet, isotropic Mises yield criterion, and Levy-Mises flow rule. Also, the minor (or second principle) strain component is assumed to be the same in regions A and B throughout the loading



process ( $\varepsilon_2^A = \varepsilon_2^B$ ), a so-called strain compatibility condition. Furthermore, the M-K method analyzes the strain state in regions A and B of the sheet under various proportional stress ratios (or loading paths). This is expressed mathematically as:

$$\alpha = \frac{\sigma_2}{\sigma_1} = \text{constant} \quad (2)$$

where  $\sigma_1$  and  $\sigma_2$  are the major and minor in-plane principal stresses as shown in A schematic drawing of sheet geometry with an imperfection band B in the thickness direction and perpendicular to the major stress axis from the original M-K model. According to the Mises yield criterion, the effective stress  $\bar{\sigma}$  in principal stress space can be expressed as:

$$\bar{\sigma} = \frac{1}{\sqrt{2}} \sqrt{(\sigma_1 - \sigma_2)^2 + (\sigma_2 - \sigma_3)^2 + (\sigma_3 - \sigma_1)^2} \quad (3)$$

From the plane stress assumption,  $\sigma_3 = 0$ , and eqns. (2) and (3) above, the following equation can be derived:

$$\phi = \frac{\bar{\sigma}}{\sigma_1} = \sqrt{\alpha^2 - \alpha + 1} \quad (4)$$

where  $\phi$  is another dimensionless stress ratio between Mises effective stress and major stress. Levy-Mises plastic flow rule relating stress and strain increments can be written as:

$$\frac{d\bar{\varepsilon}}{2\phi} = \frac{d\varepsilon_1}{2-\alpha} = \frac{d\varepsilon_2}{2\alpha-1} = \frac{d\varepsilon_3}{-1-\alpha} \quad (5)$$

where  $d\varepsilon_1$ ,  $d\varepsilon_2$ ,  $d\varepsilon_3$  and  $d\bar{\varepsilon}$  represent the major, minor, through-thickness principal strain, and effective strain increments respectively. On defining two strain ratios,  $\rho$  and  $\beta$ , as follows,

$$\rho = \frac{d\varepsilon_2}{d\varepsilon_1}; \beta = \frac{d\bar{\varepsilon}}{d\varepsilon_1} \quad (6)$$

one obtains the following relationships between strain ratios and stress ratios from eqns. (5) and (6):

$$\rho = \frac{2\alpha - 1}{2 - \alpha}; \beta = \frac{2\phi}{2 - \alpha} \quad (7)$$

Now, returning to Figure 5.1, a force equilibrium between homogeneous region A and groove region B can be written as:

$$\sigma_1^A t^A = \sigma_1^B t^B \quad (8)$$

In eqn. (8),  $t^A$  and  $t^B$  represent current thicknesses of regions A and B respectively in the plastically loaded state of the sheet material. The relationship between the original and current thickness and the through-thickness principal strain can be written as:

$$\varepsilon_3 = \ln \frac{t}{t_0} \quad (9)$$

From eqns. (1), (8) and (9), one obtains:

$$\sigma_1^A e^{\varepsilon_3^A} = \sigma_1^B f_0 e^{\varepsilon_3^B} \quad (10)$$

From eqn. (4), eq. (10) can be written as:

$$\bar{\sigma}^A = \bar{\sigma}^B \frac{\phi^A}{\phi^B} f_0 e^{\varepsilon_3^B - \varepsilon_3^A} \quad (11)$$

where,  $\phi^A = \frac{\bar{\sigma}^A}{\sigma_1^A}$  and  $\phi^B = \frac{\bar{\sigma}^B}{\sigma_1^B}$

The Field and Backofen constitutive equation (Hua et al., 2014; Kotkunde et al., 2014; Lang et al., 2015; Tsao et al., 2012) describing the material flow behaviour is expressed as:

$$\sigma = K \varepsilon^n \dot{\varepsilon}^m \quad (12)$$

The following force equilibrium equation can be obtained by combining eqns. (11) and (12):

$$(\bar{\varepsilon}_A + d\bar{\varepsilon}_A)^n (\dot{\varepsilon}_A)^m \phi_B = (\bar{\varepsilon}_B + d\bar{\varepsilon}_B)^n (\dot{\varepsilon}_B)^m \phi_A f_0 \exp(\varepsilon_3^B - \varepsilon_3^A) \quad (13)$$

By solving eqn. (13) for a given stress state, the strain states in regions A and B can be determined in increments. The forming limit of the sheet material (i.e., onset of localized necking) is reached when the effective strain increment in the groove becomes significantly larger than the effective strain increment in the homogeneous region just outside of the groove. In other words,  $\Delta\bar{\varepsilon}^B \gg \Delta\bar{\varepsilon}^A$  is satisfied. Typically, onset of localized necking of the sheet is assumed when  $\bar{\varepsilon}_1^B > 10\bar{\varepsilon}_1^A$ . A direct solution of eqn. (13) is considered complex. Therefore, a Newton-Raphson iteration procedure is employed as described below:

- 1) For a given load path (i.e.,  $1 \geq \alpha \geq 0$ ),  $\phi^A$ ,  $\rho^A$  and  $\beta^A$  can be calculated according to Eqns. (4) and (7).
- 2) Given an initial major principal strain increment of  $\Delta\varepsilon_1^A = 0.0001$ ,  $\Delta\varepsilon_1^B = \Delta\varepsilon_1^A$  is used to obtain a first guess of  $\Delta\varepsilon_1^B$ ;

- 3) According to the constancy of volume during plastic deformation, the following equations can be obtained:

$$\begin{cases} \Delta \varepsilon_2^A = \rho^A \Delta \varepsilon_1^A \\ \Delta \bar{\varepsilon}^A = \beta^A \Delta \varepsilon_1^A \\ \Delta \varepsilon_3^A = -(1 + \rho^A) \Delta \varepsilon_1^A \end{cases}$$

- 4) Based on strain compatibility condition,  $\Delta \varepsilon_2^A = \Delta \varepsilon_2^B$ , the quantities  $\rho^B$ ,  $\alpha^B$ ,  $\phi^B$  and  $\beta^B$  in the region B can be obtained as follows:

$$\begin{cases} \rho^B = \frac{\Delta \varepsilon_2^B}{\Delta \varepsilon_1^B} \\ \alpha^B = \frac{\sigma_2^B}{\sigma_1^B} = \frac{2\rho^B + 1}{\rho^B + 2} \\ \phi^B = \frac{\bar{\sigma}^B}{\sigma_1^B} = \sqrt{(\alpha^B)^2 - \alpha^B + 1} \\ \beta^B = \frac{2\phi^B}{2 - \alpha^B} \end{cases} \quad (1)$$

- 5) According to the constancy of volume during plastic deformation, equivalent strain increment and through-thickness strain increment in the region B can be calculated as follows :

$$\begin{cases} \Delta \bar{\varepsilon}^B = \beta^B \Delta \varepsilon_1^B \\ \Delta \varepsilon_3^B = -(1 + \rho^B) \Delta \varepsilon_1^B \end{cases} \quad (2)$$

- 6) On substituting  $\bar{\varepsilon}^A$ ,  $\bar{\varepsilon}^B$ ,  $\varepsilon_3^A$ ,  $\varepsilon_3^B$ ,  $\phi^A$  and  $\phi^B$  into the force equilibrium Eq. (11), the following equation can be derived:

$$\begin{cases} F = \bar{\sigma}^A - \bar{\sigma}^B \frac{\phi^A}{\phi^B} f_0 \exp(\varepsilon_3^B - \varepsilon_3^A + \Delta\varepsilon_3^B - \Delta\varepsilon_3^A) \\ \bar{\sigma}^A = \bar{\sigma}^A(\bar{\varepsilon}^A + \Delta\bar{\varepsilon}^A) \\ \bar{\sigma}^B = \bar{\sigma}^B(\bar{\varepsilon}^B + \Delta\bar{\varepsilon}^B) \end{cases} \quad (3)$$

- 7) The force balance condition  $F = 0$  in Eq. (3) should be satisfied. Nevertheless, for an arbitrary  $\Delta\varepsilon_1^B$  value, the force equilibrium probably would not be obtained. Hence, the Newton-Raphson iteration method is employed to update  $\Delta\varepsilon_1^B$  until  $F$  attains a negligibly value (typically less than  $1.0 \times 10^{-10}$ ). The Newton-Raphson iteration is then stopped and the stress and strain states in regions A and B, such as  $\varepsilon_i^A, \varepsilon_i^B, \bar{\varepsilon}^A, \bar{\varepsilon}^B, \sigma_i^A, \sigma_i^B, \bar{\sigma}^A$  and  $\bar{\sigma}^B$  (where  $i = 1, 2, 3$ ) are updated.
- 8) The ratio of  $\Delta\bar{\varepsilon}^B / \Delta\bar{\varepsilon}^A$  is then calculated to determine whether necking occurs. If  $\Delta\bar{\varepsilon}^B / \Delta\bar{\varepsilon}^A \geq 10$  is satisfied, the calculation is stopped and the major and minor strains of  $\varepsilon_1^A$  and  $\varepsilon_2^A$  are recorded as the forming limit strains for the given load path. Otherwise, another increment of  $\Delta\varepsilon_1^A$  is applied and steps 2-8 are repeated until condition  $\Delta\bar{\varepsilon}^B / \Delta\bar{\varepsilon}^A \geq 10$  is satisfied.
- 9) After the forming limit strain is determined for a given load path, another load path condition is iterated upon and the steps 1-8 are repeated. When all the load paths from uniaxial tension ( $\alpha = 0$ ) to biaxial tension ( $\alpha = 1$ ) are covered in the M-K analysis, a locus of all limit strain states gives the predicted FLC based on the M-K model.

For completeness, some papers that deal with the prediction of FLD by taking into consideration sheet material yield and work hardening anisotropy by using different constitutive material laws within the M-K approach will be first reviewed. Butuc et al. predicted the FLC of AA6016-T4 precipitation hardening aluminum sheet (Butuc et al., 2003) at room temperature by implementing different yield functions of Von Mises isotropic yield function, quadratic Hill 1948 (Hill, 1948), non-quadratic Hill anisotropic criterion 1979 (Hill, 1979) and Barlat Yld96 yield function (Barlat et al., 1997) in M-K method with Swift and Voce hardening laws. Hardening law (or constitutive law) parameters were obtained by fitting experimental flow stress-strain curves (plastic strain part) as shown in Figure 5.2.

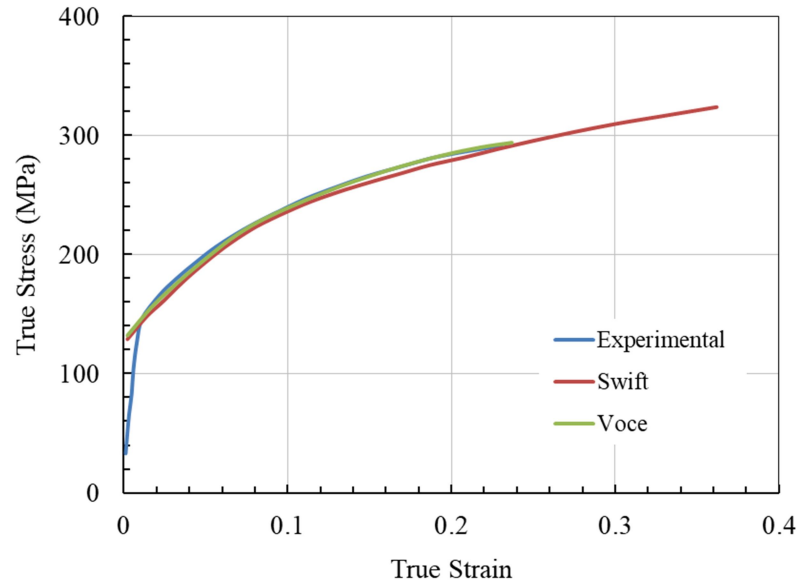


Figure 5.2 Experimental digitized flow stress-strain curve for AA6016-T4 sheet and fitted curves of Swift and Voce hardening laws (Butuc et al., 2003).

The effect of Swift and Voce constitutive laws on forming limit for AA6016-T4 sheet metal are illustrated in Figure 5.3 and Figure 5.4 respectively. It is obvious that forming limits for all yield criteria used in conjunction with Swift hardening law are located at limit strain higher than those calculated using Voce hardening law. This is probably due to better quality of fit to the experimental uniaxial tensile stress-strain curves with Voce equation and a good extrapolation for tensile curves beyond the experimental range of data. Also, predicted FLCs show good agreement with experimental FLC when Voce constitutive law is utilized with Yld96 Barlat anisotropic yield function.

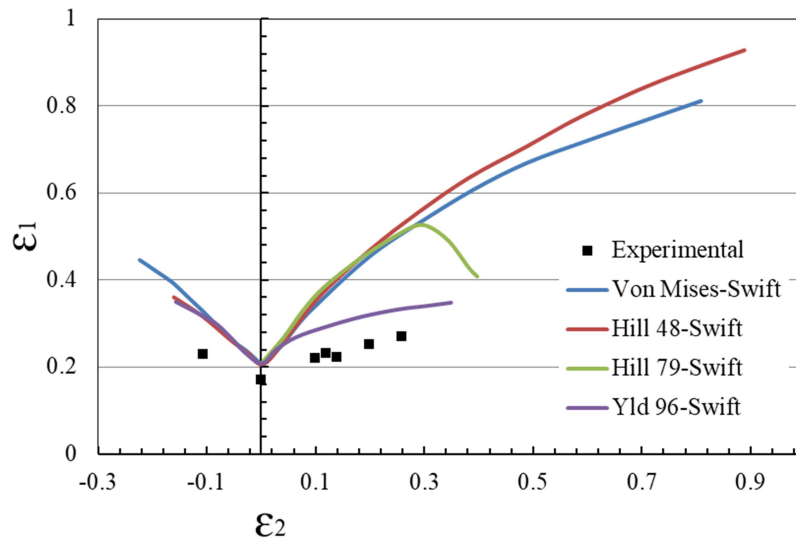


Figure 5.3 Digitized experimental and predicted FLDs with Swift hardening law (Butuc et al., 2003).

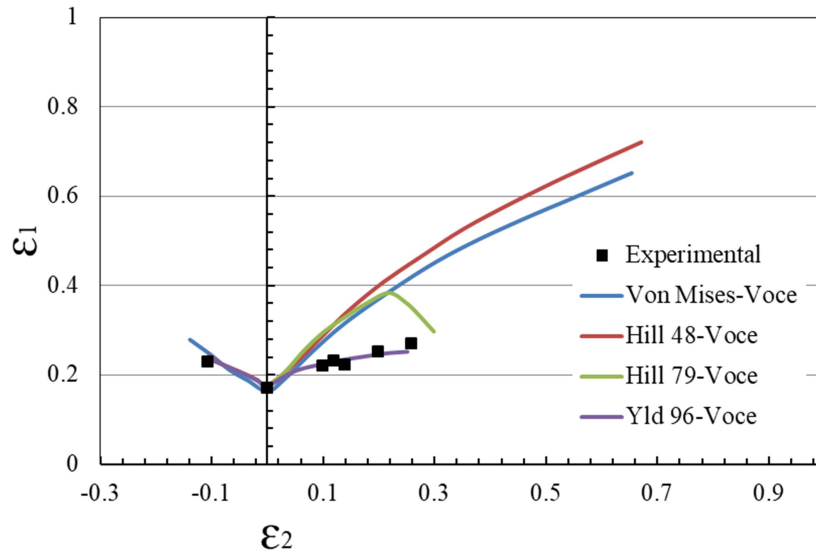


Figure 5.4 Digitized experimental and predicted FLDs with Voce hardening law (Butuc et al., 2003).

The above approach to predicting FLCs relies on continuum considerations where the quality of predicted FLCs are dependent on the quality of fit of the chosen yield criterion and hardening law to experimental data. However, such an approach has limitations where microstructure and crystallographic texture of sheet materials plays a significant role in governing plastic flow localization and limit strains, i.e., yield surface shape and stress-plastic strain curve are influenced by microstructure features such as precipitates and texture. Also, an imperfection coefficient  $f_0 = 0.998$  was implemented for all FLD predictions. Moreover, the author did not mention the sheet metal thickness or its thermal history i.e., the natural ageing (T4 temper) heat treatment procedures and the resulting microstructure.

Yang Xiying (Yang et al., 2015) used M-K model and modified M-K approach based on ductile fracture criterion, proposed by Takuda et al. (Takuda et al., 1999), to predict



forming limit for AA7075-O at room temperature. The authors obtained experimental FLC points via non-standard tests such as uniaxial tension, wide plate bending and hydraulic bulge tests. A comparison between experimental and M-K theory based predicted FLCs was made using different values for imperfection factor ( $f$ ), as shown in Figure 5.5. It was concluded that the imperfection factor has a critical effect on the forming limit at plane strain path in which a value of  $f = 0.96$  gave a much lower strain limit in plane strain than the experimental value. Also, it was observed that by increasing strain ratio ( $d\epsilon_{1b} / d\epsilon_{1a}$ ) an improvement in plane strain forming limit can be achieved.

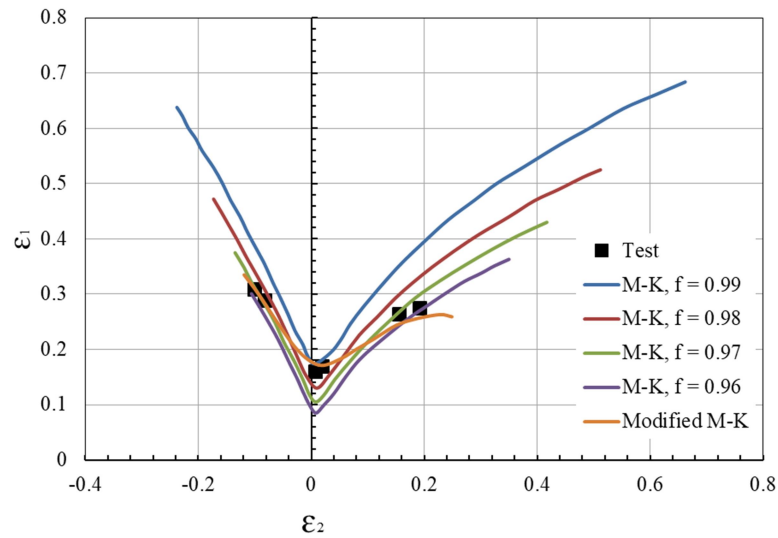


Figure 5.5 Digitized experimental and predicted FLDs for AA7075-O at room temperature with different inhomogeneity factors (Yang et al., 2015).

Sowerby and Duncan (Sowerby & Duncan, 1971) utilized quadratic Hill and isotropic Mises yield criterion within M-K framework to investigate the effect of plastic strain ratio ( $r$ -value) and strain hardening coefficient ( $n$ ) on the tension – tension side of the FLD. It was concluded that, for  $r = 1$  (or isotropic material), as  $n$  increases the limit strain

increases, and for a certain  $n$  value the limit strain increase from plane strain path up to equi-biaxial strain path (the largest increase in limit strain was obtained at  $n=1$  which is similar to FLD of half-hard aluminum or H14 temper as shown in Figure 5.6). Also, for a typical  $n$  value for a formable sheet (such as  $n = 0.2$ ), as  $r$  value increases the limit strain decreases for balanced biaxial tension and there is no effect of  $r$  value on plane strain condition as shown in Figure 5.7. Therefore, a high stretch forming in biaxial strain side in FLD can be achieved for materials have relatively high  $n$  and low  $r$ . This work utilized an arbitrary initial imperfection factor  $f_0$  of 0.98 and an initial pre-strain value  $\epsilon_0 = 0.0014$  in the Swift hardening law which were similar to those values used by Z. Marciniak and K. Kuczynski (Zdzislaw Marciniak & Kuczyński, 1967).

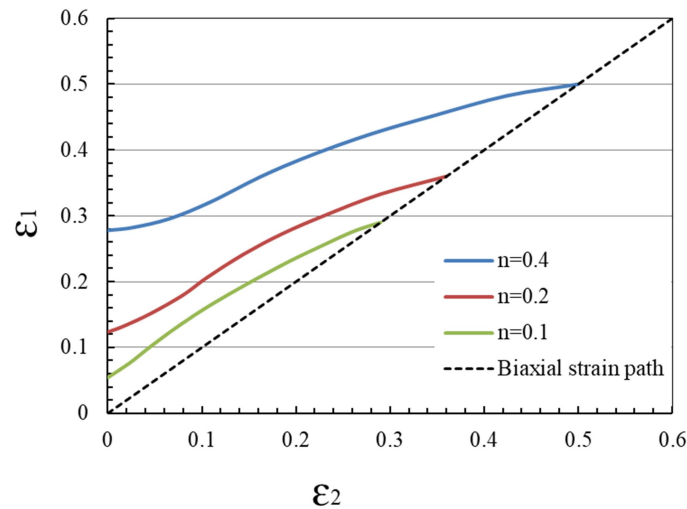


Figure 5.6 Effect of strain hardening coefficient  $n$  on stretch forming for tension – tension side of theoretical FLD for three different isotropic materials ( $r = 1$ ,  $\epsilon_0 = 0.0014$ ,  $f_0 = 0.98$ ) (Sowerby & Duncan, 1971).

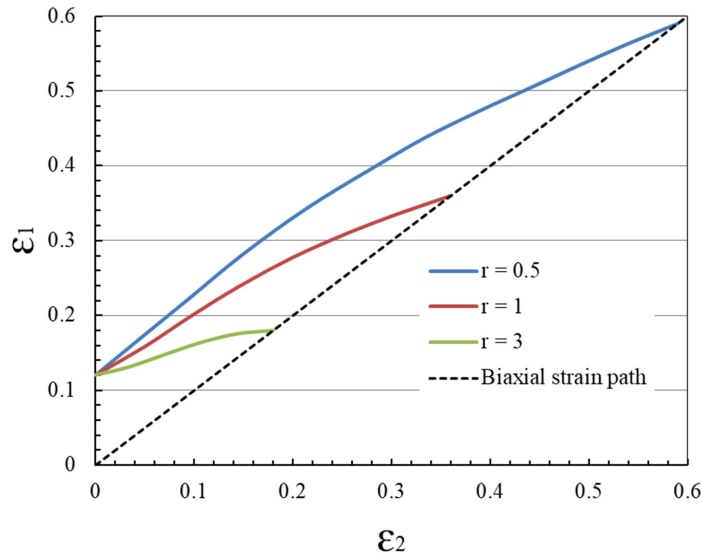


Figure 5.7 Effect of plastic strain ratio  $r$  on stretch forming for tension – tension side of theoretical FLD for three different materials ( $n = 0.2$ ,  $\varepsilon_0 = 0.0014$ ,  $f_0 = 0.98$ ) (Sowerby & Duncan, 1971).

Aretz (Aretz, 2007) considered different necking models by selecting diffuse necking model of Swift (Swift, 1952) and localized necking model of Hill (Hill, 1952) as well as plastic anisotropy, to predict forming limit of precipitation hardening aluminum alloy AA6016-T4. Experimental FLC and material properties of the adopted alloy were taken from Butuc et al (Butuc et al., 2003). The author implemented Barlat Yld96 and Yld2003 yield functions in his work. The predicted FLCs were in good agreement with experimental one in the stretching side when using Yld96 yield criterion with rigid-plastic and elastic-plastic material assumptions (see Figure 5.8). This result of lower formability for elastic-plastic model compared with rigid-plastic model related to the biaxial anisotropy ( $r$  value) which not included in the Yld96 yield function fitting. The effect of plastic strain ratio ( $r$  value) was also investigated and it was found to have some effect on FLD predictions as shown in Figure 5.9. The predicted FLD was enhanced by using  $r$ -

value of 1.2 instead of 1.58 in Yld2003 elastic-plastic model. This work also utilized an arbitrary inhomogeneity factor  $f_0$  of 0.998, same as in the Butuc simulation. Also, the author relied on the experimental work of Butuc et al., and did not provide details of sheet thickness, microstructure and thermal history (or heat treatment) of the adopted AA6016-T4 sheet material.

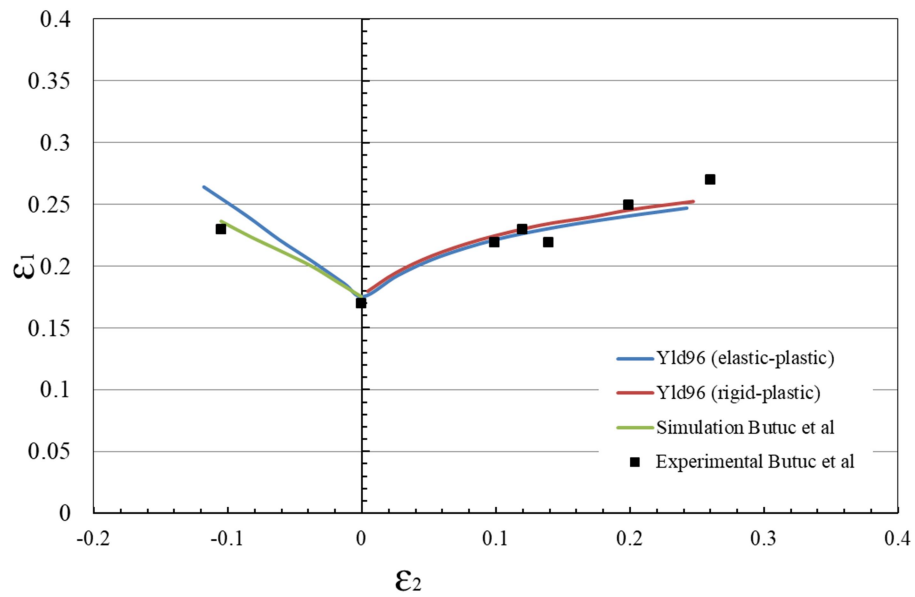


Figure 5.8 Digitized experimental and predicted FLD for AA6016-T4 by using Yld96 yield function (Aretz, 2007; Butuc et al., 2003).

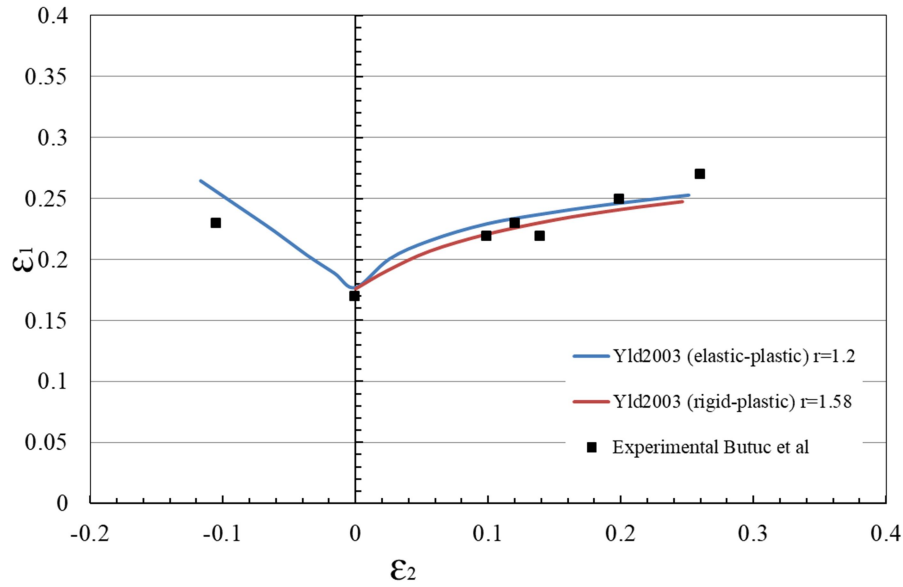


Figure 5.9 Digitized experimental and predicted FLD for AA6016-T4 by using Yld2003 yield function using different biaxial  $r$  value (Aretz, 2007; Butuc et al., 2003).

In the next sub-section, models related to M-K based prediction of FLC of current AA7075-O sheet material at a range of temperatures are presented.

## 5.2 Hutchinson-Neale (H-N) model

Hutchinson-Neale (Hutchinson & Neale, 1978) model is considered as a modification of M-K model in which an inclined groove is defined as a geometrical non-homogeneity in the sheet metal as illustrated in Figure 5.10. This inclined groove evolves during deformation to obtain a realistic prediction for left side of FLD by changing imperfection orientation angle in a range between  $0^\circ$  and  $90^\circ$  to find the minimum forming limit and extend the right side of FLD which can be predicted by classical M-K model. The author concluded that both flow and deformation plasticity theories are applicable for localized necking prediction for the tension-compression side of FLD (or left side) but not adequate

for tension-tension side (or right side) of FLD due to a significant discrepancies between predicted and experimental results in the analytical analysis which leads to contradictory and incorrect prediction of forming limit.

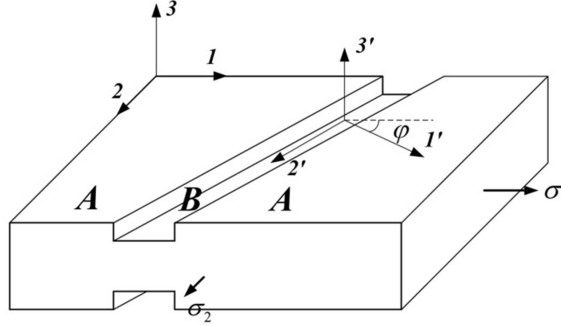


Figure 5.10 A schematic drawing of H-N model.

Due to the groove orientation angle  $\varphi$  between main principal stress and perpendicular direction of the groove, another local coordinate system  $1'-2'-3'$  was introduced in the M-K analysis. However, similar assumptions to the original M-K method were made with the H-N model such as Mises yield criterion, Levy-Mises flow rule and plane stress condition. Therefore, earlier Eqns. (1) to (7) still apply to the H-N model. The difference in the H-N analysis from the original M-K model lies in the force equilibrium condition which now takes the following form:

$$\begin{cases} f_0 e^{\epsilon_3^B - \epsilon_3^A} \sigma_{1'}^B = \sigma_{1'}^A \\ f_0 e^{\epsilon_3^B - \epsilon_3^A} \sigma_{1'2'}^B = \sigma_{1'2'}^A \end{cases} \quad (4)$$

In eqn. (4),  $\sigma_{1'}^A$  and  $\sigma_{1'}^B$  are the stress components of A and B regions in the perpendicular direction to the groove whereas  $\sigma_{1'2'}^A$  and  $\sigma_{1'2'}^B$  are the shear stress components respectively. The strain compatibility condition now becomes  $\Delta\epsilon_2^A = \Delta\epsilon_2^B$ .

The calculation procedure of H-N model is similar to that of M-K model based on an incremental method and Newton-Raphson iteration except that the initial groove angle  $\phi_0$  and its current value  $\phi$  are continuously updated in the incremental calculations. For completeness, the calculation procedure is once again presented in a stepwise manner as follows:

- 1)  $\phi^A$ ,  $\rho^A$  and  $\beta^A$  are calculated according to Eq. (4) and (7) for a given  $\alpha$  value.
- 2) An initial value of groove inclined angle  $\phi$  is assigned between 0 and  $\pi / 2$ .
- 3) An initial major principal strain increment  $\Delta\epsilon_1^A = 0.0001$  is given. According to the constancy of volume during plastic deformation, the following equations represent the incremental strain quantities:

$$\begin{cases} \Delta\epsilon_2^A = \rho^A \Delta\epsilon_1^A \\ \Delta\bar{\epsilon}^A = \beta^A \Delta\epsilon_1^A \\ \Delta\epsilon_3^A = -(1 + \rho^A) \Delta\epsilon_1^A \end{cases} \quad (5)$$

- 4) According to the constitutive model, the effective stress in region A can be calculated by  $\bar{\sigma}^A = \bar{\sigma}^A (\bar{\epsilon}^A + \Delta\bar{\epsilon}^A)$ . Hence  $\sigma_1^A = \bar{\sigma}^A / \phi$  and  $\sigma_2^A = \alpha \sigma_1^A$  can be calculated.
- 5) The evolution of  $\phi$  is then formulated as (Banabic, 2010; Butuc et al., 2003; Hutchinson & Neale, 1978):

$$\varphi = \text{atan}\left(\tan(\varphi_0)(1+\Delta\varepsilon_1^A)/(1+\Delta\varepsilon_2^A)\right) \quad (6)$$

In Eqn. (6),  $\varphi_0$  is the original groove angle and current  $\varphi$  value is calculated from the previous increment. If the current increment is the first one,  $\varphi_0$  is the initial angle between the groove's perpendicular direction and major stress direction.

- 6) The stress and strain increment in the local coordinate system of 1'-2'-3' can be calculated from the following transformation equations:

$$\begin{cases} \sigma_{1'}^A = \sigma_1^A \cos^2 \varphi + \sigma_2^A \sin^2 \varphi \\ \sigma_{2'}^A = \sigma_1^A \sin^2 \varphi + \sigma_2^A \cos^2 \varphi \\ \sigma_{1'2'}^A = (\sigma_2^A - \sigma_1^A) \sin \varphi \cos \varphi \\ \Delta\varepsilon_{1'}^A = \Delta\varepsilon_1^A \cos^2 \varphi + \Delta\varepsilon_2^A \sin^2 \varphi \\ \Delta\varepsilon_{2'}^A = \Delta\varepsilon_1^A \sin^2 \varphi + \Delta\varepsilon_2^A \cos^2 \varphi \\ \Delta\varepsilon_{1'2'}^A = (\Delta\varepsilon_2^A - \Delta\varepsilon_1^A) \sin \varphi \cos \varphi \end{cases} \quad (7)$$

Figure 5.11 shows 2D stress transformation scheme with angle of rotating of  $\theta$ .

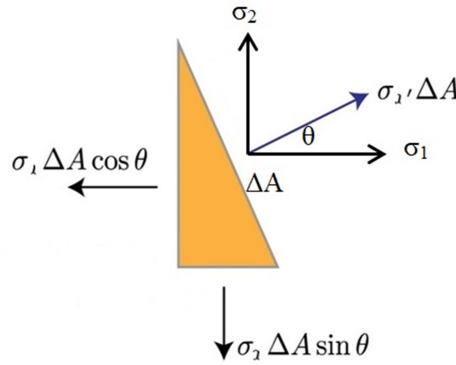


Figure 5.11 2D scheme drawing for stress transformation.

The force equilibrium equation can be written as:

$$\sum F_{1'} = 0 \quad (19)$$

Eqn. (19) can be written as,



$$\sigma_{1'}^* \Delta A - (\sigma_1^* \Delta A \cos \theta) \cos \theta - (\sigma_2^* \Delta A \sin \theta) \sin \theta = 0 \quad (20)$$

Eqn. (20) can be simplified as,

$$\sigma_{1'} = \sigma_1 \cos^2 \theta + \sigma_2 \sin^2 \theta \quad (21)$$

The same methodology was utilized for obtaining  $\sigma_{2'}$ ,  $\sigma_{1'2'}$ ,  $\Delta \varepsilon_{1'}$ ,  $\Delta \varepsilon_{2'}$  and  $\Delta \varepsilon_{1'2'}$  for region A (or safe zone). The quantities  $\Delta \bar{\varepsilon}^B$ ,  $\sigma_{1'}^B$ ,  $\sigma_{2'}^B$  and  $\sigma_{1'2'}^B$  were calculated by solving the following equations:

$$\begin{cases} \bar{\sigma}^B = \frac{1}{2} \sqrt{(\sigma_{1'}^B - \sigma_{2'}^B)^2 + (\sigma_{2'}^B)^2 + (\sigma_{1'}^B)^2 + 6(\sigma_{1'2'}^B)^2} = \bar{\sigma}^B (\bar{\varepsilon}^B + \Delta \bar{\varepsilon}^B) \\ \sigma_{1'}^A = \sigma_{1'}^B f_0 \exp(\varepsilon_3^B + \Delta \varepsilon_3^B - \varepsilon_3^A - \Delta \varepsilon_3^A) \\ \sigma_{1'2'}^A = \sigma_{1'2'}^B f_0 \exp(\varepsilon_3^B + \Delta \varepsilon_3^B - \varepsilon_3^A - \Delta \varepsilon_3^A) \\ \Delta \varepsilon_{2'}^A = \Delta \varepsilon_{2'}^B \end{cases} \quad (22)$$

A numerical method, such as 4<sup>th</sup> order Newton-Raphson method, is then employed to obtain the stress and strain state in region B.

- 7) The stress and strain states are then updated and  $\Delta \bar{\varepsilon}^B / \Delta \bar{\varepsilon}^A$  term is calculated. If  $\Delta \bar{\varepsilon}^B / \Delta \bar{\varepsilon}^A \geq 10$  is satisfied, the calculation is stopped and the major and minor strains in region A,  $\varepsilon_1^A$  and  $\varepsilon_2^A$ , are recorded as the forming limit strains for the given load path. Otherwise, another increment of  $\Delta \varepsilon_1^A$  is given and the steps 3-7 above are repeated.
- 8) A different groove angle increment of  $\varphi$  of  $\pi / 20$  is then applied and steps 3-7 above are repeated to find the lowest forming limit point which is recorded as the final result for the chosen stress ratio,  $\alpha$ .

- 9) Another  $\alpha$  is then chosen and the above steps 2-8 are repeated until all stress ratios from uniaxial tension to balanced biaxial tension are covered, and the FLC is constructed.

In the following, two different constitutive material laws proposed by (i) Field-Backofen (F-B) and (ii) Voce-Kocks (V-K) are considered within the above framework of M-K analysis to describe the temperature and strain rate dependent hardening behaviour of AA7075-O sheet. Both original M-K method as well as H-N revised M-K method for inclined groove orientation are considered for FLC prediction at different temperatures.

### 5.3 FLD prediction by using Field-Backofen constitutive law

Field - Backofen (or F-B) constitutive equation, as earlier, can be expressed as:

$$\sigma = K \varepsilon^n \dot{\varepsilon}^m \quad (23)$$

where material parameters,  $K$ ,  $n$  and  $m$  can be regarded as temperature dependent (Hua et al., 2014; Kotkunde et al., 2014; Lang et al., 2015; Tsao et al., 2012). They can be written as second order polynomial functions of temperature (in °K) scale, as follows:

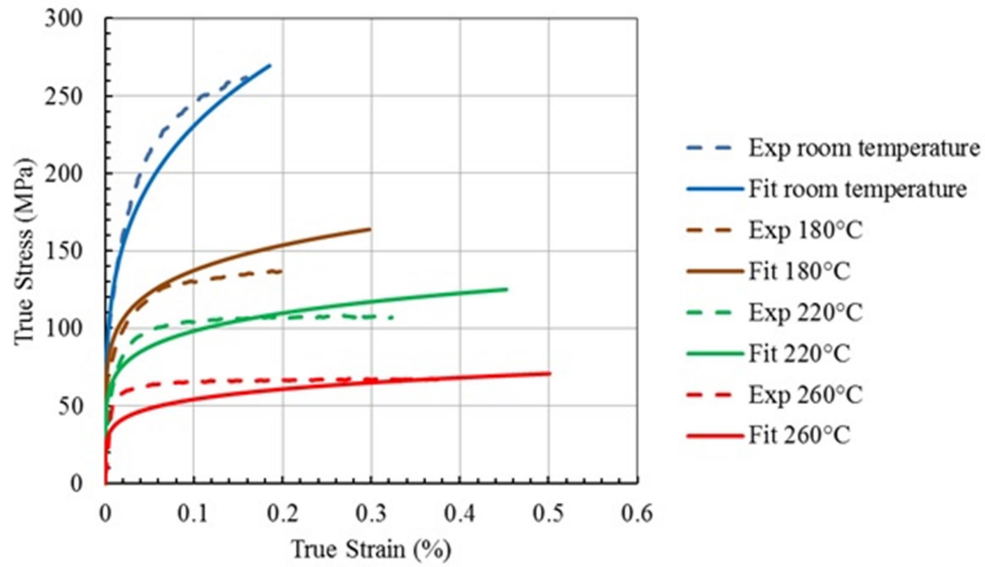
$$\begin{cases} \sigma = K(T) \varepsilon^{n(T)} \dot{\varepsilon}^{m(T)} \\ K(T) = K_0 + K_1 T + K_2 T^2 \\ n(T) = n_0 + n_1 T + n_2 T^2 \\ m(T) = m_0 + m_1 T + m_2 T^2 \end{cases} \quad (24)$$

This model was then applied to the present experimental uniaxial true stress-strain data from isothermal uniaxial tensile test results on AA7075 sheet at four different temperatures and two test speeds. Non-linear least square method was used to obtain the values of the coefficients in the above polynomial functions. A lsqcurvefit function in

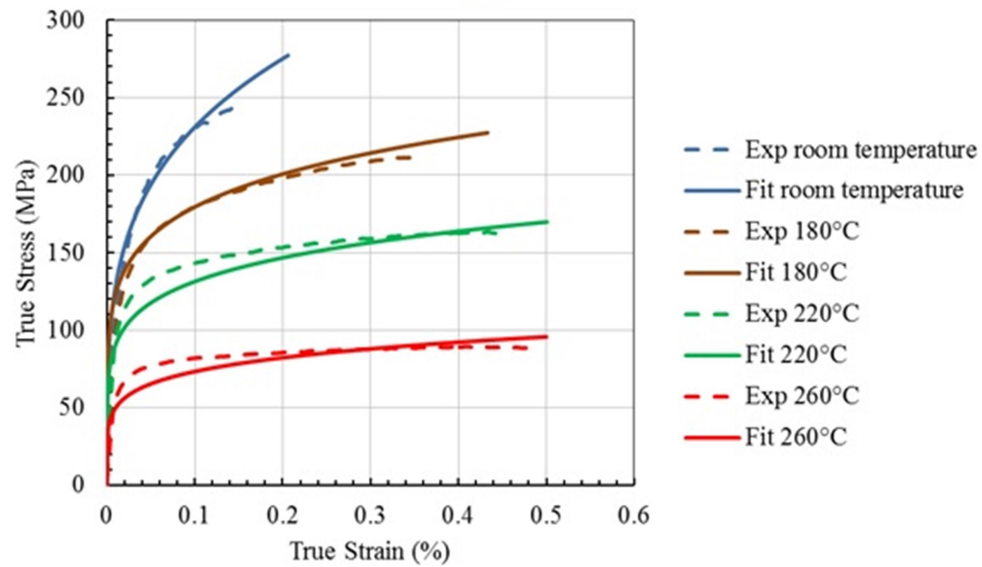
MATLAB code was employed for this purpose. The F-B model parameters from MATLAB code are listed in Table 5.1 and the fitted and experimental stress-strain curves are shown in Figure 5.12.

Table 5.1 F-B polynomial fit parameters.

Parameters	Value
$K_0$	-1.605E3
$K_1$	11.16
$K_2$	-0.01456
$n_0$	0.7545
$n_1$	-0.002460
$n_2$	2.540E-06
$m_0$	-0.4936
$m_1$	0.002318
$m_2$	-2.150E-06



(a)



(b)

Figure 5.12 Comparison of fitted and experimental curves based on the F-B model; (a) 1 mm/min; (b) 10 mm/min.

As noted earlier, strain and strain rate hardening parameters  $n$  and  $m$  have an effect on the prediction of forming limit. It is well known that greater  $n$  and  $m$  values can lead to

higher FLC. Under elevated temperature forming conditions,  $n$  and  $m$  coefficients are temperature dependent. Therefore, it is useful to assess how  $n$  and  $m$  varies with temperature, as obtained from the above fit for AA7075-O sheet. These are shown as Figure 5.13. The curve shows a reduction in strain hardening exponent ( $n$ ) with increase of temperature while strain rate sensitivity index ( $m$ ) increases with temperature which means that the strain hardening behaviour is diminished while the strain rate hardening becomes more significant at elevated temperatures. Such a trend has been observed in the literature for other aluminum alloys (Ayres & Wenner, 1979).

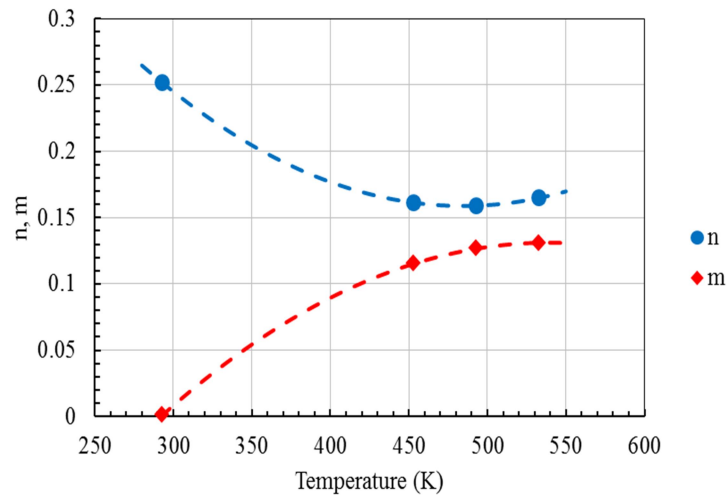


Figure 5.13 The variation of  $n$  and  $m$  with absolute temperature.

The obtained hardening parameters were then employed in the M-K model using an arbitrary initial inhomogeneity factor  $f_0$  of 0.986. A comparison of the predicted and the experimental FLCs is shown in Figure 5.14. The experimental data are shown as experimental data points corresponding to the onset of localized necking for the different

limit strain points. It is to be noted that the left side of the experimental FLD yielded rather limited experimental data.

The predicted FLCs are in good agreement with the experimental data on the right side of the FLD. The general trend of increase in FLC with the temperature is accurately captured by the F-B model. It can be observed that the strain hardening coefficient  $n$  decreases as the temperature rises. As a result, if the strain rate hardening behaviour was not considered, the FLC will shift down. However, the strain rate hardening coefficient  $m$  increases with the temperature, which leads to the better formability of material. Under the combination effects of  $n$  and  $m$ , the final FLC, as predicted by the M-K model, increases with the temperature in the range of experiments.

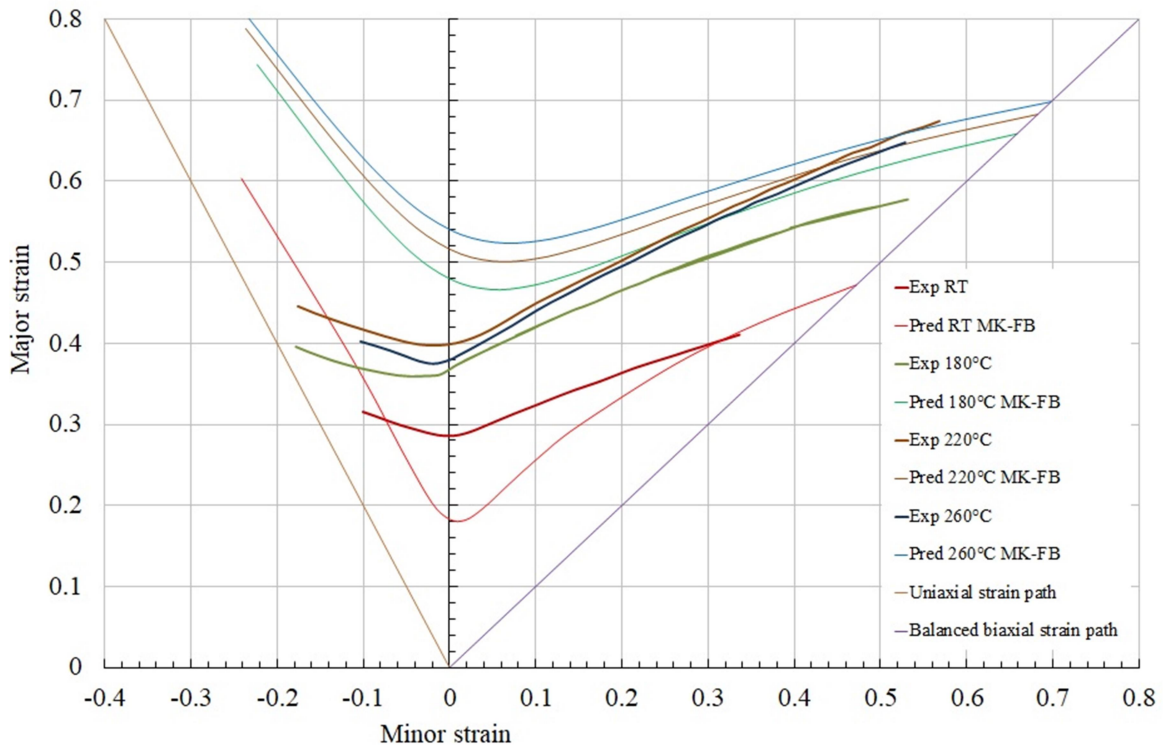


Figure 5.14 The predicted FLCs for different temperatures based on the F-B model.

In addition, the H-N model (Hutchinson & Neale, 1978), dealing with groove orientation, was also coupled with the F-B constitutive law to obtain the predictive FLCs. The angle  $\phi$  between the groove and the minor strain direction was adjusted to obtain the lowest forming limit for each strain path condition. It was found that the left side of the predicted forming limit for each strain path condition. It was found that the left side of the predicted FLC was lower in the traditional M-K model, while the right side remained unaffected. With the use of H-N model in the M-K analysis, not only the tension-compression side was raised but the slope of this side of FLD was decreased. This resulted in improvement of the tension-compression side prediction of FLD results compared to the experimental data points, as shown in Figure 5.15.

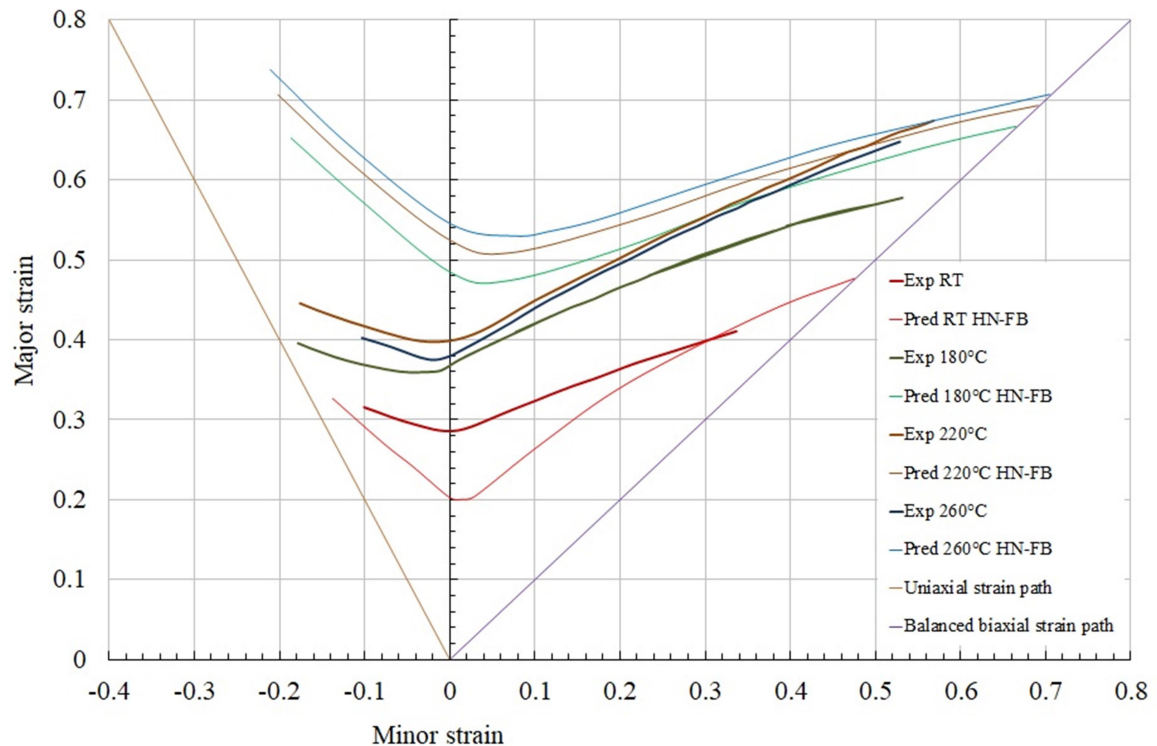


Figure 5.15 The predicted FLCs for different temperatures based on the H-N and F-B models.

#### 5.4 FLD prediction by using Voce-Kocks constitutive law

The Voce-Kocks (V-K) constitutive equation (Kocks, 1976; Voce, 1948) can be written as follows:

$$\sigma = \sigma_s + (\sigma_0 - \sigma_s) \exp\left(-\frac{\varepsilon}{\varepsilon_r}\right) \quad (25)$$

Where

$$\left\{ \begin{array}{l} \sigma_s = \sigma_{s0} \left( \frac{\dot{\varepsilon}}{y_s} \right)^{\frac{kT}{A_s}} \\ \sigma_0 = \sigma_{k0} \left( \frac{\dot{\varepsilon}}{y_k} \right)^{\frac{kT}{A_k}} \\ \varepsilon_r = \frac{\sigma_s - \sigma_0}{\theta} \end{array} \right. \quad (26)$$

In eqns. (26), the symbols  $\sigma_s$  and  $\sigma_0$  are saturation and initial yield stresses respectively and  $\varepsilon_r$  is the relaxation strain. The symbols  $\sigma_{s0}$  and  $\sigma_{k0}$  represent reference stresses for saturation and yield at  $0^\circ K$ . The symbols  $y_s$  and  $y_k$  are constants related to a reference strain rate. Usually  $y_s$  and  $y_k$  are much greater than the strain rate in experiments. The symbol  $k$  represents Boltzmann constant, and  $A_s$  and  $A_k$  are related to the shear modulus and Burgers vector of material respectively. Lastly, symbol  $\theta$  is also a material constant related to the initial work hardening rate.

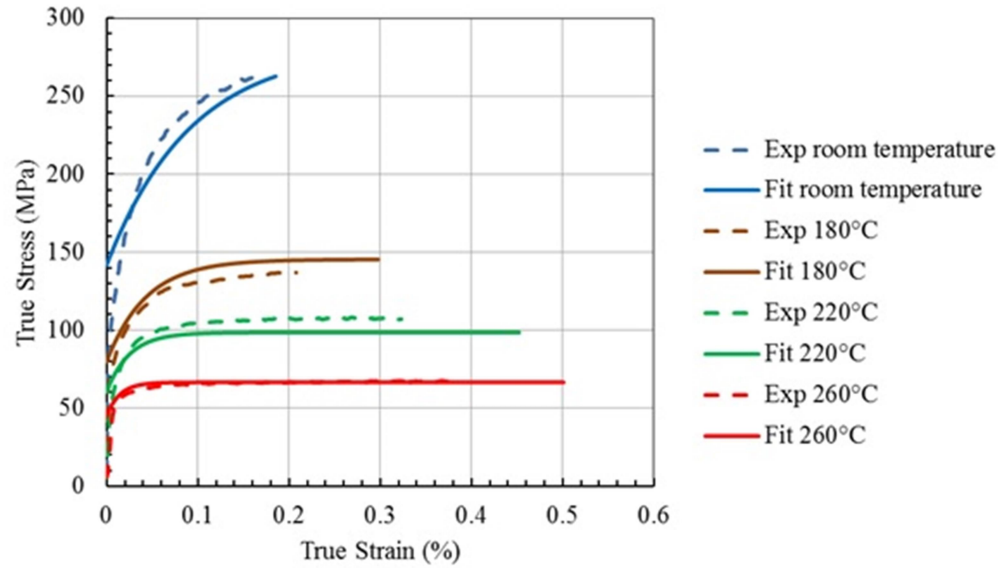
The experimental true stress-true strain curves, presented previously, were first employed to obtain the optimized values of  $\sigma_s$ ,  $\sigma_0$  and  $\varepsilon_r$  for each test condition according to eqn.



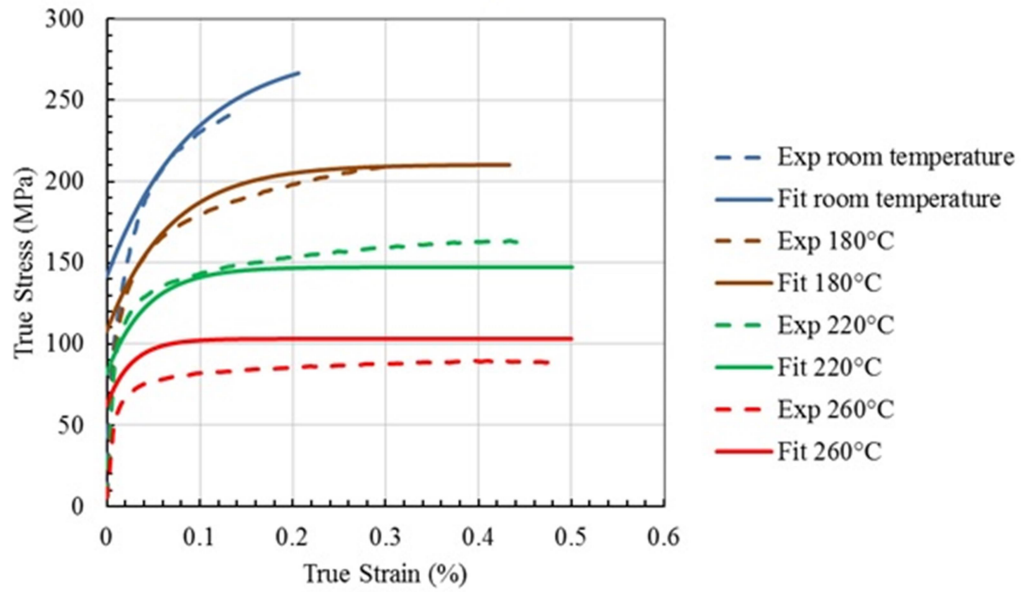
(25). Subsequently, relations between the above factors and the temperature and strain rate were established based on eqn. (26). The associated parameters in eqn. (26) were obtained from the least square method in MATLAB. The parameters values are summarized in Table 5.2 and the analytical and experimental curves are shown in Figure 5.16 (a, b) for the two different test speeds.

Table 5.2 V-K fit parameter values.

Parameters	Value
$\sigma_{s0}$	1.193E4
$y_s$	4.740E+08
$A_s$	3.868E-20
$\sigma_{k0}$	2.352E3
$y_k$	4.610E+08
$A_k$	5.072E-20
$\theta$	1.510E3
$\sigma_s^{293K}$	2.816E2
$\sigma_0^{293K}$	1.420E2



(a)



(b)

Figure 5.16 Comparison of fitted and experimental curves based on the V-K model; (a) 1 mm/min and (b) 10 mm/min.

It should be noted that the room temperature results were not used to determine the parameters. This is explained as follows. As indicated in eqn. (26),  $\sigma_s$  and  $\sigma_0$  are related

to strain rate via exponential functions of the temperature. Since  $\dot{\epsilon} / y_s$  and  $\dot{\epsilon} / y_k$  are much smaller than one,  $\sigma_s$  and  $\sigma_0$  will increase significantly as the temperature decreases. However, this may be not true as the temperature decreases to room temperature for the AA7075-O material. As shown in Figure 5.17, the experimental  $\sigma_s$  and  $\sigma_0$  results did not increase abruptly as predicted by the model. The phenomenon may be attributed to the following reasons: Firstly, the derivation of Kocks model for the saturation stress is based on the thermal activation of dislocations in the plasticity of polycrystalline materials (Kocks, 1976). The saturation stress is defined as the stress value at which the strain hardening rate (or rate of change in strain hardening) tends to zero. However, AA7075-O alloy is a more complex material that consists of intermetallic particles and dispersoids of different sizes. They are expected to influence the dislocation motion, and especially at lower temperatures and consequently higher flow stress curve with high strain hardening coefficient will be obtained. Therefore, the saturation stress value will not be reached, in other words its calculation will not be accurate according to its definition, (see Figure 5.18). This could be the major reason for the inaccurate prediction at room temperature. In addition, according to (Kocks, 1976),  $A_s$ ,  $A_k$ ,  $\sigma_{s0}$  and  $\sigma_{k0}$  are all related to the shear modulus  $\mu$  while  $\mu$  is actually temperature dependent. In the present calculation, these factors are taken as constants for simplification. However, this may also lead to the error in the room temperature condition. Therefore, instead of using the inaccurate predictive data, the experimentally-fitted  $\sigma_s$  and  $\sigma_0$  results were employed directly for the calculation of FLC at room temperature. Nevertheless, there is

a necessity to address the problem discussed above for lower temperature conditions in the future study.

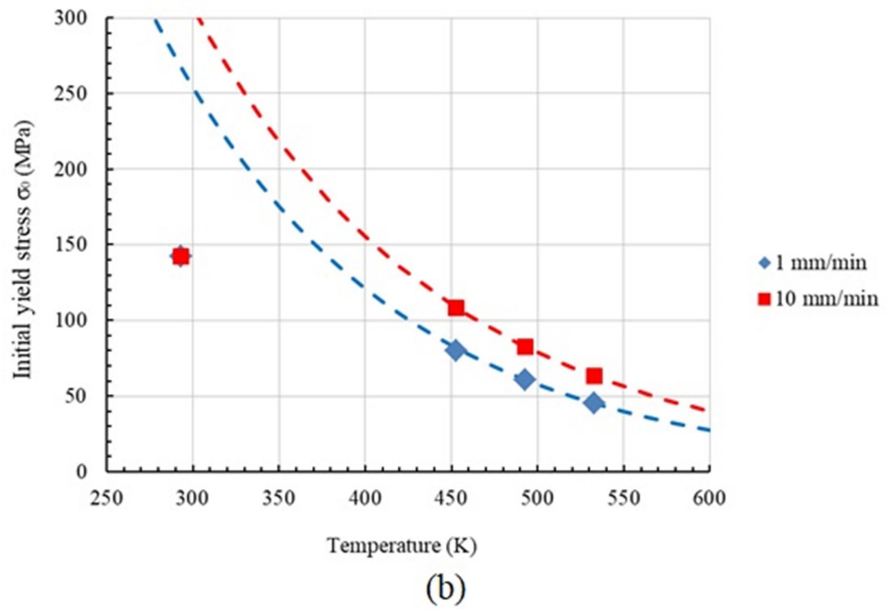
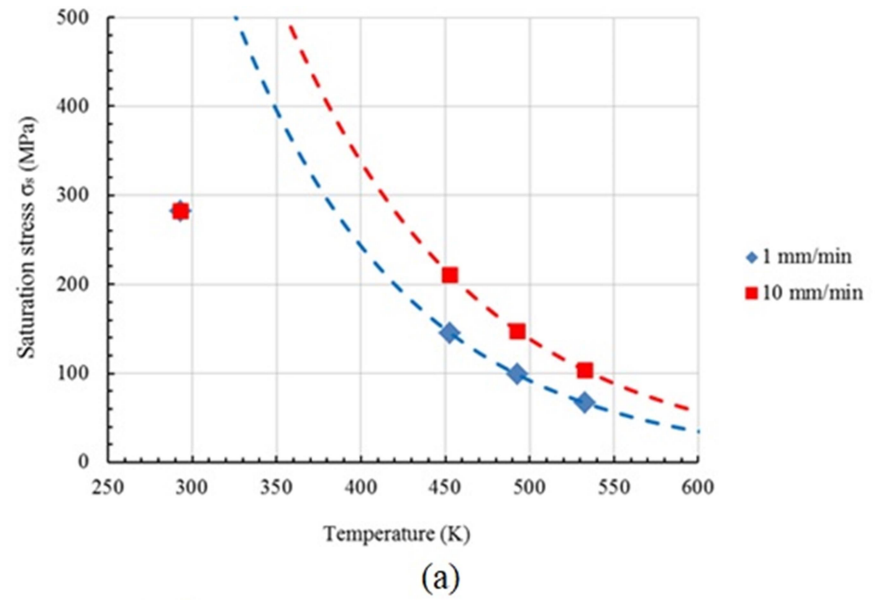


Figure 5.17  $\sigma_s$  and  $\sigma_0$  versus absolute temperature curves; (a)  $\sigma_s$  and (b)  $\sigma_0$ .

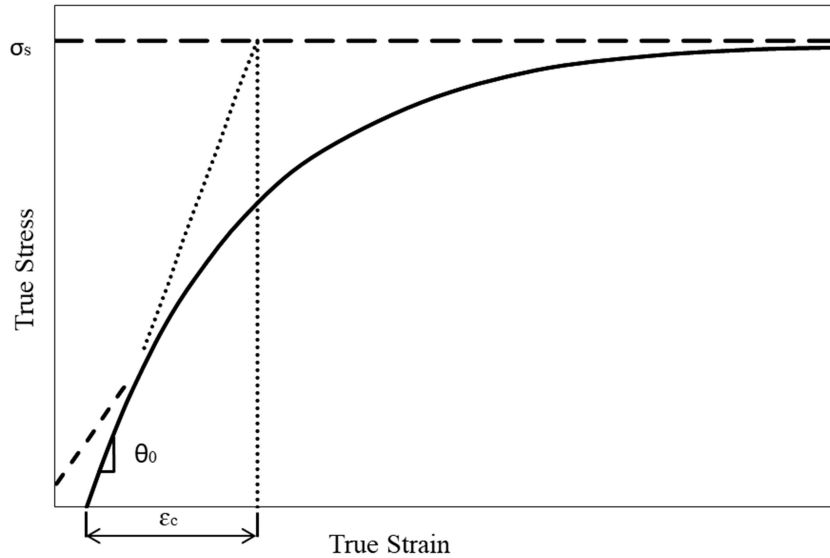
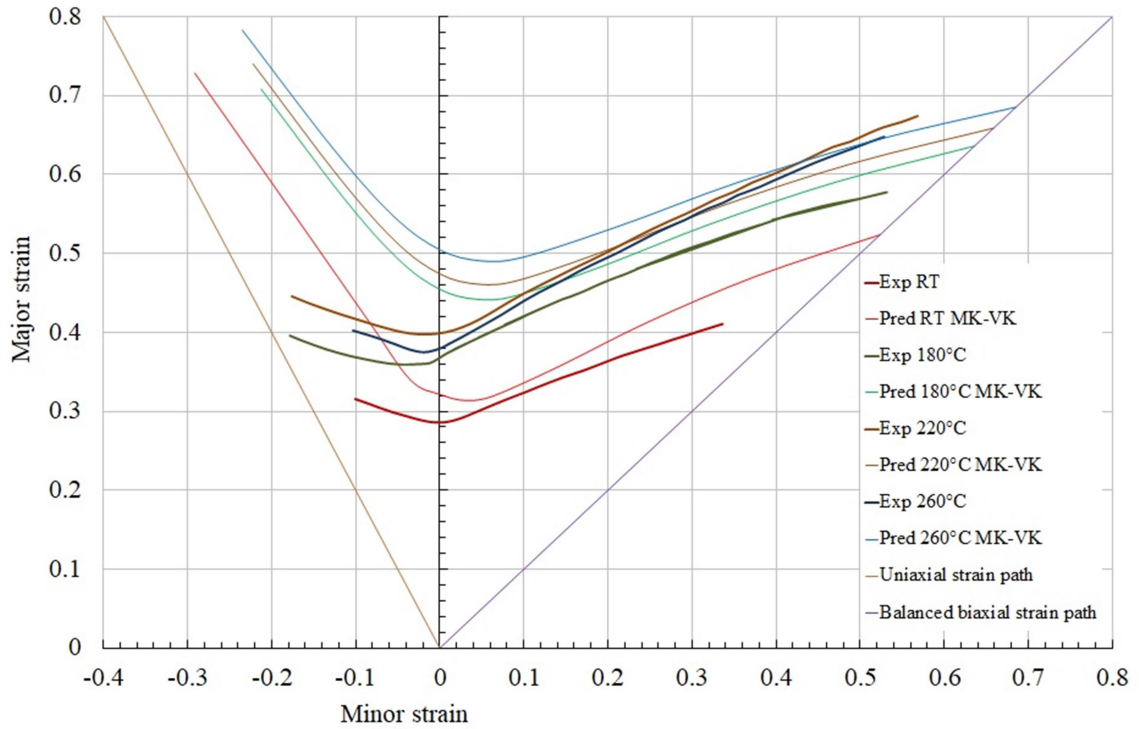
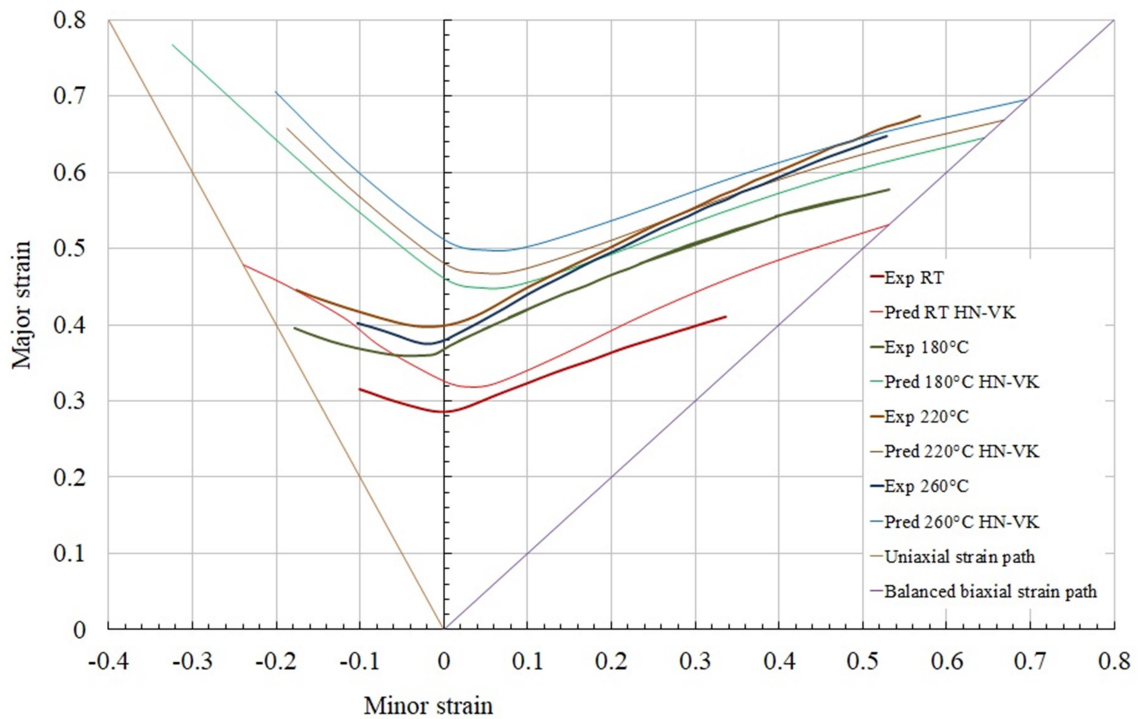


Figure 5.18 Digitized flow stress includes saturation stress ( $\sigma_s$ ), initial strain hardening rate ( $\theta_0$ ) and characteristic strain ( $\epsilon_c$ ). Dashed line represent the exact elastic part of the curve (Kocks, 1976).

After parameters determination, the V-K model was incorporated into the original M-K and H-N based M-K models to predict the FLCs. The strain increment, initial inhomogeneity factor and the forming limit condition were kept the same as with MK-FB models. The predicted and experimental FLCs are shown in Figure 5.19 (a, b).



(a)



(b)

Figure 5.19 The predicted FLCs at different temperatures based on V-K model: (a) MK-VK method and (b) HN-VK method.

The predicted FLCs based on MK-VK and HN-VK methods agree quite well with the experimental FLCs. With an increase in temperature, the predicted FLC shifts upwards as observed in the experiments. It is to be noted that these models yield better predictions in general compared to the earlier (MK-FB and HN-FB) models that employ Fields-Backofen constitutive law. A better predictive FLD prediction from the VK based models is related to its ability to incorporate physical aspects of dislocation storage and dynamic recovery in the constitutive equation. However, the effect of precipitation and its evolution with temperature is not included in either of the two constitutive models. In closing, it could be said that while these material models do yield good results for AA7075-O sheet, they may be of limited value for prediction of FLDs of AA7075-T6 sheet where aged microstructures lead to significantly higher flow stresses and reduced work hardening rate, and even work softening, at higher strains.

### **5.5 FLD prediction limitations**

Despite the good agreement of predicted FLCs with the experimental FLCs by using either FB or VK constitutive models in conjunction with MK and HN and the simplicity of assumptions which considered only the main elements of these models, there exist some limitations as follows:

- 1) The quality of flow stress-strain fitting was not quite as good and the number of parameters for fitting, for F-B constitutive model, was not optimized. Also, fitted stress-strain curves did not show good extrapolation beyond the experimental curves. Therefore, the FLD predictions could be further improved by enhancing flow stress-strain fitting.

2) The current predictions utilized Mises isotropic yield criterion, i.e.,  $r = 1$ . This assumption is to be verified with  $r$ -value measurements at different temperatures. Also, the implemented MK model doesn't have a capability to represent the complexity of microstructure features which may affect its yield and work hardening behavior in different stress states.

3) The imperfection factor ( $f_0$ ) was taken as 0.986. While others have used similar value for the imperfection factor, it is not based on initial or subsequent damage or surface roughness evolution considerations.

## 5.6 Summary

F-B and V-K constitutive material models were incorporated within the M-K analysis to predict the strain rate and temperature dependent FLCs of AA7075-O sheet material. The following remarks can be made from this investigation:

- 1) F-B model was employed to describe the constitutive behaviour of material under different temperatures and strain rate conditions. By using rather simple quadratic polynomial dependence of material parameters on temperature (e.g., strength coefficient  $K$ , strain hardening coefficient  $n$  and strain rate hardening coefficient  $m$ ), the F-B model was found to be able to describe the temperature-dependent stress-strain behaviour of the material.
- 2) F-B model was coupled with M-K and H-N models to calculate the FLCs under different temperatures. The predictive results of both models are in agreement with experimental FLDs on the right side of FLD but exhibit rather poor predictions on the left side of FLD. The combined effects of hardening coefficient



$n$  and rate hardening coefficient  $m$  were revealed to be the key factors in achieving the correct trends in the FLD data as a function of temperature and strain rate.

- 3) V-K model was employed to characterize the plastic deformation behaviour under different temperatures and strain rates. It was also further coupled with M-K and H-N models to compute the FLCs under different temperatures. The calculated FLCs from V-K constitutive model showed better agreement with the experimental FLDs compared to the F-B constitutive model for both left and right sides of FLD.

## **6-Conclusions and Future Work**

### **6.1 Conclusions**

In this research work, the relationship between basic mechanical properties, microstructure, damage development, fracture at large strains and formability were investigated experimentally for 2 mm thick AA7075 sheet metal. Uniaxial tensile deformation behaviour, material flow and forming characteristics under biaxial straining conditions were studied at different test speeds and forming temperatures. Microstructure study involved surface roughness and its evolution, void characteristics after necking and fracture, fractographic analyses of ductile void damage and bulk texture as a function of biaxial strain paths at a range of temperatures and test speeds. Also, analytical prediction of forming limits of AA7075-O sheet were carried out using the M-K model with strain rate and temperature dependent material constitutive laws proposed by Field - Backofen (F-B) and Voce-Kocks (V-K). The predicted FLCs were compared with experimental FLCs and aspects of FLC predictions were assessed.

The main conclusions drawn from this research work are:

[1]. The experimental investigation of mechanical properties, microstructural, and surface features of two different tempers of O and T6 of AA7075 at room temperature demonstrated that fully annealed (O-temper) AA7075 sheet had significantly lower strength and higher ductility compared to AA7075-T6 sheet. The increase in ductility resulted from its lower dislocation density, larger grain size, and absence of hardening precipitates which had an effect on increased material strain hardening, a better strain distribution in the neck region, reduced surface roughness development (at equivalent

strain value to T6 sheet), reduced rate of localized neck growth, slower and more extensive development of void induced damage prior to fracture, and a later onset of localized necking and fracture compared to the T6 temper sheet. The latter exhibited a large density of high strength precipitates which lead to reduced work hardening, rapid neck growth past the onset of diffuse necking, and shear-like catastrophic failure mode of fracture.

[2]. Experimental FLC of AA7075-O sheet was significantly higher than that of AA7075-T6 sheet at room temperature. This trend was more pronounced in terms of the FLC positions of the two tempers but consistent with the uniaxial tensile stress-strain curves and uniaxial tensile ductility at room temperature. The difference in forming limits is attributed to the previously mentioned microstructural characteristics of the two tempers and their effect on material work hardening. Also, the shapes of FLCs were quite different where the biaxial tensile side of FLC of O-temper sheet was more gradual whereas it was rather sharp for T6 temper sheet. This is attributed to increased damage in the T6 temper sheet under biaxial tensile loading conditions where more shear-like fracture and less ductile void growth were observed. In addition, the strain distribution across the surface of the O-temper dome specimens was more uniform up to the onset of localized necking for all strain paths compared to T6 temper sheet. Larger and more frequent undulations in strains (or larger strain instabilities) were observed over the surfaces of PST and BBT dome specimens in the T6 temper state. These undulations exhibited a clear pattern that was established in the early stage of the deformation and led to early onset of necking and fracture.

[3]. At elevated temperatures up to 260°C, the O temper AA7075 sheet continued to exhibit increased work hardening in uniaxial tension tests but at a reduced rate as the temperature increased leading to stress saturation at 260°C. The stress-strain curves moved to higher stress and strain values with increased speed from the positive effect of increased strain rate sensitivity at elevated temperature. The qualitative and quantitative microstructure investigations of uniaxial tension O-temper revealed necking prior to fracture as the test temperature increased from room temperature to 260°C. In contrast, the T6-temper sheet exhibited a different plastic response compared to the O-temper sheet. Stress softening occurred early in the deformation process and especially at 260°C, and a significant reduction in plastic strain to fracture was observed at elevated temperatures. Also, the void-induced damage development was less pronounced with more shear-like features were observed on the fracture surface compared to the O-temper sheet at all temperatures that led to an early onset of fracture. The surface roughness evolution trends in O and T6 temper uniaxial tensile samples at elevated temperature had a good correlation with sheet uniaxial tensile ductility. The T6 sheet with high dislocation density, hardening precipitates and solute atoms showed higher strength that led to lower strain to fracture and lower surface roughness and vice versa for the O-temper sheet.

[4]. A systematic test procedure for determination of elevated temperature FLDs of AA7075-O and AA7075-T6 temper sheets was developed based on the Nakazima test. Sample geometries to achieve various strain ratios were also designed. A grid classification scheme was also implemented to suitably classify the necked, un-necked, and safe regions in the vicinity of neck. The effort led to a systematic and reliable

determination of FLDs of AA7075 O and T6 temper sheet materials at a range of elevated temperatures for the first time in the literature. There is still a need to further improve the tension-compression side of the FLD based on additional tests as discussed later.

[5]. The experimental FLCs for AA7075-O steadily moved upwards from room temperature to 180°C, and from 180°C to 220°C, but only very slightly upward from 220°C to 260°C. One likely reason for this appears to be a saturation in uniaxial tensile flow stress at 260°C as observed in the uniaxial tensile tests. The lack of work hardening at 260°C likely led to an early onset of both diffuse and localized necking as explained by Considère criterion for diffuse necking and Hill's theory of localized necking for sheet material. The result is also consistent with a significant drop in the strain rate sensitivity of the AA7075 sheet reported in the literature at about 240°C and above. The qualitative and quantitative microstructure investigations for dome samples of O-temper sheet show that as the forming temperature increased from room temperature to 220°C the void dimples size increased and a slow neck growth was obtained due to increased strain rate sensitivity at 220°C and hence increase sheet formability. The experimental FLCs for AA7075-T6 temper also moved significantly upwards from room temperature to 220°C. However, its FLC at 220°C was still considerably lower than the O-temper sheet at 220°C.

[6]. The quantitative bulk texture analysis for AA7075-O dome samples deformed at room temperature and 220°C showed deformed texture components of Brass {011}<211> and/or Copper {112}<111> and/or S {123}<634> for neck region, due to large plastic deformation, while recrystallized texture component of Cube {001}<100> was obtained

for pole region for UT and PST. BBT samples revealed deformed texture components of Brass  $\{011\}\langle 211\rangle$  and/or Copper  $\{112\}\langle 111\rangle$  and/or S  $\{123\}\langle 634\rangle$  for both neck and pole regions due to low friction between sheet metal and punch that led to shifting of the neck to the pole region. AA7075-T6 showed almost same results obtained for grain orientation distribution as the O temper dome samples, however, the intensity of grain orientation was lower than O temper due to precipitation hardening. As a result, precipitates-dislocations interaction affected the grain boundary migration and led to higher strength and relatively low formability even at 220°C compared to the O temper samples deformed at room and elevated temperature of 220°C.

[7]. The predicted elevated temperature FLCs of AA7075-O sheet based on Field - Backofen constitutive material model within the framework of M-K theory, and using the assumption of an inclined through-thickness groove model of Hutchinson-Neale, showed good agreement with the biaxial tension side of experimental FLCs.

[8]. The predicted elevated temperature FLCs of AA7075-O sheet based on Voce-Kocks constitutive material model within the framework of M-K theory, and Hutchinson-Neale through-thickness groove model, showed better agreement with the biaxial tension side of experimental FLCs than the Field - Backofen model. This was due to incorporation in V-K constitutive model of physical aspects of dislocation storage and dynamic recovery that is present in most metallic systems.

## **6.2 Suggestions for Future Work**

[1]. It would be very valuable to further improve the tension-compression side of the elevated temperature experimental FLDs of AA7075-O sheet by implementing other test procedures such as hole-expansion test. Also, a new combination of lubricant and a polymer film between the punch and deforming test blank could be utilized to better fill the strain gap on the tension-tension side of FLD. Further, effect of test speed (or strain rate) on FLD of AA7075-O sheet should be studied.

[2]. In the present work the FLD of T6 temper sheet was obtained at room temperature using a different set of forming tools and a different forming test system than at 220°C. Also, the elevated temperature FLD was limited to 220°C due to experimental limitations of press capacity. It is therefore suggested that a broader range of experimental FLDs of T6 temper sheet should be obtained, and at least at two more temperatures of 180°C and 260°C. The resulting deformed dome samples should also be examined for surface roughness evolution, neck and fracture characteristics from polished LT planes, fractographic observations of fractured dome specimens, and bulk crystallographic texture. This will further extend our comparative understanding of O and T6 temper elevated temperature formability of AA7075 sheet for automotive forming applications.

[3]. Specific forming and microstructural studies should be carried out above and below the recrystallization temperature of the as-rolled sheet, and in the under-aged and over-aged conditions, to see how they will affect the formability of AA7075 sheet.

[4]. The present work on elevated temperature FLC predictions of AA7075-O temper sheet utilized basic isotropic Mises yield criterion and simpler constitutive material models (F-B and V-K) available in the literature. Since AA7075 sheet is likely anisotropic even at low temperature end of the elevated temperature forming, and is a complex higher strength precipitation-hardenable aluminum alloy where precipitate characteristics are quite temper-dependent, more advanced material models of anisotropic yield and work hardening, the ones that takes more accurately into account microstructural deformation mechanisms present in AA7075 (O and T6 tempers), should be considered for implementation into the M-K analysis and assessed for FLC prediction.

[5]. In the present work, significant effort was made to characterize microstructure and texture of AA7075 sheet samples deformed at elevated temperatures, and to correlate microstructure, surface characteristics and crystallographic texture to aspects of formability. However, using the present forming set-up, more interrupted tests should be conducted at a range of applied macroscopic strains up to the onset of necking and between the necking and fracture stages, for a better and more quantitative microstructure-formability correlation. Lastly, even more meaningful and quantitative microstructure-formability correlations should be possible by performing in-situ elevated temperature miniature uniaxial tensile and biaxial (dome) tests with computer-controlled optical microscopes and SEMs that are fitted with heating and mechanical loading stages and environmental chambers.



## Bibliography

- Alloys, W. A. (2015). International Alloy Designations and Chemical Composition Limits for Wrought Aluminum and Wrought Aluminum Alloys.
- Altan, T. (2005). LIGHTWEIGHTING IN AUTOMOTIVE INDUSTRY. <https://cpf.osu.edu>
- Altenpohl, D. G. (1982). *Aluminium viewed from within*: Aluminium-Vrlg.
- ARAMIS. (2007). ARAMIS user manual, GOM mbH. 4 (14).
- Aretz, H. (2007). Numerical analysis of diffuse and localized necking in orthotropic sheet metals. *International Journal of Plasticity*, 23(5), 798-840.
- Ayres, R. A., & Wenner, M. L. (1979). Strain and strain-rate hardening effects in punch stretching of 5182-0 aluminum at elevated temperatures. *Metallurgical Transactions A*, 10(1), 41-46.
- Baczynski, G., Guzzo, R., Ball, M., & Lloyd, D. (2000). Development of roping in an aluminum automotive alloy AA6111. *Acta Materialia*, 48(13), 3361-3376.
- Banabic, D. (2010). *Sheet metal forming processes: constitutive modelling and numerical simulation*: Springer Science & Business Media.
- Barlat, F., Maeda, Y., Chung, K., Yanagawa, M., Brem, J., Hayashida, Y., . . . Hattori, S. (1997). Yield function development for aluminum alloy sheets. *Journal of the Mechanics and Physics of Solids*, 45(11-12), 1727-1763.
- Becker, R. (1998). Effects of strain localization on surface roughening during sheet forming. *Acta Materialia*, 46(4), 1385-1401.

- Bowen, A. (1990). Texture development in high strength aluminium alloys. *Materials science and technology*, 6(11), 1058-1071.
- Broek, D. (1973). The role of inclusions in ductile fracture and fracture toughness. *Engineering fracture mechanics*, 5(1), 55-66.
- Bunge, H.-J. (2013). *Texture analysis in materials science: mathematical methods*: Elsevier.
- Bunge, H. (1987). Three-dimensional texture analysis. *International Materials Reviews*, 32(1), 265-291.
- Butuc, M., Gracio, J., & Da Rocha, A. B. (2003). A theoretical study on forming limit diagrams prediction. *Journal of materials processing technology*, 142(3), 714-724.
- Camacho, A. M., Atkinson, H., Kapranos, P., & Argent, B. (2003). Thermodynamic predictions of wrought alloy compositions amenable to semi-solid processing. *Acta Materialia*, 51(8), 2319-2330.
- Campbell, F. C. (2008). *Elements of metallurgy and engineering alloys*: ASM International.
- Charpentier, P. L. (1975). Influence of punch curvature on the stretching limits of sheet steel. *Metallurgical Transactions A*, 6(8), 1665.
- Chu, C., & Needleman, A. (1980). Void nucleation effects in biaxially stretched sheets. *Journal of Engineering Materials and Technology*, 102(3), 249-256.
- Comley, P. N. (2007). *The ASTM International standard test method for determining the Superplastic Properties of Metallic Materials*. Paper presented at the Materials science forum.

Committee, A. I. H. (1987). *ASM handbook* (Vol. 12): ASM International.

Davis, J. R. (1993). *Aluminum and aluminum alloys*: ASM international.

Di Russo, E., Conserva, M., Buratti, M., & Gatto, F. (1974). A new thermo-mechanical procedure for improving the ductility and toughness of Al–Zn–Mg–Cu alloys in the transverse directions. *Materials Science and Engineering*, 14(1), 23-36.

El-Magd, E., & Brodmann, M. (2001). Influence of precipitates on ductile fracture of aluminium alloy AA7075 at high strain rates. *Materials Science and Engineering: A*, 307(1-2), 143-150.

Engler, O., & Hirsch, J. (2009). Control of recrystallisation texture and texture-related properties in industrial production of aluminium sheet. *International Journal of Materials Research*, 100(4), 564-575.

Engler, O., & Lücke, K. (1992). Mechanisms of recrystallization texture formation in aluminium alloys. *Scripta metallurgica et materialia*, 27(11), 1527-1532.

Fribourg, G. (2009). *Precipitation and plasticity couplings in a 7xxx aluminium alloy: application to thermomechanical treatments for distortion correction of aerospace component*. Institut National Polytechnique de Grenoble-INPG.

Garrison, W., & Moody, N. (1987). Ductile fracture. *Journal of Physics and Chemistry of Solids*, 48(11), 1035-1074.

Ghosh, A. (2018). Microstructure and texture development of 7075 alloy during homogenisation. *Philosophical Magazine*, 98(16), 1470-1490.

Ghosh, A. K., & Hecker, S. S. (1974). Stretching limits in sheet metals: in-plane versus out-of-plane deformation. *Metallurgical Transactions*, 5(10), 2161-2164.

- Goodwin, G. M. (1968). Application of strain analysis to sheet metal forming problems in the press shop: SAE technical paper.
- Gray III, G. T. (2012). High-strain-rate deformation: mechanical behavior and deformation substructures induced. *Annual Review of Materials Research*, 42, 285-303.
- Guowei Zhou, M. K. J. (2015). Effects of Pre-strain Path and Other Forming Conditions on Forming Limit Diagrams of AZ31B Magnesium Sheet (M. U. Mechanical Engineering, Trans.).
- Gupta, R., Mathew, C., & Ramkumar, P. (2015). Strain hardening in aerospace alloys. *Frontiers in Aerospace Engineering*.
- Gurson, A. L. (1977). Continuum theory of ductile rupture by void nucleation and growth: Part I—Yield criteria and flow rules for porous ductile media. *Journal of Engineering Materials and Technology*, 99(1), 2-15.
- Hahn, G., & Rosenfield, A. (1975). Metallurgical factors affecting fracture toughness of aluminum alloys. *Metallurgical Transactions A*, 6(4), 653-668.
- Hansen, N., & Jensen, D. J. (1999). Development of microstructure in FCC metals during cold work. *Philosophical Transactions of the Royal Society of London A: Mathematical, Physical and Engineering Sciences*, 357(1756), 1447-1469.
- Hill. (1948). A theory of the yielding and plastic flow of anisotropic metals. *Proc. R. Soc. Lond. A*, 193(1033), 281-297.
- Hill. (1952). On discontinuous plastic states, with special reference to localized necking in thin sheets. *Journal of the Mechanics and Physics of Solids*, 1(1), 19-30.

- Hill. (1979). *Theoretical plasticity of textured aggregates*. Paper presented at the Mathematical Proceedings of the Cambridge Philosophical Society.
- Hirsch, J. (1990). Correlation of deformation texture and microstructure. *Materials science and technology*, 6(11), 1048-1057.
- Hirsch, J. (2011). Aluminium in innovative light-weight car design. *Materials Transactions*, 52(5), 818-824.
- Hörnqvist, M., & Karlsson, B. (2006). Temperature and strain rate dependence of the dynamic strain aging effect in an Al–Zn–Mg alloy. *Materials science and technology*, 22(2), 213-222.
- Hsu, E., Carsley, J. E., & Verma, R. (2008). Development of forming limit diagrams of aluminum and magnesium sheet alloys at elevated temperatures. *Journal of Materials Engineering and Performance*, 17(3), 288-296.
- Hua, L., Meng, F., Song, Y., Liu, J., Qin, X., & Suo, L. (2014). A constitutive model of 6111-T4 aluminum alloy sheet based on the warm tensile test. *Journal of Materials Engineering and Performance*, 23(3), 1107-1113.
- Huang, H., LI, D.-y., & PENG, Y.-h. (2010). Experimental study on the forming limit diagrams (FLD) of 7075-T6 aluminum alloy sheet at warm state. *Journal of Plasticity Engineering*, 17(1), 93-97.
- Hui, W., LUO, Y.-b., Friedman, P., CHEN, M.-h., & Lin, G. (2012). Warm forming behavior of high strength aluminum alloy AA7075. *Transactions of Nonferrous Metals Society of China*, 22(1), 1-7.

- Huo, W., Hou, L., Zhang, Y., & Zhang, J. (2016). Warm formability and post-forming microstructure/property of high-strength AA 7075-T6 Al alloy. *Materials Science and Engineering: A*, 675, 44-54.
- Hutchinson, J., & Neale, K. (1978). Sheet necking-II. Time-independent behavior *Mechanics of sheet metal forming* (pp. 127-153): Springer.
- Isik, K., Silva, M., Tekkaya, A., & Martins, P. (2014). Formability limits by fracture in sheet metal forming. *Journal of materials processing technology*, 214(8), 1557-1565.
- Jain, M., Lloyd, D., & Macewen, S. (1996). Hardening laws, surface roughness and biaxial tensile limit strains of sheet aluminium alloys. *International Journal of Mechanical Sciences*, 38(2), 219-232.
- Janbakhsh, M., Loghmanian, S., & Djavanroodi, F. (2014). Application of Different Hill's Yield Criteria to Predict Limit Strains for Aerospace Titanium and Aluminum Sheet Alloys. *International Journal of Advanced Design and Manufacturing Technology*, 7(1), 35.
- Jordon, J., Horstemeyer, M., Solanki, K., Bernard, J., Berry, J., & Williams, T. (2009). Damage characterization and modeling of a 7075-T651 aluminum plate. *Materials Science and Engineering: A*, 527(1), 169-178.
- Kanvinde, A., & Deierlein, G. (2007). Finite-element simulation of ductile fracture in reduced section pull-plates using micromechanics-based fracture models. *Journal of Structural Engineering*, 133(5), 656-664.
- Kaufman, J. G. (2000). *Introduction to aluminum alloys and tempers*: ASM international.

- Keeler, S. P. (1968). Circular grid system—a valuable aid for evaluating sheet metal formability: SAE Technical Paper.
- Kim, K. H., & Kim, D. W. (1983). The effect of void growth on the limit strains of steel sheets. *International Journal of Mechanical Sciences*, 25(4), 293-300.
- Kocks, U. (1976). Laws for work-hardening and low-temperature creep. *Journal of Engineering Materials and Technology*, 98(1), 76-85.
- Korbel, A., & Bochniak, W. (1995). The structure based design of metal forming operations. *Journal of materials processing technology*, 53(1-2), 229-237.
- Kotkunde, N., Deole, A. D., Gupta, A. K., & Singh, S. K. (2014). Comparative study of constitutive modeling for Ti–6Al–4V alloy at low strain rates and elevated temperatures. *Materials & Design*, 55, 999-1005.
- Kumar, M., & Ross, N. (2016). Influence of temper on the performance of a high-strength Al–Zn–Mg alloy sheet in the warm forming processing chain. *Journal of materials processing technology*, 231, 189-198.
- Kumar, M., Sotirov, N., & Chimani, C. (2014). Investigations on warm forming of AW-7020-T6 alloy sheet. *Journal of materials processing technology*, 214(8), 1769-1776.
- Laboratory, R. T. (2014). Inductively Coupled Plasma - Optical Emission Spectrometer (ICP - OES), [www.rohs-cmet.in](http://www.rohs-cmet.in).
- Lademo, O.-G., Pedersen, K., Berstad, T., Furu, T., & Hopperstad, O. (2008). An experimental and numerical study on the formability of textured AlZnMg alloys. *European Journal of Mechanics-A/Solids*, 27(2), 116-140.

- Lagattu, F., Brillaud, J., & Lafarie-Frenot, M.-C. (2004). High strain gradient measurements by using digital image correlation technique. *Materials characterization*, 53(1), 17-28.
- Lang, L., Cai, G., Liu, K., Alexandrov, S., Du, P., & Zheng, H. (2015). Investigation on the effect of through thickness normal stress on forming limit at elevated temperature by using modified MK model. *International Journal of Material Forming*, 8(2), 211-228.
- Leacock, A. G., Howe, C., Brown, D., Lademo, O.-G., & Deering, A. (2013). Evolution of mechanical properties in a 7075 Al-alloy subject to natural ageing. *Materials & Design*, 49, 160-167.
- Lee, P., Piehler, H., Adams, B., Jarvis, G., Hampel, H., & Rollett, A. (1998). Influence of surface texture on orange peel in aluminum. *Journal of materials processing technology*, 80, 315-319.
- Li, J., Carsley, J. E., Stoughton, T. B., Hector Jr, L. G., & Hu, S. J. (2013). Forming limit analysis for two-stage forming of 5182-O aluminum sheet with intermediate annealing. *International Journal of Plasticity*, 45, 21-43.
- Lin, G., Zhang, Z., Zhang, H., Peng, D., & Zhou, J. (2008). Study on the hot deformation behaviors of Al-Zn-Mg-Cu-Cr aluminum alloy. *Acta Metallurgica Sinica (English Letters)*, 21(2), 109-115.
- Liu, Z., Li, Y., & Meehan, P. A. (2013). Experimental investigation of mechanical properties, formability and force measurement for AA7075-O aluminum alloy



- sheets formed by incremental forming. *International Journal of Precision Engineering and Manufacturing*, 14(11), 1891-1899.
- Löffler, H., Kovacs, I., & Lendvai, J. (1983). Decomposition processes in Al-Zn-Mg alloys. *Journal of Materials Science*, 18(8), 2215-2240.
- Mahmudi, R. (1997). Post-uniform deformation in uniaxial and equi-biaxial stretching of aluminium alloy sheets. *Journal of materials processing technology*, 70(1-3), 93-98.
- Marciniak, Z. (1965). Stability of plastic shells under tension with kinematic boundary conditions(Stability of plastic shell under tension). *Archiwum Mechaniki Stosowanej*, 17(4), 577-592.
- Marciniak, Z., & Kuczyński, K. (1967). Limit strains in the processes of stretch-forming sheet metal. *International Journal of Mechanical Sciences*, 9(9), 609IN1613-1612IN2620.
- Marciniak, Z., Kuczyński, K., & Pokora, T. (1973). Influence of the plastic properties of a material on the forming limit diagram for sheet metal in tension. *International Journal of Mechanical Sciences*, 15(10), 789-800.
- Martínez-Donaire, A., García-Lomas, F., & Vallellano, C. (2014). New approaches to detect the onset of localised necking in sheets under through-thickness strain gradients. *Materials & Design*, 57, 135-145.
- McClintock, F. A. (1968). A criterion for ductile fracture by the growth of holes. *Journal of applied mechanics*, 35(2), 363-371.

- Moghaddam, M., Zarei-Hanzaki, A., Pishbin, M., Shafieizad, A., & Oliveira, V. (2016). Characterization of the microstructure, texture and mechanical properties of 7075 aluminum alloy in early stage of severe plastic deformation. *Materials characterization*, 119, 137-147.
- Mondal, C., & Mukhopadhyay, A. (2005). On the nature of T (Al<sub>2</sub>Mg<sub>3</sub>Zn<sub>3</sub>) and S (Al<sub>2</sub>CuMg) phases present in as-cast and annealed 7055 aluminum alloy. *Materials Science and Engineering: A*, 391(1), 367-376.
- Mukhopadhyay, A. (2009). Microstructure and properties of high strength aluminium alloys for structural applications. *Transactions of the Indian Institute of Metals*, 62(2), 113-122.
- Mukhopadhyay, A., & Prasad, K. (2011). Formation of plate-shaped Guinier–Preston zones during natural aging of an Al–Zn–Mg–Cu–Zr Alloy. *Philosophical Magazine Letters*, 91(3), 214-222.
- Nakazima, K., Kikuma, T., & Hasuka, K. (1968). Study on the formability of steel sheets. *YAWATA TECH REP, SEPT. 1968*, --264--, 8517-8530.
- Narayanan, P., Suwas, S., Sreekumar, K., Sinha, P. P., & Ranganathan, S. (2012). *Evolution of crystallographic texture in cold rolled Al-Zn-Mg alloys used in space applications*. Paper presented at the Materials Science Forum.
- Nicolas, M., & Deschamps, A. (2003). Characterisation and modelling of precipitate evolution in an Al–Zn–Mg alloy during non-isothermal heat treatments. *Acta Materialia*, 51(20), 6077-6094.

- Noell, P., Carroll, J., Hattar, K., Clark, B., & Boyce, B. (2017). Do voids nucleate at grain boundaries during ductile rupture? *Acta Materialia*, 137, 103-114.
- Nurcheshmeh, M., & Green, D. E. (2011). Investigation on the strain-path dependency of stress-based forming limit curves. *International Journal of Material Forming*, 4(1), 25-37.
- Ozturk, F., Dilmeç, M., Turkoz, M., Ece, R. E., & Halkaci, H. S. (2009). *Grid marking and measurement methods for sheet metal formability*. Paper presented at the 5th International Conference and Exhibition on Design and Production of MACHINES and DIES/MOLDS.
- Parmar, A., Mellor, P., & Chakrabarty, J. (1977). A new model for the prediction of instability and limit strains in thin sheet metal. *International Journal of Mechanical Sciences*, 19(7), 389-398.
- Pedersen, K. O., Børvik, T., & Hopperstad, O. S. (2011). Fracture mechanisms of aluminium alloy AA7075-T651 under various loading conditions. *Materials & Design*, 32(1), 97-107.
- Polmear, I. (2006). *Light metals: from traditional alloys to nanocrystals*. Elsevier, Oxford.
- Porter, D., & Easterling, K. (1981). *Phase Transformations in Metals and Alloys*, 1981 Van Nostrand Reinhold: UK.
- Prasad, N. E., Gokhale, A., & Wanhill, R. (2013). *Aluminum-lithium alloys: processing, properties, and applications*: Butterworth-Heinemann.
- Prasad, N. E., & Wanhill, R. (2017). *Aerospace Materials and Material Technologies*: Springer.

- Puttick, K. (1959). Ductile fracture in metals. *Philosophical Magazine*, 4(44), 964-969.
- Raabe, D., Sachtleber, M., Weiland, H., Scheele, G., & Zhao, Z. (2003). Grain-scale micromechanics of polycrystal surfaces during plastic straining. *Acta Materialia*, 51(6), 1539-1560.
- Rakin, M., Cvijović, Z., Grabulov, V., & Kojić, M. (2000). Micromechanism of ductile fracture initiation: void nucleation and growth. *Facta universitatis-series: Mechanical Engineering*, 1(7), 825-833.
- Rice, J. R., & Tracey, D. M. (1969). On the ductile enlargement of voids in triaxial stress fields\*. *Journal of the Mechanics and Physics of Solids*, 17(3), 201-217.
- Robinson, J. (1994). Serrated flow in aluminium base alloys. *International Materials Reviews*, 39(6), 217-227.
- Shi, C., Lai, J., & Chen, X. (2014). Microstructural evolution and dynamic softening mechanisms of Al-Zn-Mg-Cu alloy during hot compressive deformation. *Materials*, 7(1), 244-264.
- Silva, M., Martínez-Donaire, A., Centeno, G., Morales-Palma, D., Valvellano, C., & Martins, P. (2015). Recent Approaches for the Determination of Forming Limits by Necking and Fracture in Sheet Metal Forming. *Procedia Engineering*, 132, 342-349.
- Singh, S. S., Loza, J. J., Merkle, A. P., & Chawla, N. (2016). Three dimensional microstructural characterization of nanoscale precipitates in AA7075-T651 by focused ion beam (FIB) tomography. *Materials characterization*, 118, 102-111.

- Sowerby, R., & Duncan, J. (1971). Failure in sheet metal in biaxial tension. *International Journal of Mechanical Sciences*, 13(3), 217-229.
- Starink, M. (2001). Effect of compositional variations on characteristics of coarse intermetallic particles in overaged 7000 aluminium alloys. *Materials science and technology*, 17(11), 1324-1328.
- Starke, E., & Staley, J. (1996). Application of modern aluminum alloys to aircraft. *Progress in Aerospace Sciences*, 32(2-3), 131-172.
- Suwas, S., & Gurao, N. P. (2008). Crystallographic texture in Materials. *Journal of the Indian Institute of Science*, 88(2), 151-177.
- Suzuki, K., Tanaka, R., & Mori, T. (1985). Suppression of grain boundary sliding by second phase particles. *Scripta Metallurgica*, 19(8), 1005-1008.
- Swift, H. W. (1952). Plastic instability under plane stress. *Journal of the Mechanics and Physics of Solids*, 1(1), 1-18.
- Tajally, M., & Emadoddin, E. (2011). Mechanical and anisotropic behaviors of 7075 aluminum alloy sheets. *Materials & Design*, 32(3), 1594-1599.
- Tajally, M., Huda, Z., & Masjuki, H. (2009). Effect of cold rolling on bending and tensile behaviour of 7075 aluminum alloy. *Journal of Applied Sciences*, 9(21), 3888-3893.
- Tajally, M., Huda, Z., & Masjuki, H. (2010). A comparative analysis of tensile and impact-toughness behavior of cold-worked and annealed 7075 aluminum alloy. *International journal of impact engineering*, 37(4), 425-432.

- Takuda, H., Mori, K., & Hatta, N. (1999). The application of some criteria for ductile fracture to the prediction of the forming limit of sheet metals. *Journal of materials processing technology*, 95(1-3), 116-121.
- Teirlinck, D., Zok, F., Embury, J., & Ashby, M. (1988). Fracture mechanism maps in stress space. *Acta Metallurgica*, 36(5), 1213-1228.
- Thuillier, S., Maire, E., & Brunet, M. (2012). Ductile damage in aluminium alloy thin sheets: Correlation between micro-tomography observations and mechanical modeling. *Materials Science and Engineering: A*, 558, 217-225.
- Tian, H., Brownell, B., Baral, M., & Korkolis, Y. P. (2017). Earing in cup-drawing of anisotropic Al-6022-T4 sheets. *International Journal of Material Forming*, 10(3), 329-343.
- Totten, G. E., & MacKenzie, D. S. (2003). *Handbook of Aluminum: Vol. 1: Physical Metallurgy and Processes* (Vol. 1): CRC press.
- Troeger, L., & Starke, E. (2000). Microstructural and mechanical characterization of a superplastic 6xxx aluminum alloy. *Materials Science and Engineering: A*, 277(1), 102-113.
- Tsao, L., Wu, H., Leong, J., & Fang, C. (2012). Flow stress behavior of commercial pure titanium sheet during warm tensile deformation. *Materials & Design*, 34, 179-184.
- Tvergaard, V. (1981). Influence of voids on shear band instabilities under plane strain conditions. *International Journal of fracture*, 17(4), 389-407.

- Vasudevan, A., & Suresh, S. (1982). Influence of corrosion deposits on near-threshold fatigue crack growth behavior in 2xxx and 7xxx series aluminum alloys. *Metallurgical and Materials Transactions A*, 13(12), 2271-2280.
- Vasudevan, A. K., & Doherty, R. D. (2012). *Aluminum Alloys--Contemporary Research and Applications: Contemporary Research and Applications* (Vol. 31): Elsevier.
- Venkateswarlu, G., Davidson, M., & Tagore, G. (2010). Influence of process parameters on the cup drawing of aluminium 7075 sheet. *International Journal of Engineering, Science and Technology*, 2(11).
- Voce, E. (1948). The relationship between stress and strain for homogeneous deformation. *Journal of the Institute of Metals*, 74, 537-562.
- Waldman, J., Sulinski, H., & Markus, H. (1974). The effect of ingot processing treatments on the grain size and properties of Al alloy 7075. *Metallurgical and Materials Transactions B*, 5(3), 573-584.
- Wang, L., Strangwood, M., Balint, D., Lin, J., & Dean, T. (2011). Formability and failure mechanisms of AA2024 under hot forming conditions. *Materials Science and Engineering: A*, 528(6), 2648-2656.
- Wert, J. A., Paton, N., Hamilton, C., & Mahoney, M. (1981). Grain refinement in 7075 aluminum by thermomechanical processing. *Metallurgical and Materials Transactions A*, 12(7), 1267-1276.
- Wouters, O., Vellinga, W., Van Tijing, R., & De Hosson, J. T. M. (2006). Effects of crystal structure and grain orientation on the roughness of deformed polycrystalline metals. *Acta Materialia*, 54(10), 2813-2821.

- Yang, X., LANG, L., LIU, K., CAI, G., & GUO, C. (2015). Prediction of forming limit diagram of AA7075-O aluminum alloy sheet based on modified MK model. *Journal of Beijing University of Aeronautics and Astronautics*, 4, 016.
- Zhao, Radovitzky, R., & Cuitino, A. (2004). A study of surface roughening in fcc metals using direct numerical simulation. *Acta Materialia*, 52(20), 5791-5804.
- Zhao, Z., & Frankel, G. (2007). On the first breakdown in AA7075-T6. *Corrosion Science*, 49(7), 3064-3088.